

Improving the Properties of Gypsum By Using Additives

Prof. Dr. Z. A. M. Raouf , Ass. Prof. Dr. NADA MAHDY, Hadeel khalid Awad Al- Obaidi

Abstract

Gypsum Plaster is an important building materials, and because of the availability of its raw materials. In this research the effect of various additives on the properties of plaster was studied , like Polyvinyl Acetate, Furfural, Fumed Silica at different rate of addition and two types of fibers, Carbon Fiber and Polypropylene Fiber to the plaster at a different volumetric rate. It was found that after analysis of the results the use of Furfural as an additive to plaster by 2.5% is the optimum ratio of addition to that it improved the flexural Strength by 3.18%. When using Polyvinyl Acetate it was found that the ratio of the additive 2% is the optimum ratio of addition to the plaster, because it improved the value of the flexural strength by a rate of 3.44% of the value of standards fraction of the mixture of reference. It was noted that the optimum ratio for the addition of Fumed Silica to the plaster is the ratio of 1%, because this ratio of addition increases the flexural strength by 15.26%. For the addition of Carbon Fiber to the plaster it was found that the volumetric ratio of the additive 0.5% is the percentage of perfect accessory after taking into account cost and quality which gives an increase in Flexural Strength by rate of 41.43% .When using Polypropylene Fiber it was found that the optimum percentage ratio of addition 1.5%, where this ratio increases flexural strength by a rate of 23.67% . When using the mixture (PVCF), which contains 2% of Poly vinyl Acetate and 0.5% as a volumetric rate of the carbon fiber to the plaster, increases the value of Flexural Strength by a rate 62.92%. After analyzing the results for all mixtures it was found that the mixture (PVCF) is the best one to satisfy the aim of the research which is to get the best structural properties specially flexural strength for gypsum beams.

_____ -1

_____ -4

Majumdar) 1970

(⁸)

)

(

(¹⁸)

_____ -2

(Spraying Process)

%10

(⁹)

)

1986

_____ -3

(CaSO₄.2H₂O)

%1
2 / (2,8)

%3
2 / (3,9)

(
(2-1,5) (2,3)

(CaSO₄) (2)
Calcined) (20)

(CaSO₄) (8) (gypsum
(2) ()

. 2 / (2,15)
(Takeshi and Ju-He)

(¹⁰) 2001

) (CaSO₄)
(20) (

(⁵)



² / (1,15) (IB) (Internal Bond Strength)
 (1,38) %8 (IB) (MOR)
² / (9)
) 2005 %9
 (19)((12) (MOR)
 %12

 %10,17
 (0,75)
 %2,5 %28,34 (18) 2002 ()
 %5 %1,75

 :

 %54,38
 %15
 (/) %0,8
² / (1,4)
² / (1,6) %1,6

 -5
 () 1-5

 ()
) - (1,17) %12
 (27) ()
 (1) (17) 1988 (28)
 (90)

 (16) 1988 (28)

 . (2)

 %
 %4 ² / (0,9)

			2-5
			1-2-5
(161,7)	(-38,7)	Fumed Silica	
(7)	(1,16)		
		Fumed)	
		(Silica, HDK , N20	
		(3) (Wacker Silicones)	
		(14)	
		(5)	
		(6) (SiCl ₄)	
Poly vinyl	3-2-5	Strength	
Acetate (Pva)		(S.A.I)Activity Index	
homo – polymer)	((ASTM C311-02)	(1)
		%110,4	
		(C618-03	
		(2)ASTM	
(CH ₄ H ₆ O ₂) _n		(4)	
(6)			
(12)		FurFural	2-2-5
(ayla)			
(4) (BS 5270-89)			
Carbon Fiber	4-2-5		
Tenax chopped) Tenax			
(carbon fiber products		(C ₄ H ₃ OCHO)	



$$\begin{aligned} \text{MOR} &= \frac{P}{L} \\ &= \frac{P}{b \cdot d} \end{aligned} \quad (170)$$

1-7

$$V_f = 1,5 \cdot 1 \cdot 0,5 \quad (7)$$

Polypropylene fiber

(Sika)

(250×50×50)

(9)

1-7

(13)

$$V_f = 1,5 \cdot 1 \cdot 0,5 \quad (12)$$

$$V_f = 4,5 \cdot 3 \quad (18)$$

(Surfactant)

(8)

(13) (Sika)

Flexural Strength -6

(3,66)(A)

(C) (0,7) (W/J) $\frac{2}{}$

$\frac{2}{}$ (3,34)

(120)

(3,21) (C) $\frac{2}{}$ (3,77)(A)

$\frac{2}{}$

TINIUS) (250×50×50)

(50000) (OLSEN)

(226,8)

(5)

(5+ 170)

(3)(ASTM C293-02)

2-7

1-2-7

(Fur)

%2,5

(7)

(Fur₁)

$$MOR = \frac{3PL}{2bd^2} \quad (1)$$

(FS) (A)
 (28) (120) (Fur₃) %7,5
 (FS₁) %1 %5,09
² / (3,62) (Fur₁) %3,18
 (C) (Fur₃)
 %2 %3,72 %4,5
 (3,17) (FS₂)
² / %9,51
 (FS₄) %6 (11)
² / (2,85) (2) .(2)
 %18,33 (Pva)
 (28) %2
 (120)
 (3,7) %1
² / %15,26 (7)
 %2 %0,8 (PV₁) %2
 (3,2) (FS₂) / (A)
 (FS₄) %6 (PV₃) %5
² / (2,88) %5
 %10,28
 (FS) %1
 (120)
 %3,44 %2
 %5
 %1,59 (A)
 .(4) %2 (Pva)
 (5,12)
 .(3)

الجدول (1) الفحوص الفيزيائية للبورق ومقارنتها بمتطلبات المواصفة العراقية

نوع الفحص	النتائج (%)	حدود المواصفة العراقية رقم (28) (%)
درجة النعومة	(%)	100% المر من منخل رقم (16)
القوام القياس	(%)	—
زمن التماسك	(دقيقة)	25-8
مقاومة الإنضغاط	(كجم/سم ²)	لا تقل عن 50

الجدول (2) نتائج لتحليل كيميائي للبورق ومقارنتها بمتطلبات المواصفة العراقية

المكونات	النتائج (%)	حدود المواصفة العراقية رقم (28) (%)
ثالث أكسيد الكبريت SO ₃	50,74	لا يقل عن 45
أكسيد الكالسيوم CaO	36,4	لا يقل عن 30
أكسيد المغنيسيوم MgO	0,3	
ثالث أكسيد الألمنيوم Al ₂ O ₃	0,14	
ثالث أكسيد الحديد Fe ₂ O ₃	0,05	
المواد المتبقية غير التافية IR (التوابل)	2,57	لا يزيد عن 5
الماء المتحد H ₂ O	5,6	9-4
الفقدان بالحرق L.O.I	7,46	

الجدول (3) بيانات المنتج بحسب دليل شركة وكير⁽¹⁴⁾

القيمة	خصائص لنموذج لعامة
2,2 غم/سم ³	الكثافة
99,8<	محتوى ثاني أكسيد السيليكون (SiO ₂) عند الحرق بدرجة 1000 م° لمدة ساعتين
2>%	الفقدان بالوزن (عند الحرق بدرجة 1000 م° لمدة ساعتين)
(170-230)م ² /غم	المساحة السطحية
3,9-4,3	الدالة الحامضية (pH)
1,5>%	الفقدان عند التجفيف لمدة ساعتين عند درجة 105 م°
0,04>%	المتبقي على الغريال < (40) مايكرون

الجدول (4) التحليل الكيمياوي لمادة الفيوم سليكا المستخدمة في لبحث

النتائج	المركبات
99,1%>	ثاني أكسيد السيليكون SiO ₂
0,0035	ثالث أكسيد الحديد Fe ₂ O ₃
0,035>%	ثالث أكسيد الألمنيوم Al ₂ O ₃
0,006>%	ثاني أكسيد التيتانيوم TiO ₂
0,0052	أكسيد المغنيسيوم MgO
0,7>	ثالث أكسيد الكبريت SO ₃
0,7>	الفقدان بالحرق L.O.I
0,82%	الرطوبة Moisture
0,03	أكسيد الكالسيوم CaO
4,1	الدالة الحامضية pH

الجدول (5) نتائج فحوص مادة الفورفرل

النتائج	التحليل	ت
60م°	Flash Point	-1 نقطة لوميض
1,156 غم/سم ³	Density	-2 الكثافة
Cst 1,0549	Viscosity at 40C°	-3 اللزوجة بدرجة 40 م°
لا يوجد	Water Content	-4 المحتوى المائي

جدول (6) خواص مادة البولني فليل أُسبِت(12)

الخواص	
المظهر	سائل أبيض حليب
الدالة الحامضية	4-5
كثافة	1,05 غم/سم ³
الرائحة	رائحة حامض الأسيتك
درجة الغليان	<100 م°
قابلية الإمتزاج	100% مع ماء

الجدول (7) خواص ألياف لكاربون المقطع حسب دليل شركة (Tenax) (15)

الخواص العامة للمنتج	القيمة
مقاومة شد (ميكا نت/م ²)	3450
معامل شد (كيكا نت/م ²)	<207
نسبة الإستطالة عند القطع (%)	1,7
الكثافة (غم/سم ³)	1,8
طول الألياف (مم)	6
قطر الألياف (مايكرومتر)	7

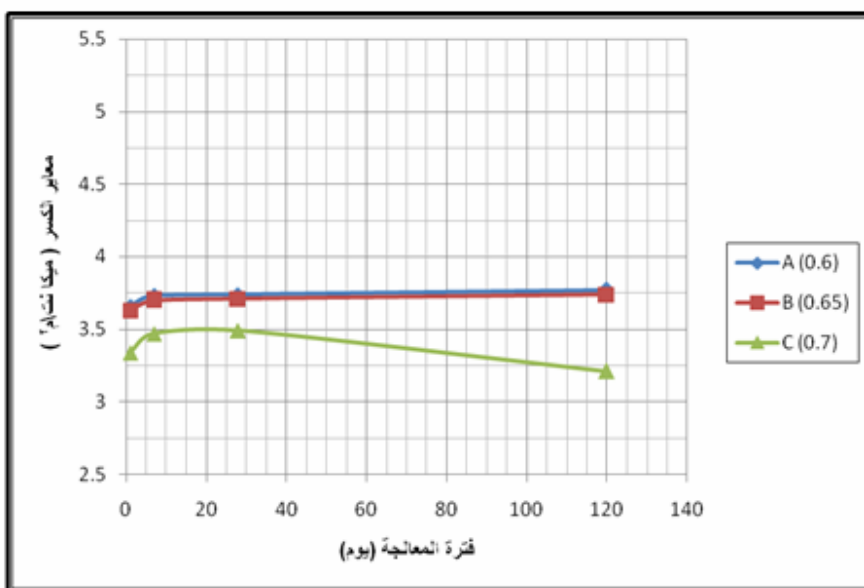


جدول (8) مواصفات ألياف البولي بروبيلين حسب دليل شركة سيكا (13)

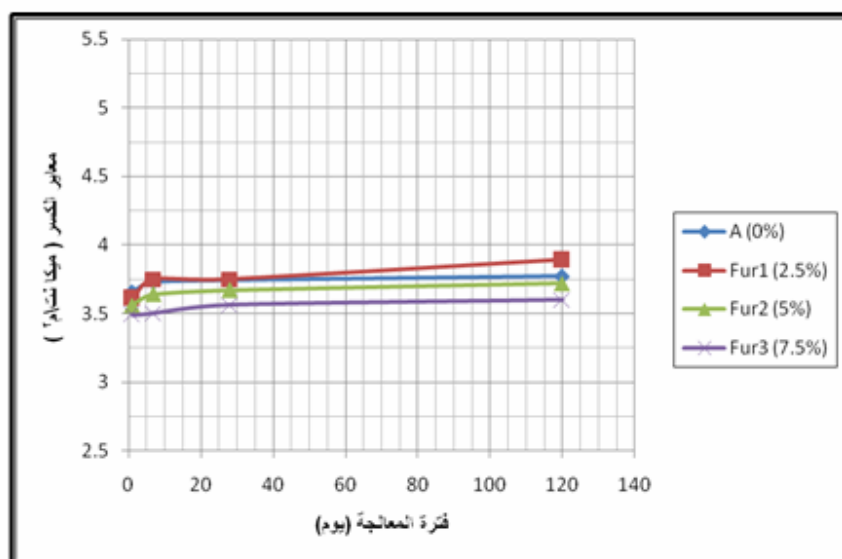
معلومات المنتج	القيمة	القيمة
القاعدة	Base	100% بولي بروبيلين نقي
اللون	Colour	طبيعي
التصميم	Design	شعيرات احادية
طول الليف	Fiber Length	12 ملم
قطر الليف	Diameter	18 مايكرون
المعلومات التقنية والفنية	Technical Data	القيمة
الكثافة	Density	0,91 غم/سم ³
الإمتصاص	Absorption	لا يوجد
المساحة السطحية	Specific Surface Area	250 م ² /كغم
التوصيل الحراري	Thermal conductivity	واضع
التوصيل الكهربائي	Electrical Conductivity	واضع
مقاومة الحواض	Acid Resistance	عالي
مقاومة القواعد	Alkali Resistance	100%
مقاومة الشد	Tensile Strength	350 ميكا نت / م ²

جدول (9) تأثير نسب المواد المضافة وفترة المعالجة على معيار الكسر للخص

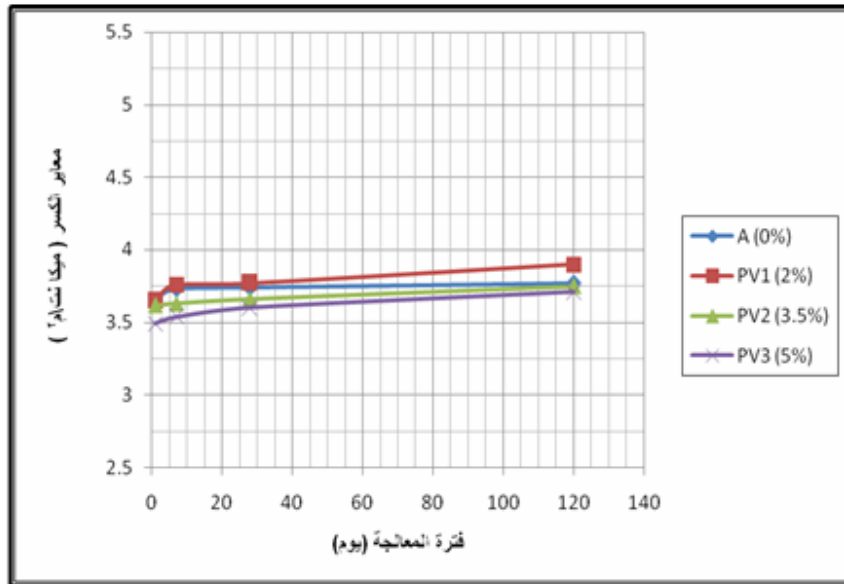
مخططات											
معيار الكسر (ميكا نتا 2)											
رمز مخطط إضافة	نسبة الإضافة %	1 يوم	نسبة التغير ر عن المرجعية %	7 يوم	نسبة التغير ع عن المرجعية %	28 يوم	نسبة التغير عن المرجعية %	120 يوم	نسبة التغير عن المرجعية %		
A	-	3.66	-	3.73	-	3.74	-	3.77	-	مخطط مكرر	
B	-	3.63	-	3.7	-	3.71	-	3.74	-		
C	-	3.34	-	3.47	-	3.49	-	3.21	-		
Fur ₁	2.5	3.61	1.366+	3.75	0.53+	3.75	0.26+	3.89	3.18+	1	
Fur ₂	5	3.56	2.63+	3.64	2.41+	3.67	1.78+	3.72	1.32+		
Fur ₃	7.5	3.46	4.64+	3.5	6.16+	3.56	4.81+	3.6	4.5+		
PV ₁	2	3.65	0.27-	3.76	0.8+	3.77	0.8+	3.9	3.44+	2	
PV ₂	3.5	3.62	1.09+	3.63	2.68+	3.66	2.13+	3.75	0.53+		
PV ₃	5	3.49	4.64+	3.54	5.09+	3.6	3.74+	3.71	1.59+		
FS ₁	1	3.54	5.98+	3.57	2.88+	3.62	3.72+	3.7	15.26+	3	
FS ₂	2	3.11	6.88+	3.14	9.51+	3.17	9.16+	3.2	0.31+		
FS ₃	4	3.04	8.98+	3.12	10.08+	3.13	10.31+	3.16	1.55+		
FS ₄	6	2.73	18.2+	2.82	18.73+	2.85	18.33+	2.88	10.28+	1	
CF ₁	0.5	4.09	22.45+	4.25	22.4+	4.32	23.78+	4.54	41.43+		
CF ₂	1	4.44	32.93+	4.48	29.1+	4.5	28.93+	4.7	46.41+		
CF ₃	1.5	4.85	45.2+	5	44.09+	5.09	45.84+	5.13	59.81+	2	
PPF ₁	0.5	3.58	7.18+	3.64	4.89+	3.67	5.15+	3.7	15.26+		
PPF ₂	1	3.73	11.67+	3.79	9.22+	3.87	10.88+	3.89	21.18+		
PPF ₃	1.5	3.82	14.37+	3.88	11.81+	3.94	12.89+	3.97	23.67+	3	
PPF ₄	3	3.68	10.17+	3.7	6.62+	3.73	9.87+	3.76	17.13+		
PPF ₅	4.5	3.49	4.49+	3.56	2.59+	3.6	3.15+	3.63	13.08+		
PVC F	PVC ⁽²⁾ F ⁽²⁾ CF	4.7	40.71+	4.85	39.76+	5.16	47.85+	5.23	62.92	مخطط مكرر	



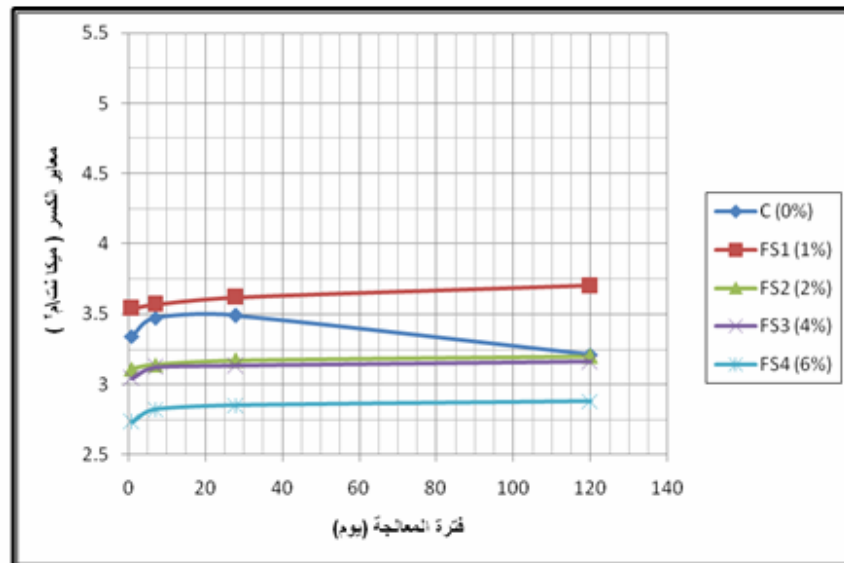
الشكل (1) تأثير اختلاف نسبة ماء المزج (W/J) على معايير كسر للجص ولفترات معالجة مختلفة



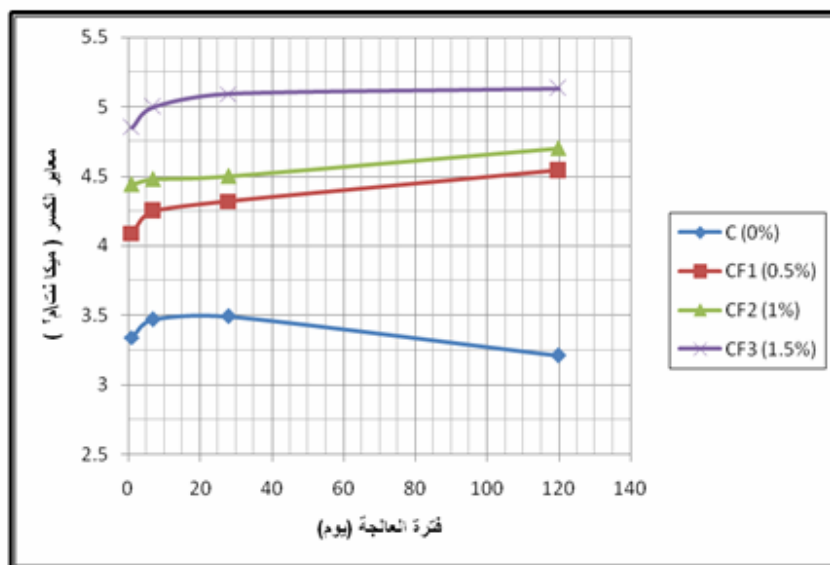
الشكل (2) تأثير نسب الإضافات لمادة الفورفورال على معايير كسر للجص ولفترات معالجة مختلفة



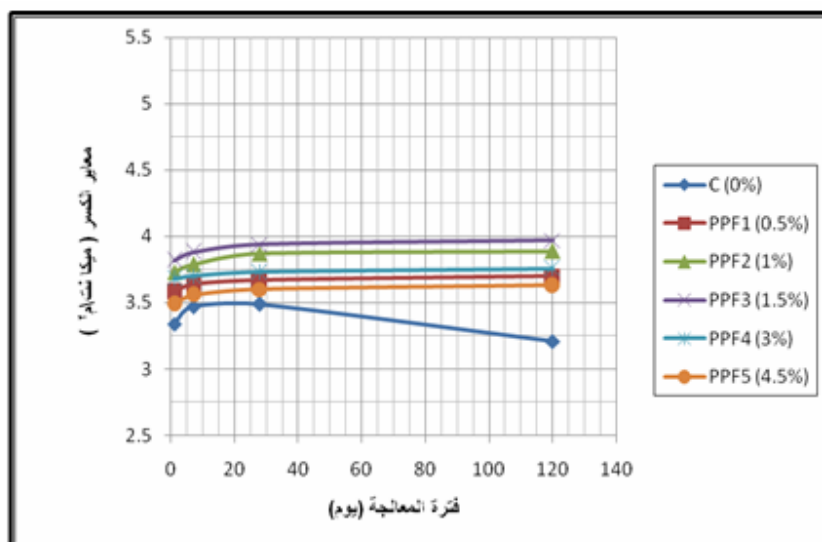
الشكل (3) تأثير نسب الإضافة لمادة (Pva) على معايير لكسر للجنس ولفترات معالجة مختلفة



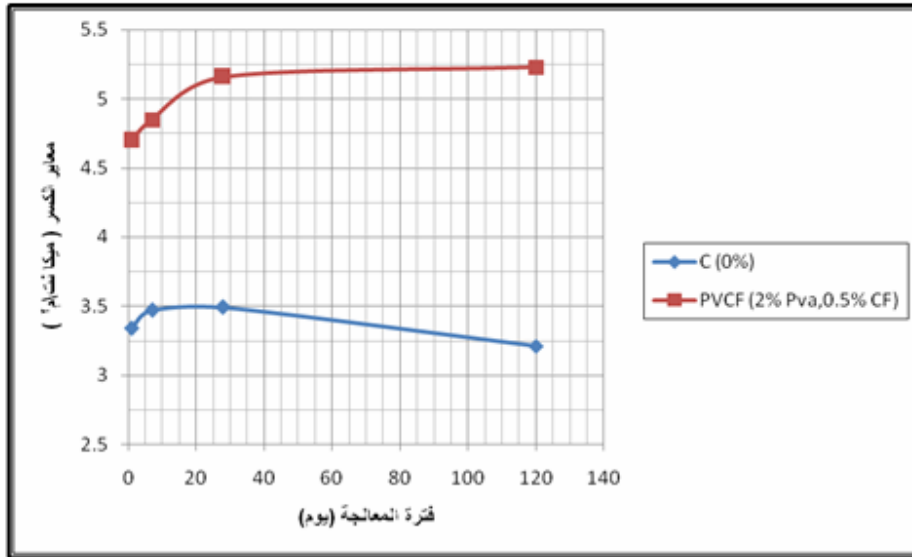
الشكل (4) تأثير نسب الإضافة لمادة الفيوم سليكا على معايير الكسر للجنس ولفترات معالجة مختلف



الشكل (5) تأثير نسب الإضافة الحجمية لألياف الكربون على معايير لكسر للجص ونفترات معالجة مختلفة



الشكل (6) تأثير نسب الإضافة الحجمية لألياف البولي بروبيلين على معايير الكسر للجص ونفترات معالجة مختلفة



الشكل (7) تأثير مضافات الخلطة (PVCF) على معايير الكسر لتجص وفترات معالجة مختلفة



Damage Detection and Assessment of Stiffness and Mass Matrices in Curved Simply Supported Beam Using Genetic Algorithm

Asst. Prof. Dr. Nabil Hassan Hadi
Dept. of Energy
College of Engineering
University of Baghdad

Aveen A. Abdulkareem
M.Sc.

ABSTRACT

In this study, a genetic algorithm (GA) is used to detect damage in curved beam model, stiffness as well as mass matrices of the curved beam elements is formulated using Hamilton's principle. Each node of the curved beam element possesses seven degrees of freedom including the warping degree of freedom. The curved beam element had been derived based on the Kang and Yoo's thin-walled curved beam theory. The identification of damage is formulated as an optimization problem, binary and continuous genetic algorithms (BGA, CGA) are used to detect and locate the damage using two objective functions (change in natural frequencies, Modal Assurance Criterion MAC).

The results show the objective function based on change in natural frequency is the best objective and no error was recorded in prediction of location and small error in detecting damage value. Also the result show that the genetic algorithm method are efficient indicating and quantifying single and multiple damage with high precision, and the prediction error for the CGA are less than corresponding value for the BGA.

الخلاصة:

في هذا البحث تم استخدام الخوارزميه الجينييه لتقييم الضرر في العتبه المقوسه، تم صياغة مصفوفتي الجساءة والكتلة لعنصر العتبه المقوسه باستعمال مبدأ هاملتون. كل عقدة في العتبه المقوسه تحوي على سبع درجات من الحرية مع الاخذ بنظر الاعتبار الاعوجاج (warping). تم اشتقاق عنصر العتبه المقوسه بالاعتماد على نظرية كانك وياو للعتبه المقوسه ذات الجدران الرقيقة. استخدمت الاعداد الحقيقيه ونظام التشغيل الثنائي للخوارزميه الجينييه لتحديد كميته الضرر وموقعه باستخدام دالتين من دوال الهدف (objective function) (change in natural frequencies) و (Modal Assurance Criterion MAC). النتائج اظهرت بأن الفرق في الترددات هي افضل داله موضوعيه و ليس هناك خطأ مسجل في التنبؤ بموقع الضرر وخطأ صغير في تحديد كميته الضرر. وكذلك اثبتت الخوارزميه الجينييه كفاءتها في ايجاد كميته وموقع الضرر المفرد والمتعدد بدقه عاليه وان نسبه الخطا باستخدام الاعداد الحقيقيه اقل نسبيا عند استخدام نظام التشغيل الثنائي.

Keywords: curved beam; Genetic Algorithm; damage detection

INTRODUCTION

At the recent years, genetic algorithms have been recognized as promising intelligent search techniques for difficult optimization problems. Genetic algorithm method is very attractive in comparison with classical methods because it does not require a solution search within the whole solution space. Instead the algorithm starts from a small initial population of approximated solutions and converges rapidly from thereon **W.M.Ostachowicz et al.1996**. **Mares and Surace 1996** employed a GA to identify damage in elastic structures. A modified version of residual force vectors in terms of the stiffness matrix of the damaged structure was chosen as an objective function to be minimized while stiffness reduction factors of all elements were chosen to be variables. **M. I. Friswell et al. 1998** developed a technique, which is based on combined use of eigensensitivity and genetic algorithms to identify the location and magnitude of damage from measured vibration data. They employ a genetic algorithm to minimize a square-value of the frequency error. Structural damage is modeled by a reduction in Young's modulus, while the element number in the finite element model gives damage location. The objective is to identify the position of one or more damage sites in a structure, and to estimate the extent of the damage at these sites. The GA is used to optimize the discrete damage location variables. For a given damage location site or sites, a standard eigensensitivity method is used to optimize the damage extent. This two-level approach incorporates the advantage of both the GA and the eigensensitivity methods. Damage at one and two sites have been successfully located in the simulated example of a cantilever beam, also successfully location in an experimental cantilever plate. **J.H. Chou and J. Ghaboussi 2001** used a GA to solve an optimization problem formulated for detection and identification of structural damage. The "output error" indicating the difference between the measured and

computed responses under static loading and the equation error indicating the residual force in the system of equilibrium equations are used to formulate the objective function to be optimized. The method proposed is capable of successfully detecting the location and magnitude of the damage as well as correctly determining the unmeasured nodal displacement, while avoiding the complete finite element analyses. **E. S. Sazonov et al. 2002** used the GA to produce a sufficiently optimized amplitude characteristic filter to extract damage information from the strain energy mode shapes. A finite element model was used to generate training data set with the known location. The filter amplitude characteristic was encoded as a GA string where the pass coefficient for each harmonic of the Discrete Fourier Transform representation was a number between 0 and 1 in an 8 bit. The genetic optimization was performed based on the minimization of the signal-to-distortion ratio. The results obtained from the GA has confirmed the theoretical predictions and allowed improvements in the method's sensitivity to damages of lower magnitude.

In this study, it had been used a binary and continuous genetic algorithm for damage detection and location in (in and out-of-plane) curved beam by minimizing or maximizing the objective function which is based on frequency difference and modal assurance criterion MAC.

I. MODELING THE DAMAGED BEAM.

In this study the equation of motion for simply curved beam acquired from Kang and Yoo's theory of thin-walled curved beams to drive the element stiffness and mass matrices respectively. The curved beam element is shown in **Fig.1** in curvilinear coordinate system. Each node of the curved beam element possesses seven degrees of freedom including the warping degree of freedom. Using Hamilton's principle, the dynamic equilibrium can

be expressed in the variation form as following **K. Young Yoon et al. 2006.**

$$\int_{t_1}^{t_2} (\delta T + \delta U + \delta V) dt = 0 \quad (1)$$

Where δT is the variation kinetic energy, δU is the variation strain energy, and δV is the variation potential energy loss due to applied loads. The symbol (δ) means the first variation. For the linear elastic body, the variation of strain energy stored in the body is

$$\delta U = \int_V \tau_{ij} \delta \epsilon_{ij} dV \quad (2)$$

Where τ_{ij} refers to the components of the stress tensor and ϵ_{ij} to those of the strain tensor. The variation in kinetic energy of a thin-walled curved beam is

$$\delta T = \int_V \rho \frac{\partial^2 u_i}{\partial t^2} \delta u_i dV \quad (3)$$

Where ρ is the mass density, u_i is the displacement components of the curved beam, and t is time. The variation potential energy loss due to applied loads with body forces neglected is

$$\delta V = - \int_l q_i \delta u_i dz \quad (4)$$

Where q_i stands for distributed loads applied on the line of shear center and l is the length of the element.

A linear stiffness matrix and a consistent mass matrix are developed so that various analyses such as linear and free vibration analyses can be performed. Using shape functions, the dynamic equilibrium given in eq. (1) yields a set of simultaneous equations

$$\delta T + \delta U + \delta V = \delta d^T [M d + K d - f] = 0 \quad (5)$$

From which one obtains.

$$M \ddot{d} + K d - f = 0 \quad (6)$$

Where K , M , d , and f are the linear stiffness matrix, the consistent mass matrix, the nodal

displacement vector, and the applied force vector of a global structural system, respectively. The nodal forces and the corresponding nodal displacements are shown in **Fig.1** in the positive senses. The nodal forces are seven components $(F_z, M_x, M_y, B, T_T, V_x, \text{ and } V_y)$. The corresponding nodal displacements are $(w_0, \gamma, -v_0, -\tau, \beta, u_0, \text{ and } v_0)$ where γ and τ are defined as

$$\gamma = u_0' + \frac{w_0}{R} \quad (7a)$$

$$\tau = \beta' + \frac{v_0}{R} \quad (7b)$$

w_0 , u_0 , and γ describe the in-plane displacements whereas v_0 , $-v_0'$, β , and $-\tau$ are the out-of-plane displacements. These two parts of displacement fields are not coupled with each other and can be formulated separately. Then, the displacement fields can be expressed in terms of nodal displacements as following **K. Young Yoon et al. 2005.**

$$\begin{Bmatrix} u_0 \\ v_0 \\ w_0 \\ \beta \end{Bmatrix} = \begin{bmatrix} N_u & 0 & 0 & 0 \\ 0 & N_v & 0 & 0 \\ 0 & 0 & N_w & 0 \\ 0 & 0 & 0 & N_\beta \end{bmatrix} \begin{Bmatrix} d^u \\ d^v \\ d^w \\ d^\beta \end{Bmatrix} \quad (8)$$

Where the shapes function, N is defined as.

$$N_u = [1 - 3\xi^2 + 2\xi^3 \quad (\xi - 2\xi^2 + \xi^3) \quad 3\xi^2 - 2\xi^3 \quad (-\xi^2 + \xi^3)] \quad (9a)$$

$$N_v = N_\beta = [1 - 3\xi^2 + 2\xi^3 \quad (-\xi + 2\xi^2 - \xi^3) \quad 3\xi^2 - 2\xi^3 \quad (-\xi^2 + \xi^3)] \quad (9b)$$

$$N_w = [1 - \xi \quad \xi] \quad (9c)$$

Where $\xi = z/l$

Where the nodal displacement, d is represented

$$d^u = [u_{oi} \quad \gamma_i \quad u_{oj} \quad \gamma_j]^T \quad (10a)$$

$$d^v = [v_{oi} \quad -v_{oi}' \quad v_{oj} \quad -v_{oj}']^T \quad (10b)$$

$$d^w = [w_{oi} \quad w_{oj}]^T \quad (10c)$$

$$d^\beta = [\beta_i \quad -\tau_i \quad \beta_j \quad -\tau_j]^T \quad (10d)$$

From the variation of strain energy presented in eq. (2) and the shape function in equations (9a), (9b), and (9c) the element stiffness matrix for curved beam is derived as shown **K.Young Yoon et al. 2005.**

$$[k_w] = \begin{bmatrix} EI_y K_a & 0 & 0 & 0 \\ 0 & EI_x K_b & 0 & 0 \\ 0 & 0 & EAK_c & 0 \\ 0 & 0 & 0 & EI_w K_d + GK_T K_e \end{bmatrix} \quad (11)$$

Where:

$$K_a = \int_l N_u^T N_u dz =$$

$$\frac{1}{l^3} \begin{bmatrix} 12 & 6l & -12 & 6l \\ & 4l^2 & -6l & 2l^2 \\ \text{Sym.} & & 12 & -6l \\ & & & 4l^2 \end{bmatrix}$$

$$K_b = \int_l N_v^T N_v dz =$$

$$\frac{1}{l^3} \begin{bmatrix} 12 & 6l & -12 & 6l \\ & 4l^2 & -6l & 2l^2 \\ \text{Sym.} & & 12 & -6l \\ & & & 4l^2 \end{bmatrix}$$

$$K_c = \int_l N_w^T N_w dz = \frac{1}{l} \begin{bmatrix} 1 & -1 \\ \text{Sym.} & 1 \end{bmatrix}$$

$$K_d = \int_l N_\beta^T N_\beta dz =$$

$$\frac{1}{l^3} \begin{bmatrix} 12 & -6l & -12 & -6l \\ & 4l^2 & 6l & 2l^2 \\ \text{Sym.} & & 12 & 6l \\ & & & 4l^2 \end{bmatrix}$$

$$K_e = \int_l N_\beta^T N_\beta dz =$$

$$\frac{1}{30l} \begin{bmatrix} 36 & -3l & -36 & -3l \\ & 4l^2 & 6l & -l^2 \\ \text{Sym.} & & 36 & 3l \\ & & & 4l^2 \end{bmatrix}$$

From the variation kinetic energy presented in eq. (3) and following the similar procedure as used for the element stiffness matrix for curved beam formulation, the mass matrix is derived.

$$[m_w] = \rho \begin{bmatrix} AM_a + I_y M_e & 0 & 0 & 0 \\ 0 & AM_b + I_x M_b & 0 & 0 \\ 0 & 0 & AM_c & 0 \\ 0 & 0 & 0 & (I_x + I_y) M_a + I_w M_f \end{bmatrix} \quad (12)$$

Where:

$$M_a = \int_l N_u^T N_u dz =$$

$$\frac{l}{420} \begin{bmatrix} 156 & 22l & 54 & -13l \\ & 4l^2 & 13l & -3l^2 \\ \text{Sym.} & & 156 & -22l \\ & & & 4l^2 \end{bmatrix}$$

$$M_b = \int_l N_v^T N_v dz =$$

$$\frac{l}{420} \begin{bmatrix} 156 & -22l & 54 & 13l \\ & 4l^2 & -13l & -3l^2 \\ \text{Sym.} & & 156 & 22l \\ & & & 4l^2 \end{bmatrix}$$

$$M_c = \int_l N_w^T N_w dz = \frac{l}{6} \begin{bmatrix} 2 & 1 \\ \text{Sym.} & 2 \end{bmatrix}$$

$$M_e = \int_l N_\beta^T N_\beta dz =$$

$$\frac{1}{30l} \begin{bmatrix} 36 & 3l & -36 & 3l \\ & 4l^2 & -3l & -l^2 \\ \text{Sym.} & & 36 & -3l \\ & & & 4l^2 \end{bmatrix}$$

$$M_f = \int_l N_\beta^T N_\beta dz =$$

$$\frac{1}{30l} \begin{bmatrix} 36 & -3l & -36 & -3l \\ & 4l^2 & 3l & -l^2 \\ \text{Sym.} & & 36 & -3l \\ & & & 4l^2 \end{bmatrix}$$

II. APPLICATION OF A GENETIC ALGORITHM.

GA is a global probabilistic search algorithm inspired by Darwin's survival-of-the-fittest theory. In this optimization method, information about a problem, such as variable parameters, is coded into a genetic string known as an individual (chromosome). Each of these individuals has an associated fitness value, which is usually determined by the objective function to be maximized or minimized. Genetic algorithms have been shown to be able to solve the optimization problem through mutation, crossover and selection operation applied to individuals in the population.

II.I Population

The initial population are created randomly by generating the required number of individuals but a new population developed from this initial population and to do this must apply the genetic operator. The initial populations are generated by the following equation **L. Randy Haupt, S. Ellen Haupt 2004:**

$$P = X_{LB} + \text{rand}(N_{\text{pop}}, N_{\text{var}})(X_{UB} - X_{LB}) \quad (13)$$

Where:

(X_{UB}, X_{LB}) means the range of maximum and minimum values allowed for each variable respectively.

N_{pop} = The number of population.

N_{var} = The number of variable.

In this population, there are several individuals carrying different "genetic information" in their string or coding. When working with binary coded genetic algorithms each of the real parameters to be optimized is translated to binary codes.

- To transform the real values (b_i) to binary codes the following equation is used **H. M. Gomes and N. R. S. Silva (2007)**

$$s = \text{bin}_n \left\{ \text{round} \left(2^{n \text{ bit}} - 1 \right) \left[\frac{b_i(k) - X_{LB}}{X_{UB} - X_{LB}} \right] \right\} \quad (14)$$

Where bin_n indicates a binary translation to a string s , and n bit means the number of bit.

- To transform the binary codes to real values (decoding) the following equation is used.

$$b_i(k) = X_{LB} + \text{bin}^{-1}(s) \left[\frac{X_{UB} - X_{LB}}{2^{n \text{ bit}} - 1} \right] \quad (15)$$

Where $\text{bin}^{-1}(s)$ is the nonnegative integer decoded from the base 2 binary representation, From this equation it is obvious that the precision by the binary coding is $(X_{UB} - X_{LB}) / (2^{n \text{ bit}} - 1)$

II.II Fitness Function

In order to determine the ability of an individual to search better solution, a fitness function is used to quantify how good the solution represented by a chromosome is. Depending on the problem characteristic, the fitness function can be any form of mathematical formulation, can be either a maximized or minimized function. This function generates an output from the set of input variables of a chromosome. The goal is to modify the output in some desirable fashion by finding the appropriate values of input variables.

In this work the two objective functions are used to assess the presence of damage in beam.

- Changes in Natural Frequencies.
- Modal Assurance Criterion.

Changes in Natural Frequencies

The natural frequency used as a diagnostic parameter in structural assessment procedures using vibration monitoring. One great advantage of using only eigenvalue in the damage assessment of structures is that they are cheaply acquired and the approach can

give an inexpensive structural assessment technique. The objective function to be minimized is defined as follows **M. T. V. Baghmisheh et al 2008:**

$$\Delta\omega = \sum_{i=1}^n (\omega_i^m - \omega_i^c)^2 \quad (16)$$

Where:

i = Mode Number ($i=1,2,3,\dots,n$)

ω_i^m = Test natural frequencies

ω_i^c = Calculated natural frequencies.

The ω_i^m are the natural frequencies which are applied to our damage detection system as inputs. An objective value of zero indicates an exact match between the values of frequencies.

Modal Assurance Criterion.

The Modal Assurance Criterion MAC value indicates the degree of correlation between two modes and varies from 0 to 1, with 1 for full correlation, and 0 for no- correlation. The deviation from 1 can be interpreted as a damage indicator in structures. This index is based on comparisons between the changes in the mode shapes obtained both from tests and from calculations, the MAC is defined by **W. M. Ostachowicz et al. 1996:**

$$MAC(\phi_i, \phi_j) = \frac{(\phi_i^T \phi_j)^2}{\phi_i^T \phi_i \phi_j^T \phi_j} \quad (17)$$

ϕ_i = Test mode shape vector.

ϕ_j = calculate mode shape vector.

II.III Selection (reproduction)

Reproduction is the first operator applied on a population. The first step in the reproduction is fitness assignment. Each individual receives a reproduction probability depending on

the own objective (fitness) value and the objective value of all other individuals in the population. The evaluation of this objective function indicates which individuals will have more chances to procreate and to generate a large offspring.

There are various selection processes that are utilized in genetic algorithms such as roulette wheel selection, rank selection and tournament selection. A common processes and used in this work are the roulette wheel selection. This selection method was used to copy individuals according to their fitness values, individuals with higher fitness have a higher probability of contributing one or more offspring in the next generation. For each population individual a probability of being selected for copying is given by the following equation **D. E. Goldberg 1989:**

$$P_i = \frac{f_i}{\sum_{j=1}^{P_{size}} f_j}$$

$$i, j = 1, 2, \dots, P_{size} \quad (18)$$

Where f_j is the fitness of individual j , the sum is taken over all population members (P_{size}), and P_i is the probability of individual i with fitness f_j receiving an additional copy.

II.IV Recombination (Crossover)

Crossover is one of the recombination operators that is used for information exchange between any two individuals to create two offspring. Each pair of parents have a probability, P_c , of producing offspring. Usually, a high crossover probability is used.

- Real value Recombination: The variable values of the offspring are chosen somewhere around and between the variable values of the parents. Offspring are produced according to the rule **H. Pohlheim 2007:**

$$\text{Var}_i^o = \text{var}_i^{p1} \cdot \alpha_i + \text{var}_i^{p2} \cdot (1 - \alpha_i)$$

$$i \in (1, 2, \dots, N_{var}) \quad (19)$$

Where α is a scaling factor chosen uniformly a random over an interval $[-0.25, 1.25]$ for each a new.

- Binary valued Recombination: The some of the crossover operators available in GA are single point crossover, two-point crossover and uniform crossover. In this work a single point crossover is applied, where one crossover position (n) a long the string is selected randomly between 1 and the string length less one. Two new strings are created by swapping all characters between the individuals about this point.

II.V Mutation

Mutation means a random change in the information of a chromosome, to add diversity to the genetic characteristics of the population. It is applied at a certain probability, P_m , to each gene of the offspring, the mutation probability also called mutation rate, is usually a small value, to ensure that good solutions are not distorted too much. Mutation of real variables means, that randomly created values are added to the variables selected. The mutation rule is:

$$C = P + \text{rand} (X_{UB} - X_{LB}) \quad (20)$$

Where C is mean the child and P mean parent For binary mutation, randomly change a particular gene in a chromosome, thus, 1 may be changed to a 0 or vice versa.

II.VI Elitism

In the process of the crossover and mutation- taking place, there is high chance that the optimum solution could be lost. There is no guarantee that these operators will preserve the fittest string. To avoid this, the elitist models are often used. Elitism refers to the process of ensuring that the best chromosome (or few best chromosomes) of the current population

survive to the next generation. The best individuals are copied to the new population without being mutated. Elitism can rapidly increase the performance of GA, because it prevents a loss of the best found solution **M. Obitko1998**

II.VII Termination

The GA may be terminated by using the convergence criterion in order to get an acceptable approximate solution, the terminate if there is no improvement over a number of consecutive generation, by monitoring the fitness of the best individual if there is no significant improvement over a time, GA is to stop. Or if the objective function value of the fittest individual is 0 or very small number, which means that the optimal solution has been found.

In the present work the chromosome has two variables, the damage location and the stiffness reduction. The objective function generates an output from the set of input variables of a chromosome. The goal is to modify the output in some desirable fashion by finding the appropriate values of input variables. **Fig.2** shows the flowchart of the method of damage detection using genetic algorithms.

III. NUMERICAL SIMULATION

The processes of damage detection are demonstrated using (in and out-of-plane) simply supported curved beam. The dimensions and material properties for the simply supported in and out-of-plane curved beam are shown in **Table 1** and **Table 2** respectively.

In and out-of-plane simply supported curved beam is divided into 30 finite elements of equal length, where the value of first natural frequency is used for convergent test for checking the stability of the results as shown in the **Fig. 3** and **Fig. 4** for in and out-of-plane respectively.

Six damage scenarios are investigated and are summarized in **Table 3**.In the first four

cases for single damage, the scenarios were simulate by reducing the stiffness of an element near the beam's end and near the beam's mid-span. The remaining damage cases D5 and D6 in the same table correspond to a multiple damage scenario and were simulated by reducing the stiffness of assumed elements at two different locations. The following parameters of the GA have been used: size of the population is 40, probability of crossover P_c is 0.9, probability of mutation P_m is 0.05, number of elitism is 2 and number of bit is 20.

IV. RESULTS AND DISSCUSION

The frequency predictions from the FEM model of undamaged beam are validated by comparing with other researches as shown in **Tables 4** and **Table 5** for in and out-of-plane curved beam respectively.

IV.I Objective Function Based on Change in Natural Frequency.

The input first five natural frequencies of damage scenarios are shown in **Table 6** and **Table 7** for out-of-plane and in-plane curved beam respectively. A population of individuals is generated randomly then the natural frequencies and objective function are calculated for each individual. The GAs theory is used to find the optimal location and stiffness reduction by minimizing the eq. (16). For each scenario the algorithm is run from five different initial random population and the identified values for damage scenarios by using CGA and BGA are shown in **Table 8** for out-of-plane and **Table 9** for in-plane curved beam. In all scenarios there are no error recorded in prediction of damage element and the errors for the CGA are less than corresponding values for the BGA, because in the CGA deals with real values without using any encoding method.

Fig. 5 show the typical objective function curve for out-of-plane at D4 by using CGA, it is see that the objective function value tends to zero with the increasing number of generations and reach zero at around 21 generations. The

Fig. 6 shows the objective function curves at same damage scenario but using BGA, the convergence occurs at 28 generation.

IV.II Objective Function Based on Modal Assurance Criterion (MAC)

The mode shapes are calculated numerically using finite element model for the damaged scenarios, these used as test inputs for the GA operator. A population of individuals is generated randomly then the objective function is calculated for each individual and the GAs theory is applied. For each scenario the algorithm is run in five different initial randomly generated populations and the average results obtained by CGA and BGA listed in **Table 10** for out-of-plane and **Table 11** for in-plane curved beam. The errors for CGA are less than corresponding values for the BGA.

For out-of-plane curved beam the objective function with multi damage for D5 using CGA is shown in **Fig. 7** it can seen that convergence occurs at 15 generations.

V. CONCLUSIONS

The main conclusions from the present work may be stated as follows:

- The study shows that the genetic algorithm is effective in identifying positions and extents in single and multi damage.
- The results obtained from continuous genetic algorithms are more accurate then those obtained from binary genetic algorithms in damage assessment.
- The length of the run (in terms of generation number) and results depends on the initial randomly generated population and GA parameters and the test point.
- The objective function based on change in natural frequency is the best objective function, because the stiffness reduction has a relatively large



effect on the natural frequencies, as compared with mode shapes, it is insensitive of the modes to the damage.

REFERENCES

- Andrew Chipperfield, Peter Fleming, Hartmut Pohlheim and Carlos Fonscca, "Genetic algorithm Toolbox for use with Matlab" User's Guide, Version 1.2
- D. E. Goldberg, "Genetic Algorithms in Search, Optimization, and Machine Learning", Addison-Wesley, 1989.
- E. S. Sazonov, P. Klinkhachorn and U. B. Halabe (2002). "Genetic algorithms-based parameter optimization of non-destructive damage detection method". IEEE Trans
- H. M. Gomes and N. R. S. Silva (2007). "Some comparisons for damage detection on structures using genetic algorithms and modal sensitivity method". Journal of Applied Mathematical Modeling.
- H. Y. Guo and Z. L. Li (2008). "A two-stage method to identify structural damage sites and micro-search genetic algorithm". Journal homepage: [www.elsevier.com / locate/ jnlabr/ymssp](http://www.elsevier.com/locate/jnlabr/ymssp)
- H. Pohlheim, "Evolutionary algorithm: Overview, Methods and Operators". Version 3.7, November, 2007. Available At www.Geatbx.Com/
- J. H. Chou and J. Ghaboussi (2001). "Genetic algorithm in structural damage detection". Journal of Computers and Structures". Vol. 79, Pages 1335-1353.
- Ki-Young Yoon, Nam Hoi Park, Young Joon Choi, and Young-Jong Kang (2006). "Natural frequency of thin-walled curved beams" Journal of Finite Element in Analysis and Design. Vol. 42, Pages 1176 – 1186.
- Ki-Young Yoona, Young-Jong Kangb, Young-Joon Choic, and Nam-Hoi Parkb. "Free vibration analysis of horizontally curved steel I-girder bridges". Journal of Thin-Walled Structures. Vol. 43, Pages 679–699(2005).
- M. Obitko, Genetic Algorithm, available at <http://cs.felk.cvut.cz/~xobitko/go/main.Html>, 1998.
- M. I. Friswell, J. E. T. Penny, S. D. Garvey (1998). "A combined genetic and eigensensitivity algorithm for the location of damage in structures". Journal of Computers and Structures. Vol. 69, Pages 547-556.
- C. Mares, C. Surace (1996). "An application of genetic algorithms to identify damage in elastic structures" Journal of Sound and Vibration. Vol. 195, No. 2, Pages 195-215.
- M. T. V. Baghmisheh, M. Peimani, M. H. Sadeghi, M. M. Etefagh (2008). "Crack detection in beam-like structures using genetic algorithms" Journal of Applied Soft Computing. Vol. 8, Pages 1150-1160.
- L. Randy ,S. Ellen Haupt (2004). "Practical genetic algorithms", Jone Wiley and Sons Publishers, Second edition (book).
- R. Song He and S. F. Hwang (2006). "Damage detection by an adaptive real-parameter simulated annealing genetic algorithm" Journal Computers and Structures. Vol. 84, Pages 2231-2243.
- W. M. Ostachowicz, M. Krawczuk and M. P. Cartmell (1996). "Genetic algorithms in health monitoring of structures", University of Glasgow, Department of Mechanical Engineering, James Watt Bulding, Glasgow, Scotland, Internal Report.

Notation

A	Sectional area (m^2)
B_i	Bimoment (N .m)
E	Young modulus (N/m^2)
G	Shear modulus (N/m^2)
GA	Genetic Algorithm.
I_y	Area moment of inertia about y-axis (m^4)
I_x	Area moment of inertia about x-axis (m^4)
I_ω	Warping moment of inertia (m^6)
J	Area polar moment of inertia (m^4)
K_T	St Venant constant of a straight member(m^4)
l	Length of the finite element (m, cm)
M_x, M_y	Moment about x- and y-axis (N.m)
MAC	Modal Assurance Criterion
m_x, m_y, m_z	Uniform distributed moments about x-, y-, and z-axis
m_ω	Uniform distributed bimoment
N_{POP}	Number of population
N_{var}	Number of variable
P_{siz}	Population size
q_x, q_y, q_z	Uniform distributed forces about x-, y-, and z-directions
R	Radius of initial curvature (m)
T	Kinetic energy (N.m)
U	Strain energy (N.m)
u_o, v_o	Displacement components of the shear center in x- and y- directions, respectively
V	Volume of body (m^3)
V_x, V_y	Transverse shear forces (N)
w_o	Average longitudinal displacement of cross-section
X_{UB}	Maximum value of variable
X_{LB}	Minimum value of variable

Greek letters

ρ	Mass density (Kg/m^3)
β	Rotation of the cross-section about z-axis
θ	Subtended angle (degree)
ϵ_{ij}	Components of strain tensor
δ	Variation
γ, τ	Nodal displacements
τ_{ij}	Components of stress tensor



Table 1 Material properties of the in-plane curved beam

Area of cross section (A)	$4 \times 10^{-3} \text{m}^2$
Radius of the arch (R)	2.438 m
Mass density (ρ)	7850 kg/m^3
Subtended angle (θ)	97°
Modules of Elasticity (E)	200 GPa
Modules of Rigidity (G)	77 GPa
Moment of inertia (I)	$6.45 \times 10^{-6} \text{m}^4$

Table 2 Material properties of the out-of- plane curved beam

Area of cross section (A)	$9.3 \times 10^{-3} \text{m}^2$
Length (L)	10 m
Mass density (ρ)	7850 kg/m^3
Subtended angle (θ)	89°
Modules of Elasticity (E)	200 GPa
Modules of Rigidity (G)	77GPa
Moment of inertia (Ix)	$1.13 \times 10^{-4} \text{m}^4$
Moment of inertia (Iy)	$3.88 \times 10^{-5} \text{m}^4$
Warping moment of inertia (I ω)	$5.56 \times 10^{-7} \text{m}^6$
Venant constant (K_T)	$5.38 \times 10^{-7} \text{m}^4$



Table 3 Damage scenario for in and out-of-Plane curved beam

Damage Scenario	Damage Element	Stiffness reduction %
D1	8	25
D2	11	50
D3	16	25
D4	25	50
D5	6,15	25
D6	8,25	25

Table 4 Comparisons of modal frequencies for in-plane curved beam

Mode No.	Natural Frequency(rad/sec)		Error (%)
	[Ki. Young et al] Results	Present Numerical Results	
1	396.98	396.936	0.011
2	931.22	930.94	0.03
3	1797.31	1796.67	0.035

Table 5 First natural frequencies for the simply supported out-of- plane curved beam

Subtended Angle (degree)	Natural Frequency (rad/sec)			Error (%)
	Analytical Results[Ki-Young et al]	Numerical Results[Ki-Young et al]	Present Numerical Results	
0	53.3000	53.3000	53.266	0.06379
10	31.8648	31.8669	31.863	0.0056
20	19.9616	19.9614	19.9592	0.01202
30	13.9944	13.9931	13.9915	0.0207
40	10.5386	10.5372	10.5343	0.0408
50	8.2946	8.2888	8.28753	0.08523
60	6.7121	6.7012	6.70043	0.1739
70	5.5270	5.5090	5.50836	0.33725
80	4.5991	4.5707	4.57020	0.62838
90	3.8479	3.8048	3.87485	0.70038

Table 6 Natural frequencies for out-of-plane curved beam

Damage Scenario	ω_1	ω_2	ω_3	ω_4	ω_5
D1	3.8583	45.456	168.575	381.32	661.097
D2	3.8452	45.113	168.525	373.46	647.75
D3	3.8664	45.532	168.139	381.2	658.47
D4	3.867	45.629	168.98	381.195	664.313
D5	3.8461	45.286	166.86	379.147	565.786
D6	3.8372	45.211	167.29	379.23	660.017

Table 7 Natural frequencies for in-plane curved beam

Damage Scenario	ω_1	ω_2	ω_3	ω_4	ω_5
D1	392.685	926.68	1796.3	1980.6	2897.9
D2	389.175	929.03	1747.9	1963.6	2869.4
D3	396.876	921.37	1795.6	1980.4	2885.7
D4	386.261	905.81	1770.2	1960.9	2901.9
D5	386.182	878.912	1767.5	1923.3	2825.8
D6	374.657	893.524	1768.9	1926.9	2858.3

Table 8 Identified stiffness parameters for out-of-plane curved beam based on change in natural frequency

Test Element No.	Stiffness Parameters				
	Actual	Identified by CGA	Error %	Identified by BGA	Error %
8	0.75	0.7491003	0.11	0.749992	0.001
11	0.5	0.5002577	0.051	0.500381	0.076
16	0.75	0.7503839	0.051	0.7500715	0.01
25	0.5	0.4999999	0.00001	0.5000152	0.003
6,15	0.75	0.7555629	0.48	-	-
8,25	0.75	0.7334992	2.2	-	-



Table 9 Identified stiffness parameters for in-plane curved beam based on change in natural frequency

Test Element No.	Stiffness Parameters				
	Actual	Identified by CGA	Error %	Identified by BGA	Error %
8	0.75	0.7499999	0.00001	0.7500007	0.00009
11	0.5	0.5001478	0.03	0.4999847	0.003
16	0.75	0.7499999	0.00001	0.7499988	0.0001
25	0.5	0.5000117	0.002	0.5000152	0.003
6,15	0.75	0.7514097	0.18	-	-
8,25	0.75	0.7481410	0.24	-	-

Table 10 Identified stiffness parameters for out-of-plane curved beam based on MAC

Test Element No.	Stiffness Parameters				
	Actual	Identified by CGA	Error %	Identified by BGA	Error %
8	0.75	0.7505467	0.07	0.753685	0.5
11	0.5	0.5023270	0.46	0.5076601	1.5
16	0.75	0.7517007	0.22	0.7468184	0.42
25	0.5	0.5046008	0.92	0.5088810	1.77
6,15	0.75	0.7340752	2.2	-	-
8,25	0.75	0.7702559	2.7	-	-

Table 11 Identified stiffness parameters for in-plane curved beam based on MAC

Test Element No.	Stiffness Parameters				
	Actual	Identified by CGA	Error %	Identified by BGA	Error %
8	0.75	0.7430990	0.92	0.7757013	3.4
11	0.5	0.5044385	0.88	0.4923729	1.5
16	0.75	0.7547156	0.63	0.7459007	0.54
25	0.5	0.5123102	2.4	0.5155471	3.1
6,15	0.75	0.7256023	3.2	-	-
8,25	0.75	0.7829436	4.3	-	-

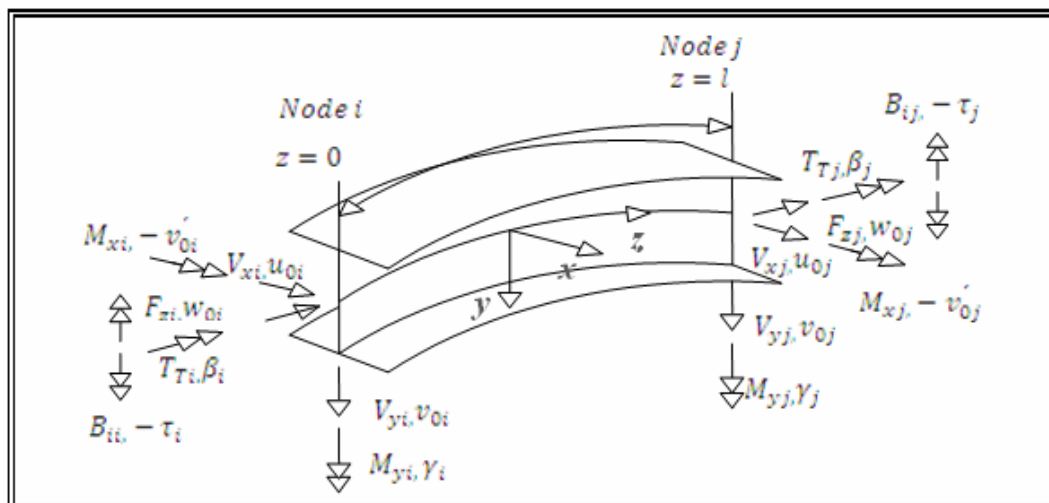


Fig. 1. Curved beam element

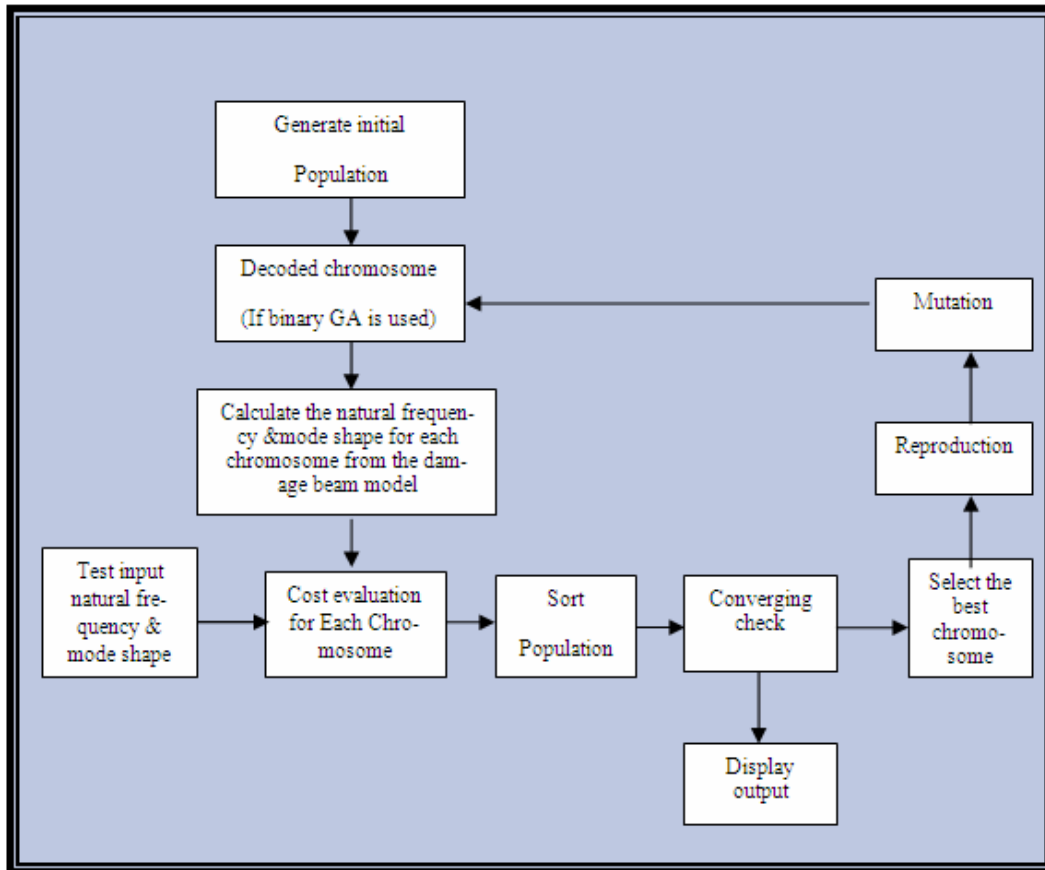


Fig. 2 Flowchart of suggested damage detection method using GAs

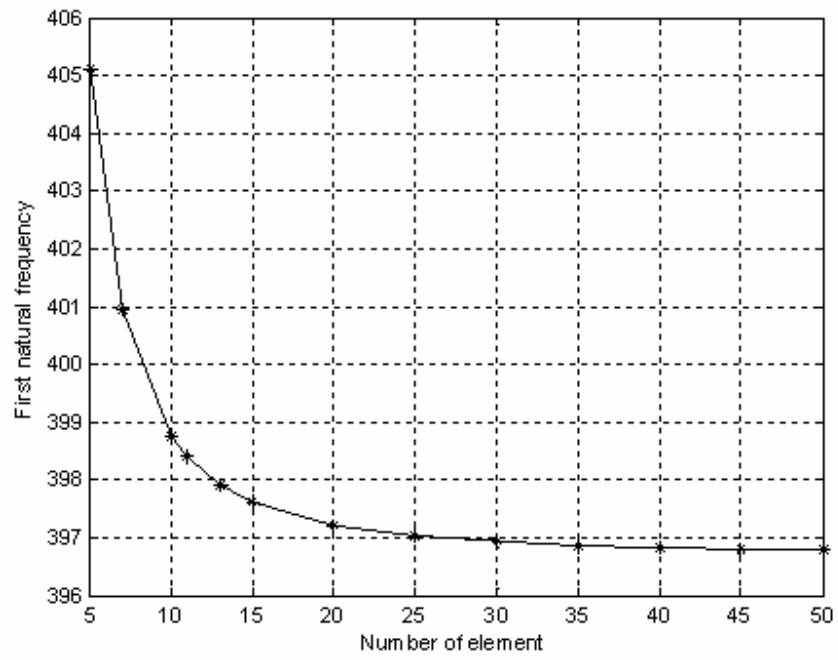


Fig. 3 Convergence test for in-plan curved beam

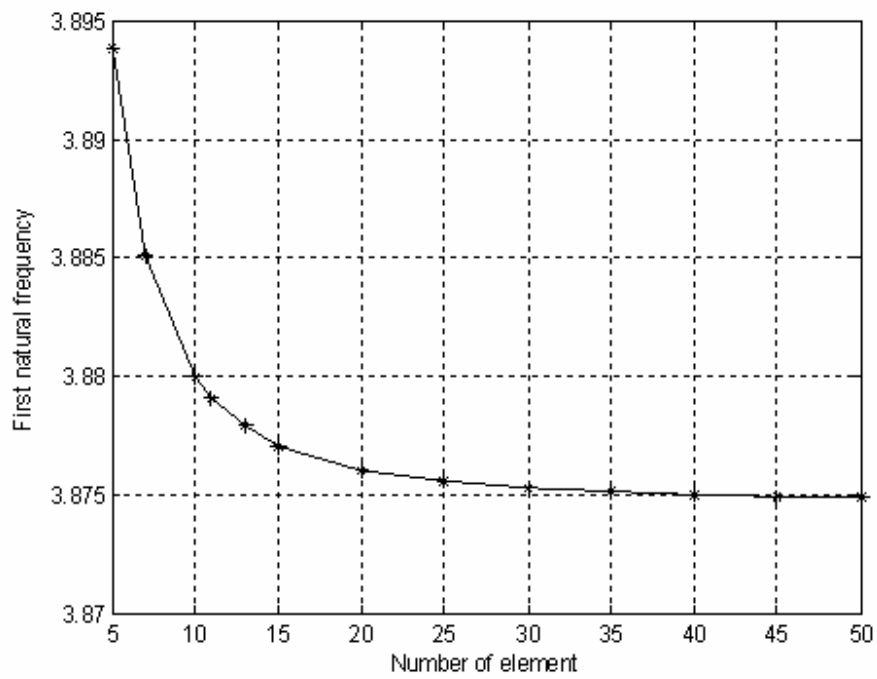


Fig. 4 Convergence test for out-of-plan curved beam

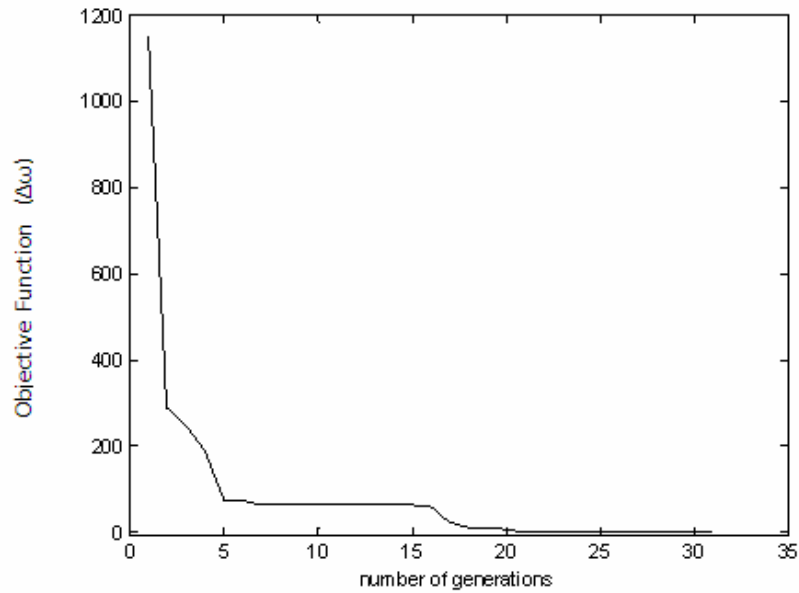


Fig. 5 A Typical objective function curve of CGA for out-of-plane curved beam

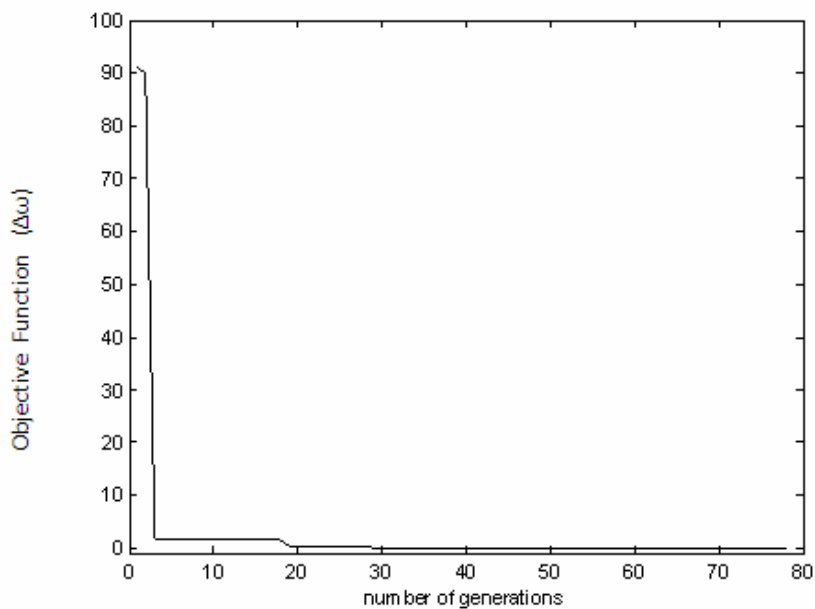


Fig. 6 A Typical objective function curve of BGA for out-of-plane curved beam

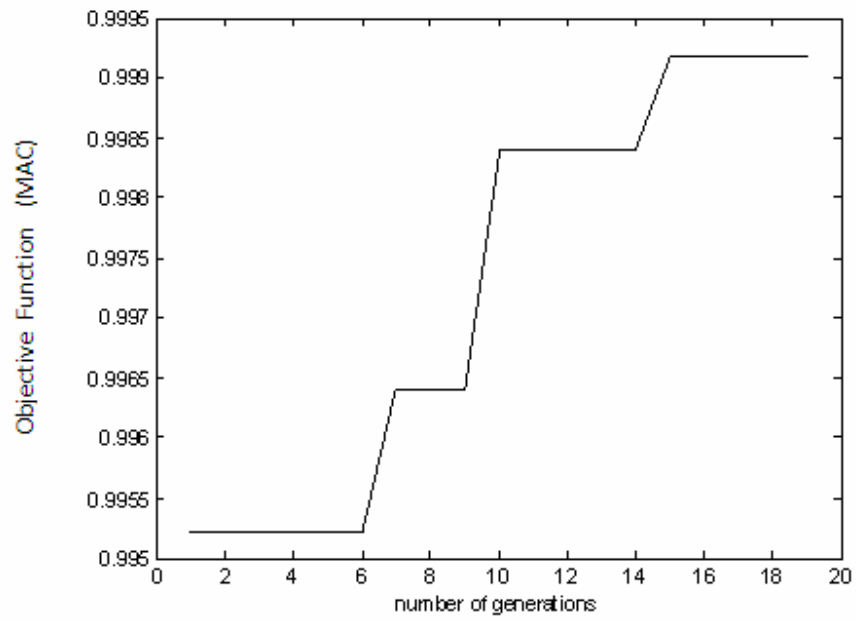


Fig. 7 A Typical objective function curve of CGA for out-of-plane curved beam

EFFECT OF CHANGE IN THE COEFFICIENT OF PERMEABILITY ON CONSOLIDATION CHARACTERISTICS OF CLAYS

Mohammed Y. Fattah⁽¹⁾

Maysam Th. Al-Hadidi⁽²⁾

Ahmed S. al-Shammary⁽²⁾

- 1) Building and Construction Engineering Dept., University of Technology, Baghdad, Iraq.
- 2) Civil Engineering Dept., College of Engineering, University of Baghdad, Iraq.

ABSTRACT:

The settlement rate and pore water pressure dissipation rate are mainly controlled by the permeability of soil. Both laboratory and field tests show that the permeability is varied during the loading and consolidation process. It is known that consolidation process is accompanied by decrease in void ratio which leads to decrease in the coefficient of permeability. The importance of the decrease of the coefficient of permeability on the time rate of settlement and pore water pressure needs to be investigated.

This paper takes into account the change in coefficient of permeability during consolidation and studies its effect on consolidation characteristics of a clay layer. The finite element method is used in the analysis and the package Geo-Slope is adopted through coupling the programs SIGMA/W and SEEP/W. The relationship between the applied pressure and permeability was determined experimentally for three samples.

It was concluded that the effect of permeability is clear at later times of consolidation due to decrease in void ratio and hence slower dissipation of pore water pressure. Taking into account variable permeability leads to longer times of consolidation. At later times (after 400 days), the excess pore water pressure predicted for the case of variable permeability is greater than conventional case by about (10 – 12) %.

الخلاصة

ان معدل نسبة الهطول ومعدل تبدد ضغط الماء المسامي يمكن ان يسيطر عليه بشكل رئيسي من خلال نفاذية التربة. وقد اظهرت كلتا الاختبارات الحقلية والمختبرية أنّ النفاذية متغيرة أثناء عملية التحميل والانضمام، ومن المعروف أيضاً بأنّ عملية الانضمام تكون مصحوبة بنقصان في نسبة الفراغات و التي تؤدي إلى تغيير في معامل النفاذية، لذا وجد من الضروري أن يتم التحري عن تأثير نقصان معامل النفاذية على المعدل الزمني للهبوط وضغط الماء المسامي.

لذلك في هذا البحث تم دراسة تأثير التغيير في معامل النفاذية أثناء عملية الانضمام على معاملات الانضمام في التربة الطينية، حيث تم استعمال طريقة العناصر المحددة في التحليل والبرنامجين المسميين SIGMA/W و SEEP/W و التي يمكن من خلالها حساب ذلك التأثير من خلال اعتماد العلاقة بين الضغط والنفاذية الموجودة ضمناً في هذين البرنامجين ولثلاث عينات .

استنتج بأنّ تأثير النفاذية يمكن ملاحظته بشكل أكثر وضوحاً خلال الفترة التي تلت 400 يوم من تسليط الاحمال بسبب النقصان في نسبة الفراغات والتبدد البطيء في ضغط الماء المسامي. اخذين في الحسبان ان النفاذية المتغيرة تقود الى زيادة في وقت الانضمام. كما وجد ان ضغط الماء المسامي الفائض في حالة النفاذية المتغيرة اكبر من الحالة التقليدية بحوالي (10 – 12) %.

Keywords: Consolidation, coefficient of permeability, settlement, pore water pressure.

INTRODUCTION

Consolidation is generally related to fine-grained soils such as silts and clays. Since water can flow out of a saturated soil in any direction, the process of consolidation is essentially three-dimensional. However, in most field situations, water will not be able to flow out of the soil by flowing horizontally because of the vast expanse of the soil in horizontal direction. Therefore, the direction of flow of water is primarily vertical or one-dimensional. As a result, the soil layer undergoes one-dimensional (1-D) consolidation settlement in the vertical direction.

Consolidation theory is required for the prediction of both the magnitude and the rate of consolidation settlements to ensure the serviceability of structures founded on a compressible soil layer. Terzaghi's theory of 1-D consolidation makes the following assumptions including that the soil is homogeneous and fully saturated, the solid particles and the pore water are incompressible, the flow of water and compression of soil are one-dimensional (vertical), strains are small, Darcy's law is valid at all hydraulic gradients, but the most important assumption is that the coefficient of permeability and the coefficient of volume compressibility remain constant throughout the consolidation process. Terzaghi gave a theory of soil consolidation based on the effective stress principle, which was derived on several ideal assumptions to get a simplified theory. To avoid the limitations involved in Terzaghi's theory, many efforts are being made by scholars to solve the problems in practical engineering situations.

It is known that consolidation process is accompanied by decrease in void ratio which leads to decrease in the coefficient of permeability. Effect of the decrease of the coefficient of permeability on the time rate of settlement and pore

water pressure needs to be investigated. Cavalcante and Assis (2002) showed the influence of the permeability gradient during the construction of tailings dams, built by the upstream method, using the hydraulic fill technique. During the hydraulic disposition, two mechanisms affect the tailings permeability: the hydraulic segregation and the consolidation due to the staged construction procedure. These mechanisms influence considerably the permeability distribution along the fill and, consequently, the behaviour of the dam. Results show that the pore pressure immediately after deposition may reach quite high values (532 kPa), but dissipates in a short period of time (1 to 10 days). Then, this effect should be taken into account in a short-term stability analysis of tailings dams. On the other hand, after pore pressure dissipation, there is a gain in the shear strength (13 %), which should also be considered, but in a long-term stability analysis of tailings dams.

The settlement rate and pore water pressure dissipation rate are mainly controlled by the permeability of soil. Both laboratory and field tests show that the permeability is varied during the loading and consolidation process. The formula proposed by Taylor (1948) and verified by Tavenas et al. (1983) can be used to represent variation of the permeability of soft clay during the consolidation:

$$k = k_o \cdot 10^{\left[\frac{-(e_o - e)}{c_k} \right]} \quad (1)$$

where: e_o : the initial void ratio,
 e : the void ratio at the condition under consideration,
 k : the permeability,
 k_o : the initial permeability, and
 c_k : constant which is equal to 0.5
 e_o (Tavenas et al., 1983).

A semi-analytical solution was presented by Ying et al. (2005) for the case

of void ratio e -log effective stress p and e -log permeability conductivity k_v , especially. The semi-analytical results were compared with those obtained from experimental investigations with a set of advanced consolidation system. Furthermore, the behavior of nonlinear consolidation of soils is analyzed and the differences between the semi-analytical results and Davis's nonlinear theory were discussed. It was concluded that the semi-analytical solution is a very effective method for solving the difficult consolidation problems taking varied compressibility and permeability into account. The degree of consolidation defined by effective stress and by settlement is different in this method. The advanced consolidation system with back pressure is an effective method for analyzing the consolidation behavior of clay. Fairly good agreement exists between theoretical results and the consolidation test results.

This paper takes into account the change in coefficient of permeability during consolidation and study its effect on consolidation characteristics of a clay layer.

DESCRIPTION OF THE PROBLEM:

The problem consists of tracing the settlement and pore water pressure changes in a clay layer under the effect of uniformly distributed load 80 kN/m^2 . The finite element method is used in the analysis and the package Geo-Slope is adopted through coupling the programs SIGMA/W and SEEP/W.

LABORATORY WORK:

In order to define the coefficient of permeability as a function of the applied pressure, a testing program was planned on samples taken from three sites located in Baghdad city. These soil samples are named by S_1 , S_2 and S_3 .

The identification and classification tests included grain size distribution, Atterberg limits and specific gravity. Table 1 shows

the index properties of the soils from the three sites.

Consolidation test was carried out on undisturbed soil samples according to the specification of ASTM D-2435-02. For each load increment, the coefficient of consolidation, c_v , was calculated using Casagrande's procedure in addition to the coefficient of volume change, m_v . Then the coefficient of permeability, k , was calculated according to the following relation:

$$k = m_v \cdot c_v \cdot \gamma_w \quad (2)$$

where γ_w is the unit weight of waater.

The relationship between the applied pressure and permeability is plotted for each sample as shown in Figure 1.

FINITE ELEMENT ANALYSIS:

SIGMA/W is a finite element software product that can be used to perform stress and deformation analyses of earth structures. Its comprehensive formulation makes it possible to analyze both simple and highly complex problems. For example, one can perform a simple linear elastic deformation analysis or a highly sophisticated nonlinear elastic-plastic effective stress analysis. When coupled with SEEP/W (another GEO-SLOPE software product), it can also model the pore-water pressure generation and dissipation in a soil structure in response to external loads. SIGMA/W has application in the analysis and design for geotechnical, civil, and mining engineering projects.

Hydraulic Conductivity Functions

Analyzing saturated seepage processes requires establishing the hydraulic conductivity versus pore-water pressure relationship. In the case of a transient analysis, the volumetric water content function must also be defined. Both of these functions can be either measured directly in the laboratory or predicted using a variety of methods. The

volumetric water content function can be predicted from the grain-size distribution curve and the hydraulic conductivity function can be predicted using the volumetric water content function and the measured saturated hydraulic conductivity.

The capacity of soil to conduct water can be viewed in terms of hydraulic conductivity (or the coefficient of permeability). The hydraulic conductivity is dependent on the water content. Since the water content is a function of pore-water pressure and the hydraulic conductivity is a function of water content, it follows that hydraulic conductivity is also a function of pore-water pressure. Figure 2 presents the form of the relationship between hydraulic conductivity and pore-water pressure. This relationship is known as a conductivity function.

The variation of hydraulic conductivity with pore-water pressure makes the finite element equations nonlinear, and an iterative process is consequently required to solve the equations. Hydraulic head (pore-water pressure plus elevation) is the primary unknown computed. Since the hydraulic conductivity is related to hydraulic head, the appropriate hydraulic conductivity is dependent on the computed results. During transient processes, the amount of water entering an elemental volume of soil may be larger than the amount of water exiting the volume, or vice versa. This results in a certain amount of water either being retained or released during a particular time increment.

Elastic-Plastic Model

The elastic-plastic model describes an elastic, perfectly-plastic relationship. Stresses are directly proportional to strains until the yield point is reached. Beyond the yield point, the stress-strain curve is perfectly horizontal.

Plastic Matrix, Elastic-Plastic Model

In SIGMA/W, soil plasticity is formulated using the theory of incremental plasticity (Hill, 1950). Once an elastic-plastic material begins to yield, an incremental strain can be divided into elastic and a plastic component.

Only elastic strain increments, $d\epsilon^e$, will cause stress changes. As a result, stress increments can be written as follows.

$$\{d\sigma\} = [C_e] \{d\epsilon^e\} \quad (3)$$

Consequently, the yield function can be written as follows in equation form.

$$F = F(\sigma_x, \sigma_y, \sigma_z, \tau_{xy}) \quad (4)$$

An incremental change in the yield function is given by:

$$dF = \frac{\partial F}{\partial \sigma_x} d\sigma_x + \frac{\partial F}{\partial \sigma_y} d\sigma_y + \frac{\partial F}{\partial \sigma_z} d\sigma_z + \frac{\partial F}{\partial \tau_{xy}} d\tau_{xy} \quad (5)$$

Alternatively, this equation can be written in the following matrix form.

$$dF = \left\langle \frac{\partial F}{\partial \sigma} \right\rangle \{d\sigma\} \quad (6)$$

The theory of incremental plasticity dictates that the yield function, $F < 0$, and, when the stress state is on the yield surface, dF is zero. This latter condition is termed the neutral loading condition, and, can be written mathematically as:

$$dF = \left\langle \frac{\partial F}{\partial \sigma} \right\rangle \{d\sigma\} = 0 \quad (7)$$

The plastic strain is postulated to be:

$$\{d\epsilon_p\} = \lambda \left\{ \frac{\partial G}{\partial \sigma} \right\} \quad (8)$$

Where:

G = plastic potential function, and
 λ = plastic scaling factor.

Substituting the plastic strain from equation (8) into the incremental stress equation (equation 3) gives

$$\{d\sigma\} = [C_e]\{d\varepsilon\} - [C_e]\lambda \left\{ \frac{\partial G}{\partial \sigma} \right\} \quad (9)$$

Substituting the stress vector, $\{ds\}$, into the neutral loading condition (equation 6), the following expression for the plastic scaling factor, λ , can be derived.

$$dF = \left\langle \frac{\partial F}{\partial \sigma} \right\rangle [C_e] \{d\varepsilon\} - \left\langle \frac{\partial F}{\partial \sigma} \right\rangle [C_e] \lambda \left\{ \frac{\partial G}{\partial \sigma} \right\} = 0 \quad (10)$$

$$\lambda = \frac{\left\langle \frac{\partial F}{\partial \sigma} \right\rangle [C_e] \{d\varepsilon\}}{\left\langle \frac{\partial F}{\partial \sigma} \right\rangle [C_e] \left\{ \frac{\partial G}{\partial \sigma} \right\}}$$

From equations (8) and (10), a relationship between stress increments and strain increments can be obtained.

$$\{d\sigma\} = \left([C_e] - [C_p] \right) \{d\varepsilon\} \quad (11)$$

Where:

$$[C_p] = \frac{[C_e] \left\{ \frac{\partial G}{\partial \sigma} \right\} \left\langle \frac{\partial F}{\partial \sigma} \right\rangle [C_e]}{\left\langle \frac{\partial F}{\partial \sigma} \right\rangle [C_e] \left\{ \frac{\partial G}{\partial \sigma} \right\}} \quad (12)$$

To evaluate the plastic matrix, $[C_p]$, the yield function, F , and the plastic potential function, G , need to be specified.

The following equation provides a common form of the Mohr-Coulomb criterion expressed in terms of principal stresses (Chen and Zhang, 1991).

$$F = \sqrt{J_2} \sin \left(\theta + \frac{\pi}{3} \right) - \sqrt{\frac{J_2}{3}} \cos \left(\theta + \frac{\pi}{3} \right) \sin \phi - \frac{I_1}{3} \sin \phi - c \cos \phi \quad (13)$$

Figure 3 shows the finite element mesh used in this case. A layer of clay 25 m thick is modeled. The water table is assumed to be at the ground level. Eight node isoparametric elements are used. Due to symmetry, only half of the axisymmetric problem is considered. The right and left boundaries are allowed to move vertically, while the bottom boundary is restrained both horizontally and vertically.

Analysis Results:

Finite element analysis was carried out for two cases; in the first case, the coefficient of permeability is considered constant during the consolidation process while in the second case, the coefficient of permeability is changed with the applied pressure (effective stress) during consolidation. Figure 4 shows a comparison of the total surface settlement calculated after 1000 days for the two cases. It can be noticed that the maximum effect of permeability occurs below the center of the problem. A decrease in the maximum surface settlement of the order of (12 - 15) % can be predicted when the permeability change is considered. Another comparison is made in Figure 5 at time 450 days. The figures show that during consolidation, the effect of permeability is clear, then the difference decreases at the end of consolidation (after 1000 days).

The same results are also noticed in Figure 6 which displays the percent of settlement at the end of load application to the final (total) consolidation settlement.

Figure 7 shows the distribution of the final consolidation settlement with depth along the centerline. It can be noticed that the effect of change of the permeability increases with depth. The maximum difference between the settlements predicted in these cases is in the percentage of (16 - 22) %. Similar relations are shown in Figure 8 after 450 days of consolidation, but also the difference between the two cases is greater

at middle periods of consolidation, and then decreases at the end.

Figure 9 presents the variation of horizontal displacement along sec. (a-a), (shown in Figure 3), 5 meters away from the problem centerline. It can be noticed that the effect of changing the coefficient of permeability is pronounced at the ground surface and a difference of about (12 - 14) can be noticed. Similar results are presented in Figure 10 which shows that the effect of permeability is greater at time 450 days.

The effect of permeability on the time rate of settlement is explained in terms of consolidation ratio (degree of consolidation) as shown in Figure 11. The degree of consolidation of the clay layer at any time is calculated as the ratio between the excess pore water pressures dissipated at that time to the initial excess pore water pressure. It is evident that the effect of permeability is clear at later times of consolidation due to decrease in void ratio and hence slower dissipation of pore water pressure. Taking into account variable permeability leads to longer times of consolidation.

Figure 12 traces the dissipation of pore water pressure at point (a) 12 m deep with time. It is noticed that the pore water pressure predicted in the case of variable permeability is greater than in conventional constant permeability case due to smaller rate of dissipation.

Figure 13 shows the isochrones of excess pore water pressure at different times. At early stages, the effect of permeability is not clear, while at later times (after 400 days), the excess pore water pressure predicted for the case of variable permeability is greater than conventional case by about (10 – 12) %.

CONCLUSIONS:

1. The maximum effect of permeability occurs below the center of the problem. A decrease in the maximum surface settlement

of the percentage of (12 - 15) % can be predicted when the permeability change during consolidation is considered.

2. The effect of permeability is clear at later times of consolidation due to decrease in void ratio and hence slower dissipation of pore water pressure. Taking into account variable permeability leads to longer times of consolidation. At later times (after 400 days), the excess pore water pressure predicted for the case of variable permeability is greater than conventional case by about (10 – 12) %.

REFERENCES

- ASTM D2435, (2002), "Standard Test Methods for One-Dimensional Consolidation Properties of Soils," Annual Book of ASTM Standards, Vol. 04.08, ASTM International, West Conshohocken, PA, pp. 1–10.
- Cavalcante, L. B., Assis, A. P., (2002), "Effects of Nonhomogeneity of Permeability on Tailings Dams", International Journal of Mining, Reclamation and Environment, Volume 16, Issue 4 , pp. 314 – 330.
- Chen, W.F., Zhang, H., (1991), "Structural Plasticity: Theory, Problems, and CAE Software", Springer-Verlag.
- Hill, R., (1950), "The Mathematical Theory of Plasticity", Oxford University Press.
- Tavenas, F., Jean, P., Leblond, P., and Leroueil, S. (1983), "The Permeability of Natural Soft Clays, Part II: Permeability Characteristics", Canadian Geotechnical Journal, Vol. 20, pp. 645-660.
- Taylor, D. W., (1948), "Fundamentals of Soil Mechanics", John Wiley and sons.



- User's Guide Manual of SIGMA/W, (2002), GEO-SLOPE International Ltd, Calgary, Alberta, Canada.
- Ying, Z., Kang, X., Xi, L., (2005), "Nonlinear Analysis of Consolidation with Variable Compressibility and

Permeability", Journal of Zhejiang University SCIENCE, Vol. 6A, No. 3, pp.181-187, <http://www.zju.edu.cn/jzus>.

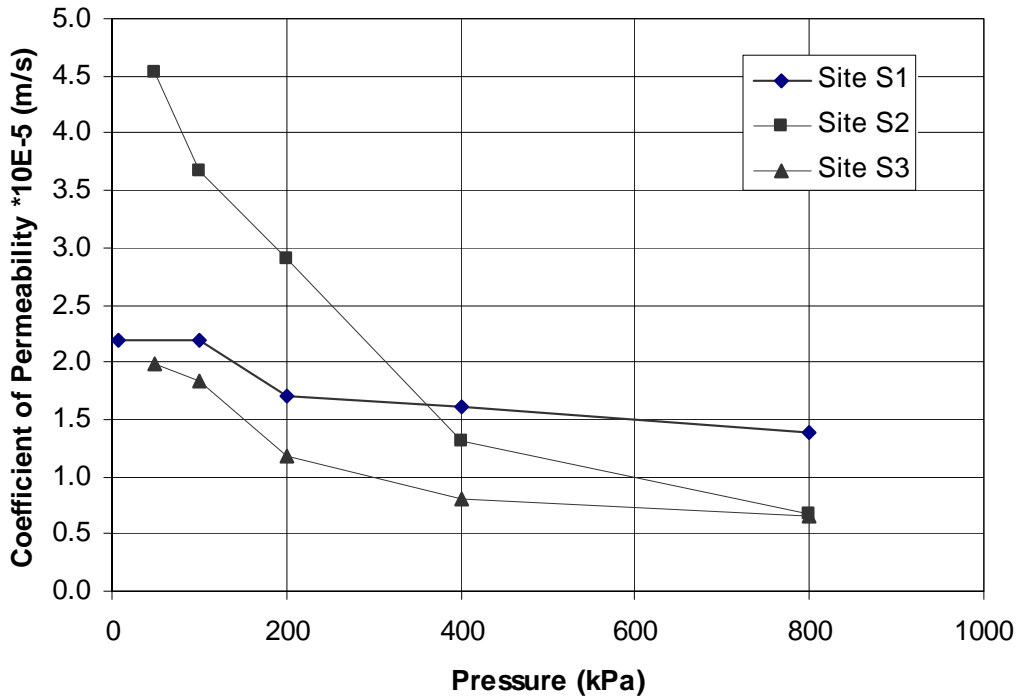


Fig.(1) Variation of the coefficient of permeability with pressure for the three soils.

Table 1: Index properties of the three soils.

Property	Soil 1	Soil 2	Soil 3
Initial water content %	23.90	25.12	25.64
Liquid limit	56	56	50
Plastic limit	25	23	24
Plasticity index	31	33	26
Specific gravity	2.79	2.80	2.79
% fines (Silt + clay)	98	97	81
Cohesion (kN/m ²)	118.0	177.0	93.23
Angle of friction (degrees)	0	0	0
Soil Description	Gray to brown silty clay stiff to very stiff	Brown to gray stiff clay	Brown silty clay ,stiff

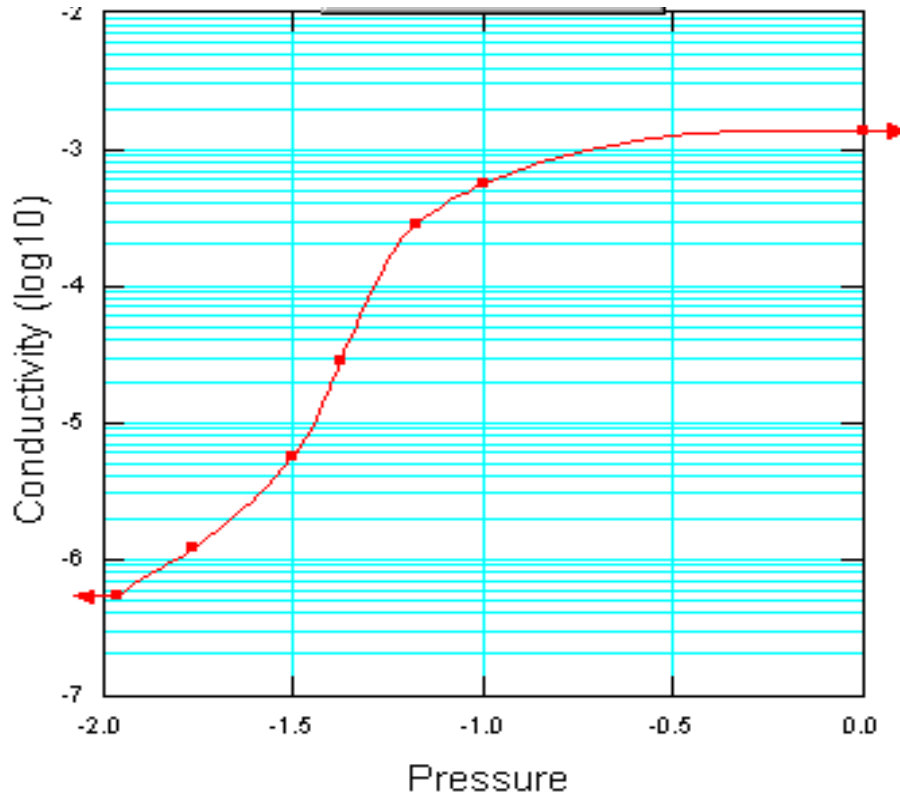


Fig. 2: A typical hydraulic conductivity function (SIGMA/W Manual, 2002).

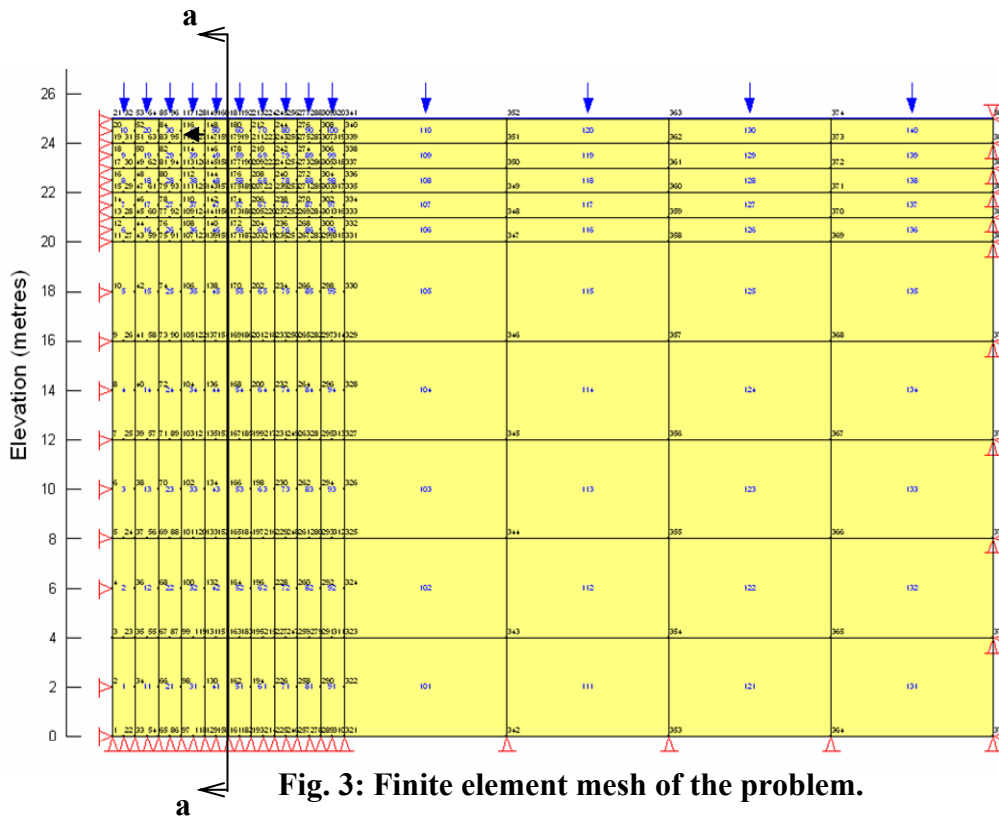
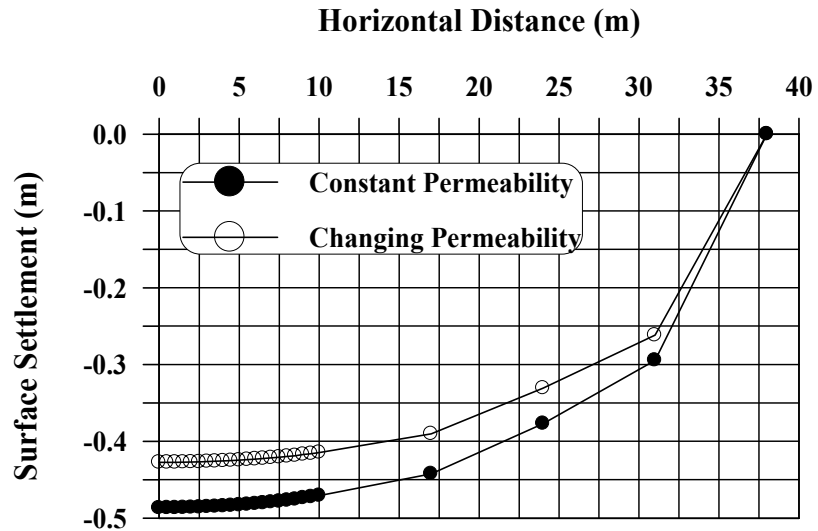
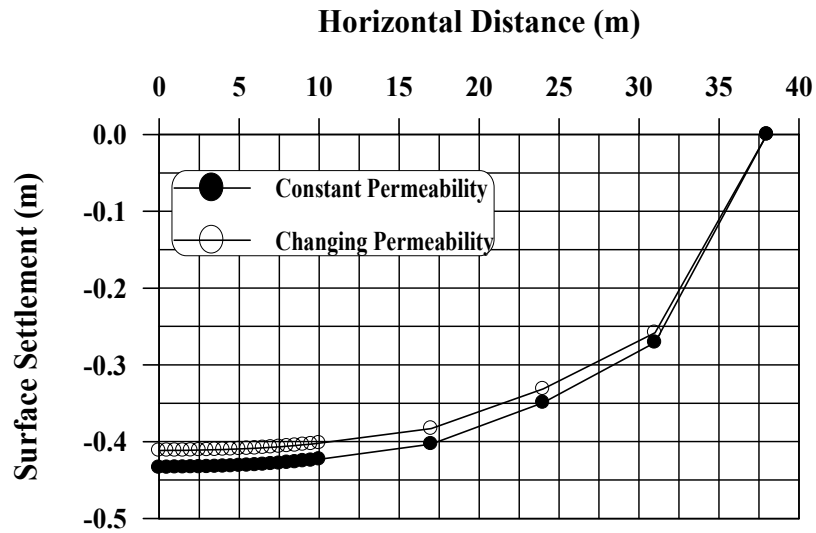


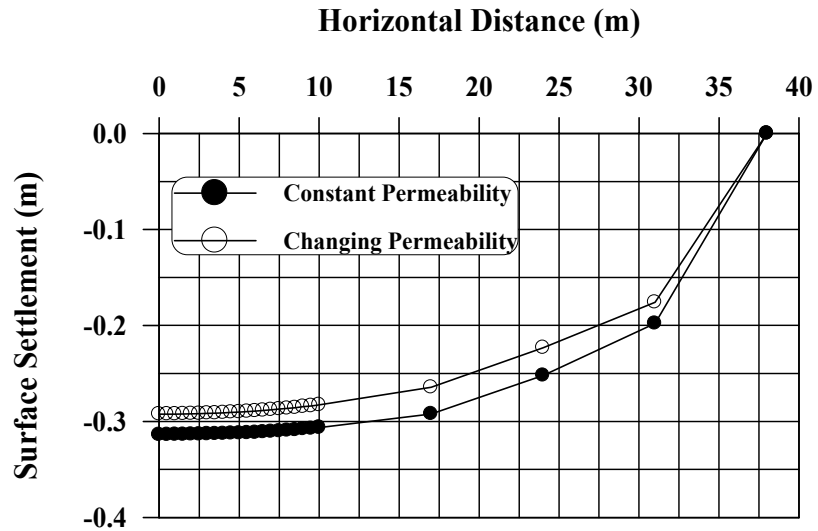
Fig. 3: Finite element mesh of the problem.



a. Site S1

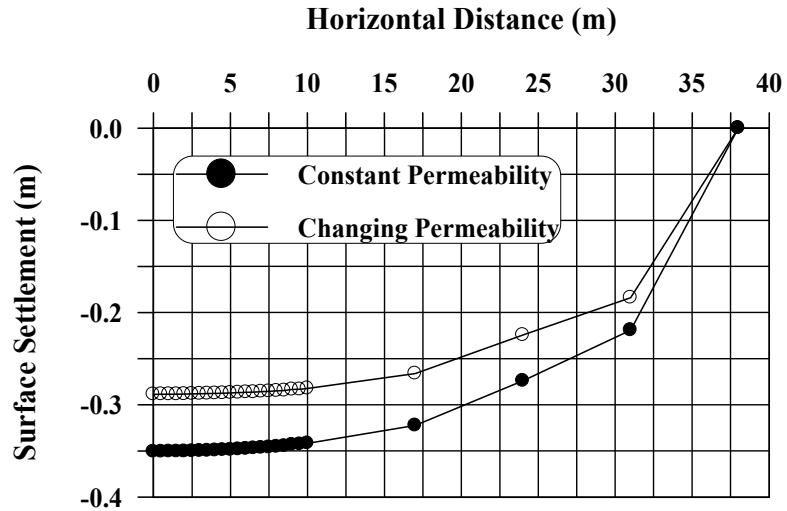


b. Site S2

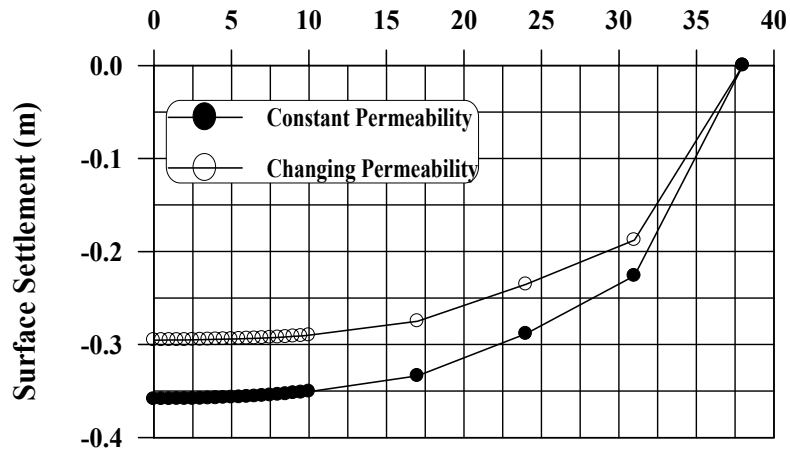


c. Site S3

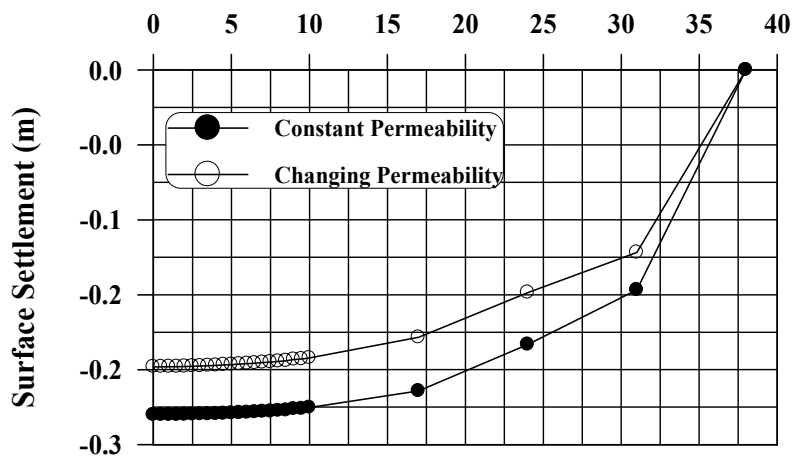
Fig. 4: Effect of different conditions of permeability on the surface settlement at the end of consolidation (1000 days).



a. Site S1
Horizontal Distance (m)

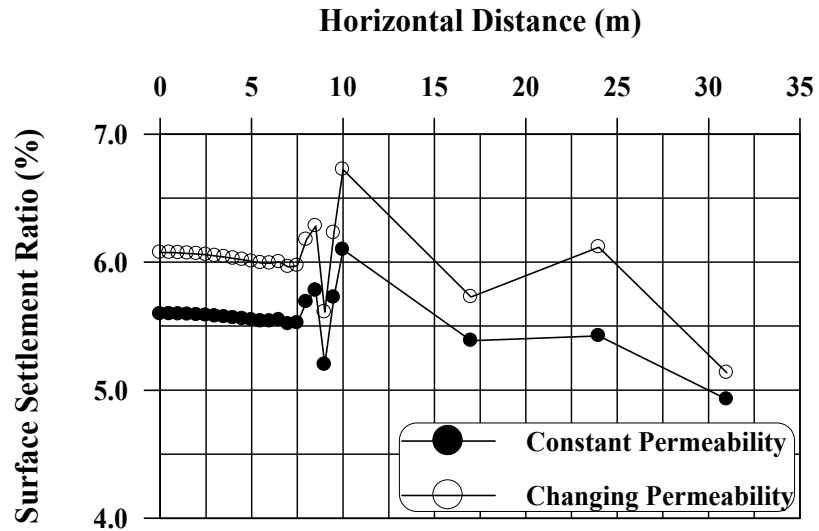


b. Site S2
Horizontal Distance (m)

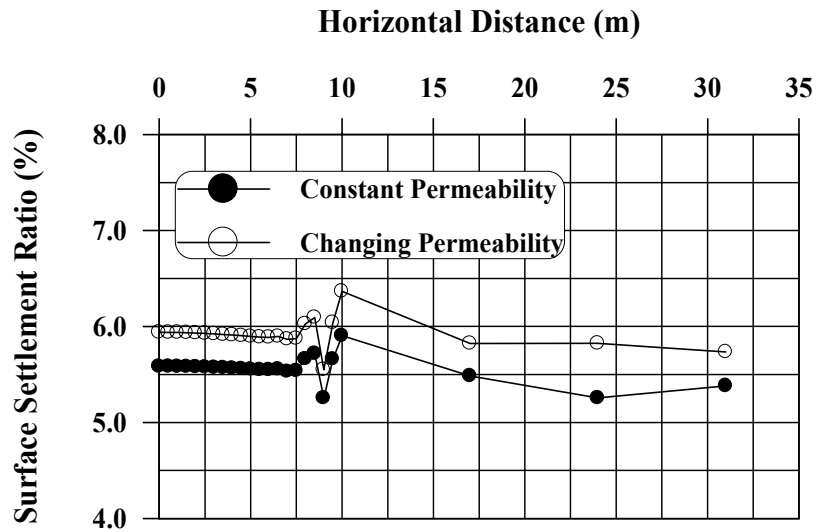


c. Site S3

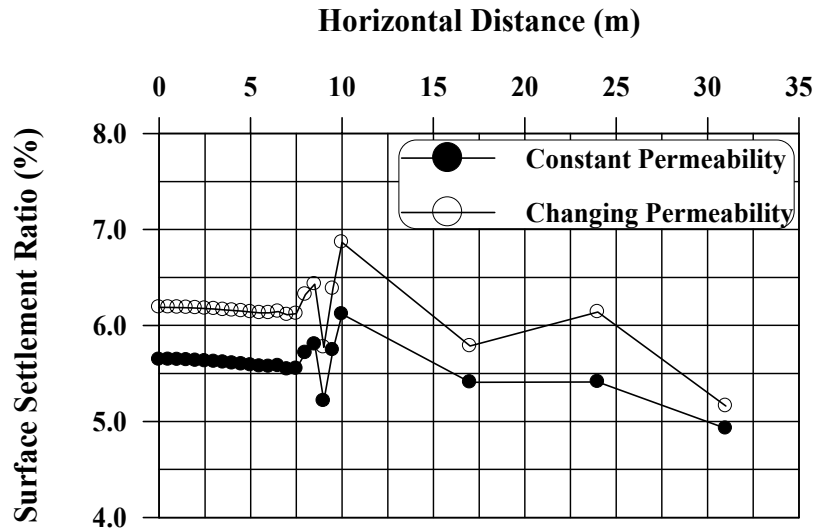
Fig.5: Effect of different conditions of permeability on the surface settlement at (450 days).



a. Site S1

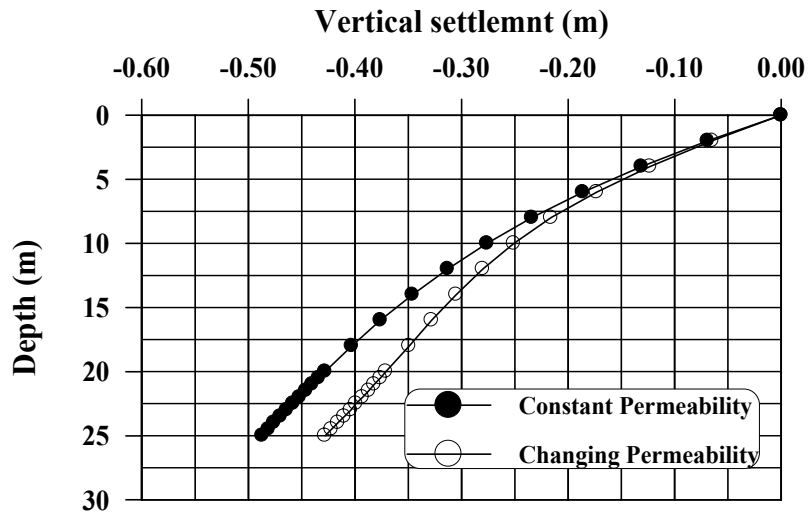


b. Site S2

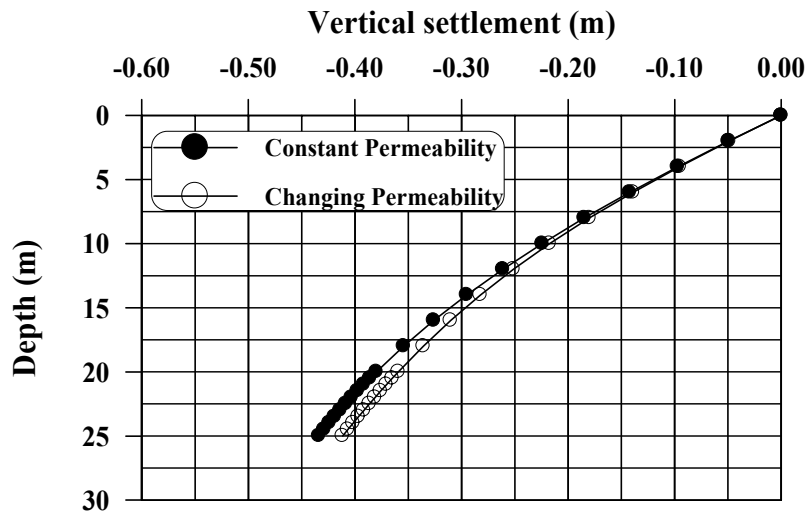


c. Site S3

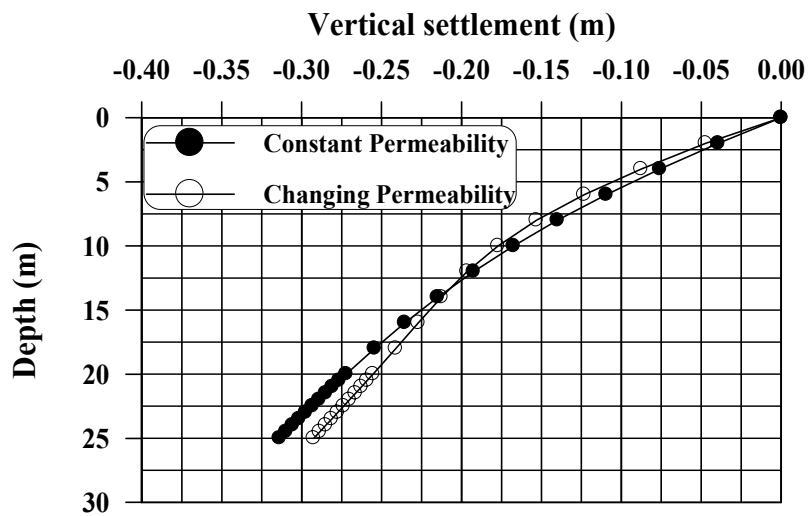
Fig. 6: Effect of different conditions of permeability on the surface settlement.



a. Site S1

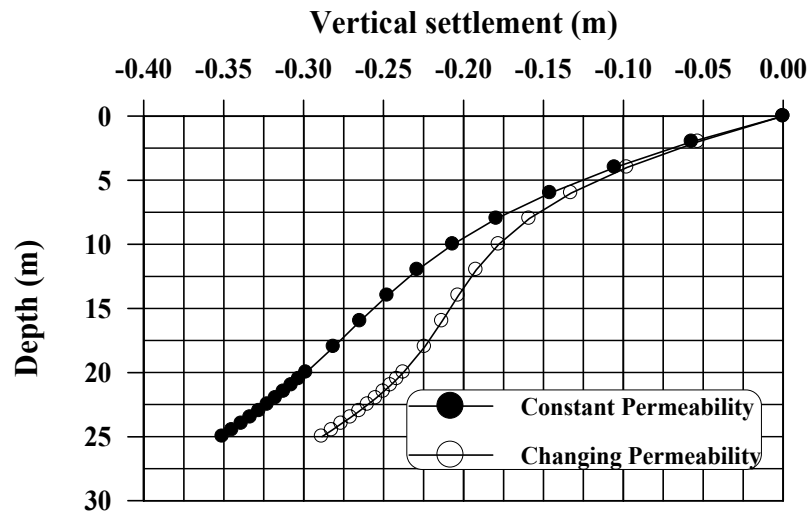


b. Site S2

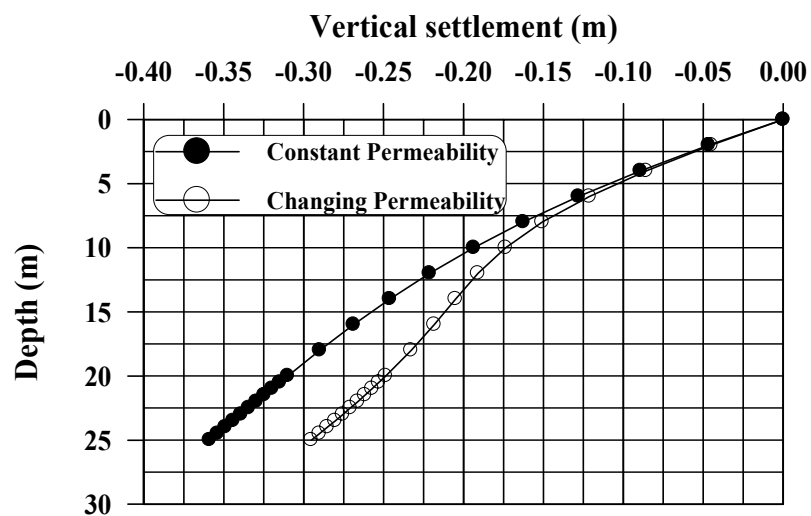


c. Site S3

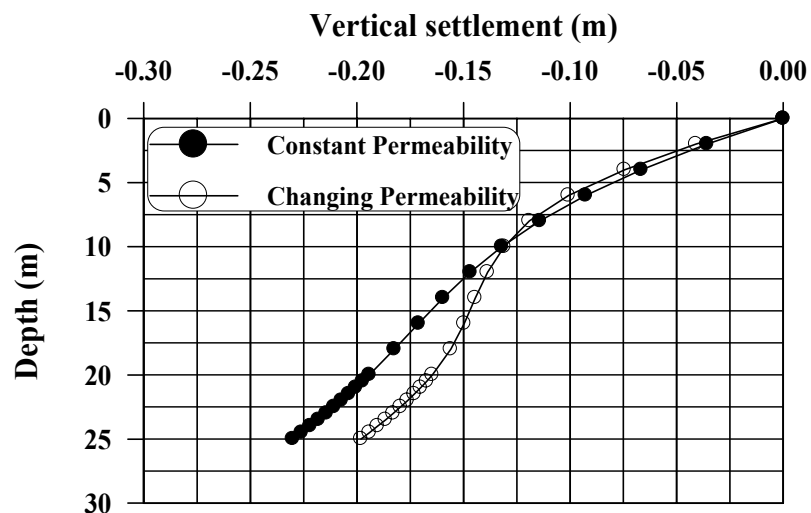
Fig. 7: Variation of vertical displacement along the foundation centerline at the end of consolidation (1000 days).



a. Site S1

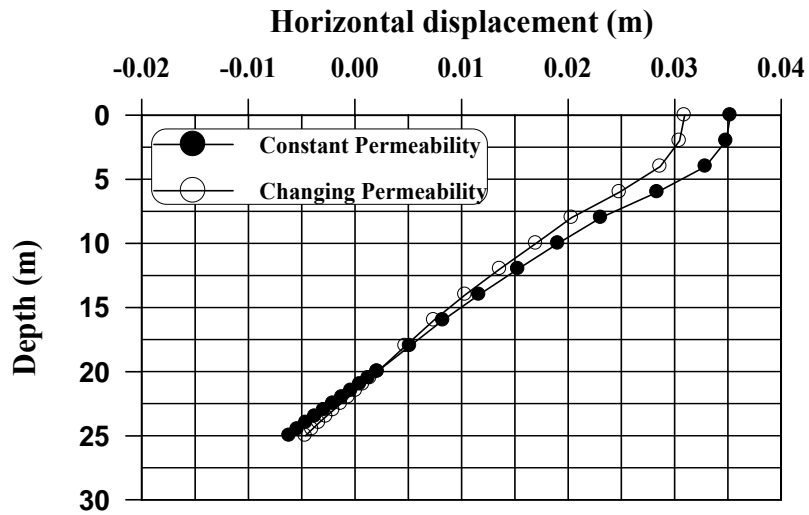


b. Site S2

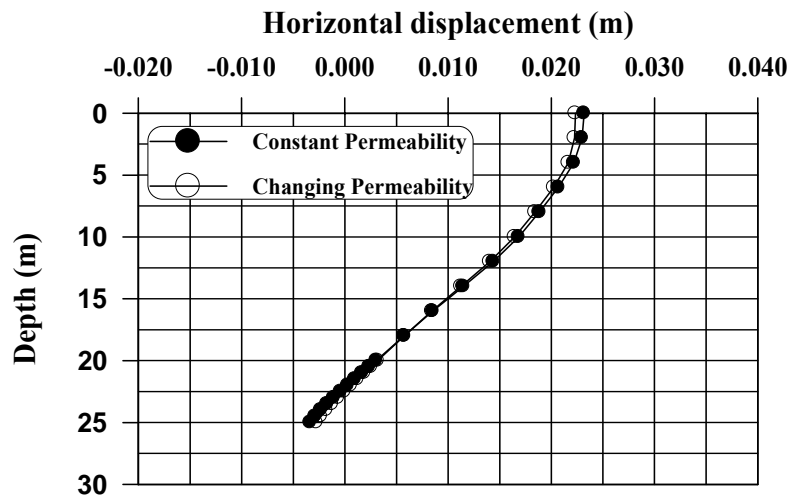


c. Site S3

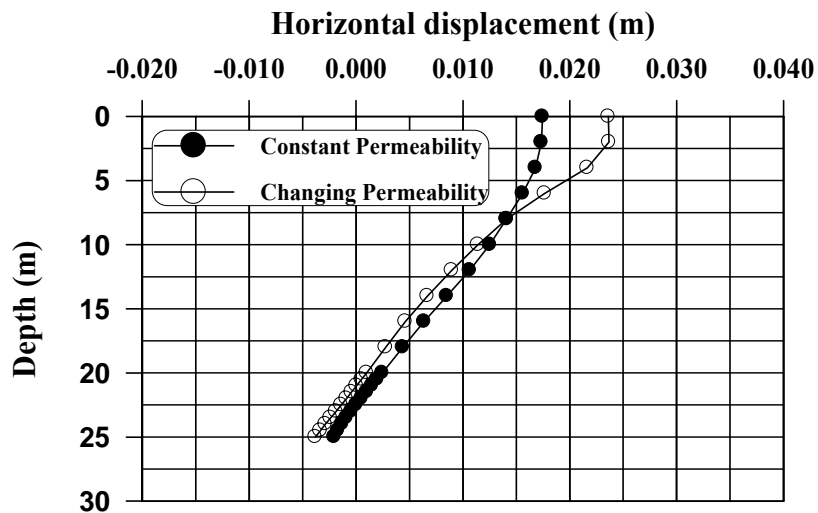
Fig. 8: Variation of vertical displacement along the foundation centerline at (450 days).



a. Site S1



b. Site S2



c. Site S3

Fig. 9: Effect of different conditions of permeability on the distribution of horizontal displacement with depth along the foundation centerline at the end of consolidation (1000 days).

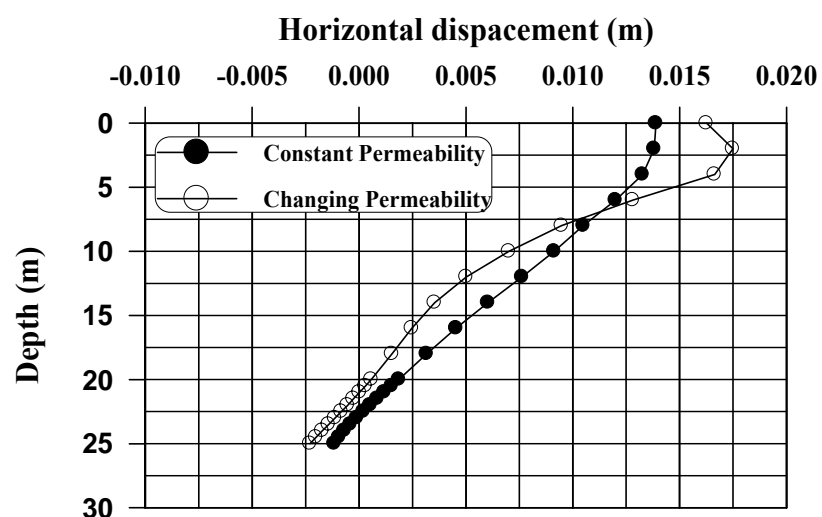
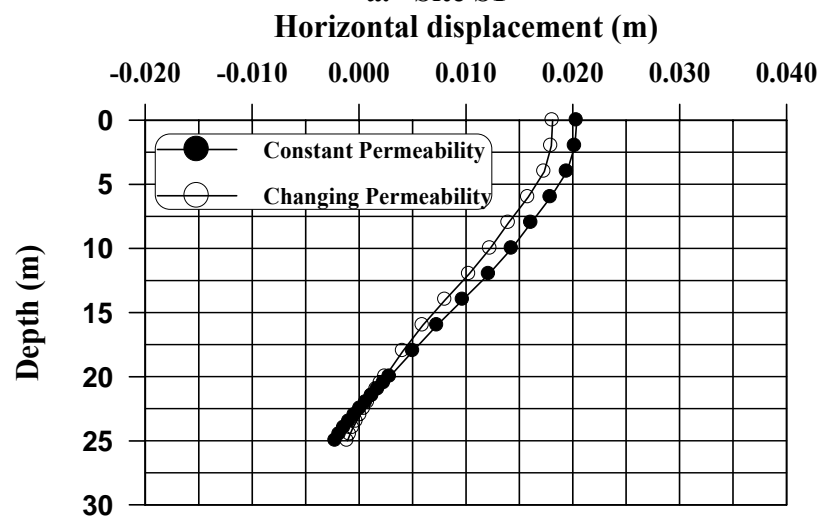
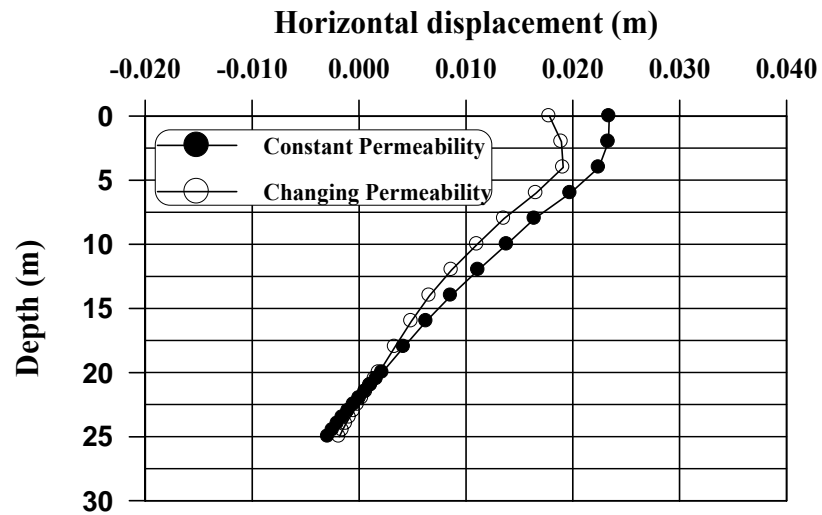


Fig. 10: Effect of different conditions of permeability on the distribution of horizontal displacement with depth along the foundation centerline at (450 days).

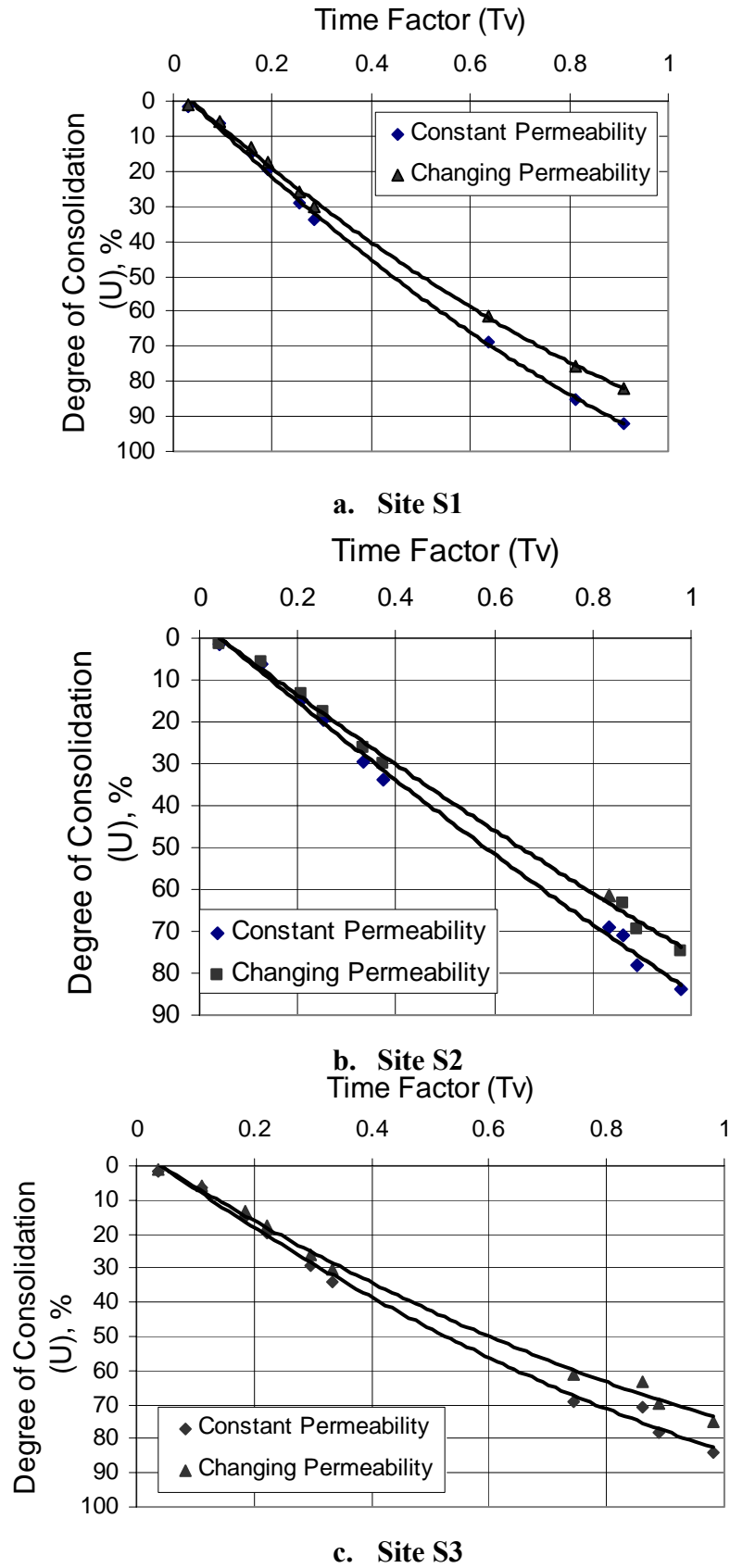
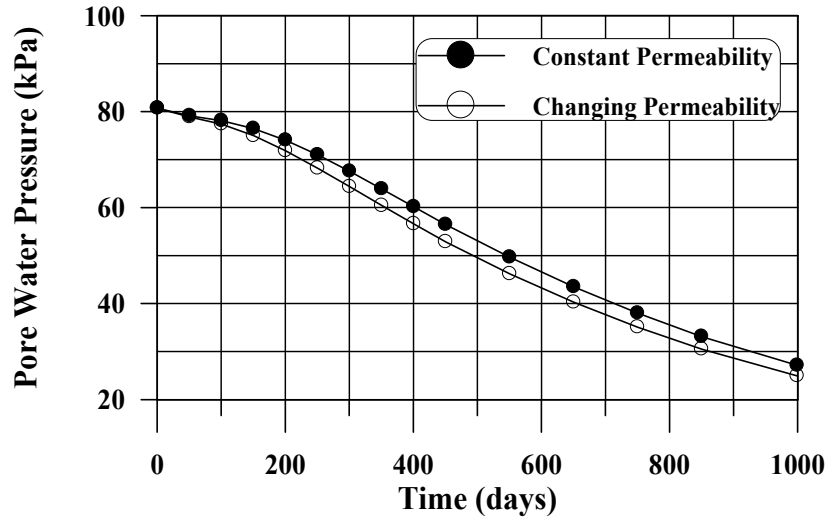
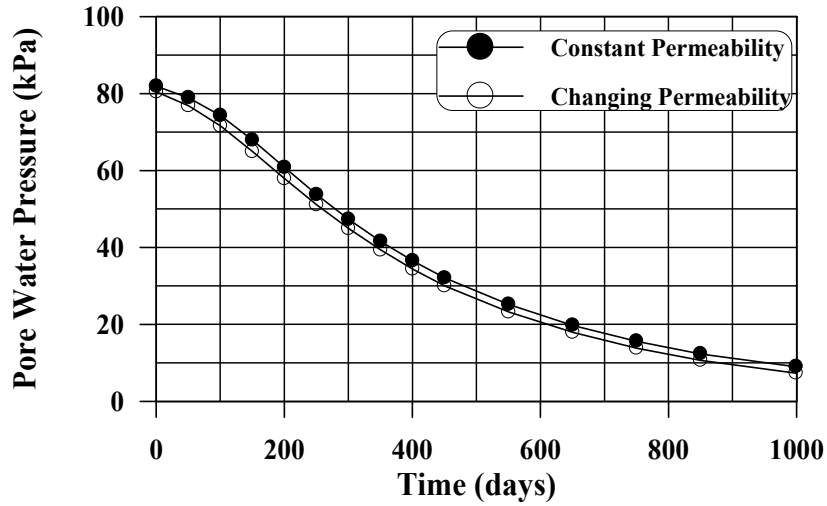


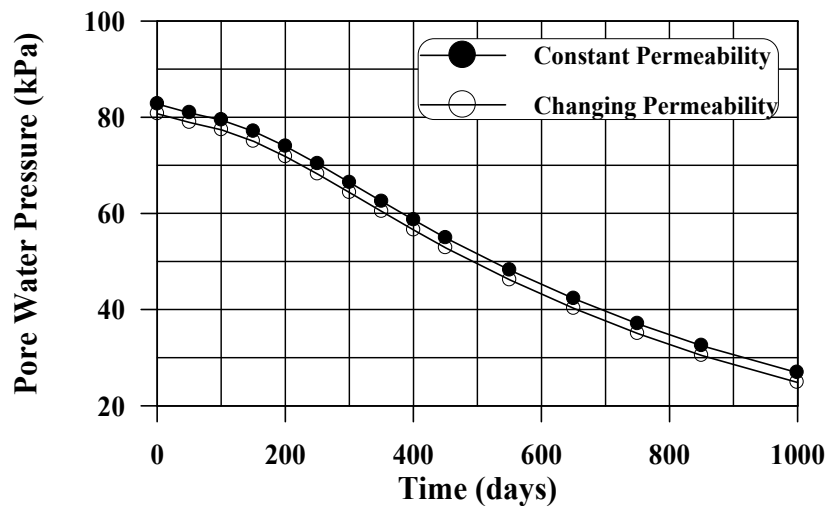
Fig. 11: Effect of different conditions of permeability on the degree of consolidation with time at node (a) 12 m deep.



a. Site S1

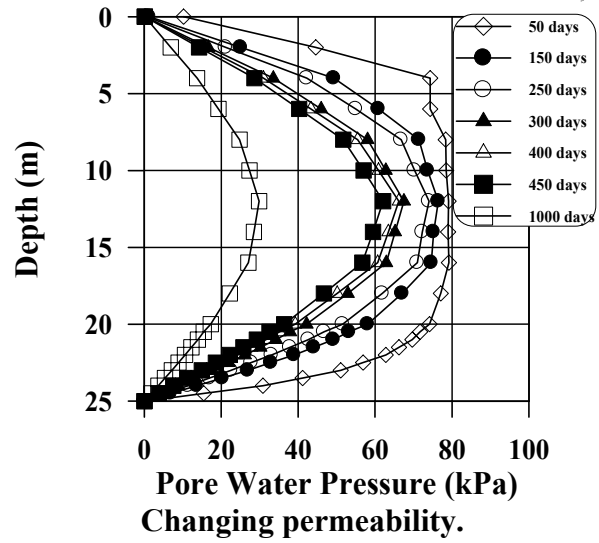
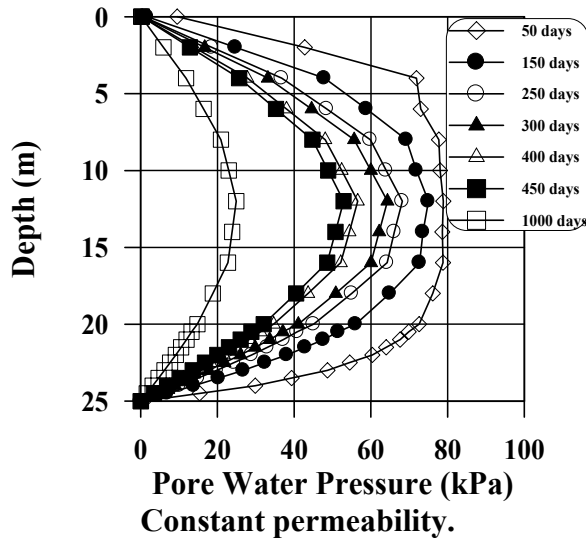


b. Site S2

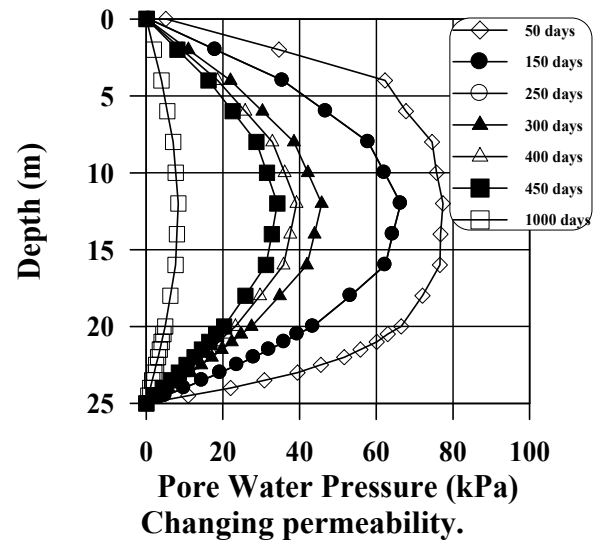
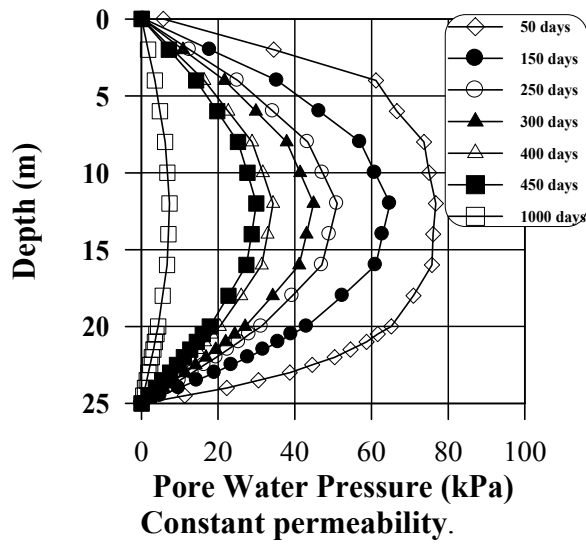


c. Site S3

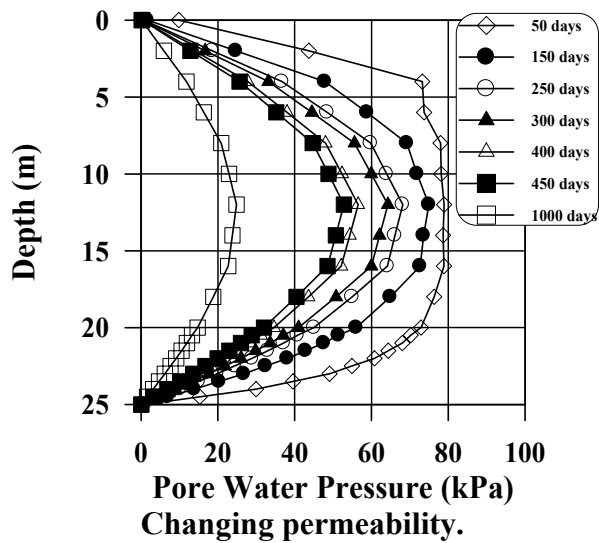
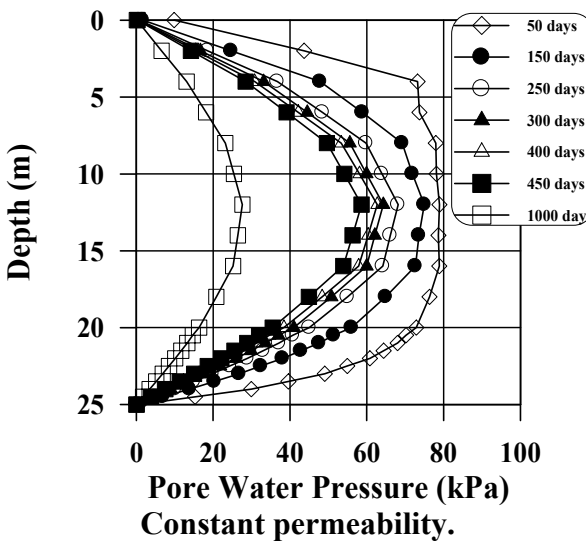
Fig. 12: Effect of different conditions of permeability on the change in pore water pressure with time at node (a).



a. Site S1



b. Site S2



c. Site S3

Fig. 13: Effect of different conditions of permeability on the change in pore water pressure along the centerline at time of load application.

ADSORPTION STUDY OF HYDRODESULPHURIZATION CATALYST

Tariq M.Naife

Chemical Engineering Department-College of Engineering
University of Baghdad

Abstract

Physical and chemical adsorption analyses were carried out by nitrogen gas using ASTM apparatus at 77 K and hydrogen gas using volumetric apparatus at room temperature respectively. These analyses were used for determination the effect of coke deposition and poisoning metal on surface area, pore size distribution and metal surface area of fresh and spent hydrodesulphurization catalyst $\text{Co-Mo/Al}_2\text{O}_3$.

Samples of catalyst (fresh and spent) used in this study are taken from AL-Dura refinery.

The results of physical adsorption shows that surface area of spent catalyst reduced to third compare with fresh catalyst and these catalysts exhibit behavior of type four according to BET classification, so, the pores of these samples are cylindrical, and the pores of fresh catalyst suffers during the hydrodesulphurization.

The result of chemical adsorption shows that the metal surface area of fresh catalyst is 50.72 m^2/g while it reduced to 39.04 m^2/g for spent catalyst.

الخلاصة

تم اجراء تحاليل الامتزاز الفيزيائي والكيميائي باستعمال غاز النتروجين وبواسطة جهاز ASTM وبدرجة حرارة 77 K، واستعمال غاز الهيدروجين بواسطة منظومة حجمية للامتزاز وبدرجة حرارة الغرفة على التوالي، هذه التحاليل تستعمل لحساب تاثير المواد الكربونية والسمية على المساحة السطحية وحجم التوزيع المسامي والمساحة السطحية للمعدن للعامل المساعد $\text{Co-Mo/Al}_2\text{O}_3$ الطازج والمستهلك المستعمل في عملية ازالة الكبريت.

جميع نماذج العامل المساعد (الطازجة والمستهلكة) تم أخذها من مصفى الدورة. تبين النتائج المستحصلة لعملية الامتزاز الفيزيائي بان قيمة المساحة السطحية للعامل المساعد المستهلك قلت للثلث مقارنة بالعامل المساعد الطازج وان هذه العوامل المساعدة أظهرت النمط الرابع وفقا لتصنيف BET لمتساويات درجة الحرارة للامتزاز، لذا فان مسامات هذه المواد هي من النوع الاسطواني. وقد عانى العامل المساعد الطازج نتيجة الاستخدام إلى فقدان الكثير من مساميته ومساحته السطحية بسبب عملية السلفرة الهيدروجينية.

أظهرت نتائج الامتزاز الكيميائي إلى ان المساحة السطحية للمعدن الطازج 50.72 $\text{م}^2/\text{غم}$ بينما تقل لتساوي 39.04 $\text{م}^2/\text{غم}$ للعامل المساعد المستهلك.

Keywords

Physical Adsorption, Chemical Adsorption, Surface Area, Pore Size distribution, HDS catalyst

Introduction

Catalysts are used in a variety of applications from the production of consumer goods to the protection of the environment. Optimum design and efficient utilization of catalysts require a thorough understanding of the surface structure and surface chemistry of the active material. Gas adsorption is extensively used in characterizations of micro – and mesoporous materials and is often considered as a technique that accurately determines the amount of gas adsorbed on a solid material, which is a direct measure for the porous properties and structure (Francoise Rouquerol, 1999).

Since the catalytic phenomena occur in the internal surface of the solid, lying within the pores, optimizing of pore size becomes important for the mass transfer and diffusion of the reactant to the active sites. The pores are not only the path for the reactants and products but also influence the incorporation of active metals during preparation of catalysts and coke deposition during deactivation (Wiwel, 1991).

Morphological characteristics like surface area, pore volume, pore size distributions have to meet the specification for a longer catalyst life time. Chemical adsorption (chemisorption) analysis techniques provide much of the information necessary to evaluate catalyst materials in the design and production phases. Hydrogen plays a very important role in catalysis; in addition to its applications as reducing agent and as reactant, and it is extensively used as a probe molecule. Its selective chemisorption on noble metals allows it to be used as an ideal probe to perform metal surface area measurement and catalyst characterization. (P. Ferreira-Aparicio, 1997)

Hydrodesulphurization is a heterogeneously catalyzed reaction. Supported metal sulfides have been found to be the best catalysts for the hydrodesulphurization reaction. Alumina-supported CoMo catalyst structures of both precursor and final catalysts have been extensively studied and the nature of active sites have been proposed (H. Topsøe, 1984). Both molybdenum and tungsten sulfides are active catalysts in the hydrodesulphurization reaction. Nowadays however, mainly molybdenum-based catalysts are used worldwide in the processes connected with

sulfur removal. Different promoters have been tested and nickel and cobalt were found to give the

highest enhancement of the activity towards desired products. Alumina support has a very important role in the activity and stability of the hydrodesulphurization catalyst as well and the γ -phase is the most suitable for the operation (Mohamadbeigy, 2005).

Co-Mo/Al₂O₃ is superior hydrodesulphurization catalyst whose structure and activity have been studied extensively (Beather, 1960), Richardson found that its activity varies with the concentration of metals, and that a Co/Mo weight ratio of 1/5 apparently is optimum (Richardson, 1964). Cobalt and Molybdenum are two of the more common metals that are used in HDS catalyst. When these two metals are used together as a HDS catalyst is more tolerant to the poisoning agent and is usually classed as being suitable for wide variety of feedstocks.

Studies of increasing the dispersion of the active metal on support catalyst were studied by (R. Prins, 1989, B. Delmon, 1996). The physicochemical properties of alumina-supported CoMo catalysts were studied by (Ch. Papadopoulou, 2003). Various efforts have been made to increase the activities of conventional CoMo-based alumina catalysts. These include loading of the active metals in greater amounts, improving dispersion of the active metals, and manipulating the acidity level of the alumina support. The first two objectives have been achieved by increasing the surface area of the support and also by using better metal loading techniques. (Mignard, 1996), and well-defined pore structures in mesoporous materials have attracted much attention as supports for CoMo based HDS catalysts. (Turaga, 2003, Song, 2003). The higher surface areas allow loading of higher levels of the active metals without affecting dispersion.

This work deals with the study of physisorption and chemisorption of fresh and spent CoMo/Al₂O₃ catalysts.



Experimental Work

1- Materials

1-1 Catalyst

A fresh and its spent CoMo/Al₂O₃ HDS catalyst supplied from AL-Dura refinery are used in this study. Properties of fresh and spent catalysts are listed in Table (1).

1-2 Gases

1-2-1 Nitrogen

Nitrogen was supplied from Baghdad factory for drug industry with purity 99.9 %.

1-2-2 Helium

Helium was supplied from AL-Mansour plant with purity 99.9 %.

1-3 Liquid Nitrogen

Liquid Nitrogen was supplied from Baghdad factory for drug industry with purity 99.9 %.

2- Physical adsorption by ASTM BET method

BET method covers the determination of nitrogen adsorption and desorption isotherms of catalysts and catalyst carriers at the boiling point of liquid nitrogen. A static volumetric measuring system is used to obtain sufficient equilibrium adsorption points on each branch of the isotherm to adequately define the adsorption and desorption branches of the isotherm, provides data for establishing the pore shape and pore size distribution of catalysts.

The apparatus of physisorption shown in fig.1 consist measuring device, vacuum pump, two gas supplies, sample container, manometer and liquid nitrogen coolant. (ASTM, D4222-83, 1986).

Prior to determination of adsorption isotherm, all physisorbed material was removed from the surface of the adsorbent. This is achieved by exposure of the surface to high vacuum with heating at 250 C° for 3 h.

Then dead space volume is determined by adding helium gas into the system, and recording the pressure (P_{H1}) and temperature (T_{H1}), then opening sample valve to admit helium to the sample, recording the pressure (P_{H2}) and temperature (T_{H2}) at equilibrium. The vacuum valve was open to remove the helium gas and to obtain the desired value of vacuum pressure.

The adsorption isotherm was determined by adding nitrogen, step wise to the system, and recording the pressure P_{1(1+n)} and the temperature T_{1(1+n)} , where n= 0,1,2,3..etc ,then valve of sample container was open for admitting nitrogen to the catalyst, and P_{2 (1+n)} and T_{2 (1+n)}, were recording at equilibrium . For recording multipoint of adsorption isotherm repeating the steps above.

After reaching to the saturation adsorption when there is no change in pressure noticed, the desorption isotherm procedure was started, which is summarized in recording pressure and temperature after each evacuated interval.

Method of Calculation

Volume of nitrogen in the dead – space $V_{ds}(i)$ calculated by equation 1. (ASTM,D4222-83,1986)

$$V_{ds}(i) = (V_s + P_2) \left[1 + \frac{0.05 P_{2(i)}}{760} \right] \quad (1)$$

Where ,V_s Volumetric factor of dead space and was calculated by equation 2.

$$V_s = 273.2 \frac{V_d}{760} P_{H_2} \left[\left(\frac{P_{H_2}}{T_{H_1}} + 273.2 \right) - \left(\frac{P_{H_2}}{T_{H_2}} + 273.2 \right) \right] \quad (2)$$

Where,

V_d = Volume of manifold (cm^3)

P_{H_1} = Initial hydrogen pressure (torr)

T_{H_1} = Temperature of manifold at initial helium pressure (K)

P_{H_2} = Helium pressure at equilibrium (torr)

T_{H_2} = Temperature of manifold after equilibrium (K)

The quantity of gas adsorbed was calculated by equation 3.

$$V_{ad}(i) = \frac{[Vt(i) - V2(i) - Vds(i)]}{W_s} \quad (3)$$

Where, $V1(i)$ volume of N_2 in manifold + volume valve open and calculated by equation 4.

$$V1(i) = (V_d + V_x) \left[\frac{P_{1(1+n)}}{T_{1(1+n)}} \times \frac{273.2}{760} \right] \quad (4)$$

$V2(i)$ = Volume of N_2 in manifold + volume of valve calculated by equation 5.

$$V2(i) = (V_d + V_x) \left[\frac{P_{2(1+n)}}{T_{2(1+n)}} \times \frac{273.2}{760} \right] \quad (5)$$

Where,

V_x = Volume of extra volume bulb (cm^3)

$P_{1(1+n)}$ = Initial N_2 pressure (torr)

$P_{2(1+n)}$ = pressure after equilibrium (torr)

$T_{1(1+n)}$ = Manifold temperature of initial N_2 pressure (K)

$T_{2(1+n)}$ = Manifold temperature after equilibrium (K)

Total inventory of nitrogen $Vt(i)$ in the system calculated by equation 6 :

$$Vt(i) = Vt(i-1) + V1(i) - V2(i-1) \quad (6)$$

Where ; $Vt_{(0)} = 0$

Surface area by the BET plot was calculated by equation 7.

$$S_{BET} (m^2/g) = \frac{V_M \times N \times N_s}{22414 \times 10^{18} nm^2 / m^2} \quad (7)$$

Where, V_M Volume of adsorbate required to complete one statistical monolayer (cm^3/g), I intercept, and S , slop were calculated using equations 8, 9, 10, respectively (Richardson^b,1989).

$$V_M = \frac{1}{S + I} \quad (8)$$

$$I = \frac{1}{V_M C} \quad (9)$$

$$S = \frac{C - 1}{V_M C} \quad (10)$$

N = Avogadro's number (molecule/mole)

N_s = surface area of gas molecule (for $N_2=0.168$).

C = Constant, indicator of adsorbate – surface interaction.

Heat of adsorption (E_1-E_2) by nitrogen gas determined from equation 11 (S.Brunauer, 1938)

$$E_1 - E_2 = RT \ln C \quad (11)$$

Where,

E_1 = average heat of adsorption in monolayer (J/gmol).

E_2 = heat of condensation (J/gmol).

R = gas constant.

T = temperature of experiment (77 K).

Pore Size Distributions

Pore radius r_p obtained from equation 12.



$$r_p = r_k + t \quad (12)$$

Where r_k Kelvin radius was calculated by Kelvin equation 13, assuming zero wetting angles θ . (K.S.W.Sing,1976).

$$\ln \left[\frac{P}{P^0} \right] = \frac{-2\gamma\bar{V}}{r_k RT} \cos \theta \quad (13)$$

P = equilibrium vapor pressure of liquid (torr)

P^0 = equilibrium pressure of the same liquid exhibiting a plane surface (torr)

γ = surface tension (N / m²)

\bar{V} = Molar volume (mol/ m³)

θ = contact angle with which the liquid meets the pore wall

The film depth t (A^0) calculated from the Halsey equation 14(Lowell.S,1984):

$$t = \left[\frac{13.99}{0.03 \gamma - \log \left(\frac{P}{P^0} \right)} \right]^{\frac{1}{2}} \quad (14)$$

The actual pore volume V_p evaluated by recalling the volume evaporated out of the center cores plus the volume desorbed from the film on the pore walls was calculated by equation 15.

$$\Delta V_p = \left(\frac{\bar{r}_p}{\bar{r}_k} \right)^2 [\Delta V_k] \quad (15)$$

Where, \bar{r}_p and \bar{r}_k are the mean two incremental values of r_p and r_k respectively.

ΔV_k , the amount of the decrease in gas condensate in the pores calculated by equation 16.

$$\Delta V_k = \Delta V_{gas} - \Delta V_{liq} \quad (16)$$

Where, ΔV_{gas} difference in interval gas adsorbed and ΔV_{liq} , Volume of liquid determined by equation 17 (Lowell,1984).

$$\Delta V_{liq} = 0.064 \times \Delta t \sum \Delta S_p \quad (17)$$

Where, ΔS_p surface area of the pore walls calculated from the pore volume by equation 18. (K.S.Sing,1982).

$$\Delta S_p = 31.2 \frac{\Delta V_p}{r_p} \quad (18)$$

The total specific surface of catalyst calculated by equation 19.

$$S_{tot.} = S_{BET} + \sum \Delta S_p \quad (19)$$

The percentage of the internal $S_{int.}$ and external $S_{ext.}$ surfaces calculated by equations 20 and 21 respectively.

$$\%S_{int.} = \frac{\sum \Delta S_p}{S_{tot.}} \times 100 \quad (20)$$

$$\%S_{ext.} = \frac{S_{BET}}{S_{tot.}} \times 100 \quad (21)$$

Specific pore size V_p calculated from equation 22.

$$V_p = 0.00156 \times \sum \Delta V_p \quad (22)$$

3-Chemisorptions by Volumetric Apparatus

Volumetric chemical adsorption was done in volumetric apparatus using hydrogen gas at room temperature on fresh and spent Co-Mo\Al₂O₃ catalysts .

The numbers of cobalt atoms exposed on the catalyst surface were evaluated by measuring the hydrogen adsorption at room temperature

according to a procedure and method of calculation described in the literature (abdul-Halim 2002).

The amount of adsorbed H_2 covering the catalyst surface with monomolecular layer was obtained by extrapolating to zero the curve relating the amount of H_2 adsorbed to the adsorption equilibrium pressure of H_2 .

Metal area was calculated by equation 23.

$$A = \frac{NmXm}{M} \quad (23)$$

Where, Nm is the monolayer coverage at zero pressure expressed in surface atoms per gm metal determined by back extrapolation to zero pressure, M is the number of metal atoms per unit area of crystalline surface and Xm is the chemisorptions stoichiometry which is to be taken one (Geus.j.W,1971).

The percentage metal dispersion D is defined as the ratio of the number of the surface atoms to the total number of metal atoms present in the sample.

Percentage metal dispersion can be calculated from the catalyst composition and the metal surface area by equation 24.

$$D = \frac{AW}{NaX} \quad (24)$$

Where, W is the molecular weight of metal, N is Avogadro's number, a is the area per surface metal atom, X is the mass fraction of a metal.

Results and Discussion

Physisorption

1- Surface area

BET plots (P/P^0 Vs $P/[V(P^0 - P)]$) are shown in Figures 2 and 3 for fresh and spent $Co-Mo/Al_2O_3$ catalysts, respectively. These plots used to calculate the volume of gas adsorbed at monolayer

coverage. The results of surface area values for fresh and spent $Co-Mo/Al_2O_3$ catalyst show a decrease in the surface area of spent catalyst. This may be due to blockage a lot of pores or deformity of crystalline surface due to high temperature leads coke deposition and thermal deactivation caused by long time work at relatively high temperature of HDS process (J.Kiurski,1998). These results well agreed with those obtained by Jim Linder (Jim Linder et al,1992).

The higher value of E_1-E_2 for fresh catalyst compared with spent catalyst (Table 2) means that some fraction of surface is unoccupied in spent catalyst and the energy of the adsorption process on a surface located in a narrow pore would be different from that in a wide pore. The sizes of the pore can influenced both the poisoning characteristics of the surface of fresh and spent catalysts (S.H.AL-Khowaiter,1996). High value of E_1-E_2 in fresh catalyst also means higher affinity between nitrogen gas and catalyst surface (L.F.Jones,1977).

2. Pore Size Distribution

Tables 3 and 4 show the pore size distribution calculations of fresh and spent catalysts, respectively. The values of internal surface area in two samples occupied more than 50 % from the total surface area, and the reduction occur in both internal and external surface area of the spent catalyst. This means that a reduction in pore sites is occur and this lead to a reduction in the activity of catalysts and this is may be due to carbon deposition or blocking some pores leading into catalyst activity reduction.

Figures 4 and 5 show pore size distribution of fresh and spent catalyst, respectively. The adsorption curves exhibits behavior type four



according to BET classification, so the pores of these samples are cylindrical.

Chemisorptions

Table 5 shows the results of monolayer coverage, metal area and dispersion of fresh and spent catalysts. It was noticed that metal surface area of spent catalyst reduced compared with fresh which indicates that the amount of hydrogen adsorbed on fresh catalyst is higher than that for spent catalyst. Lower percentage of dispersion for spent catalyst compared with fresh may be due to damage some of metal atom which play as active metal in catalyst (Satterfield,C.N,1969) .This is well agreed with the earlier study of Anderson and Dehghani (Anderson et al, 1949; A.Dehghani, 2009).The high temperature in reactor up to 673k may be the cause of poisoning some of the active sites of catalyst, so, the activity of catalyst decreased. Also the sintering and chemical deposition materials during operation leads to deactivation of spent HDS catalyst (S.Kressmann,1998).This results well agreed with those obtained by Mikhail (Mikhail,R,1973).

Figures 6 and 7 show hydrogen chemisorption isotherms of fresh and spent catalysts, respectively. The values of monolayer coverage obtained in the chemisorption curves show that the the amount of hydrogen chemisorbed in the smaller pore grows rapidly, and then becomes slower until reaching monolayer coverage.

References

Abdul Halim A.-K.Mohammed ,Mazin A. Radhi and Tariq M. Naife (I.J.C.P.E) Vol 3,December 2002 .

A.Dehghani,KH.Forsat et al, Petroleum & Coal Published by Slovnaft VÚRUP , Slovakia, 51(3) 176 ,2009.

American National Standard (ASTM) D4222-83 ,1986 .

Anderson,R.B.Hall,W.Keith,Krieg,J.Amer .Chem.Soc.71,183,1949.

B.Delmon,G.Froment,Catal.Rev.- Sci.Eng.38,69,1996.

Beather,H and Flinn ,R.A,Pet.Ref. ,39,4(34),1960.

Ch.Papadopoulou,J.Vakros,H.K.Matralis,Ch.Kordulis,A.Lycourghiotis,j.colloid interface Sci,261,164,2003.

Francoise Rouquerol,lean Rouquerol and Kenneth Sing, " Adsorption by powders and porous solids", Academic press. 1999.

Geus.j.W., Chemisorption and Reactions on Metallic Films ,j.R.Anderson,ed.Clarendon Press ,London,Vol .1 ,1971 .

H.Topsoe,B.S.Clausen,Catal.Rev.Sci.Eng.26,395, 1984.

Jim Linder,Amit Sachdev et al,J catal.,135,427,1992.

J.Kiurski,D.Z.Obadovic,et al,The scientific journal FACTA UNIVERSITATIS,Vol. 1,135,1998.

Kh.Mohamadbeigy and R.Binesh , Petroleum & Coal, Published by Slovnaft VÚRUP , Slovakia, 47 (3), 21-25, 2005.

K.S.W.Sing, Characterization of Powder Surface,Academic Press,London,1976.

K.S.W.,Sing,S.J.,Gregg, Adsorption Surface Area and Porosity, Academic Press,Inc.,1982.

L.F.Jones,D.Dollimore and R.Robinson ,J.Colloid Interface Sci. 64,237,1977.

Lowell.S,and John.E.Shields,powder surface area and porosity ,Chapman and Hill,London and New York,1984.

Mignard, S.; Kasztelan, S.; Dorbon, M.; Billon, A.; Sarrazin, P. stud.surf.sci.Catal.1996. 100-209 .

Mikhail,R,etal.,J.Appl.Chem.Biochnol.,23,419,1973.

P. Ferreira-Aparicio,a A. Guerrero-Ruizb and I. Rodriguez-Ramos J. Chem. Soc., Faraday Trans., 1997, 93(19), 3563-3567 .

P.Wiwel ,P,Zeuthen and A.C. Jacobsen, "Catalyst Deactivation", Elsevier Amsterdam,1991.

Richardson_a ,J.T.I & EC.Fund.,3(1),54,1964.

R.Prins,V.H.J.deBeer,G.A.Somorjai, Catal.Rev.-Sci.Eng.31,1,1989.

Richardson_b ,J.T.Principle of Catalyst Development,Houston,Texas,Plenum press,New York,1989.

S.Brunauer, P.H.Emmet and Teller
j.Amer.Chem.Soc.,60,309,1938.

S.H.AL-Khowaiter,A.A.AL-Owais and N.R.EL-Nazar,J.King Saud Univ.,Vol.8 .Science 1,63,1996.

S. Shokri, S Zarrinpashne, Petroleum & Coal Published by Slovnaft VÚRUP , Slovakia, 48(1) 27-33 ,2006.

S.Kressmann,F.Morel,V.Harle,S.Kasztelan,Catal. Today,43,203,1998.

Song, C.; Ma, X. *Appl. Catal. B* **2003**, *41*, 207

Turaga, U. T.; Song, C. *Catal. Today* **2003**, *86* (1-4), 129.

**Table 1 Properties of Fresh and Spent CoMo/Al₂O₃ catalysts**

Fresh CoMo/Al ₂ O ₃ catalyst		Spent CoMo/Al ₂ O ₃ catalyst	
Mo , wt%	12	Mo , wt%	12.6
CoO , wt%	4	CoO , wt%	5.2
NiO , wt%	0.06	NiO, wt%	0.13
Fe , wt%	0.03	Fe, wt %	0.06
SO ₄ , wt%	1.5		
Al ₂ O ₃	Balance		
Form	Extrudate		
Normal Size ,mm	2.5		
Surface Area , m ² /g	280		
Pore Size , Cm ³ /g	0.55		
Porosity %	0.67	Porosity %	0.38

Table 2 Monolayer Capacity, Surface Area and heat of adsorption

Catalyst	V _m Cm ³ /g	S _{BET} m ² /g	E ₁ -E ₂ J/gmol
Fresh Co-Mo\Al ₂ O ₃	62.88	273.76	2878.898
Spent Co-Mo\Al ₂ O ₃	28.169	122.625	878.766

Table 3 Pore Size Distribution of Fresh Catalyst

P/P ⁰	V _{gas}	r _k	t	r _p	r _p ⁻	r _K ⁻	Δt	ΔV _{gas}	ΔV _{liq}	ΔV _k	ΔV _p	ΔS _p	ΣΔS _p
0.964	300.8	259.3	18.2	277.5	237.6	220.4	2.1	1.1	0.0	1.1	1.3	0.2	0.2
0.949	299.7	181.6	16.1	197.7	178.1	162.6	1.2	0.3	0.0	0.3	0.3	0.1	0.3
0.936	299.4	143.7	14.9	158.6	123.1	109.7	2.9	5.5	0.1	5.4	6.7	1.7	2.0
0.828	293.9	75.7	12.0	87.7	74.6	62.8	0.4	3.4	0.1	3.3	4.6	1.9	3.9
0.827	290.5	50.7	11.6	61.6	53.9	43.3	2.1	5.3	0.5	4.8	7.4	4.3	8.2
0.772	285.2	36.7	9.5	46.2	41.7	23.6	0.8	10.7	0.4	10.3	16.8	12.5	20.7
0.717	274.5	28.5	8.7	37.2	34.1	52.7	0.6	29.6	0.8	28.8	50.7	46.4	67.1
0.661	244.9	22.9	8.1	31.0	28.8	20.9	0.5	59.5	2.1	57.4	108.9	117.9	185.0
0.607	185.4	19.0	7.6	26.6	24.8	17.4	0.5	41.5	5.9	35.6	72.3	90.9	275.9
0.550	143.9	15.9	7.1	23.0	21.6	14.7	0.3	21.5	5.3	16.2	37.9	50.4	326.3
0.496	122.4	13.5	6.8	20.3	19.1	12.5	0.3	13.6	6.3	7.3	17.0	27.7	354.0
0.439	108.8	11.5	6.5	18.0									
Σ(ΔS _p)=354.0 m ² /g ,S _{total} =273.76+354.0=627.76 m ² /g ,S _{ext.} %=43.7 ,S _{int.} %=56.3 ,V _p =0.5 Cm ² /g													

Table 4 Pore Size Distribution of Spent Catalyst

P/P ⁰	V _{gas}	r _k	t	r _p	r _p ⁻	r _K ⁻	Δt	ΔV _{gas}	ΔV _{liq}	ΔV _k	ΔV _p	ΔS _p	ΣΔS _p
0.964	260.2	259.3	18.2	277.5	245.8	228.4	1.6	0.6	0.0	0.6	0.7	0.1	0.1
0.953	259.6	197.5	16.6	214.1	187.6	171.8	1.6	0.3	0.0	0.3	0.4	0.1	0.2
0.937	259.3	146.1	15.0	161.1	124.8	111.2	2.9	5.2	0.0	5.2	6.5	1.6	1.8
0.883	254.1	76.4	12.1	88.5	74.6	63.3	1.6	11.6	0.2	11.4	15.8	6.6	8.4
0.828	242.5	50.3	10.5	60.8	53.4	43.5	1.1	32.9	0.6	32.3	48.7	28.4	36.8
0.772	209.6	36.7	9.4	46.1	41.7	32.7	0.7	58.3	1.6	56.7	92.2	68.9	105.7
0.718	151.3	28.7	8.7	37.4	34.3	25.9	0.6	40.1	4.1	36.0	63.1	57.4	163.1
0.663	111.2	23.1	8.1	31.2	28.9	21.1	0.5	21.4	5.2	16.2	30.4	32.8	195.9
0.608	89.8	19.1	7.6	26.7	24.9	17.5	0.4	9.9	5.0	4.9	9.9	12.4	208.3
0.552	79.9	16.0	7.2	23.2									
Σ(ΔS _p)=208.3 m ² /g ,S _{total} =122.625+208.3=330.925 m ² /g ,S _{ext.} %=44.9 ,S _{int.} %=55.1 ,V _p =0.417 Cm ² /g													

Table 5 Results of chemisorption calculations

Catalyst	N _s (Monolayer Coverage of Monolayer H ₂)	Area m ² /g	Dispersion %
fresh Co-Mo\Al ₂ O ₃	6.34×10 ²⁰	50.72	88.76
spent Co-Mo\Al ₂ O ₃	4.88 ×10 ²⁰	39.04	57.13

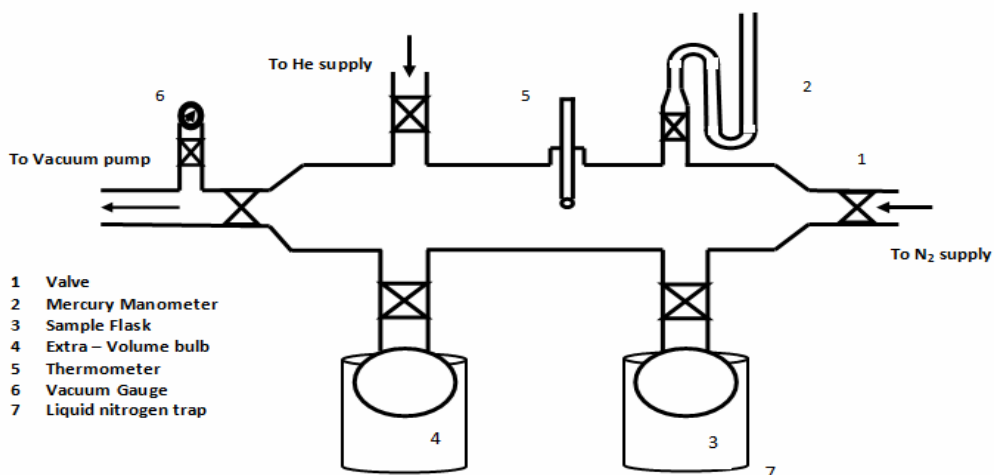


Fig.1 ASTM apparatus of adsorption measurements

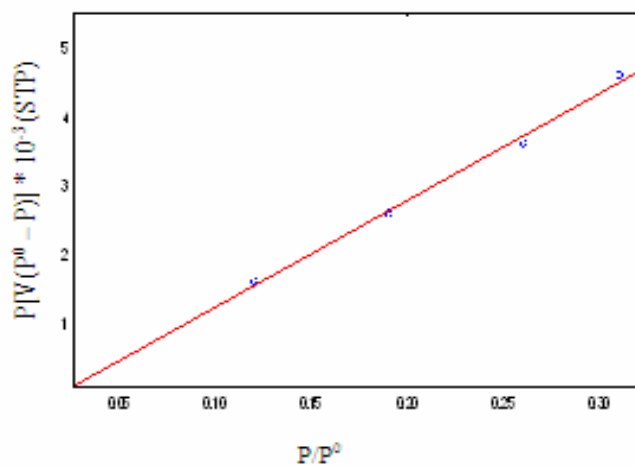


Fig.2 BET plot of adsorption data of Fresh Co-Mo\Al₂O₃ catalyst

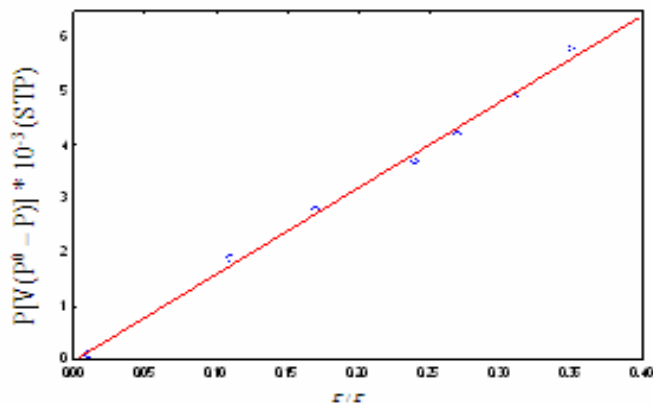


Fig.3 BET plot of adsorption data of Spent Co-Mo\Al₂O₃ catalyst

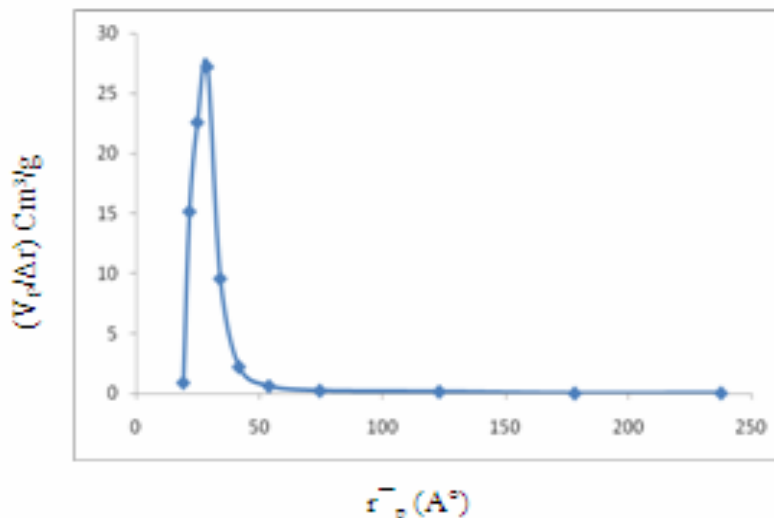


Fig. 4 Pore Size distribution of Fresh Co-Mo/Al₂O₃ catalyst

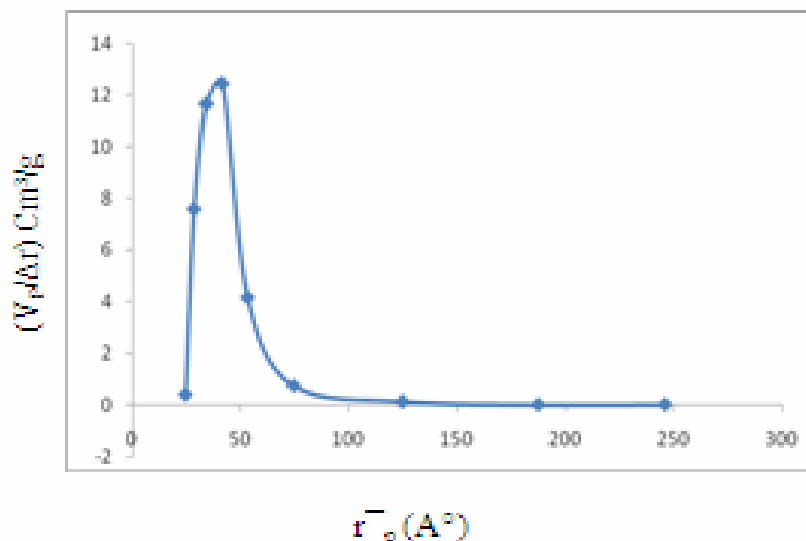


Fig. 5 Pore Size distribution of Spent Co-Mo/Al₂O₃ catalyst

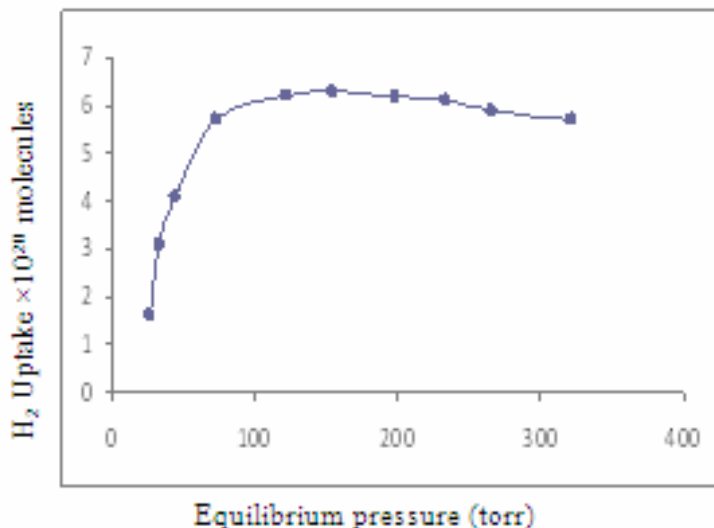


Fig.6 Chemisorption isotherm of Fresh Co-Mo/Al₂O₃

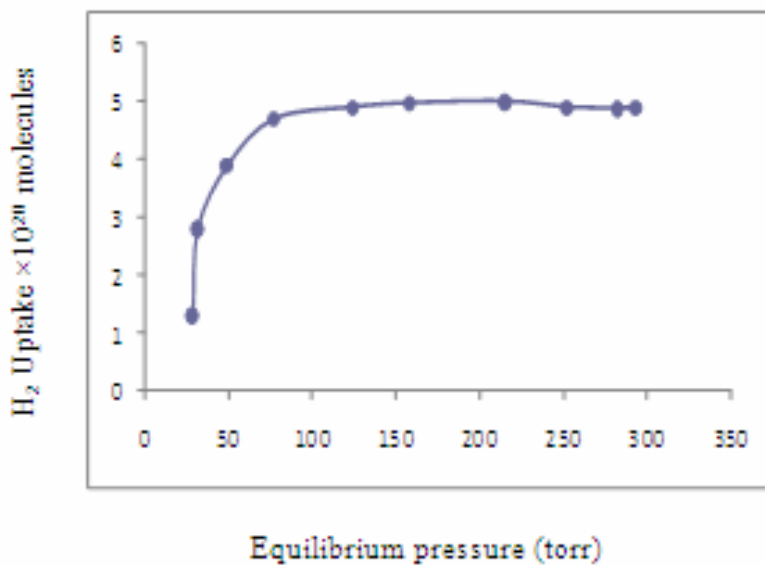


Fig.7 Chemisorption isotherm of Spent Co-Mo/Al₂O₃



ADAPTIVE CYCLIC PREFIX LENGTH FOR CONVOLUTIONAL CODE OFDM SYSTEM IN FREQUENCY SELECTIVE CHANNEL

Ashwaq A. Abed Aljanaby

Malathe Salah AL-Deen

University of Baghdad / Engineering college

ABSTRACT:

Orthogonal Frequency Division Multiplexing (OFDM) is one of recent years multicarrier modulation used in order to combat the Inter Symbol Interference (ISI) introduced by frequency selective mobile radio channel. The circular extension of the data symbol, commonly referred to as cyclic prefix is one of the key elements in an OFDM transmission scheme. This paper study The influence of the cyclic prefix duration on the BER performance of an OFDM-VCPL (Orthogonal frequency division multiplexing - Variable Cyclic Prefix Length) system and the conventional OFDM system with frame 64-QAM modulation is evaluated by means of computer simulation in a multipath fading channel. The adaptation of CP is done with respect to the delay spread estimation of the channel.

الخلاصة:

النظام المبني على التقسيم المتعدد المتعامد للترددات (OFDM) هو احد الاساليب المبنية لمكافحة التداخل المرز (Inter-Symbol-Interference) الذي يحدث نتيجة القنوات الراديوية التي تتغير خصائصها مع الزمن بسبب الانتشار المتعدد المسار. هذا البحث يدرس تأثير (Cyclic Prefix) وهو احد العوامل المؤثرة في مخطط نقل العناصر الممكن استخدامها في نظام التقسيم المتعدد المتعامد للترددات (OFDM-VCPL) على نظام اداء (convolutional coded OFDM) الذي يتم تقييمه عن طريق (64-QAM) وتكيف ال CP مع تقدير تأخير الامتداد (delay spread) للقناة (multipath Fading channel) والذي يتم عن طريق المحاكاة الحاسوبية .

INTRODUCTION:

Orthogonal frequency division multiplexing (OFDM) is an important broadband wireless communication scheme. Originally developed in the late 1950s and 1960s, is being used or considered in various wireless communication systems. (Peter Fertl, 2009 & Gregory E. Bottomley, 2006) In a wireless communication the signals that are sent from a sender to a receiver can follow multiple paths with each its own characteristics (attenuation, delay, etc.). This is called multi-path propagation. This multi-path propagation of a wireless channel often introduces Inter Symbol Interference (ISI). (Jeroen Theeuwes, 2004)

To counteract the ISI, the high efficiency Orthogonal frequency division multiplexing (OFDM) modulation first splits the high-rate data stream into a number of parallel sub-streams and modulates them onto different orthogonal sub-carriers and thus lower the symbol rate, and then add a Cyclic Prefix (CP) to the head of each symbol to reduce the influence of adjacent symbol interference. (ZHANG Zhao, 2004)

Although the concept of Cyclic Prefix has been traditionally associated with OFDM systems, the CPs are crucial to OFDM system, they introduce significant overhead. For example, in 802.11 a wireless LAN, a fixed proportion of 1/5 of the energy and time is spent on CPs. As system design rule, the CP length should be about two times the RMS (Root-Mean-Squared) delay spread (Van Nee and Prasad, 2000).

Obviously, the RMS delay spread is not constant in a wireless mobile communication environment. Conventional OFDM system usually chooses a fixed CP length based on the average or even maximum delay spread

the mobile terminal may experience. According to a measurement conducted in (Van Nee and Prasad, 2000), when the mobile terminal is in an office building room, the RMS delay spread is about 35ns, but when the mobile terminal moves into a factory, the RMS delay spread will change to 300 ns. If the receiver is designed based on the measurement in the office, it will undergo severe ISI when the user moves to a factory.

On the other hand, if the receiver is designed according to the measurement in the factory, some of the guard interval is unnecessary which will consume the scarce spectral and power resources but achieve no extra gain. So it is natural to think that if we can estimate the RMS delay spread and change the length of CP accordingly, the overhead of CPs will be reduced when delay spread becomes large. (ZHANG Zhao, 2004 & Van Nee and Prasad, 2000)

THE BLOCK DIAGRAM OF OFDM:

In the fig-1-, a classical OFDM transmission scheme using FFT (Fast Fourier Transform) is illustrated. The input data sequence is baseband modulated, using a digital modulation scheme. Various modulation schemes could generally be employed such as BPSK, QPSK (also with their differential form) and QAM with several different signal constellations. In our system, 64-QAM method is chosen in order to encode the binary information. Data is encoded „in-frame” (the baseband signal modulation is performed on the serial data, that is inside of what we name a „DFT frame”, or equivalently an OFDM symbol). The data symbols are parallelized in N different sub-streams. Each sub-stream will modulate a



separate carrier through the IFFT modulation block, which actually generates the OFDM symbol, performing the multicarrier modulation. A cyclic prefix is inserted in order to eliminate the inter-symbol interference. The data are back-serial converted, forming an OFDM symbol that will modulate a high-frequency carrier before its transmission through the channel. The radio channel is generally referred to as a linear time-variant system. To the receiver, the inverse operations are performed in order to estimate the transmitted symbols. (Werner Henkel ,2002 & Marius Oltean ,2003)

CYCLIC PREFIX:

Cyclic prefix is a crucial feature of OFDM used to combat the Inter-Symbol-Interference (ISI) introduced by the multi-path channel through which the signal is propagated. The basic idea is to replicate part of the OFDM time-domain waveform from the back to the front to create a guard period. The duration of the guard period T_g should be longer than the worst-case delay spread of the target multi-path environment. However the use of CP reduces the efficiency of the system by the factor $N/(N+v)$ (where v is the length of CP). (Buthaina Mosa Omran,2007) Fig-2- illustrates the idea. At the receiver, certain position within the cyclic prefix is chosen as the sampling starting point, which satisfies the criteria

$$\tau_{\max} < T_x < T_g$$

where τ_{\max} is the worst-case multi-path spread. As illustrated in the following figure, once the above condition is satisfied, there is no ISI since the previous symbol will only have effect over samples within $[0, \tau_{\max}]$. (Yun Chiu ,2000)

Generally, the radio channel exhibits both time variant and frequency selective

characteristics. If we shall consider however that the channel parameters remain unchanged during the transmission of an OFDM symbol, the way that the transmission medium distorts each particular frame is similar to the distortion caused by an electric filter. (B.Sklar,1997) Under this assumption we can consider the equivalent discrete response of the channel as a linear FIR filter of order L , of which the equation is given below:

$$H(z) = \sum_{l=0}^L h(l)z^{-l} \quad (1)$$

the equivalent baseband signal at the channel output can be obtained by the operation of convolution, as follows:

$$y_{cp}[n] = x_{cp}(n) * h(n) \quad (2)$$

Discarding the L CP samples from the received sequence, the remaining (useful) signal can be expressed as:

$$y(n) = x(n) \circledast h(n) \quad (3)$$

Where " \circledast " denotes the circular convolution

operator. (Chini A., 1994)

The noticeable thing about the eq.3 is that the circular convolution preserves the temporal support of the signal. In our case, N transmitted signal samples convolved with $L+1$ channel impulse response samples will conduce to a received symbol of length N that will be used in the demodulation process. Since the circular convolution will not "spread" the signal, the receiver can independently process each data block. The interference from the previous transmitted

blocks is totally eliminated through this operation of CP insertion/extraction.

Furthermore, since $x[n] = \text{IDFT}\{X[k]\}$ and taking into account the effect of the DFT demodulator, the received symbols $Y[k]$ can be expressed as:

$$Y(k) = \text{DFT}\{\text{IDFT}\{X(k)\} \otimes h(n)\}, \quad k=0,1,\dots, N-1 \quad (4)$$

Since the DFT of a circular convolution of two discrete time signals will conduce to a spectral multiplication:

$$\begin{aligned} Y(k) &= \text{DFT}\{\text{IDFT}\{X(k)\}\} \cdot \text{DFT}\{h(n)\} \\ &= X(k) \cdot H(k) \quad k = 0, 1, \dots, N-1 \end{aligned} \quad (5)$$

where $H[k]$ represents the sampled frequency response of the equivalent baseband discrete channel, corresponding to the frequencies $\Omega_k = k(2\pi/N)$. The crucial consequence of the relation above is that each modulation symbol $X[k]$ could be recovered to the receiver by a simple pointwise division operation, commonly referred to as a "one-tap frequency domain equalizer", as can be seen from the relation (6).

$$\hat{X}(k) = Y(k) \cdot H^{-1}(k) \quad k=0,1,\dots,N-1 \quad (6)$$

FREQUENCY SELECTIVE CHANNEL MODEL:

In wireless communications systems, the transmitted signal typically propagates via several different paths from the transmitter to the receiver. This can be caused, e.g., by reflections of the radio waves from the surrounding buildings or other obstacles, and is typically called multipath propagation. Each of the multipath components have generally different relative propagation delays

and attenuations which, when summing up in the receiver, results in filtering type of effect on the received signal where different frequencies of the modulated waveform are experiencing different attenuations and/or phase changes. This is typically termed **frequency-selective fading**. (Eero Maki-Esko, 2007)

Frequency-selective channels are characterized by a constant gain and linear-phase response over a bandwidth that is smaller than the bandwidth of the signal to be transmitted. Equivalently, in the time domain, the length of the impulse response of the channel is equal to or longer than the width of the modulation signal. (Haris Vikalo, 2004)

SYSTEM MODEL:

The proposed adaptive OFDM system used in the test is shown in Fig-3. The system consists of a transmitter, a receiver and a frequency selective channel.

At the receiving end, the channel estimation is performed and the channel frequency response is used in estimation of the delay spread. This delay spread is feedback to the transmitter to adapt the length of the cyclic prefix, so when the delay spread is large, the length of the CP increase and when it small the length of the CP decreases.

The transmitter codes the input data by the convolutional coder, that is efficient in the multipath fading channel. The encoded data are punctured to generate high code rates from a mother code rate, The coded serial bit sequences are converted to the parallel bit sequences and then modulated. The OFDM time signal is generated by an inverse FFT and is transmitted over the Rayleigh fading channel after the cyclic extension has been inserted. In the receiver side, the received signal is serial to parallel converted and passed to a FFT operator, which converts the



signal back to the frequency domain. This frequency domain signal is coherently demodulated. Then the binary data is decoded by the Viterbi hard decoding algorithm.

Punctured Convolutional Codes

The characteristics of a wireless channel typically vary with time, and therefore to obtain optimal performance it is necessary to adapt the error coding scheme to the changing channel characteristics. Code puncturing allows an encoder / decoder pair to change code rates, i.e., code error correction capabilities, without changing their basic structure.

Code puncturing involves not transmitting certain code bits. The encoder for a punctured code can be fabricated using the original low-rate convolutional encoder followed by a bit selector which deletes specific code bits according to a given puncturing rule. Only the bit selection rule is changed to generate different rates of codes. At the receiver side, a Viterbi decoder based on the mother code decoder is used for decoding the punctured codes of the family.

To decode different rate codes, only metrics are changed according to the same puncturing rule used by the encoder (the deleted bits are not counted when calculating the path metrics). Fig-4- shows the puncturing pattern of IEEE802.11a used to generate 3/4 code rate, coming from the mother code rate, high lighted bits are the deleted bits (Fernando H. Gregorio,2006).

Channel Estimation and Equalization

Channel estimation can be achieved by transmitting pilot OFDM symbol as a preamble. To design a channel estimator for wireless systems with both low complexity and good channel tracking ability, one must

choose a way of how pilot information (data/signals known to the receiver) should be transmitted. These pilots are usually needed as a point of reference for such estimator.

A fading channel requires constant tracking so pilot information has to be transmitted more or less continuously. However, an efficient way of allowing continuously update channel estimate is to transmit pilot symbol instead of data at certain location of the OFDM time frequency lattice.

Assuming P is the transmitted pilot data, the received signal after FFT is:

$$Y(k) = H(k)P(k) + W(k) \quad (7)$$

Where $w(k)$ is the noise components, and since, the pilot data is known at the receiver, then the simplest way to estimate the channel is by dividing the received signal by the known pilot :

$$\hat{H}(K) = Y(K)/P(K) \quad (8)$$

Where $\hat{H}(K)$ is the estimate of the channel, and without noise, this gives the correct estimation. When noise is present, there could be an error (Buthaina Mosa Omran ,2007).

The channel estimation can be performed by either inserting pilot tones into all of the subcarriers of OFDM symbols with a specific period or inserting pilot tones into each OFDM symbol.

Although the guard time which has longer duration than the delay spread of a multipath channel can eliminate ISI because of the previous symbol, but it is still have some ISI because of the frequency selectivity of the channel. In order to compensate this distortion, a one-tap channel equalizer is needed. At the output of FFT on the receiver side, the sample at each subcarrier is multiplied by the coefficient of the corresponding channel equalizer.(Kamran arshad,2002)

DELAY SPREAD ESTIMATION:

The knowledge about the delay spread of the channel can be used for designing better systems which adapt themselves to the changing nature of the transmission media. (Tevfik, 2006)

We consider a noisy time-varying channel characterized by its impulse response $h_{l,m}(l=0,1,\dots,L)$ with $L \leq N_g$ the maximum delay and by the noise $n_{m,i}$ assumed AWGN with variance σ^2 .

We propose a delay spread estimator based on the frequency correlation function of the channel estimate in frequency domain. According to the (El Kefi Hlel, 2003) the channel frequency correlation function at a given OFDM symbol is defined by:

$$r_{HH}(\Delta f) = \frac{\sigma_H^2}{1 + j2\pi\tau_d\Delta f} \quad (9)$$

where σ_H^2 is the variance of the channel frequency response, Δf is the sub-channel spacing of the OFDM symbol and τ_d is the channel delay spread.

Two ML estimates of σ_H^2 and $\hat{r}_{HH}(\Delta f)$ are given by the following expressions:

$$\hat{r}_{HH}(\Delta f) = \frac{1}{(N-1)P_0} \sum_{k=0}^{N-2} \sum_{i=0}^{P_0-1} \hat{H}_{k,i} \hat{H}_{k+1,i}^* \quad (10)$$

and

$$\hat{\sigma}_H^2 = \frac{1}{NP_1} \sum_{k=0}^{N-1} \sum_{i=0}^{P_1-1} \hat{H}_{k,i} \hat{H}_{k,i}^* \quad (11)$$

Where P_0 and P_1 are integers ≥ 1 .

Finally, the estimation of the delay spread can be deduced using equations (9),(10) and (11):

$$\hat{\tau}_d = \frac{\sqrt{\frac{\hat{\sigma}_H^2}{\text{Re}(\hat{r}_{HH}(\Delta f))} - 1}}{2\pi\Delta f} \quad (12)$$

Decoding

There are several different approaches to decode convolutional codes. These are joined in two basic categories, Sequential decoding and Maximum Likelihood decoding (Viterbi decoding).

The Viterbi decoder examines an entire received sequence of a given length. The decoder computes a metric for each path and makes a decision based on this metric. All paths are followed until two paths converge on one node. Then the path with the higher metric is kept and the one with lower metric is discarded. The paths selected are called the survivors.

For an N bit sequence, the total number of possible received sequences is 2^N . The Viterbi algorithm applies the Maximum Likelihood principles to limit the comparison to 2 to the power of kL surviving paths instead of checking all paths. The most common metric used is the Hamming distance metric, *Hard Decoding*. This is just the dot product between the received codeword and the allowable codeword. (Fernando H. Gregorio, 2006)

SIMULATION RESULTS:

We evaluate the performance of the proposed scheme by choosing communication link of Tx/Rx for adaptive OFDM-VCPL system. The OFDM symbol period is $4\mu s$ (80 samples). The modulation is 64-QAM and the number of sub-channels is 64 carriers, sampling frequency 20 MHz, and sampling time 50 nsec. The cyclic prefix duration $0.8\mu s$ (16 samples) and the data duration is $3.2\mu s$ (64 samples). Using frequency selective channel with 8 paths Rayleigh fading channel Fig.-5-, sample time 50 nsec, max Doppler frequency is 30 Hz the paths gains = [-1 -2 -3 -4 -5 -6 -7 -8] dB and Paths delay = [1 2 3 4 5 6 7 8] * T sec In order to change the length of the cyclic prefix adaptively, we must estimate the channel impulse response, and the delay



spread of it. Fig-6- shows the normalized mean square error (NMSE) of the delay spread estimation verses SNR.

When we know the delay spread of channel then the duration of the CP of the next transmission as $2 \times$ (max delay spread) according to the design rule(choosing the worst case of delay channel).

Fig. -7- shows the BER performance of the OFDM system. The BER is obtained under the assumption that synchronization and carrier recovery are perfect and only noise and channel estimation error is considered.

Fig. -8- is the maximum achievable coded data rates the system can get using 64 QAM as its modulation method. The system with fixed CP length can achieve 72 Mb/s. it is fixed no matter where the transceiver is. But for the OFDM-VCPL, its maximum coded data rates can be as high as 90 Mb/s. it achieves 18 Mb/s gain over fixed scheme. It is very desirable considering that the spectrum is very scarce.

As can be seen from the Fig.-9-, increasing the cyclic prefix duration improves the BER performance for the OFDM-VCPL system. Theoretically, if the cyclic prefix duration spans more than the maximum delay spread of the channel, the errors can be completely eliminated. This assumes however a perfect knowledge of the channel impulse response (or, equivalently, of the channel transfer function), which is a mandatory condition for implementing the eq.6. Since in our implementation channel estimation techniques are employed, the exact form of the channel impulse response constitutes information that can be exploited in the data estimation process. The correct detection is entirely based on the robustness and simplicity of the digital modulation scheme that is involved, namely 64-QAM. A noticeable thing resulting from the fig.-9- is that while identical for cyclic prefix lengths which cover the channel impulse response, the performance degrades for the cases where the cyclic prefix duration becomes insufficient. Thus, if a cyclic prefix of length 8 is used, the transmission offers the

best performance between all the considered situations, but only starting with a value of the normalized delay that overtakes the length of the circular extension for all the other cases.

CONCLUSION:

An adaptive OFDM –VCPL system is described .the CP length is changed based on the estimation result. simulation result at fig.- 8- show that the system with fixed CP length achieve 72Mb/s and with variable CP length can achieve as high as 90Mb/s. it achieve 18 Mb/s gain over fixed scheme. The cyclic prefix duration influences the performance of an adaptive OFDM system. The transmission is sensitive to the parameter obtained as multi-path delay of channel normalized by the cyclic prefix duration. A noticeable thing resulting from the fig.-9- is that while identical for cyclic prefix lengths which cover the channel impulse response, the performance degrades for the cases where the cyclic prefix duration becomes insufficient. Thus, if a cyclic prefix of length 8 is used, the transmission offers the best performance between all the considered situations, but only starting with a value of the normalized delay that overtakes the length of the circular extension for all the other cases.

I- REFERENCES:

B.Sklar, "Rayleigh Fading Channels in Mobile Digital Communication System"IEEE Commun.Mag., July 1997

Buthaina Mosa Omran ,“IMPROVEMENT TECHNIQUES FOR SATELLITE DIGITAL VIDEO BROADCASTING USING OFDM”, P.HD. Thesis, in electronic and

communication engineering, University of Baghdad, 2007.

Chini A., " Multicarrier Modulation in Frequency Selective Fading Channel", Ph.D.thesis, Carleton University, chapter 3, 1994

Eero Maki-Esko, Mikko Valkama, and Markku Renfors,"Time-and Frequency – Selective Fading Channel",ICE University of Technology,Finland, 8 Jan 2007

Fernando H. Gregorio,"802.11a - OFDM PHY Coding and Interleaving", Helsinki University of Technology, Vol. 4, Issue 8, pp. 1-6, 2006

Gregory E. Bottomley and Leif R. Wilhelmsson "Recycling the Cyclic Prefix in an OFDM System" 2006 IEEE

Haris Vikalo, Babak Hassibi, Bertrand Hochwald,and Thomas Kailath "On the Capacity of Frequency –Selective Channels in Training-Based Transmission Schemes" IEEE transaction on signal processing, VOL,52,NO.9,SEPTEMBER 2004

Jeroen Theeuwes, Frank H.P Fitzek, Carl Wijting,"Multihopping for OFDM Wireless Networks"Center for TeleInfrastruKtur (CTiF),Aalborg University,June 2004

Kamran arshad, "Channel Estimation In OFDM Systems", M.Sc. Thesis, King Fahd University of Petroleum and Minerals, Dhahran, Saudi Arabia,2002

Marius Oltean, Miranda Naformita " The Cyclic Prefix Length Influence on OFDM-Transmission BER", tom 48(62),Fascicola 2,2003

Peter Fertl and Gerald Matz , "EFFICIENT OFDM CHANNEL ESTIMATION IN MOBILE ENVIRONMENTS BASED ON IRREGULAR SAMPLING" Gusshausstrasse 25/389,A-1040 Vienna,Austria,2009

Van Nee,R.,Prasad,R.,2000 "OFDM for Wireless Multimedia Communications" Artech House, Boston,p.46.

Werner Henkel, Georg Tauböck, Per Ödling, Per Ola BÖrjesson, Niklas Petersson" the Cyclic Prefix of OFDM/DMT-An Anaqlysis"2002 International Zurich Seminar on Broadband Communication Access-Transmission-Networking February 19-21,ETH Zurich,Switzerland

Yun Chiu, Dejan Markovic, Haiyun Tang, Ning Zhang " OFDM Receiver Design", EE225C Final Report, 12 December 2000

ZHANG Zhao-yang, LAI Li-feng " Anovel OFDM transmission scheme with length-adaptive Cyclic Prefix", paper, 2004

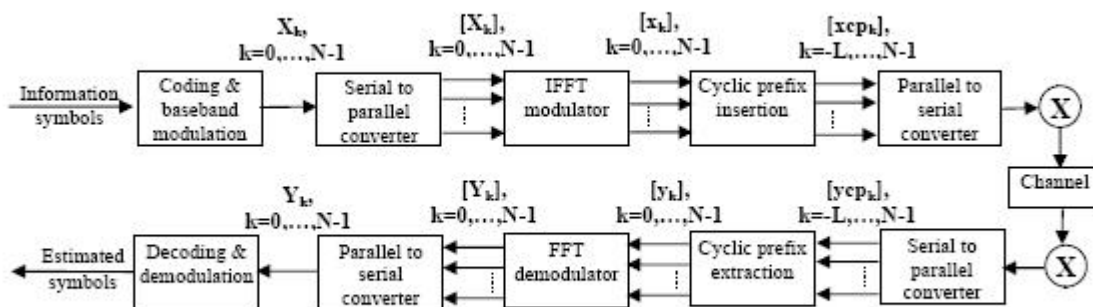


Fig-1- The block diagram of general OFDM system

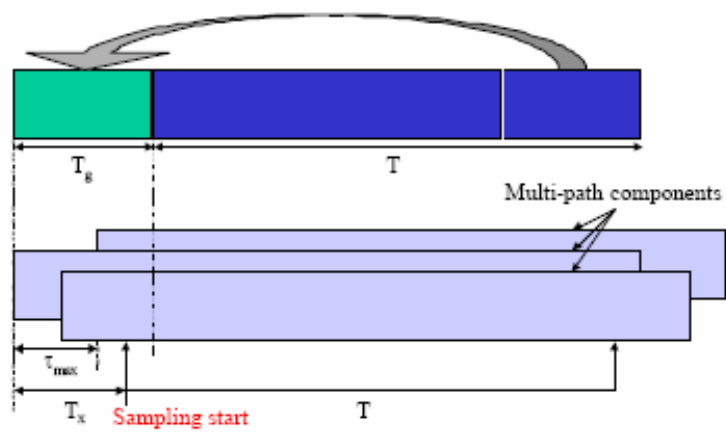


Fig-2- cyclic prefix

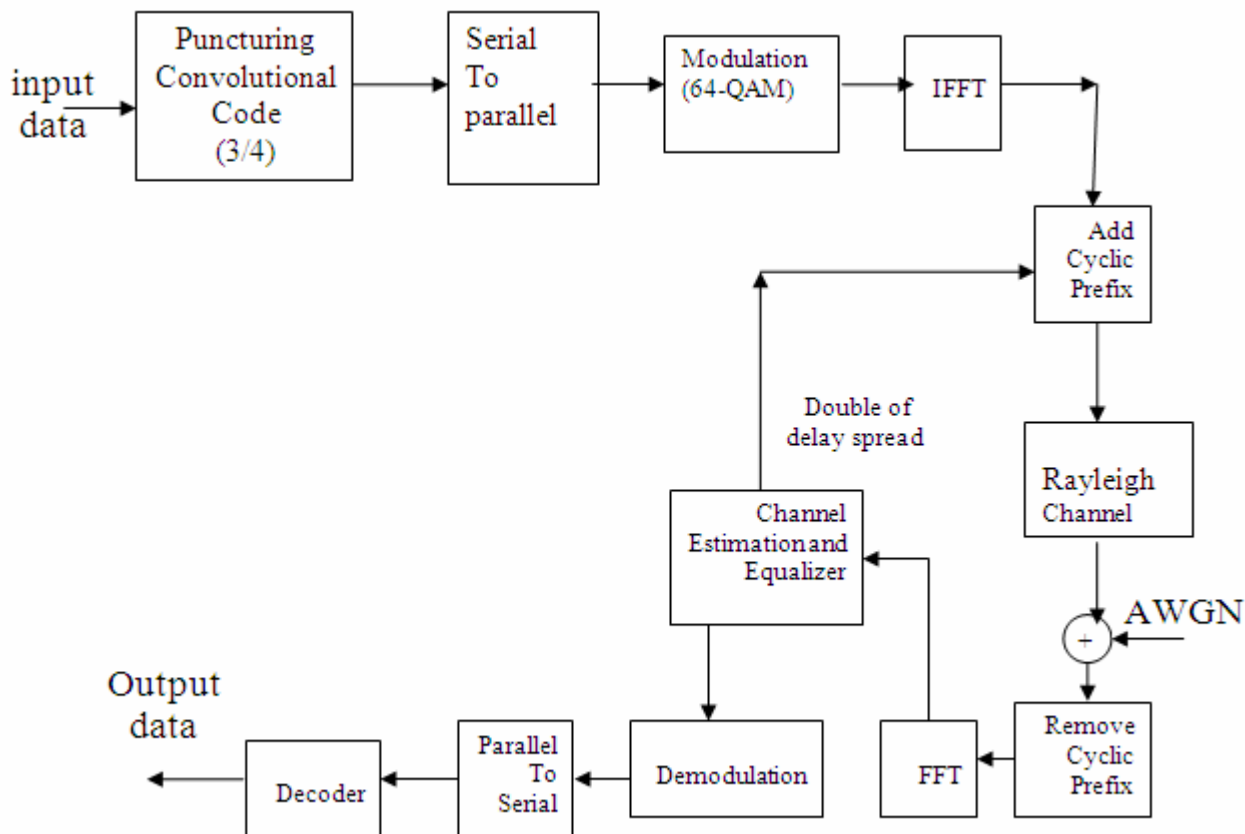


Fig-3- the proposed block diagram of an OFDM-VCPL system

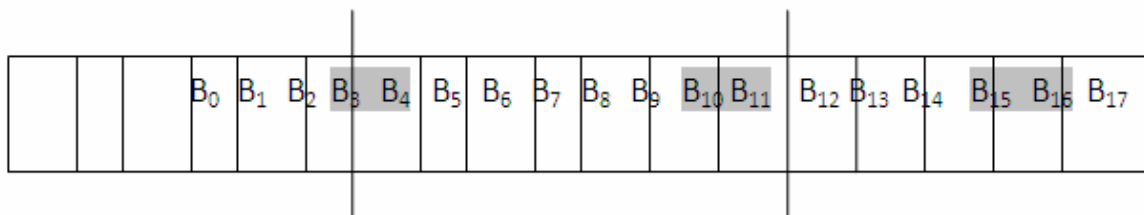


Fig-4- Puncturing patterns of IEEE802.11a, 3/4 code rate.

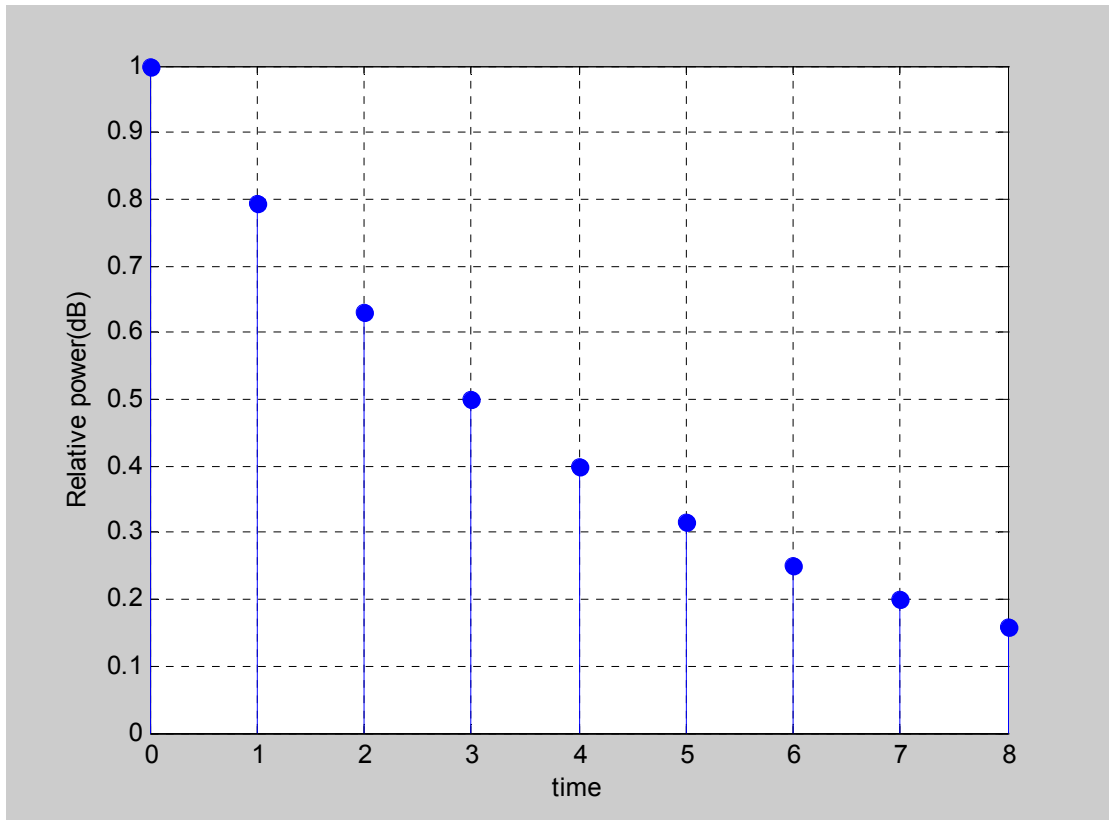


Fig-5- Channel model

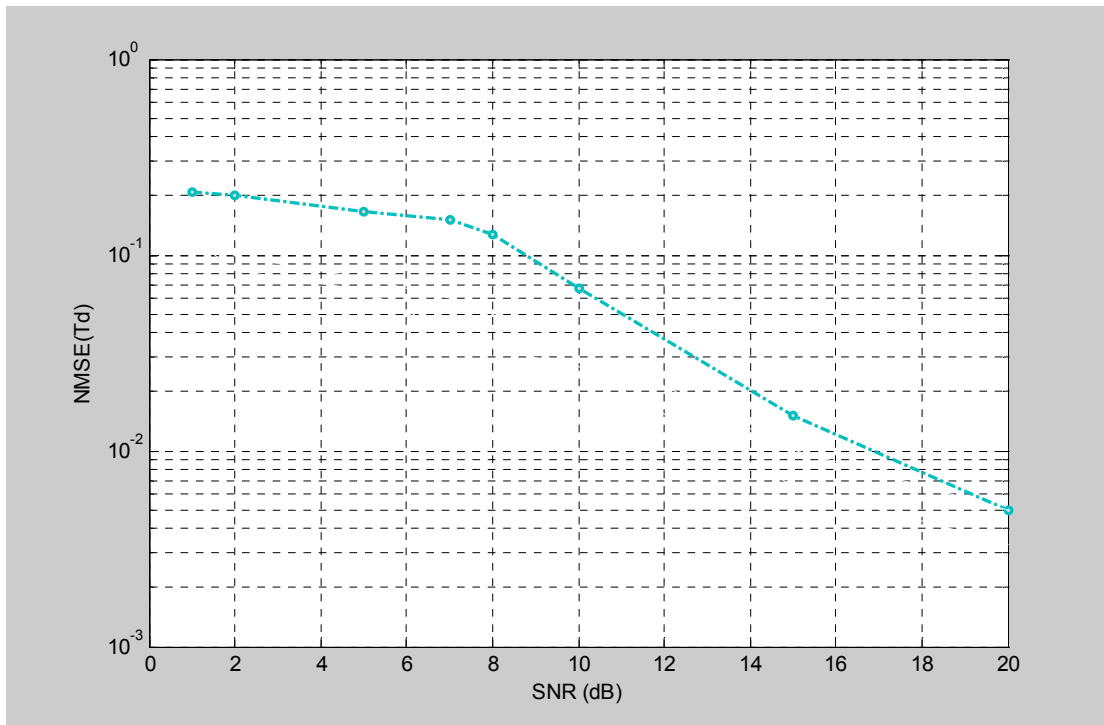


Fig- 6- NMSE(T_d) versus SNR

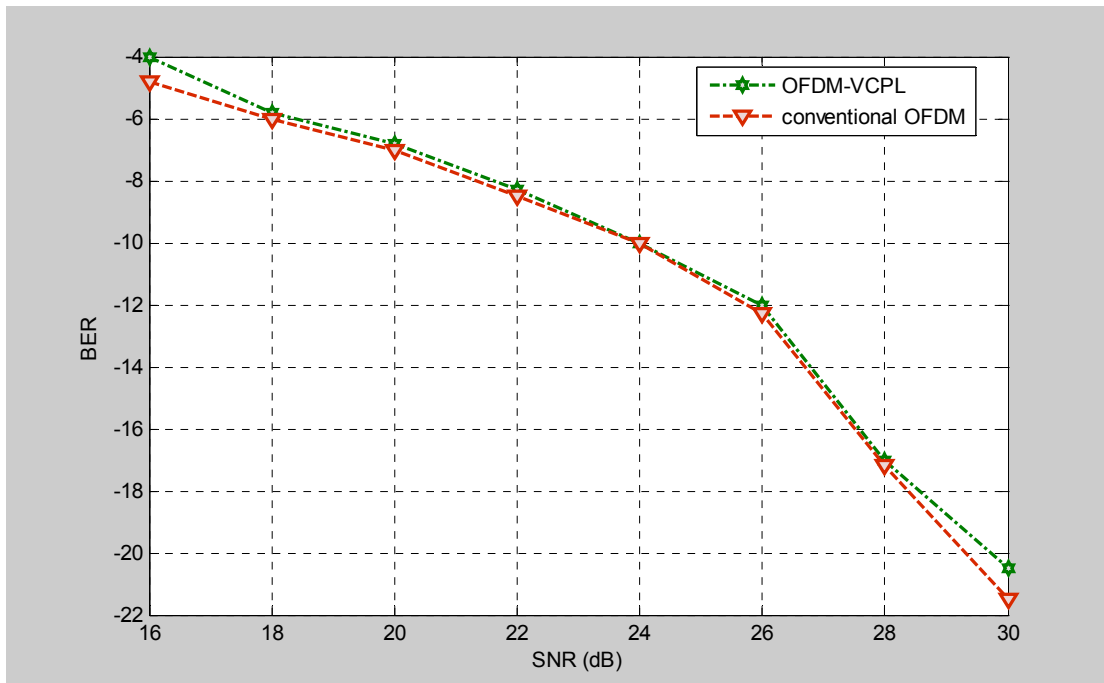


Fig-7- BER versus SNR

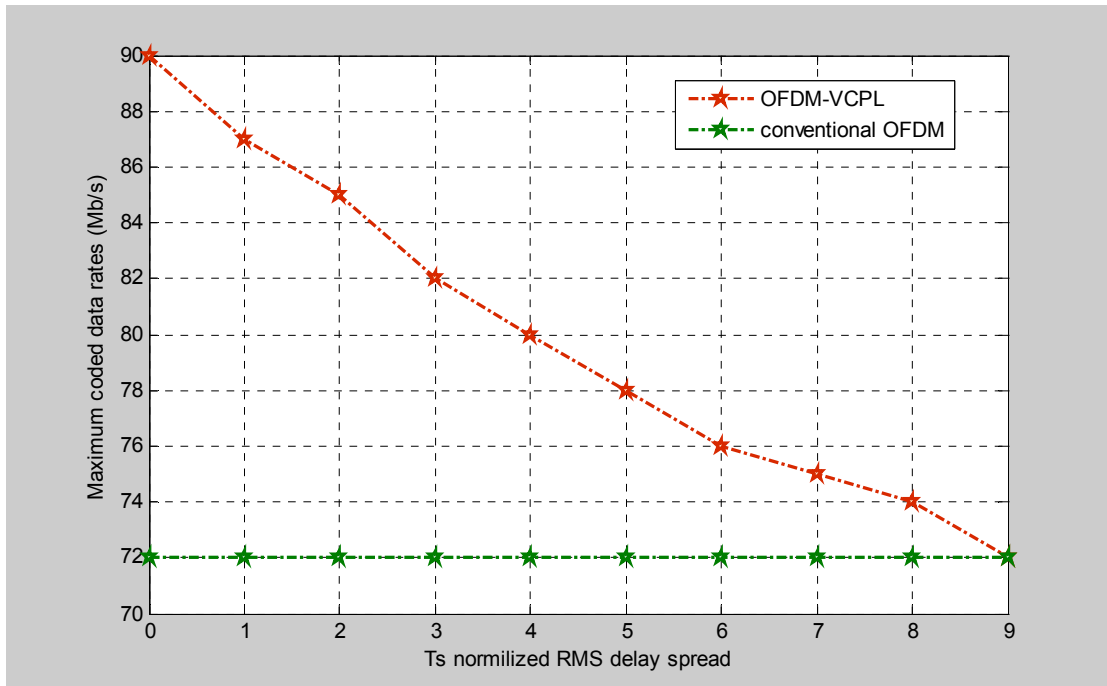
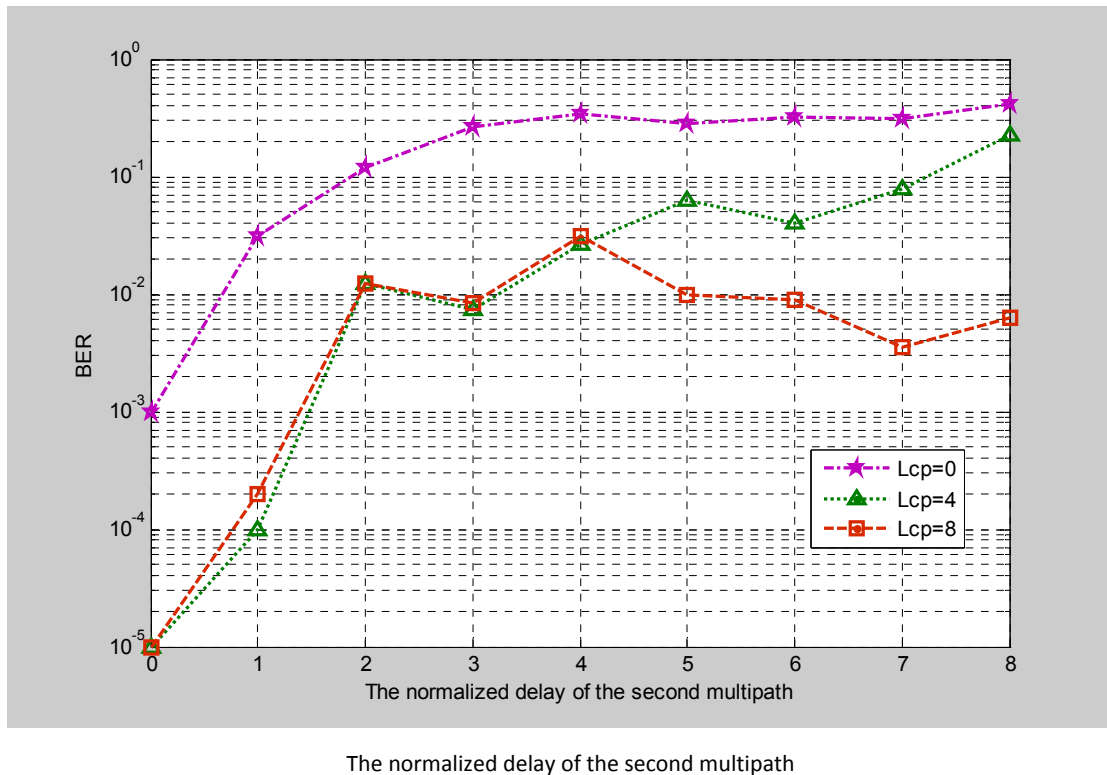


Fig-8- Maximum achievable data rates versus delay spread



The normalized delay of the second multipath
Fig-9- The influence of the cyclic prefix duration on BER performance for 64-QAM-OFDM system, Rayleigh channel



REMOVAL OF PHENOLIC COMPOUNDS FROM AQUEOUS SOLUTIONS BY ADSORPTION ONTO ACTIVATED CARBONS PREPARED FROM DATE STONES BY CHEMICAL ACTIVATION WITH $FeCl_3$

Samar K. Dhidan

Chemical Engineering Department-College of Engineering-University of Baghdad-Iraq

E-mail: samarkarim26@yahoo.com

Abstract

Activated carbon prepared from date stones by chemical activation with ferric chloride (FAC) was used as an adsorbent to remove phenolic compounds such as phenol (Ph) and p-nitrophenol (PNPh) from aqueous solutions. The influence of process variables represented by solution pH value (2-12), adsorbent to adsorbate weight ratio (0.2-1.8), and contact time (30-150 min) on removal percentage and adsorbed amount of Ph and PNPh onto FAC was studied. For PNPh adsorption, (97.43 %) maximum removal percentage and (48.71 mg/g) adsorbed amount was achieved at (5) solution pH, (1) adsorbent to adsorbate weight ratio, and (90 min) contact time. While for Ph adsorption, at (4) solution pH, (1.4) adsorbent to adsorbate weight ratio, and (120 min) contact time gave maximum removal percentage (86.55 %) and (43.27 mg/g) adsorbed amount. Equilibrium adsorption data of PNPh and Ph onto FAC were well represented by Langmuir isotherm model, showing maximum adsorbed amounts of (185.84 mg/g) and (159.27 mg/g) for PNPh and Ph, respectively.

الخلاصة

يهدف البحث إلى إزالة المركبات الفينولية مثل الفينول والبارانايتروفينول من المحاليل المائية باستخدام الكربون المنشط والمحضر من نوى التمر بطريقة التنشيط الكيميائي مع كلوريد الحديد كمادة مازة. تم دراسة تأثير قيمه pH (2-12)، نسبة المادة المازة إلى المادة الممتزة (0.2-1.8)، وزمن امتزاز (30-150 دقيقة) على النسبة المئوية للإزالة والكمية الممتزة لكل من الفينول والبارانايتروفينول. تم الحصول على نسبة إزالة بارانايتروفينول (97.43 %) وسعة امتزاز (48.71 ملغم/غرام) عند الظروف التشغيلية: pH (5)، نسبة مادة مازة إلى ممتزة (1)، وزمن امتزاز (90 دقيقة). في حين لامتزاز مادة الفينول، تم الحصول على نسبة إزالة (86.55 %) وسعة امتزاز (43.27 ملغم/غرام) عند الظروف التشغيلية: pH (4)، نسبة مادة مازة إلى ممتزة (1.4)، وزمن امتزاز (120 دقيقة). تم استخدام معادله لانكماير بشكل ناجح لتمثيل نتائج امتزاز كل من الفينول والبارانايتروفينول على الكربون المحضر، حيث أعطى أعلى سعة امتزاز للفينول (159.27 ملغم/غرام) وأعلى سعة امتزاز للبارانايتروفينول (185.84 ملغم/غرام).

KEYWORDS: Activated carbon, chemical activation, ferric chloride, date stones, phenolic compounds

1. INTRODUCTION

Phenolic compounds are classified to be extremely toxic for human beings and for all aquatic life. One of the most hazardous polluting phenolic compounds to the environment is phenol, which can exert negative effects on different biological processes and their present even at low concentrations can cause unpleasant taste and odor of drinking water and can be an obstacle to the use of waste water (Dabrowski et al., 2005). The other important polluting phenolic is p-nitro phenol, which is known to be persistent, bioaccumulative, and high toxic. It can enter the human body through all routes and its toxic action is much like that of aniline. P-nitro phenol aids the conversion of hemoglobin to methamoglobin, which is caused by the oxidation of iron (II) to iron (III) with the result that the hemoglobin can no longer transport oxygen in the body. Therefore, the complete removal of p-nitro phenol or in some cases reduction of its concentration in wastewaters to an acceptable level has become a major challenge (Al-Asheh et al., 2004). Industrial sources of environmental containments such as oil refineries, coal gasification sites, and petrochemical and pharmaceutical industries generate large amounts of these polluting materials (Canizares et al., 2006).

Several ways have been developed to remove phenolic compounds from wastewaters, including electrochemical oxidation (Juttner et al., 2000), chemical coagulation (Tomaszewska et al., 2004), solvent extraction (Lazarova and Boyadzhieva, 2004), membrane separation (Kujawski et al., 2004), and photo catalytic degradation (Sona et al., 2007). Yet, still the adsorption technique using activated carbon is the most favorable method. The relative advantages of adsorption over other conventional advanced treatments methods are: it can remove both organic as well inorganic constituents even all very low concentration, it is relatively easy and safe

to operate, both batch and continuous equipment can be used, no sludge formation, and the adsorbent can be regenerated and reused again. Moreover the process is economical because it requires low capital cost and there are abundant low cost materials available which can be used as adsorbents (Halouli and Drawish., 1995).

Activated carbon is the most popularly used adsorbent for phenol and its derivatives. Despite its frequent use, activated carbon remains an expensive material. Petroleum residues, natural coal and woods were for along time, the main activated carbon precursor (Guo and Lua, 2003). But, since a few years, other precursors at low cost and easily available were used. Biomass mainly derived from agricultural solid waste is a preferable option for activated carbon precursors. Biomass materials are cheaper, renewable and abundantly available; also these materials constitute an environmental problem. As in most of the tropical countries, agricultural by products are very abundant in the Caribbean. The reuse of these solid wastes can be important for the regional economy, because high value products are obtained from low cost materials, and simultaneously bring solutions to the problem of wastes (Aduata et al., 2007).

Palm trees are abundant in several countries in the world such as Iraq, Saudi Arabia, Iran, Egypt, and other Mediterranean countries. The world annual production of dates was more than 5 million tons in 2004. Date stones as a waste stream have been a problem to the date industry. Therefore, its recycling or reutilization is useful (Haimour and Emeish, 2006). The use of date stones as a raw material produces activated carbon of high yield with good adsorption capacity for phenolic compounds adsorption (Alhamed, 2008).

Basically, activated carbon can be produced by either physical or chemical activation. Physical activation involves carbonization or pyrolysis of the



carbonaceous materials at elevated temperatures (500-900 °C) in an inert atmosphere in order to eliminate the maximum of oxygen and hydrogen dioxide (Bouchelta et al., 2008). By chemical activation it is possible to prepare activated carbon in only one step. Pyrolysis and activation are carried out simultaneously in the presence of dehydrating agents such as $ZnCl_2$, H_3PO_4 , and KCl (Li et al., 2010).

The use of activated carbon prepared by chemical activation with ferric chloride for removal of phenolic compounds is not completely new. (Olivera et al., 2009) used activated carbons prepared from coffee husks by chemical activation with ferric chloride for removal of phenol from aqueous solutions. However, there are no descriptions of the removal of phenolic compounds from aqueous solutions using activated carbon prepared from date stones by chemical activation with ferric chloride.

The aim of the present work is to study the removal of phenol and p-nitro phenol from aqueous solutions by adsorption onto activated carbon prepared from date stones by ferric chloride activation. The effect of contact time, pH of solution, and adsorbent to adsorbate weight ratio on the removal percentage and uptake of these compounds are also studied.

2. EXPERIMENTAL WORK

2.1 Materials

2.1.1 Precursor: Date stones were used as the precursor in the preparation of activated carbon. The stones as received were first washed with water to get rid of impurities, dried at 110 °C for 24 h, crushed using disk mill, and sieved.

Only the fraction of particle sizes comprised between 1 and 3 mm was selected for the preparation.

2.1.2 Activators: Ferric chloride (purchased from Didactic company) of purities 99.9%

were used as chemical reagents for activation of date stones.

2.1.3 Adsorbate: Phenol (Ph) and p-nitro phenol (PNPh) (supplied by BDH chemicals Ltd company) of purities higher than 99 % were used as adsorbate in this study.

2.1.4 Chemicals: All other chemical used such as hydrochloric acid, sodium thiosulfate, iodine and sodium hydroxide were of analytical grades.

2.1.5 Adsorbents: Commercial activated carbon (CAC1) (supplied by Didactic company) of purity 99.9% made in Espan with surface area 1080.11 (m^2/g) and bulk density 0.454 (g/ml), Charcoal activated granular (CAC2) (supplied by Carlo Erba Reagenti company), with surface area 555(m^2/g) and bulk density 0.529 (g/ml).

2.2 Activated carbon preparation

10 g of dried stones was well mixed with 100 ml of $FeCl_3$ solution at an impregnation ratio of 2, (activator to date stones weight ratio), for 24 h at room temperature. The impregnated samples were next dried at 110 °C and stores in a desiccator. For the carbonization of dried impregnated samples a stainless steel reactor (2.5 cm diameter x 10 cm length) was used. The reactor was sealed at one end and the other end had a removable cover with 2 mm hole at the center to allow for the escape of the pyrolysis gases. The reactor was placed in a furnace and heated at constant rate of 10 °C /min and held at an activation temperature of 700 °C for an activation time of 1 h. At the end of activation time the carbonized samples were withdrawn from the furnace and allowed to cool. Then the samples were soaked with 0.1 M HCl solution such that the liquid to solid ratio is 10 ml/g. The mixtures were left overnight at room temperature, and then filtered and subsequently the samples were repeatedly washed with distilled water until the pH of filtrate reach 6.8 (Tan et al., 2007). After that, the samples were dried at 110 °C for 24

h. Finally the samples were stored in tightly closed bottles.

2.3 Characteristics of prepared activated carbon

The prepared activated carbon was characterized by selected physical properties including bulk density and surface area, chemical properties including ash content, pH and conductivity, and adsorption properties including iodine number.

2.3.1 Bulk density

Bulk or apparent density is a measure of the weight of material that can be contained in a given volume under specified conditions. The volume used in this determination includes, in addition to the volume of the skeletal solids, the volume of voids among the particles and the volume of the pores within the particles. A 10 ml cylinder was filled to a specified volume with activated carbon that had been dried in an oven at 80 °C for 24 h (Ahmedna et al., 1997). The bulk density was then calculated as follows:

$$\text{bulk density} = \frac{W_C}{V_C} \quad (1)$$

Where W_C is the weight of dried activated carbon (g) and V_C is cylinder volume packed with dried activated carbon (ml).

2.3.2 Ash content

The ash content of an activated carbon is the residue that remains when the carbonaceous portion is burned off. The ash content of activated carbon was determined by standard methods (ASTM Designation D-2866-94, 2000). 0.5 g of activated carbon of particle size 0.250 mm was dried at 80 °C for 24 h and placed into weighted ceramic crucibles. The samples were heated in an

electrical furnace at 650 °C for 3 h. Then the crucibles were cooled to ambient temperature and weighed. The percent of ash was calculated as follows:

$$\text{ash (\%)} = \frac{W_{S3} - W_{S2}}{W_{S1}} \times 100 \quad (2)$$

Where W_{S3} is the weight of crucible containing ash (g), W_{S2} is the weight of crucible (g), and W_{S1} is the weight of original activated carbon used (g).

2.3.3 Moisture content

The moisture content of prepared activated carbon was determined using oven drying method (Adekola and Adegoke, 2005). 0.5 g of activated carbon of particle size 250 μm was placed into weighed ceramic crucible. The samples were dried at 110 °C to constant weight. Then the samples were cooled to ambient temperature and weighed. The moisture content was calculated by the following equation:

$$\text{moisture (\%)} = \frac{W_{m3} - W_{m2}}{W_{m1}} \times 100 \quad (3)$$

Where W_{m3} is the weight of crucible containing original sample (g), W_{m2} is the weight of crucible containing dried sample (g), and W_{m1} is the weight of original sample used (g).

2.3.4 pH measurement

The pH value of prepared activated carbon was determined by immersing 1 g sample in 100 ml deionized water and stirring at 150 rpm for 1 h and the pH of slurry taken (Egwaikhide et al., 2007).

2.3.5 Conductivity measurement

Electrical conductivity was measured by using the method of (Ahmedna et al. 1997). A 1 wt% solution of sample in deionized water was stirred at 150 rpm at room



temperature for 20 min. Electrical conductivity was measured using an EDT instrument BA 380 conductivity meter with values micro siemens per meter ($\mu\text{s/m}$).

2.3.6 Iodine number

Iodine number is defined as the milligrams of iodine adsorbed by one gram of activated carbon. Basically, iodine number is a measure of the micropore content of activated carbon (0 to 20 Å) by adsorption of iodine from solution. Iodine number of the prepared carbon was determined as follows: 10 ml of 0.1 N iodine solution in a conical flask is titrated with 0.1 N sodium thiosulfate solution in the presence of 2 drops of 1 wt% starch solution as an indicator, till it becomes colourless. The burette reading is corresponding to V_b . Then weigh very accurately 0.05 g of activated carbon and add it to conical flask containing 15 ml of 0.1 N iodine solution, shake the flask for 4 min and filter it, then titrate 10 ml of filtrate with standard sodium thiosulfate solution using 2 drops of starch solution as indicator, now the burette reading is corresponding to V_s . The iodine number was then calculated by using the following equation (Lubrizol, 2007):

$$IN = \frac{(V_b - V_s) \cdot N \cdot (126.9) \cdot (15/10)}{M} \quad (4)$$

Where IN is iodine number (mg/g), V_b and V_s are volumes of sodium thiosulfate solution required for blank and sample titrations (ml), respectively, N is the normality of sodium thiosulfate solution (mole/l), 126.9 is atomic weight of iodine, and M is the mass of activated carbon used (g).

2.3.7. Surface area

The surface areas of the prepared activated carbon was estimated through a calibration curve which has a correlation coefficient of 0.997 between the iodine numbers and BET surface area of some established activated carbons from the literature (Fadhil et al., 2008) as shown in Fig. 1.

2.4. Adsorption experiments

The ability of the prepared activated carbons by ferric chloride activation (FAC) to remove Ph and PNPh from aqueous solutions was determined under batch mode conditions. 50 ml samples of Ph or PNPh solutions with initial concentrations of 50 mg/l were mixed with FAC of 250 μm particle size at 0.5-2.5 adsorbent to adsorbate weight ratio. The mixtures were added to 100 ml Erlenmeyer flasks, and the flasks were shaken in a shaker (type B. Baun Karlkolb) at 120 rpm at room temperature for 30-150 min., aqueous solutions of different pH 2-12 were used. The value of pH was varied by using 0.1 M NaOH solution or 0.1 M HCl solution. Then the samples were filtered and the residual concentrations of Ph or PNPh in the filtrate were analyzed by a UV-Visible Spectrophotometer (Shimadzu UV-160A) at maximum wave lengths of 269 and 400 nm for Ph and PNPh, respectively. The adsorbed amount at equilibrium, q_e (mg/g), and removal percentage of Ph and PNPh onto FAC were calculated according to the following expressions:

$$q_e = \frac{(C_o - C_e) V}{W} \quad (5)$$

$$RP (\%) = \frac{C_o - C_e}{C_o} \times 100 \quad (6)$$

Where RP removal percentage (%), C_o and C_e are the initial and equilibrium concentrations of Ph or PNPh solution (mg/l), respectively, V is the volume of

solution (l), and W is the weight of activated carbon used (g).

2.5. Adsorption isotherm of Ph and PNPh on FAC at optimum conditions

The maximum adsorption capacity of the prepared activated carbon for Ph and PNPh were determined by performing adsorption tests in a set of 100 ml Erlenmeyer flasks where 50 ml of Ph or PNPh solutions with initial concentrations of 50-250 mg/l were placed in these flasks. Then the flasks were shaken in a shaker (type B. Baun Karlkolb) at 120 rpm at room temperature. Other operating parameters such as activated carbon dosage, solution pH, and contact time were constant at their optimum values for each of Ph and PNPh adsorption onto FAC. The concentrations of Ph or PNPh solutions were similarly measured and the amount of adsorption at equilibrium, q_e (mg/g) was calculated using Eq. (5). To determine the maximum Ph or PNPh adsorption capacity of prepared activated carbon, the experimental adsorption data obtained were fitted to the Langmuir isotherm model, which can be written as follows:

$$q_e = \frac{q_m BC_e}{1 + BC_e} \quad (7)$$

Where q_e is the amount of Ph or PNPh adsorbed per unit mass of activated carbon (mg/g), q_m is the maximum amount of Ph or PNPh adsorbed per unit mass of activated carbon (mg/g), C_e is the equilibrium concentration of the Ph or PNPh (mg/l), and B is the Langmuir constant (l/mg). The Langmuir isotherm model which based on the assumption of a homogeneous adsorbent surface with identical adsorption sites has been successfully used by many researchers to correlate the experimental adsorption data of phenolic compounds on activated carbons

(Liu et al., 2010; Mohd Din et al., 2009).

3. RESULTS AND DISCUSSION

3.1 Characterization of activated carbon prepared

The property of FAC prepared was determined and compared with those determines of two types of commercial activated carbons are summarized in Table 1. The results of this table show that the surface area of FAC is 780.06 m²/g. This result is in agreement with that obtained by Rufford et al. (2010). Who showed that the surface area of activated carbon prepared by chemical activation of coffee grounds with ferric chloride was 846 m²/g. The iodine number FAC in this study are higher than that obtained by Haimour and Emeish (2006), who reported an iodine number of 495 mg/g for activated carbon prepared by chemical activation of date stones using phosphoric acid.

3.2. Effect of solution pH

The effect of pH on the adsorbed amount and removal percentage of phenolic compounds onto FAC is shown in Figs. 2 and 3, respectively.

It is clear from Fig.2 that the adsorbed amount increases with pH up to 4 for Ph and 5 for PNPh, thereafter it decreases. For PNPh adsorption, an increase in pH from 2 to 5 leads to an increase in adsorbed amount from 42.5 to 48.71 mg/g. While for Ph adsorption an increase in pH from 2 to 4 causes an increase in adsorbed amount from 28.4 to 35.04. The decrease in adsorbed amount of Ph or PNPh at high pH values may be due to the increase in magnitude of negative charges on Ph, PNPh, and FAC, which generate repulsion between adsorbate and adsorbent so that the amounts of Ph and PNPh adsorbed begin to decrease as mentioned by Goud et al. (2005) and Tang et al. (2007).



Fig.3 shows that 70.08 % maximum removal percentage of Ph is achieved at pH value of 4. While for PNPh, a maximum removal percentage of 97.43 % is obtained at pH of 5. Therefore, the values of 4 and 5 are considered to be the optimum pH for removal of Ph and PNPh, respectively. Similar results were reported by Mohanty et al. (2006) and Ofomaja (2011). They found that the optimum pH values were 3.5 and 4 for removal of Ph and PNPh from aqueous solutions, respectively.

3.3. Effect of adsorbent to adsorbate ratio

Figs. 4 and 5 show the effect of adsorbent to adsorbate weight ratio on adsorbed amount and removal percentage of Ph and PNPh, respectively.

Fig. 4 shows that the adsorbed amount of Ph and PNPh on FAC decreases as the adsorbent to adsorbate weight ratio increases. An increase in weight ratio from 0.2 to 1.8 leads to a decrease in adsorbed amount from 134.45 to 23.05 mg/g and from 217.9 to 27.1 mg/g for Ph and PNPh adsorption onto FAC, respectively. This decrease in adsorbed amount with increase in weight ratio of adsorbent to adsorbate may be due to the split in the flux or the concentration gradient between adsorbate concentration in the solution and the adsorbate concentration in the surface of the adsorbent as mentioned by Kumar et al. (2011).

Fig. 5 shows that the removal percentage of Ph and PNPh increases with increasing adsorbent to adsorbate weight ratio up to a certain value and then there is no further increase in removal percentage for both Ph and PNPh. For Ph adsorption onto FAC, an increase in weight ratio from 0.2 to 1.4 leads to an increase in removal percentage from 53.78 to 81.83 %. While for PNPh an increase in weight ratio from 0.2 to 1 causes an increase in removal percentage from 87.17 to 97.43. Therefore, the values of 1.4 and 1 can be considered as the best weight ratios which give maximum removal percentage of Ph and PNPh, respectively.

The increase in removal percentage with increasing adsorbent to adsorbate weight ratio is explained by the greater adsorbent surface area and pore volume available at higher adsorbent dosage providing more functional groups and active adsorption sites that result in a higher removable percentage as mentioned by Li et al. (2010).

3.4. Effect of contact time

The effect of contact time on adsorbed amount and removal percentage of Ph and PNPh is shown in Figs. 6 and 7, respectively.

The adsorbed amount of Ph and PNPh onto FAC increases with the increase of contact time, as shown in Fig. 6, and the adsorption reached equilibrium in about 90 and 120 min for PNPh and Ph, respectively. For PNPh adsorption, a rapid increase in adsorbed amount from 35.27 to 48.71 mg/g is achieved during the first 90 min. The fast adsorption at the initial stage may be due to the higher driving force making fast transfer of PNPh ions to the surface of FAC particles and the availability of the uncovered surface area and the remaining active sites on the adsorbent as mentioned by Aroua et al. (2008). While for Ph adsorption an increase in adsorbed amount from 33.42 to 43.27 mg/g is obtained with increasing contact time from 30 to 120 min.

Fig. 7 shows that the equilibrium is attained at a contact time of 90 and 120 min, giving a maximum removal percentage of 97.43 and 86.55 % for PNPh and Ph, respectively.

3.5. Adsorption isotherms of Ph and PNPh on prepared activated carbon

As concluded from sections 3.2, 3.3 and 3.4, the operating conditions which give maximum Ph removal percentage were chosen as 5 solution pH, 1.4 adsorbent to

adsorbate weight ratio, and 120 min contact time. While for PNPh, the operating conditions were selected as 4 solution pH, 1 adsorbent to adsorbate weight ratio, and 90 min contact time.

The experimental equilibrium data for Ph and PNPh adsorption at optimum conditions on FAC are compared with those for adsorption on two types of commercial activated carbons (CAC1) and (CAC2). These data, calculated by Eq. (5), are fitted with Langmuir isotherm model, Eq. (7), and presented in Fig. 8. The calculated constants of Langmuir isotherm equation for Ph and PNPh on the three samples along with the correlations coefficients values R^2 are presented in Table 2. This table shows that the maximum Ph uptake of FAC, CAC1, and CAC2 are 159.27, 167.97, 152.68 mg/g, respectively. While for PNPh adsorption, the maximum uptake of FAC, CAC1, and CAC2 are 185.84, 193.77, and 165.45, respectively. It is clear that the adsorption capacities of the probe molecules on each activated carbon is different suggesting that the adsorption processes are associated with different chemical affinities towards the adsorbent surface area (Oliveira et al, 2009).

This result for Ph adsorption onto FAC is higher than that reported by Oliveira et al (2009), 60 mg/g, for activated carbon prepared from coffee husks by chemical activation with ferric chloride. Also, these results are higher than that obtained by Aber et al. (2009) for adsorption of Ph and PNPh onto activated carbon prepared from kenaf natural fibers using K_2HPO_4 as chemical activator, they showed that the maximum adsorbed amount of Ph and PNPh were 140.84 and 136.99 mg/g, respectively.

4. CONCLUSIONS

1. A maximum PNPh removal percentage of 97.43 % and 48.71 mg/g adsorbed amount were obtained at 5 solution pH, 1 FAC to PNPh weight ratio, and 90 min contact time.

2. Solution pH of 4, FAC to Ph weight ratio of 1.4, and 120 min contact time gave maximum Ph removal percentage of 86.55 % and 43.27 mg/g adsorbed amount.

3. Equilibrium adsorption data of PNPh and Ph onto FAC were well represented by Langmuir isotherm model, showing maximum adsorbed amounts of 185.84 and 159.27 mg/g for PNPh and Ph, respectively.

ACKNOWLEDGEMENT

We gratefully acknowledge university of Baghdad for assist and support of this work.

REFERENCES

- Aber S., Khataee A. and Sheydaei M., (2009) Optimization of activated carbon fiber preparation from kenaf using K_2HPO_4 as chemical activator for adsorption of phenolic compounds, *Bioresour. Technol.*, 100, 6586-6591.
- Adiuata D., Wan Daud W.M.A., and Aroua M.K., (2007) preparation and characterization of activated carbon from palm shell by chemical activation with K_2CO_3 , *Bioresour. Technol.*, 98, 145-149.
- Adekola F.A. and Adegoke H.I., (2005), Adsorption of blue-dye on activated carbons produced from Rice Husk, Coconut Shell and Coconut Coir pitch, *Ife Journal of Science*, 7(1), 151-157.
- Ahmedna M., Marshall W.E., Rao R.M., and Clarke S.J., (1997), Use of filtration and buffers in raw sugar colour measurement, *J. Sci. Food Agric.*, 75(1), 109-116
- Al-Asheh S., Banat F., and Masad A., (2004) Kinetics and equilibrium sorption studies of 4-nitro phenol on pyrolysed and activated oil shale residue, *Environmental Geology*, 45, 1109-1117.
- Alhamed Y.A., (2008) Phenol removal using granular activated carbon from date stones, *Bulg. Chem. Comm.*, 41, 26-35.



Aroua M.K., Leong S.P.P., Teo L.Y., and Daud W.M.A.W., (2008) Real time determination of kinetics of adsorption of lead (II) onto shell based activated carbon using ion selection electrode, *Bioresou. Technol.*, 99, 5786-5792.

ASTM standard, (2000), Standard test method for total ash content of activated carbon, Designation D2866-94.

Bouchelta C., Medjran M.S., Bertrand O., and Bellat J., (2008) Preparation and characterization of activated carbon from date stones by physical activation with steam, *J. Anal. Appl. Pyrolysis*, 28, 70-77.

Canizares P., Carmona M., Baraga O., and Rodrigo M.A., (2006) Adsorption equilibrium of phenol onto chemical modified activated carbon F400, *J. Hazardous Materials*, 131, 243-248.

Dabrowski A., Podkosielnny P., Hubicik Z., and Barczak M., (2005) Adsorption of phenolic compounds by activated carbon- a critical review, *Chemosphere*, 58, 1049-1070.

Egwaikhide P.A., Akporhonor E.E, and Okieimen, (2007), Utilization of Coconut fibre Carbon in the removal of Soluble Petroluem fraction polutted water, *International Journal of physical sciences*, 2(2), 047-049.

Fadhil A.B. and Deyab M.M., (2008), Conversion of some fruit stones and shells into activated carbons, *The Arabain Journal for Science and Engineering*, 33(2A), 175-184.

Goud V.V., Mohanty K., Rao M.S., and Jayakumar N.S., (2005) Phenol removal from aqueous solutions using tamarind nut shell activated carbon: batch and column study, *Chem. Eng. Technol.*, 28, 814-821.

Guo J. and Lua A.C., (2003) Textural and chemical properties of adsorbent prepared

from palm shell by phosphoric acid activation, *Materials Chemistry and Physics*, 80, 114-119.

Haimour N.M. and Emeish S., (2006) Utilization of date stones for production of activated carbon using phosphoric acid, *Waste Management*, 26, 651-660.

Halouli K.A. and Drawish N.M., (1995) Effect of pH and inorganic salts on the adsorption of phenol from aqueous systems on activated decolorizing charcoal, *Sep. Sci. Technol.*, 30, 3313-3324 .

Juttner K., Galla U., and Schmieder H., (2000) Electrochemical approaches to environmental problems in the process industry, *Electrochim. Acta*, 45, 2575-2954.

Kujawski W., Warszawski A., Ratajczak W., and Capala W., (2004) Removal of phenol from waste water by different separation techniques, *Desalination*, 163, 287-296.

Kumar P.S., Ramalingam S., and Sathishkumar K., (2011) Removal of methylene blue dye from aqueous solution by activated carbon prepared from cashew nut shell as a new low cost adsorbent, *Korean J. Chem. Eng.*, 28(1), 149-155.

Lazarova Z. and Boyadzhieva S., (2004) Treatment of phenol-containing aqueous solutions by membrane-based solvent extraction in coupled ultra filtration modules, *Chem. Eng. J.*, 100, 129-138.

Li Y., Du Q., Wang X., and Xia Y., (2010) Removal of lead from aqueous solution by activated carbon prepared from *Enteromorpha prolifera* by zinc chloride activation, *J. Hazardous Materials*, 183, 583-589.

Liu Q.S., Zheng T., Wang P., Jiang J.P., and Li N., (2010) Adsorption isotherm, kinetics and mechanism of some substituted phenols on activated carbon fibers, *Chem. Eng. J.*, 157, 348-356.

Li Y., Du Q., Wang X., and Xia Y., (2010) Removal of lead from aqueous solution by activated carbon prepared from *Enteromorpha prolifera* by zinc chloride activation, *J. Hazardous Materials*, 183, 583-589.

Lubrizol standard test method, (2006), iodine value, test procedure AATM 1112-01, October 16.

Mohanty K., Das D., and Biswas M.N., (2006) Preparation and characterization of activated carbons from *sterculia alata* nutshell by chemical activation with zinc chloride to remove phenol from waste water, *Adsorption*, 12, 119-132.

Mohd Din A.T., Hameed B.H., and Ahmad A.L., (2009) Batch adsorption of phenol onto physicochemical activated coconut shell, *J. Hazardous Materials*, 161, 1522-1529.

Ofomaja A.E., (2011) Kinetics and pseudo isotherm studies of 4-nitrophenol adsorption onto *mansonia* wood sawdust, *Industrial Crops & Products*, 33, 418-428.

Oliveira L.C.A., Pereira E., Guimaraes I.R., and Sapag K., (2009) Preparation of activated carbons from coffee husks utilizing

FeCl_3 and ZnCl_2 as activating agents, *J. of Hazardous Materials*, 165, 87-94.

Rufford T.E., Hulicova-Jurcakova D., Zhu Z., and Lu G.Q., (2010), A comparative study of chemical treatment by FeCl_3 , MgCl_2 , and ZnCl_2 on microstructure, surface chemistry, and double-layer capacitance of carbons from waste biomass, *J. of Material Research*, 25 (8), 1451-1459.

Sona N., Yamamoto T., Yamamoto D., and Nakaiwa M., (2007) Degradation of aqueous phenol by simultaneous use of ozone with silica-gel and zeolites, *Chem. Eng. Process*, 46, 513-519.

Tan I. A. W., Hameed B. H. and Ahmad A. L., (2007) Equilibrium and Kinetic studies on basic dye adsorption by oil palm fiber activated carbon, *J. Chem. Eng.*, 127, 111-119.

Tang D., Zheng Z., Lin K., and Zhang J., (2007) Adsorption of p-nitro phenol from aqueous solutions onto activated carbon fiber, *J. Hazardous Materials*, 143, 49-56.

Tomaszewska M., Mozia S., and Morawski W., (2004) Removal of organic matter by coagulation enhanced with adsorption on PAC, *Desalination*, 162, 79-87.

NOMENCLATURE

Notation

B	: Langmuir adsorption constant (l/mg)
C_o	: Initial concentration of Ph or PNPh (mg/l)
C_e	: Equilibrium concentration of Ph or PNPh (mg/l)
q_m	: Maximum amount of Ph or PNPh adsorbed per unit mass of activated carbon (mg/g)
R	: adsorbate to adsorbent weight ratio (g/g)
R^2	: Correlation coefficient

t	: contact time (min)
V	: Volume of aqueous Ph or PNPh solution (l)
W	: Weight of activated carbon used (g)

Abbreviations

CAC	: Commercial activated carbon
FAC	: Activated carbon by ferric chloride activation
Ph	: Phenol
PNPh	: P-nitro phenol

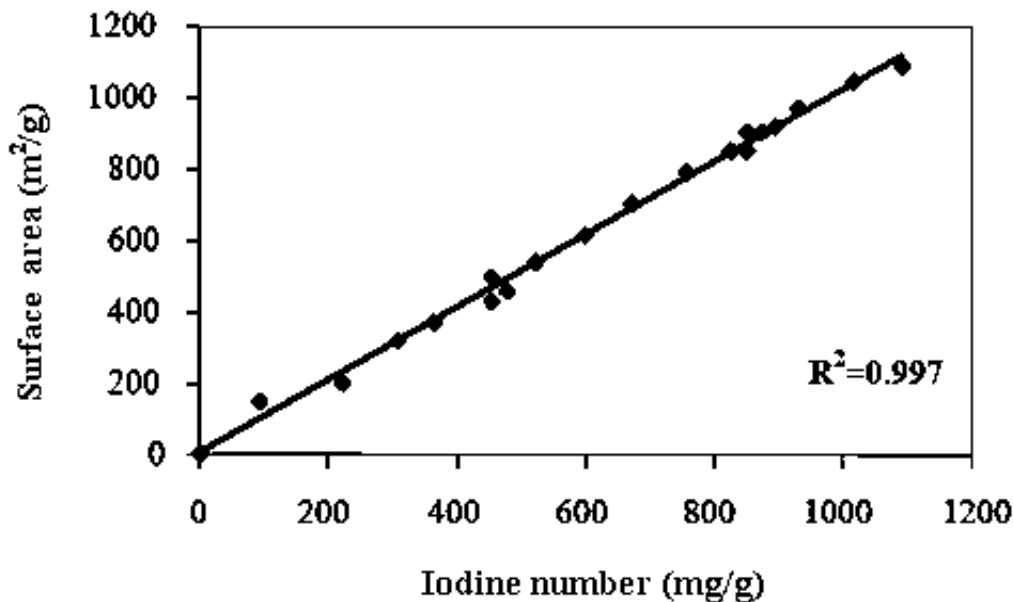


Fig. 1, Estimated surface area calibration curve

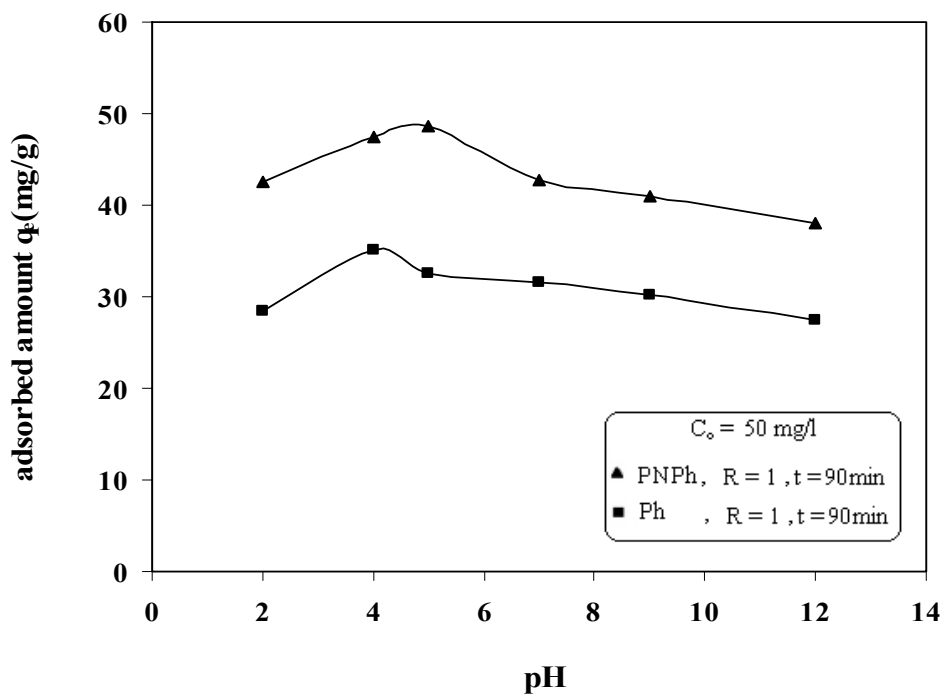


Fig. 2, Effect of solution pH on adsorbed amount

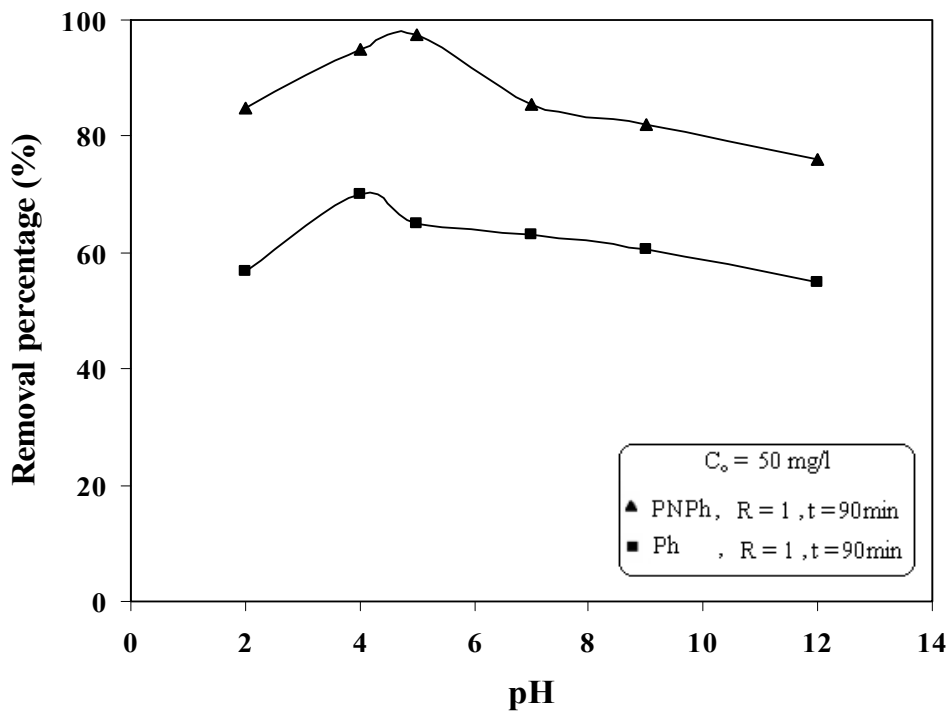


Fig. 3, Effect of solution pH on removal percentage

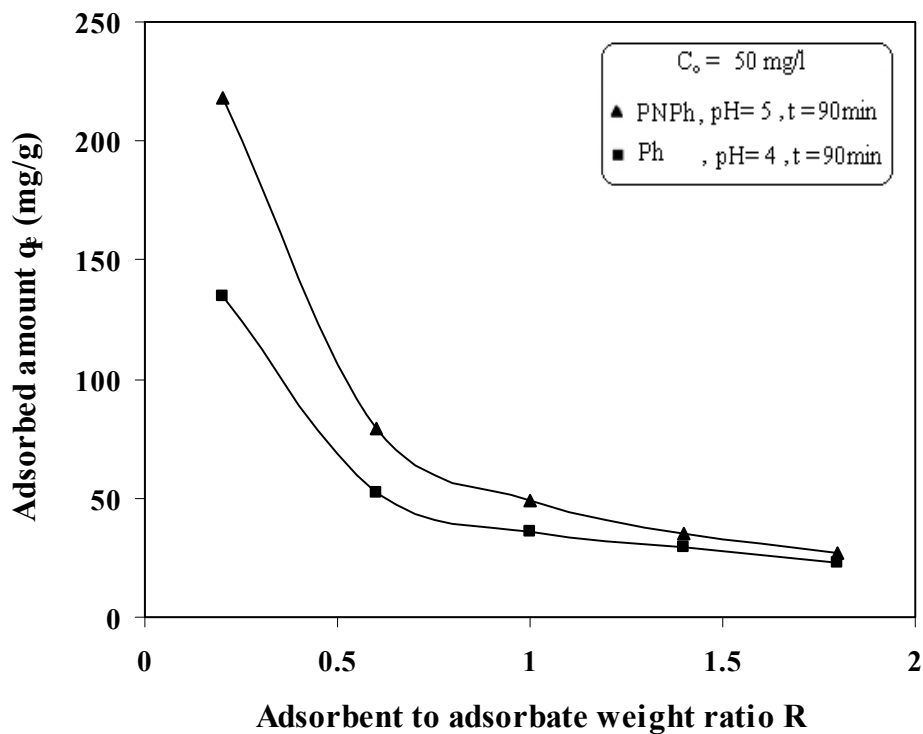


Fig. 4, Effect of adsorbent to adsorbate ratio on adsorbed amount

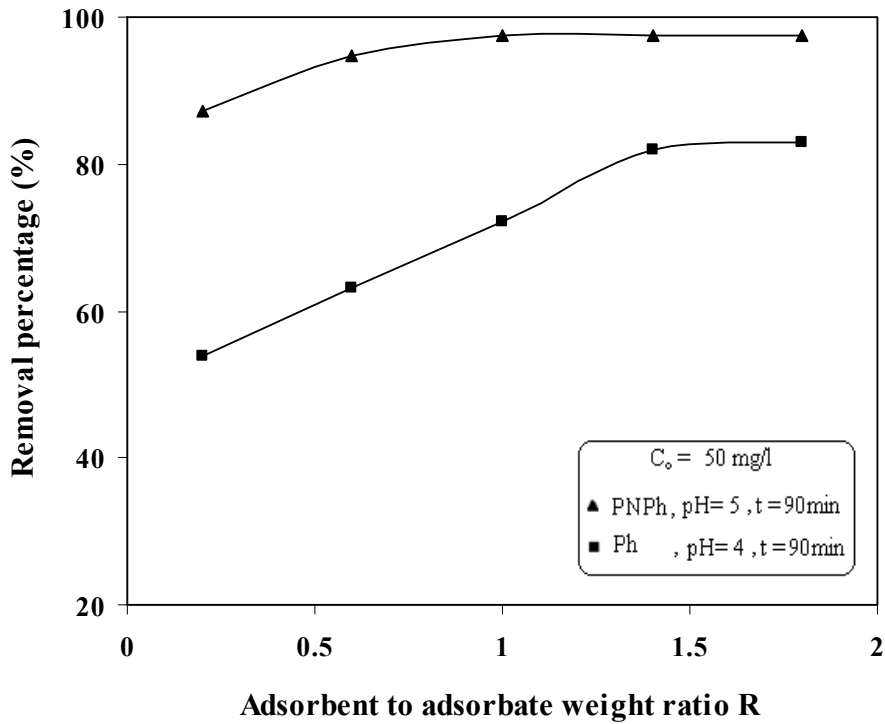


Fig. 5, Effect of adsorbent to adsorbate ratio on removal percentage

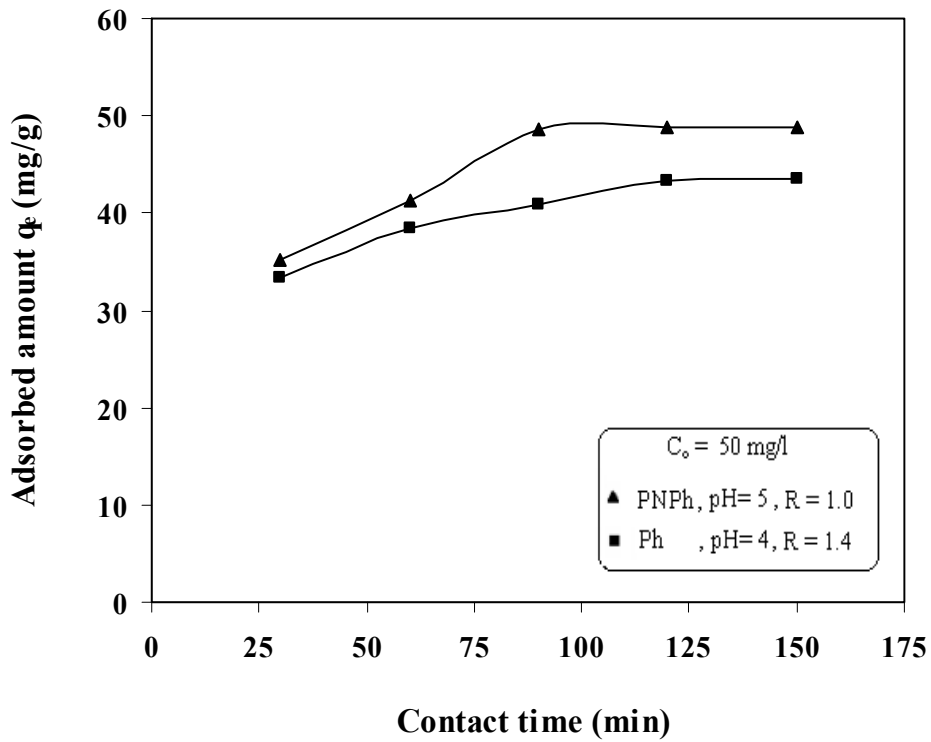


Fig. 6, Effect of contact time on adsorbed amount

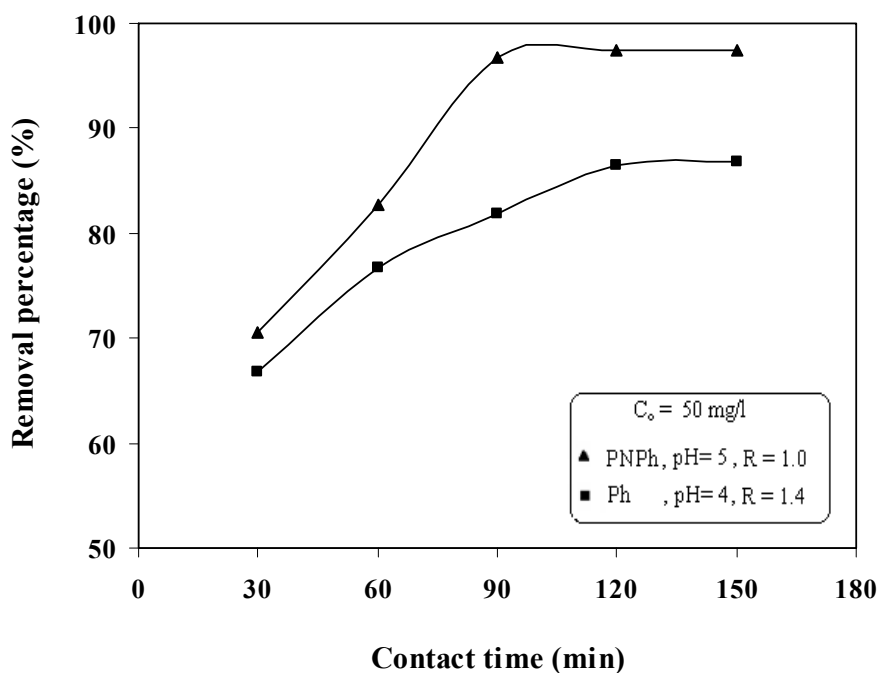


Fig. 7, Effect of contact time on removal percentage

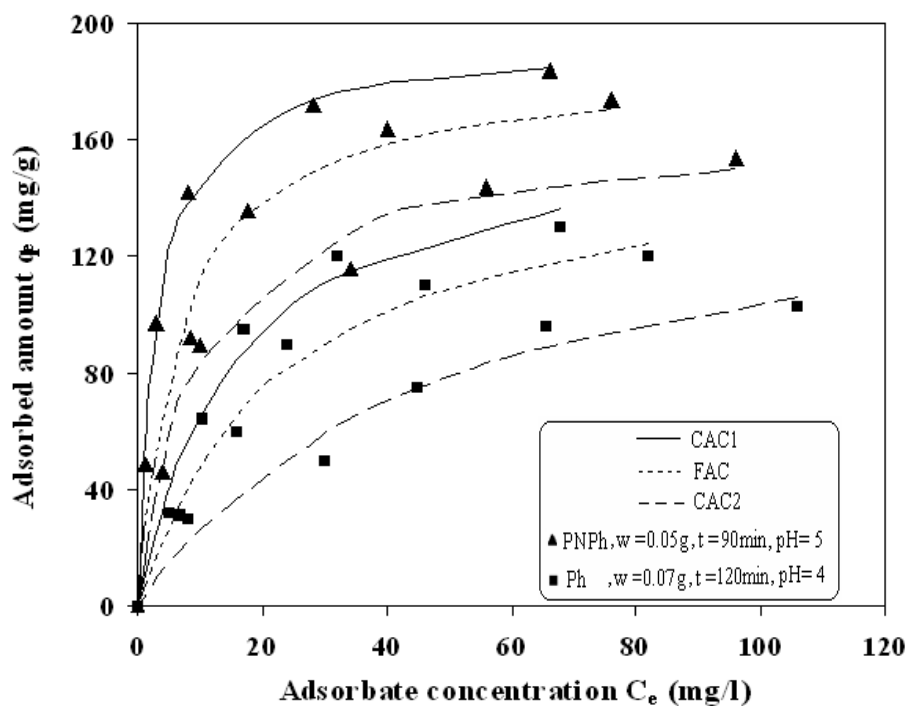


Fig. 8, Equilibrium isotherm of Ph and PNPPh adsorption on activated carbons samples correlated with Langmuir equation

**Table 1, Characteristics of activated carbons samples .**

Characteristic	FAC	CAC1	CAC2
bulk density (g/ml)	0.271	0.454	0.529
surface area (m ² /g)	780.06	1080.11	555
ash content (%)	8.62	4.24	8.80
moisture content (%)	15.54	11.57	3.51
pH	6.5	7.3	7
conductivity (μs/m)	290	370	330
iodine number (mg/g)	761.40	1047.54	552

Table 2, Equilibrium isotherm results

Ph and PNPh isotherm results correlated with Langmuir equation				
adsorbate	adsorbent	q _m (mg/g)	B (l/mg)	R ²
Ph	FAC	159.27	0.0436	0.985
	CAC1	167.97	0.0637	0.980
	CAC2	152.68	0.0212	0.974
PNPh	FAC	185.84	0.1472	0.979
	CAC1	193.77	0.3109	0.997
	CAC2	165.45	0.1011	0.987



3-D OBJECT RECOGNITION USING MULTI-WAVELET AND NEURAL NETWORK

Dr. Tariq Zeyad Ismail

Zainab Ibrahim Abood

ABSTRACT

This search has introduced the techniques of multi-wavelet transform and neural network for recognition 3-D object from 2-D image using patches. The proposed techniques were tested on database of different patches features and the high energy subband of discrete multi-wavelet transform DMWT (gp) of the patches. The test set has two groups, group (1) which contains images, their (gp) patches and patches features of the same images as a part of that in the data set beside other images, (gp) patches and features, and group (2) which contains the (gp) patches and patches features the same as a part of that in the database but after modification such as rotation, scaling and translation. Recognition by back propagation (BP) neural network as compared with matching by minimum distance, gave (94%) and (83%) score by using group (1), (gp) and features respectively, which is much better than the minimum distance. Recognition using (gp) neural network (NN) gave a (94%) and (72%) score by using group (2), (gp) and features respectively, while the minimum distance gave (11%) and (33%) scores. Time consumption through the recognition process using (NN) with (gp) is less than that minimum distance.

الخلاصة

هذا البحث يقدم تقنيات تحويل الموجة المتعددة والشبكة العصبية الاصطناعية لتمييز الأجسام الثلاثية الأبعاد من صور ثنائية الأبعاد باستعمال الشرائح. التقنيات المقترحة تختبر عن طريق بيانات تحوي خصائص الشرائح المختلفة و الجزء ذات الطاقة العالية بعد استخدام اسلوب يعتمد على تحويل الموجة المتعددة للشرائح. مجموعة الاختبار تحتوي على مجموعتين المجموعة الأولى تحتوي على صور وشرائح وخصائص الشرائح و الجزء ذات الطاقة العالية بعد استخدام اسلوب يعتمد على تحويل الموجة المتعددة للشرائح تشابه بعض تلك الموجودة في قاعدة البيانات. أما المجموعة الثانية فتحتوي على صور، شرائح، خصائص الشرائح و الجزء ذات الطاقة العالية بعد استخدام اسلوب يعتمد على تحويل الموجة المتعددة للشرائح تشابه بعض تلك الموجودة في قاعدة البيانات لكن بعد إجراء تحويلات عليها مثل التدوير، التصغير، التكبير والتزجيف. التمييز باستخدام الشبكات العصبية الاصطناعية للمجموعة الأولى أعطت نسبة (94%) و (83%) باستخدام الخصائص و الجزء ذات الطاقة العالية للشرائح على الترتيب والتي هي أفضل مقارنة بالتمييز بطريقة قياس المسافة الأقل للتشابه. أما بالنسبة للتمييز باستخدام الشبكات العصبية الاصطناعية للمجموعة الثانية فقد أعطت نسبة (94%) و (72%) باستخدام الخصائص و الجزء ذات الطاقة العالية للشرائح على الترتيب والتي هي أفضل مقارنة بالتمييز بطريقة قياس المسافة الأقل للتشابه والتي أعطت نسبة (11%) و (33%) على الترتيب. كذلك الوقت المستغرق خلال عملية التمييز باستخدام الشبكات العصبية الاصطناعية أقل مما في طريقة قياس المسافة الأقل للتشابه.

KEYWORD: Object recognition, feature extraction, patches, multi-wavelet, neural network.

INTRODUCTION

Object recognition is at the top of a visual task hierarchy. In its general form, this is a very difficult computational problem, which will probably play an important role in the eventual building of intelligent machines. A large number of psychological and neurophysiologic studies support the idea that humans represent three-dimensional objects internally as a small set of bi-dimensional images [R. Cesar, 2005]. View-based method has been proposed by some researchers in which the object is described using a set of 2-D characteristic views or aspects. Main disadvantage of this method is the inherent loss of information in the projection from 3D object to 2D image. A single 2D view-based approach may not be appropriate for 3-D object recognition since only one side of an object can be seen from any given viewpoint. [M. Y. Mashor, 2004]. A better alternative is to obtain the features from several 2-D views from a few static cameras as suggested in this proposed approach. An effective representation of 3-D object properties using 2-D images is considered. With multiple views technique enables this technique to be used in 3-D object modeling.

It is a classic difficult problem for a computer to recognize images that is because a computer lacks ability of adaptive learning. The inductive processes embody the universal and efficient means for extracting and encoding the relevant information from the environment, the evolution of intelligence could be seen as a result of interactions of such a learning mechanism with the environment. In consensus with this, any one strongly believe that the pivot of image recognition should be arranged around learning processes at all levels of feature extraction and object recognition [Y. Min, 2005].

THE PROPOSED ALGORITHM

The proposed algorithm illustrated in the following steps:

1. Input all images of all views and I is the number of image.
249 image for generating a training set.
68 image for generating a test set.
2. Preprocess these images by filtering them using median filter.
3. Edge detection using canny edge detector and select patches to get features from them.
4. Two methods of feature extraction from the patches are used:
 - a. (21) features about patches shape and location.
 - b. High energy subband results from decompose each patch of each image by using
5. Store the features of the training set in the data base and the others stored as a test set in order to be ready to inter to the image recognition stage.
6. Recognition stage contains two methods of recognition, minimum distance and neural network.

Figure (1) shows the block diagram of generation training and testing sets.

Figure (2) shows the flow chart of overall proposed system.

The block diagram of the Image recognition stage is shown in figure (3).

DATA BASE

The model that is stored in the memory as a data base (reference images) consists of (249) image, each of size (449×267) , the (gp) patches and features of each patch in each image in each model. These images are divided into (4) sets. The sets contain car model 1, car model 2, airplane model 1 and airplane model 2. They are named as: c1, c2, a1 and a2 respectively. There are (3) views, izo, side and top view (with rotation) for each model which are named as: i, s and t respectively. The images are named according to the set which they are belong to, their view and their number in this view, i.e. c1s018 means that it is belong to (c1) set, side view and number of image in this view



is 18. Figure (4) shows samples of data base images.

In the test set there are two groups which are group (1) and group (2) each of (34) image. Group (1) means that the test set contains images, their (gp) patches and patches features of the same images as a part of that in the data set beside other images, (gp) patches and features, While group (2) means that the test sets contains the (gp) patches and patches features the same as a part of that in the database but after modification such as rotation, scaling and translation. Figure (5) shows samples of test set images.

FEATURE EXTRACTION

Two methods of feature extraction are used. The first method is the extraction of (21) features from the patches which are represented something about their locations and shapes, it is used in order to compare it with the second method of feature extraction which use the high energy subband results from decompose each patch of each image by using DMWT.

Each patch is a part of object so all rules (in this work) for the object in image is the same as for the patch, i.e. these features are extracted from the patches.

The location of the patch can be determined by calculating the coordinates of the centroid and area of each patch as in the following steps:

***Area of object:** The object area given by:

$$A = \sum_i \sum_j f[i, j] \tag{1}$$

where $f[i, j]$ represents the object pixels, The area is thus computed as the total number of object pixels in the object [S. E. Umbaugh, 1995].

***Location of object:** The location of the object is usually given by the center of mass which is given by:

$$\bar{i} = \frac{\sum_i \sum_j [if(i, j)]}{A}, \bar{j} = \frac{\sum_i \sum_j [jf(i, j)]}{A} \tag{2}$$

Where \bar{i} and \bar{j} are the coordinates of the centroid of the object and A is the area of the object [T. Acharya, 2005].

Other features are:

*** Orientation of an Object:** When the objects have elongated shape, the axis of elongation is the orientation of the object. The axis of elongation is a straight line so that the sum of the squared distances of all the object points from this straight line is minimum. The distance here implies the perpendicular distance from the object point to the line [Y. Amit, 2002]. The axis corresponds to the about which it takes the least amount the energy to spin an object of like shape or the axis of least inertia. If the origin was moved to the center of area (i, j) and θ is the angle between the x-axis and the axis of least second moment counterclockwise, then the axis of least second moment ($\tan(2\theta)$) will be defined as follows [S. E. Umbaugh, 1995]:

$$\tan(2\theta) = 2 \frac{\sum_{i=0}^{N-1} \sum_{j=0}^{N-1} ijf(i, j)}{\sum_{i=0}^{N-1} \sum_{j=0}^{N-1} i^2 f(i, j) - \sum_{i=0}^{N-1} \sum_{j=0}^{N-1} j^2 f(i, j)} \tag{3}$$

• Euler number of an image: It is defined as the number of object minus the number of holes. For a single object, it tells that how many closed curves the object contains [S. E. Umbaugh, 1995].

• Projection of an object onto a line: The projections of an image provide good information about the image. The projections may be computed along horizontal, vertical, or diagonallines. The horizontal projection is obtained by counting the number of object pixels in each column of the image, while the total number of

object pixels in each row yields the vertical projection as follows [T. Acharya, 2005]:

$$P_{hor}(i) = \sum_j f(i, j) \quad (4)$$

$$P_{ver}(j) = \sum_i f(i, j) \quad (5)$$

INVARIANT MOMENTS

M.K.Hu represented the concept of the invariant moments in 1961 firstly. The invariant moments are the highly compressed image features, which meet the invariability of the translation, the ratio and the rotation to the continuous function [Z. Song, 2007].

Basic Theory

i. For the digital image, the discrete invariant moments are used, the geometric moments m_{pq} of the $(p+q)^{th}$ order (p and q are the arbitrary non-negative integer respectively) are:

$$m_{pq} = \sum_i \sum_j i^p j^q f(i, j) \quad (6)$$

where $p, q = 0, 1, 2, \dots$ and $f(i, j)$ is the function of the image value, i and j are the image coordinates respectively.

ii. Because of the translation invariability of m_{pq} , the central moments of the $(p+q)^{th}$ order are [R. C. Gonzalez, 2002, Z. Song, 2007]:

$$\mu_{pq} = \sum_i \sum_j (\bar{i} - \bar{i})^p (\bar{j} - \bar{j})^q f(i, j) \quad \text{where} \\ \bar{i} = \frac{m_{10}}{m_{00}}, \quad \bar{j} = \frac{m_{01}}{m_{00}} \quad \text{and} \quad \mu_{01} = \mu_{10} = 0 \quad (7)$$

where \bar{i} and \bar{j} are the image center coordinates [Z. Song, 2007].

The normalized central moments shown below will add scale invariance [R. C. Gonzalez, 2002]:

$$\eta_{pq} = \frac{\mu_{pq}}{\mu_{00}^r} \quad \text{where} \quad r = \frac{p+q}{2} + 1 \\ \text{for} \quad p+q = 2, 3, \dots \quad (8)$$

Therefore Hu made seven invariant moments [Z. Song, 2007].

$$\begin{aligned} \phi_1 &= \eta_{20} + \eta_{02} \\ \phi_2 &= (\eta_{20} - \eta_{02})^2 + 4\eta_{11}^2 \\ \phi_3 &= (\eta_{30} - 3\eta_{12})^2 + (3\eta_{21} - \eta_{03})^2 \\ \phi_4 &= (\eta_{30} + \eta_{12})^2 + (\eta_{21} + \eta_{03})^2 \\ \phi_5 &= (\eta_{30} - 3\eta_{12})(\eta_{30} + \eta_{12})[(\eta_{30} + \eta_{12})^2 - \\ & 3(\eta_{21} + \eta_{03})^2] + (3\eta_{21} - \eta_{03})(\eta_{21} + \eta_{03}) \\ & [3(\eta_{30} + \eta_{12})^2 - (\eta_{21} + \eta_{03})^2] \\ \phi_6 &= (\eta_{20} - \eta_{02})[(\eta_{30} + \eta_{12})^2 - (\eta_{21} + \eta_{03})^2] + \\ & 4\eta_{11}(\eta_{30} + \eta_{12})(\eta_{21} + \eta_{03}) \\ \phi_7 &= (3\eta_{21} - \eta_{03})(\eta_{30} + \eta_{12})[(\eta_{30} + \eta_{12})^2 - \\ & 3(\eta_{21} + \eta_{03})^2] - (\eta_{30} - 3\eta_{12})(\eta_{21} + \eta_{03}) \\ & [3(\eta_{30} + \eta_{12})^2 - (\eta_{21} + \eta_{03})^2] \end{aligned} \quad (9)$$

Invariant Moment's Expansion

The actual invariant moments are:

$$I_k = \text{Log}_{10} |\phi_k| \quad (10)$$

where $k = 1, 2, 3, \dots, 7$

It is supposed that two images $f_1(i, j)$ and $f_2(i', j')$ have difference in the contrast, the ratio, the translation and the rotation, but their content is same. In order to obtain more general discrete invariant moments, their mutual relationships can be expressed using the following equation:



$$f_2(i', j') = kf_1(i, j) \quad \text{so}$$

$$\begin{bmatrix} i' \\ j' \end{bmatrix} = c \begin{bmatrix} \cos \theta & \sin \theta \\ -\sin \theta & \cos \theta \end{bmatrix} \begin{bmatrix} i \\ j \end{bmatrix} + \begin{bmatrix} t_i \\ t_j \end{bmatrix} \quad (11)$$

where k is the contrast factor; c is the ratio factor; θ the rotation angle; and (t_i, t_j) are the displacement in the i and j direction respectively.

The more general discrete invariant moments can be taken using equations (9), (10) and (11):

$$\beta_1 = \frac{\sqrt{I_2}}{I_1} \quad \beta_2 = \frac{I_3}{I_2 I_1} \quad \beta_3 = \frac{I_4}{I_3} \quad \beta_4 = \frac{\sqrt{I_5}}{I_4}$$

$$\beta_5 = \frac{I_6}{I_4 I_1} \quad \beta_6 = \frac{I_7}{I_5} \quad (12)$$

where I_1, I_2, \dots, I_7 are actual invariant moments [Z. Song, 2007].

MULTI-WAVELET TRANSFORM

Wavelet transforms provide both spatial information about the image and also frequency information [R. William Ross, 1999]. The resulting from the wavelet transform is a set of two signals, each half the length of the original. The overall effect of the lowpass filter is a lower resolution representation of the original signal scaled by some factor. The high-pass filter leaves behind only the high frequency components. Multi-resolution analysis is accomplished by continuing the process on the result of the low-pass filter [H. Chung, 2002].

Until 1999, only wavelets were known. These are wavelets generated by one scaling function. But one can imagine a situation where there is more than one scaling function. This leads to the notation of multi-wavelets [M. Alfaouri, 2008] which are use several scaling functions and mother wavelets [H. Soltanian - Zadeha, 2004].

Motivation of Multi-wavelets

Using several scaling functions and mother wavelets adds several degrees of

freedom in multi-wavelet design and makes it possible to have several useful properties such as symmetry, orthogonality short support, and a higher number of vanishing moments simultaneously. The usefulness of these properties is well known in wavelet design. Symmetric property allows symmetric extension when dealing with the image boundaries, this prevents discontinuity at the boundaries and therefore a loss of information in these points would be prevented. Orthogonality generates independent sub-images. A higher number of vanishing moments result in a system capable of representing high-degree polynomials with a small number of terms [H. Soltanian - Zadeha, 2004].

Computing discrete multi-wavelet transform, scalar wavelet transform can be written as follows [M. Alfaouri, 2008]:

$$\begin{bmatrix} H_0 & H_1 & H_2 & H_3 & 0 & 0 \\ G_0 & G_1 & G_2 & G_3 & 0 & 0 \\ 0 & 0 & H_0 & H_1 & H_2 & H_3 \\ 0 & 0 & G_0 & G_1 & G_2 & G_3 \end{bmatrix} \quad (13)$$

where H_i and G_i are low and high pass filter impulse responses, are 2-by-2 matrices which can be written as follows [M. Alfaouri, 2008]:

$$\begin{bmatrix} H_0 & H_0 & H_1 & H_1 & \dots & \dots & \dots & \dots & \dots \\ H_0 & H_0 & H_1 & H_1 & \dots & \dots & \dots & \dots & \dots \\ G_0 & G_0 & G_1 & G_1 & \dots & \dots & \dots & \dots & \dots \\ G_0 & G_0 & G_1 & G_1 & \dots & \dots & \dots & \dots & \dots \\ 0 & 0 & 0 & 0 & H_0 & H_0 & H_1 & H_1 & \dots \\ 0 & 0 & 0 & 0 & H_0 & H_0 & H_1 & H_1 & \dots \\ 0 & 0 & 0 & 0 & G_0 & G_0 & G_1 & G_1 & \dots \\ 0 & 0 & 0 & 0 & G_0 & G_0 & G_1 & G_1 & \dots \end{bmatrix} \quad (14)$$

For computing discrete multi-wavelet transform, scalar wavelet transform matrix must be used as in eq. (13) where a system with H_k for GHM four scaling matrices defined as follows [M. Alfaouri, 2008]:

$$\begin{aligned}
 H_0 &= \begin{bmatrix} 3/5\sqrt{2} & 4/5 \\ -1/20 & -3/10\sqrt{2} \end{bmatrix} \\
 H_1 &= \begin{bmatrix} 3/5\sqrt{2} & 0 \\ 9/20 & 1/\sqrt{2} \end{bmatrix} \\
 H_2 &= \begin{bmatrix} 0 & 0 \\ 9/20 & -3/10\sqrt{2} \end{bmatrix} \\
 H_3 &= \begin{bmatrix} 0 & 0 \\ -1/20 & 0 \end{bmatrix}
 \end{aligned} \tag{15}$$

And a system with G_k for GHM four scaling matrices defined as follows [M. Alfaouri, 2008]:

$$\begin{aligned}
 G_0 &= \begin{bmatrix} -1/20 & -3/10\sqrt{2} \\ 1/10\sqrt{2} & 3/10 \end{bmatrix} \\
 G_1 &= \begin{bmatrix} 9/20 & -1/\sqrt{2} \\ -9/10\sqrt{2} & 0 \end{bmatrix} \\
 G_2 &= \begin{bmatrix} 9/20 & -3/10\sqrt{2} \\ 9/10\sqrt{2} & -3/10 \end{bmatrix} \\
 G_3 &= \begin{bmatrix} -1/20 & 0 \\ -1/10\sqrt{2} & 0 \end{bmatrix}
 \end{aligned} \tag{16}$$

Computation of 2-D DMWT Algorithm

Repeated row preprocessing (Over-sampling scheme) is used here [Sudhakar. R, 2006], so, for computing a single-level 2-D multi-wavelet transform the next steps should be followed:

1. Checking input dimensions: Input matrix (patch matrix) should be a square matrix of length $N \times N$, where N must be power of two. If the patch is not a square matrix some operation must be done to the patch like resizing the patch or adding rows or column of zeros to get a square matrix.

2. Constructing a transformation matrix: An $N \times N$ transformation matrix should be constructed using GHM low and high pass filters matrices given in eq.'s (15) and (16). The transformation matrix can be written as eq. (13). After substituting GHM matrix filter coefficients values, a $2N \times 2N$ transformation matrix results with the same

dimensions as the input patch matrix dimensions after preprocessing will be obtained.

3. Preprocessing rows: Row preprocessing doubles the number of the input matrix rows. So if the 2-D input is $N \times N$ matrix elements, after row preprocessing the result is $2N \times N$ matrix. The odd rows 1, 3... $2N-1$ of this resultant matrix are the same original matrix rows values 1, 2, 3..., N respectively. While the even rows numbers 2, 4... $2N$ are the original rows values multiplied by α , for GHM system functions $\alpha = 1/\sqrt{2}$.

4. Transformation of input rows: can be done by

a. Apply matrix multiplication to the $2N \times 2N$ constructed transformation matrix by the $2N \times N$ preprocessing input matrix.

b. Permute the resulting $2N \times 2N$ matrix rows by arranging the row pairs 1,2 and 5, 6, ..., $2N-3, 2N-2$ after each other at the upper half of the resulting matrix rows. Then arrange the row pairs 3, 4 and 7, 8, ..., $2N-1, 2N$ below them at the next lower half.

5. Preprocess columns: It can be done by repeating the same procedure used in preprocessing rows:

a. Transpose the $2N \times N$ transformed matrix from step (4).

b. Repeat step (3) to the $N \times 2N$ matrix which results in $2N \times 2N$ column preprocessed matrix.

6. Transformation of input columns:

a. Apply matrix multiplication to the $2N \times 2N$ constructed transformation matrix by the $2N \times 2N$ column preprocessed matrix.

b. Permute the resulting $2N \times 2N$ matrix rows by arranging the row pairs 1,2 and 5,6..., $2N-3,2N-2$ after each other at the upper half of the resulting matrix rows. Then arrange the row pairs 3,4 and 7,8,..., $2N-1,2N$ below them at the next lower half.

7. To get the final transformed matrix the following should be applied:

a. Transpose the resulting matrix from column transformation step.

b. Apply coefficients permutation to the resulting transpose matrix. Coefficient permutation is applied to each of the basic



four subbands of the resulting transpose matrix so that each subband permutes rows then permutes columns.

Finally, a $2N \times 2N$ DMWT matrix results from the $N \times N$ original patch matrix by using repeated row preprocessing [M. Alfaouri, 2008].

The results of implementing this algorithm is shown in figure (6).

The normalized energy for the DMWT subband is computed and the high energy subband (L1L1) will be taken as a feature and it will be known as (gp) i.e. ghm patch to refer to the patch after transformation by 2-D multi-wavelet transform.

CLASSIFICATION

After generating training and test sets, they should be stored as a database to be used later for testing and evaluation. If a complete set of discriminatory features for each pattern class can be found, classification can be reduced to a simple matching process. However, this assumption is really too quixotic to be achieved in practical pattern recognition problems.

Therefore, only some, or the best discriminatory features are usually adopted. As to classification, its aim is similar to that of feature extraction, which is to find the best class that is the closest to the classified pattern [Y. Kai Wang, 1996].

RECOGNITION METHODS

After the extraction of 21 features from each patch and the high energy subband of each patch in the other side, the minimum distance [T. Zeyad, 2001] and neural network [M. Kantardzic, 2003] methods are used.

In a Minimum distance method, when dealing with a one dimensional vector with more than one element, Euclidean distance is a good measurement for the difference between the two vectors. In this search, the two vectors are two patches vectors which are of the same or different size or rotation angle, translation distance or location (one from the test set and the other from the

training set), i.e. the patches features vectors of the training set and the test set and then the (gp) patches of the training set and the test set. So if the difference is 0, it is surely the best match.

A neural network trained to perform a particular function by adjusting the values of the connections (weights) between elements. Commonly neural networks are trained, so that a particular input leads to a specific target output. There, the network is adjusted, based on a comparison of the output and the target then the error is calculated and the result is fed-back from output layer and the weights are adjusted. These steps represented for all the inputs in the training set and each time the weights are adjusted. The training continues until the mean square error value between the values of the output and the target reaches. Then this net will be used to train an unknown input image that is wanted to recognize.

In this search the parameters of NN training are:

- * Performance function is MSE.
- * No. of hidden layers is 2 layers, the activation functions used are tan sigmoid in the first hidden layer and purelin in the second hidden layer.
- * Epoch 1000 iterations (maximum number of epoch to train)
- * Gradient is $1.00e-10$

Neural network training is shown in Figure (7).

TESTING AND EVALUATION OF RESULTS

This example will be represented for testing and evaluation the proposed algorithms.

1. Enter the test image c2i03, figure (8).
2. Preprocess the image using median filters.
3. Apply canny edge detection and patch selection and then (21) features are extracted from each patch of this image.

4. Decompose each patch of this image by using DMWT.
5. Extract the high energy subband of each patch of this image.
6. Matching by minimum distance and (BP) neural network respectively.

Recognize the image when the result is for the same image (using above two methods), so it is labeled as true (**T**) but when it is **not recognized**, the result is wrong and it is labeled as false (**F**).

As shown in the figure, recognize the image except for the gp patches in group (1) and (2) in the matching by minimum distance which is wrong, i.e. recognize the image for features in matching by minimum distance, while it is recognized for features and gp patches in group (1) and (2) in the recognition by neural network.

The results of implementing the algorithms of matching by minimum distance and BP neural network are shown in table (1), where **recognize** the image is labeled as true (**T**) and when it is **not recognized**, the result is wrong and it is labeled as false (**F**), i.e. when matching the patch features of the test image such as (c1i01) with the patch features of the data base images by using minimum distance, the result is (T) because it is recognized, but when matching the (gp) patches of the same test image (c1i01) with the (gp) patches of the data base images the result is (F) because it is not recognized. while, when matching the patch features of the same test image (c1i01) with the patch features of the data base images by using neural network, the result is (T) because it is recognized and when use the (gp) patches

the result is also (T) because it is recognized. For (a1i09), when matching the patch features using minimum distance, the result is (T) because it is recognized, but when matching the (gp) patches the result is (F) because it is not recognized. While, when matching the patch features using neural network, the result is (F) because it is not recognized and when use the (gp) patches the result is (T) because

it is recognized. For (a2i07), when matching the patch features or (gp) patches using minimum distance, the result is (F) because it is not recognized. While, when matching the patch features using neural network, the result is (T) because it is recognized and when use the (gp) patches the result is (F) because it is not recognized, and so on....

Conclusions

From the above simulation one can be concluded that the proposed techniques are much better performance in comparison with minimum distance for the group (1) or group (2). Recognition by back propagation (BP) neural network as compared with matching by minimum distance, gave (94%) and (83%) score by using group (1), (gp) and features respectively, which is much better than the minimum distance. Recognition using (gp) neural network (NN) gave (94%) and (72%) score by using group (2), (gp) and features respectively, while the minimum distance gave (11%) and (33%) score. Using multi-wavelet transform to gain better feature extractor to each patch and high energy subband of multi-wavelet transform of the patch gave high recognition score than patches features. Time consumption through the recognition process using (NN) with (gp) is less than that when using the minimum distance.



References

- H. Chung, K. Yu Lai, A. Lip, and J. Yip, "Selective Image Compression of Passport Photographs Using Wavelets and Neural Networks", PhD Thesis, University of Manitoba, 2002, pp 16.
- H. Soltanian - Zadeha, F. Rafiee - Rad, S. Pourabdollah - Nejad, "Comparison of multi-wavelet, Wavelet, Haralick, and Shape Features for micro calcification Classification in Mammograms", Journal, Pattern recognition 37, (2004), E-mail: hamids@rad.hfh.edu
- M. Alfaouri, "Image Recognition using Combination of Discrete Multi-wavelet and Wavenet Transform", American journal of applied sciences 5 (4): 418-426, 2008.
<http://www.scipub.org/fulltext/ajas/ajas54418-426.pdf>
- M. Kantardzic, "Data Mining: Concepts, Models, Methods, and Algorithms", John Wiley and Sons© 2003, ch9.
- M. Y. Mashor, M. K. Osman and M. R. Arshad, "3D Object Recognition using 2D Moments and HMLP Network", Proceedings of the International Conference on Computer Graphics, Imaging and Visualization (CGIV'04), IEEE, 0-7695-2178-9/04, 2004.
- R. Cesar, A. Rosa, "3D Object Prototype-Based Recognition from 2D Images using Features net", 2005, pp. 155-162.**
<http://portal.acm.org/citation.cfm?id=1369800>
- R. C. Gonzalez, and R. E. Woods, "Digital Image Processing" Second Edition, 2002, pp. 24, 29, 77, 78, pp. 673-674, Publisher: Tom Robbins.
- R. William Ross, "Target Recognition Using Neural Networks for Wind Tunnel Model Deformation Measurements", Msc. Thesis, Christopher Newport University, 1999, pp28.
- S. E. Umbaugh, "Computer Vision and Image Processing: A Practical Approach Using CVIP tools", PhD, Book, 1995, ch2 (pp61, pp133, pp136).
- Sudhakar. R, and Jayaraman. S, "Fingerprint Compression Using Multiwavelets", pp79-80, International Journal of Signal Processing 2; 2 © www.waset.org Spring 2006, pp78-87.
- T. Acharya and A. K. Ray, "Image Processing, Principles and Applications", 2005, pp84, pp49-52, Published by John Wiley & Sons, Inc., Hoboken, New Jersey.
- T. Zeyad, "Recognition of 3-D Objects", PhD Thesis, Baghdad university, 2001.
- Y. Amit, "2D Object Detection and Recognition", Models, Algorithms and Networks, 2002, pp12, 13, 190, MIT Press, Cambridge, Massachusetts, London, England.
- Y. Kai Wang' and K. Fan', "Applying Genetic Algorithms on Pattern Recognition: An Analysis and Survey", IEEE, 1996, P740.
E-mail: ykwang@iis.sinica.edu.tw ,
kcfan@csie.ncu.edu.tw
- Y. Min', J. Zhtwei', Y. Wensheng', and Z. Xiaornin, "Applications of Generalized Learning in Image Recognition", IEEE, First International Conference on Neural Interface and Control Proceedings, 26-28 May 2005.
- Z. Song, B. Zhao, Z. Zhu, E. Mao "Research on Traffic Number Recognition Based on Neural Network and Invariant Moments", Proceedings of the Sixth International Conference on Machine Learning and Cybernetics, Hong Kong, 19-22 August 2007, China Agricultural University, E-mail: songzhenghe@cau.edu.cn zb1981@sina.com

List of Abbreviations

NN:	Neural network
BP:	Back-propagation
DMWT:	Discrete multi-wavelet transforms
GHM:	Filter proposed by Geronimo, Hardian, Masopute
gp:	High energy subband multi- wavelet transform (ghm patch)
<i>HH</i> :	High-high
<i>HL</i> :	High-low
<i>LH</i> :	Low-high
<i>LL</i> :	Low-low
2-D:	Two dimensional
3-D:	Three dimensional

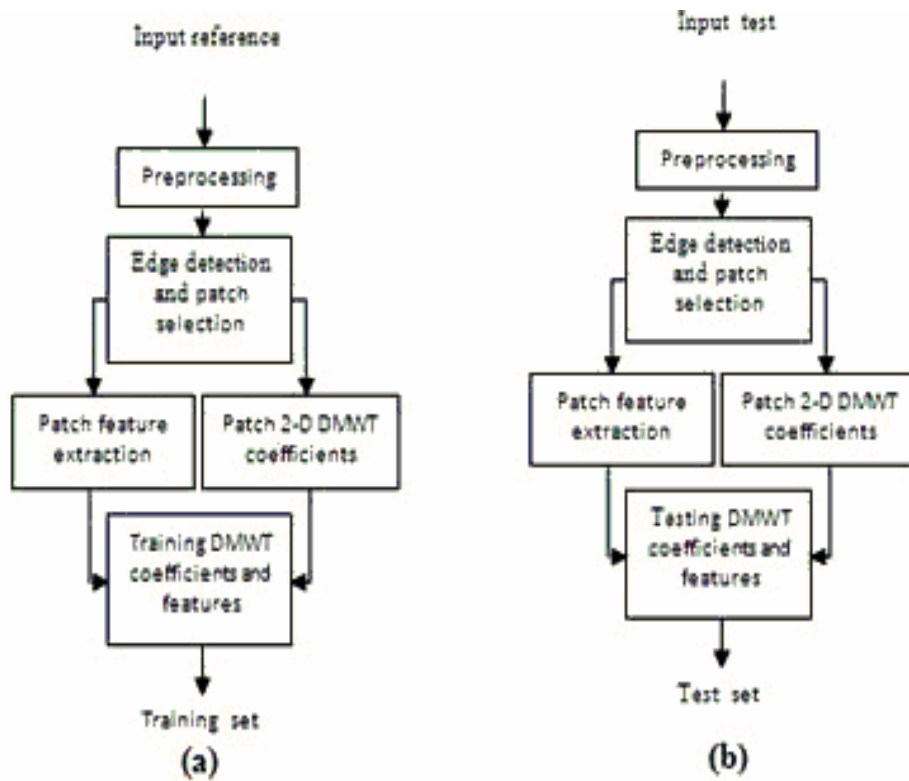


Fig. (1): Block diagrams of: a. Generation training set b. Generation testing set

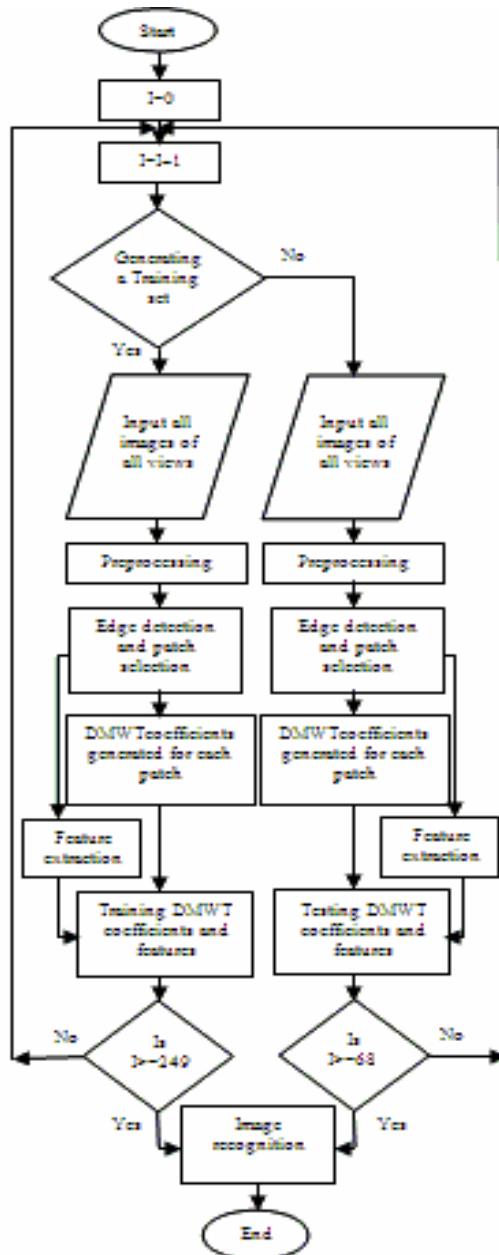


Fig. (2): Flow chart of overall proposed system

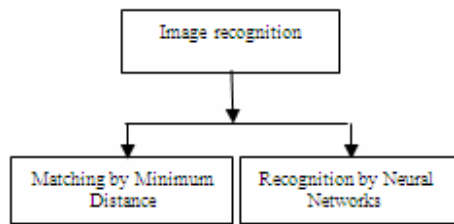


Fig. (3): Block diagram of Image recognition stage

Set (c1)



Set (c2):



Set (a1):



Set (a2):



Fig. (4): Samples of database images



Fig. (5): Samples of test set images.

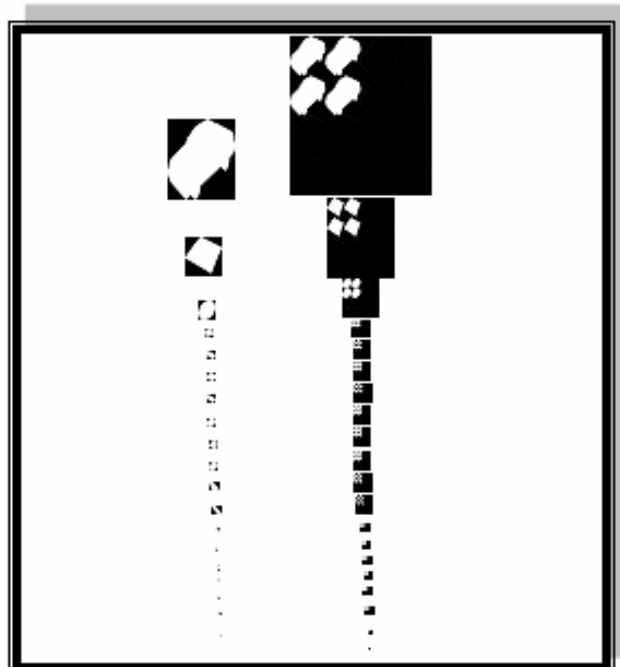


Fig. (6): DMWT implementation of iso view car
(1) Patches after conversion to square and power of 2
(2) Patches after applying DMWT

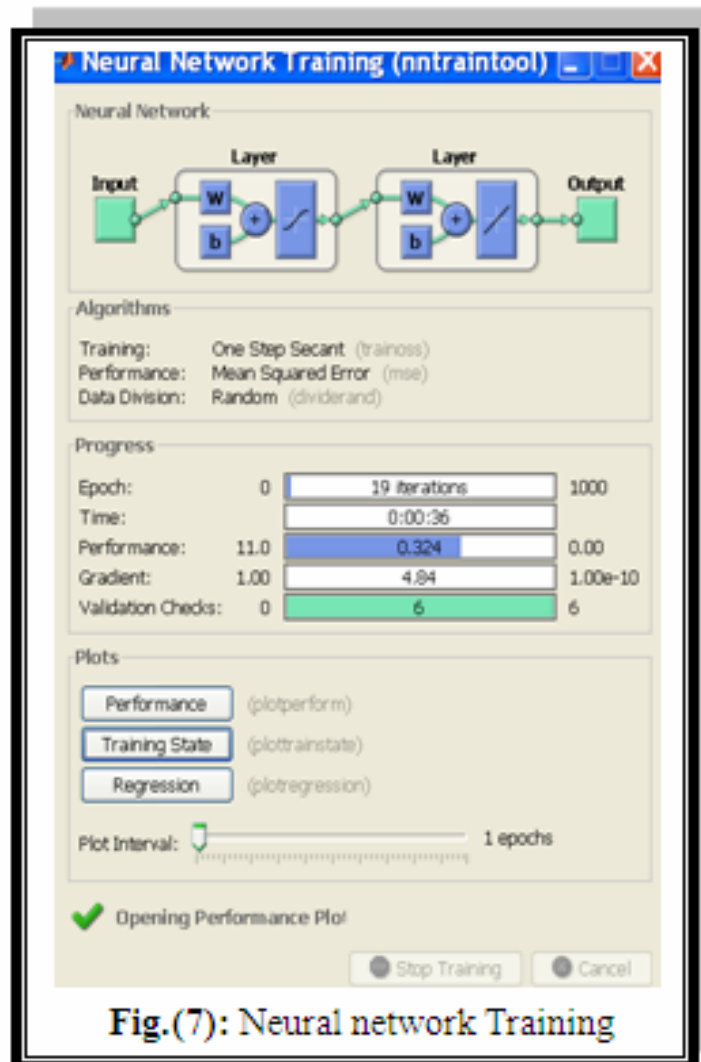


Fig.(7): Neural network Training

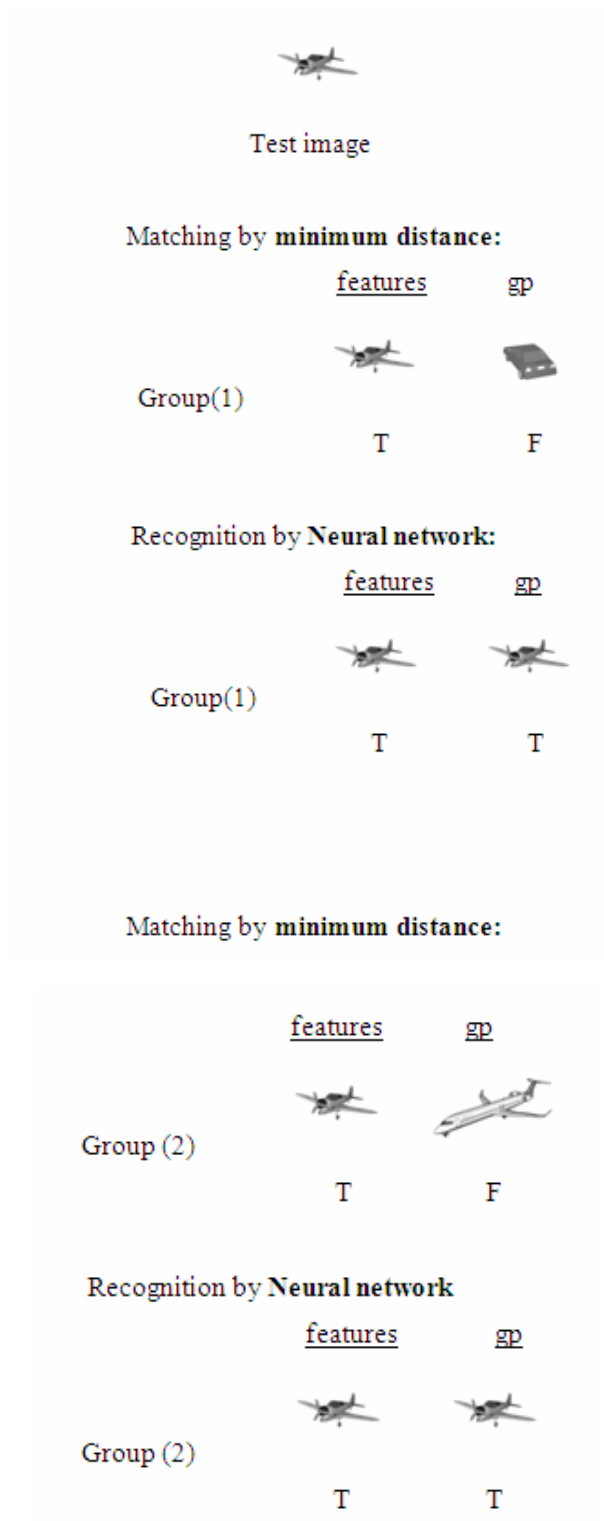


Fig. (8) Evaluation and testing



Table (1): Matching by minimum distance and BP neural network

	Mm. dist. Using feat-ures	Mm. dist. Using (gp) Patc-hes	NN. using Feat-ures	NN. using (gp) patc-hes
cli01	T	F	T	T
cli08	T	F	T	T
cls01	T	F	T	T
cls016	T	F	T	T
clt014	T	F	T	T
c2i03	T	F	T	T
c2s01	T	F	T	T
c2s019	T	F	T	T
c2t015	T	F	T	T
ali09	T	F	F	T
als011	T	F	F	T
alt03	T	F	T	T
alt05	T	F	F	T
a2i03	T	F	T	T
a2i07	F	F	T	F
a2s04	T	F	T	T
a2s05	T	F	T	T
a2t017	T	F	T	T



ANALYTICAL SOLUTION OF UNSATURATED SOIL WATER FLOW FROM A POINT SOURCE

Maysoon B. Abid

Instructor, Dept. of Water Resources
College of Engineering
University of Baghdad

Safa N. Hamad

Instructor, Dept. of Water Resources
College of Engineering
University of Baghdad

Sabah M. Hussain

Instructor, Dept. of Water Resources
College of Engineering
University of Baghdad

ABSTRACT

Water flow into unsaturated porous media is governed by the Richards' partial differential equation expressing the mass conservation and Darcy's laws. The Richards' equation may be written in three forms, where the dependent variable is pressure head or moisture content, and the constitutive relationships between water content and pressure head allow for conversion of one form into the other. In the present paper, the "moisture-based" form of Richards' equation is linearized by applying Kirchhoff's transformation, which combines the soil water diffusivity and soil water content. Then the similarity method is used to obtain the analytical solution of wetting front position. This exact solution is obtained by means of Lie's method of infinitesimal transformation groups. The predicted results of the analytical solution agreed well with available results of experiments and numerical solutions.

الخلاصة

جرى خلال العقد الاخير تقدم كبير في تصميم و ادارة نظام الري بالتنقيط ، و بضمنه دراسة و تحليل حركة الماء داخل التربة من مصدر نقطي.. تم وصف انتشار الماء من مصدر نقطي على سطح التربة في وسط متماثل و متجانس بمعادلة ريتشاردز (Richards' Equation) التفاضلية الجزئية ، التي تربط بين قانوني حفظ الكتلة و الطاقة، و قد تكتب هذه المعادلة بثلاث صيغ قياسية وهي اما على اساس الضغط، او على اساس الرطوبة، او على اساس مختلط. قد تم في هذا البحث ايجاد حلاً تحليلياً لمعادلة ريتشاردز الموصوفة ، بصيغة اساسها الرطوبة ، باستخدام بعض الفرضيات منها ان التربة متجانسة و متماثلة الخواص الفيزيائية، و عدم حدوث تبخر من سطح التربة، و المحتوى الرطوبي الابتدائي خلال التربة منتظم، و عدم حدوث تداخل بين انماط الرطوبة من المنقطات المنفردة، و كون تأثيرات الجاذبية قابلة للاهمال، اي ان الجريان يحدث في تربة ناعمة أو متوسطة النسجة. كما تم أيضا افتراض كون الجريان متماثل محوريا (على طول المحور الشاقولي)، و بذلك يمكن تحديد المحتوى المائي الحجمي بدلالة المسافة من المصدر النقطي و الوقت. قد تم استخدام تحويل كيرشوف (Kirchhoff's transformation)، الذي يدمج أنتشارية ماء التربة و المحتوى الرطوبي للتربة، لتحويل المعادلة التفاضلية الجزئية غير الخطية إلى معادلة تفاضلية جزئية خطية، و من ثم استخدمت طريقة التماثل (التشابه) لتحويل المعادلة التفاضلية الجزئية الخطية إلى معادلة تفاضلية اعتيادية من اجل الحصول على الحل التحليلي.

قد تم التحقق من نتائج الحل التحليلي للنموذج الرياضي باستخدام بيانات مقياسه مختبريا"، و نتائج حلول عددية لدراسات سابقة، و قد تبين ان هناك توافق جيد بين نتائج الحل التحليلي و القياسات المختبرية و القيم المحسوبة من الحل العددي في المراحل المبكرة من عملية الارتشاح ، بعد هذه الفترة تبدأ قيم الحل النظري بالابتعاد عن مثيلاتها للبحوث العملية و الحلول العددية السابقة ، و ذلك بسبب إهمال تأثير الجاذبية. ان الحل الذي تم الحصول عليه مفيد للغاية عند تصميم منظومات الري بالتنقيط ، و ذلك لانه يوفر وسيلة لمعرفة حجم التربة المبتلة بدلالة الزمن ، و بذلك يمكن ان تساهم النتائج في تحديد فواصل المنقطات أو وقت الارواء .

KEYWORDS: Unsaturated flow, Richards' equation, trickle irrigation, point source, Kirchhoff's transformation, similarity.

INTRODUCTION

Trickle irrigation is the most common micro-irrigation method based on supplying water close to the rooted soil volume. This irrigation method allows the effective wetted soil volume to be reduced, thus, evaporation and deep percolation (water and nutrients) to be limited. Trickle irrigation management requires prediction of the wetted soil volume because an over application of water results in loss of both water and fertilizers beyond the root zone. Information on moisture distribution patterns under point source trickle emitters is a pre-requisite for the design and operation of trickle – irrigation systems. The distribution pattern is influenced by the soil properties and the manner water is applied and withdrawn from the soil profile. Flow from a point – source trickle emitter, because of its multi-dimensional nature and high frequency of water application, leads to complexities in modeling soil moisture dynamics (Narda and Lubana, 2001). Wetting pattern from trickle source can be obtained by either direct measurement of soil wetting in field, which is site - specific, or by simulation using some numerical or analytical models. In most of models, the Richards' equation governing water flow under unsaturated flow conditions have been used to simulate soil water matrix potential or water content distribution in wetted soil. Also the hydraulic conductivity in unsaturated flow equations is highly nonlinear and show high spatial variable. Numerical and analytical methods have been used to solve unsaturated flow equations (Battam, et al., 2003).

Several studies have been conducted to determine the flow pattern from trickle sources (Bresler, et al., 1971; Clothier and Scotter, 1982; Hachum, et al., 1976). Mathematical models have been developed to analyze multidimensional infiltration under trickle sources by using non-linear water flow equation (Brandt, et al., 1971; Taghavi, et al., 1984; Lafolie, et al., 1989). Analytical solutions for the corresponding linearized form of the water flow equation with or without plant uptake have been developed for steady-state conditions (Philip, 1971; Raats, 1971). The time-dependent infiltration equation for surface sources of water with various two and three-dimensional geometries has been treated by Warrick (1974) and Lomen and Warrick (1976) by using a linearization approach. By using the unsteady, linearized solution, the wetting-front locations during infiltration were determined by

considering the advance of parabolas of constant matric flux potential with time. Clothier and Scotter (1982) and Clothier, et al., (1985) studied infiltration from a hemispherical cavity by using simple absorption theory. They developed an analytical solution for three-dimensional infiltration with an assumption that, at early times, the gravity term in the flow equation is insignificant relative to the sorption term. Chung (1987) studied a three-dimensional infiltration from a point source by applying an alternating direction implicit (ADI) finite difference method. He used a Darcy-law based soil water equation with a cylindrical coordinate system and a constant flow rate at the point source. Two analytical techniques for studying infiltration from a surface point source have been proposed by Ben-Asher, et al., (1986) and Healy and Warrick, (1988). Analytical models provide a rapid method for determining the wetting front position (Revol, et al., 1997; Cook, et al., 2003). These models are based on the assumption of a point source and certain forms for the physical properties of soil and water content distributions (Philip, 1984; Revol, et al., 1997).

The analysis presented here is simplified by the assumptions of homogeneous and isotropic soils, no evaporation from the soil surface, uniform initial moisture contents, no overlapping between moisture patterns from point sources, and gravity effects are negligible, i.e., a case of flow in medium or fine-textured soils is considered. The technique avoids other limitations of analytical methods such as steady flow.

WATER FLOW EQUATION

The soil-water flow equation can be developed by combining the continuity equation and Darcy's equation. The governing equation for the soil - water flow can be expressed as (Philip, 1969):

$$\frac{\partial \theta}{\partial t} = \nabla \cdot [K(\theta) \nabla \psi(\theta)] \quad (1)$$

where

θ : volumetric soil water content which is a function of location and time, L^3/L^3 ,

$K(\theta)$: unsaturated soil hydraulic conductivity which is a function of volumetric soil water content, L/T ,



$\psi(\theta)$: total water head which is a function of the volumetric soil water content, L ,

t : time, T ,

∇ : the del operator (gradient operator), and

$\nabla \cdot$: the divergence operator.

It is usually convenient to separate the total potential into gravitational and matric potentials. Such a separation yields the general form of Richards' equation, or:

$$\frac{\partial \theta}{\partial t} = \nabla \cdot [K(\theta) \nabla h(\theta)] - \frac{\partial K(\theta)}{\partial z} \quad (2)$$

where

h : matric potential head, L , and

z : gravitational potential head expressed as the depth below soil surface (positive downward), L .

The infiltration phenomenon from a surface point source into a homogeneous and isotropic soil of a uniform initial volumetric water content, θ_i , can be described by the equation governing moisture flow in an unsaturated soil. The moisture-based form is (Philip, 1969):

$$\frac{\partial \theta}{\partial t} = \nabla \cdot [D(\theta) \nabla \theta] - \frac{\partial K(\theta)}{\partial z} \quad (3)$$

where

$D(\theta)$ = unsaturated soil water diffusivity, L^2/T .

At short times during three-dimensional infiltration and in medium or fine-textured soils the gravity term in eq. (3) is insignificant relative to the sorption term, so the infiltration process is approximately absorption (gravity-free) with radial symmetry (Clothier and Scotter, 1982). Therefore, eq. (3) reduces to the nonlinear diffusion equation (Philip, 1969):

$$\frac{\partial \theta}{\partial t} = \nabla \cdot [D(\theta) \nabla \theta] \quad (4)$$

In the present study, consider a systems exhibiting spherical radial symmetry, then the volumetric

water content, θ , can be expressed in terms of the radial distance from the source, r , and the time, t . Thus, eq. (4) can be written as:

$$\frac{\partial \theta}{\partial t} = \frac{1}{r^2} \frac{\partial}{\partial r} \left(D(\theta) r^2 \frac{\partial \theta}{\partial r} \right) \quad (5)$$

The initial and boundary conditions are (as shown in Fig. 1):

$$\theta = \theta_i, \text{ at } t=0, \quad r > 0$$

$$\theta = \theta_s, \text{ at } t > 0, \quad r = 0, \text{ and} \quad (6)$$

$$\theta = \theta_i, \text{ at } t > 0, \quad r = \infty$$

where

r = radial distance from the source, L ,

θ_i = initial soil water content, L^3/L^3 , and

θ_s = saturated soil water content, L^3/L^3 .

MODEL DEVELOPMENT

A similarity substitution usefully reduces the number of independent variable in a partial differential equation only when the variables removed from the equation are removed also from all the governing conditions by the same substitution. A similarity solution of a partial differential equation is obtained by first transforming it into an ordinary differential equation. The equation has been solved by two methods one solution utilized the Boltzmann's transformation and the other utilized similarity techniques. The complete solution is described in detail elsewhere by Abid, (2006); the following is a brief description.

1. Boltzmann Similarity Transformation

The form of eq. (5) can be modified by the application of Kirchhoff's integral transformation in which the dependent variable θ is transformed into a new variable ϕ by means of:

$$\phi = \int_{\theta_i}^{\theta} D(\theta) d\theta \quad (7)$$

where

ϕ = matric flux potential, L^2/T .

Application of Kirchhoff's integral transformation to eq. (5) yields:

$$\frac{1}{D_*} \frac{\partial \phi}{\partial t} = \frac{1}{r^2} \frac{\partial}{\partial r} \left[r^2 \frac{\partial \phi}{\partial r} \right] \quad (8)$$

where

D_* = soil water diffusivity of linearized model, L^2/T .

which will be subjected to the following conditions:

$$\left. \begin{aligned} \phi &= 0, \quad \text{at } t=0, \quad r > 0 \\ \phi &= \mu_i, \quad \text{at } t > 0, \quad r = 0, \text{ and} \\ \phi &= 0, \quad \text{at } t > 0, \quad r = \infty \end{aligned} \right\} \quad (9)$$

where

$$\mu_i = \int_{\theta_i}^{\theta_s} D(\theta) d\theta \quad (10)$$

To eliminate the r^2 term in eq. (8), the following substitution can be used:

$$\phi = \frac{\lambda(r, t)}{r} \quad (11)$$

Therefore, eq. (8) reduces to:

$$\frac{\partial^2 \lambda}{\partial r^2} = \frac{1}{D_*} \frac{\partial \lambda}{\partial t} \quad (12)$$

which is now subjected to the conditions:

$$\left. \begin{aligned} \lambda &= 0, \quad \text{at } t=0, \quad r > 0 \\ \lambda &= r \mu_i, \quad \text{at } t > 0, \quad r = 0, \text{ and} \\ \lambda &= 0, \quad \text{at } t > 0, \quad r = \infty \end{aligned} \right\} \quad (13)$$

Eq. (12) may be transformed into an ordinary differential equation by applying the well-known Boltzmann's transformation (Boltzmann, 1894, this has been cited in Remson, et al., 1971). Such a transformation is defined by:

$$\left. \begin{aligned} \rho &= \frac{r}{2 \sqrt{D_* t}} \\ \lambda(\rho) &= \lambda(r, t) \end{aligned} \right\} \quad (14)$$

where

ρ = the similarity variable, and

$$D_* = \frac{\mu_i}{(\theta_s - \theta_i)} = \frac{1}{(\theta_s - \theta_i)} \int_{\theta_i}^{\theta_s} D(\theta) d\theta \quad (15)$$

Thus, application of the similarity transformation, defined by eq. (14) to eq. (12) yields the ordinary differential equation:

$$\frac{d^2 \lambda}{d \rho^2} + 2\rho \frac{d \lambda}{d \rho} = 0 \quad (16)$$

subjected to:

$$\left. \begin{aligned} \lambda(0) &= r \mu_i, \text{ and} \\ \lambda(\infty) &= 0 \end{aligned} \right\} \quad (17)$$

After separating the variables, integrating, and rearranging, the resulting equation is:



$$\int_{\theta_i}^{\theta} D(\theta) d\theta = \mu_i \operatorname{erfc}(\rho) \quad (18)$$

Substituting μ_i for $\int_{\theta_i}^{\theta_s} D(\theta) d\theta$ gives the following:

$$\int_{\theta_i}^{\theta} D(\theta) d\theta = \operatorname{erfc}(\rho) \int_{\theta_i}^{\theta_s} D(\theta) d\theta \quad (19)$$

The analytical solution to the water flow equation for some cases of soil water diffusivity is shown in **Table 1**.

2. Classical Similarity Reductions

The classical method for finding symmetry reductions of partial differential equations is the Lie- group method of infinitesimal transformations (Ames, 1967; and Bluman and Cole, 1974; Ovsianikov, 1982; Bluman and Kumei, 1989; Olver, 1993). The method of solution depends on the application of one-parameter group transformation to the partial differential equation [eq. (12)]. Under this transformation the two independent variables will be reduced by one, and a differential equation in only one independent variable is obtained, which is the similarity variable.

To apply the classical method to the second order partial differential eq. (12). A one parameter group of infinite infinitesimal transformations is sought which takes the (r, t, λ) - space into itself and under which eq. (12) is invariant, i. e.:

$$\left. \begin{aligned} \bar{r} &= r + \varepsilon \xi(r, t, \lambda) + O(\varepsilon^2), \\ \bar{t} &= t + \varepsilon \tau(r, t, \lambda) + O(\varepsilon^2), \text{ and} \\ \bar{\lambda} &= \lambda + \varepsilon \eta(r, t, \lambda) + O(\varepsilon^2). \end{aligned} \right\} \quad (20)$$

where

ε = group parameter, and

$O(\varepsilon^2)$ = order of the parameter, ε .

Also the derivatives of λ are transformed according to:

$$\left. \begin{aligned} \bar{\lambda}_{\bar{t}} &= \lambda_t + \varepsilon [\tilde{\eta}_t] + O(\varepsilon^2), \text{ and} \\ \bar{\lambda}_{\bar{r}\bar{r}} &= \lambda_{rr} + \varepsilon [\tilde{\eta}_{rr}] + O(\varepsilon^2). \end{aligned} \right\} \quad (21)$$

where

$[\tilde{\eta}_t]$, and $[\tilde{\eta}_{rr}]$ = infinitesimals for transformations of the derivatives η_t and η_{rr} , respectively.

and

$$\begin{aligned} [\tilde{\eta}_t] &= \frac{\partial \eta}{\partial t} + \left[\frac{\partial \eta}{\partial \lambda} - \frac{\partial \tau}{\partial t} \right] \lambda_t - \frac{\partial \xi}{\partial t} \lambda_r \\ &\quad - \frac{\partial \tau}{\partial \lambda} \lambda_t^2 - \frac{\partial \xi}{\partial \lambda} \lambda_r \lambda_t. \end{aligned} \quad (22)$$

$$\begin{aligned} [\tilde{\eta}_{rr}] &= \frac{\partial^2 \eta}{\partial r^2} + \left(2 \frac{\partial^2 \eta}{\partial r \partial \lambda} - \frac{\partial^2 \xi}{\partial r^2} \right) \lambda_r \\ &\quad - \frac{\partial^2 \tau}{\partial r^2} \lambda_t + \left(\frac{\partial^2 \eta}{\partial \lambda^2} - 2 \frac{\partial^2 \xi}{\partial r \partial \lambda} \right) \lambda_r^2 \\ &\quad - 2 \frac{\partial^2 \tau}{\partial r \partial \lambda} \lambda_r \lambda_t - \frac{\partial^2 \xi}{\partial \lambda^2} \lambda_r^3 \\ &\quad - \frac{\partial^2 \tau}{\partial \lambda^2} \lambda_r^2 \lambda_t + \left(\frac{\partial \eta}{\partial \lambda} - 2 \frac{\partial \xi}{\partial r} \right) \lambda_{rr} \\ &\quad - 2 \frac{\partial \tau}{\partial r} \lambda_{rr} - 3 \frac{\partial \xi}{\partial \lambda} \lambda_r \lambda_{rr} - \frac{\partial \tau}{\partial \lambda} \lambda_t \lambda_{rr} \\ &\quad - 2 \frac{\partial \tau}{\partial \lambda} \lambda_r \lambda_{rt}. \end{aligned} \quad (23)$$

Invariance of eq. (12) under eq. (20) gives:

$$(D_*\lambda_{rr} - \lambda_t) + \varepsilon(D_*[\tilde{\eta}_{rr}] - [\tilde{\eta}_t]) + O(\varepsilon^2) = 0 \quad (24)$$

Then, substituting for $[\tilde{\eta}_{rr}]$ and $[\tilde{\eta}_t]$ from eqs. (23) and (22), respectively, and substituting for λ_{rr} from eq. (12) gives:

$$\begin{aligned} & D_* \left[\eta_{rr} + (2\eta_{r\lambda} - \xi_{rr})\lambda_r - \tau_{rr}\lambda_t \right. \\ & + (\eta_{\lambda\lambda} - 2\xi_{r\lambda})\lambda_r^2 - 2\tau_{r\lambda}\lambda_r\lambda_t \\ & - \xi_{\lambda\lambda}\lambda_r^3 - \tau_{\lambda\lambda}\lambda_r^2\lambda_t + (\eta_{\lambda} - 2\xi_r) \left(\frac{1}{D_*}\lambda_t \right) \\ & - 2\tau_r\lambda_{rt} - 3\xi_{\lambda}\lambda_r \left(\frac{1}{D_*}\lambda_t \right) - \tau_{\lambda}\lambda_t \left(\frac{1}{D_*}\lambda_t \right) \\ & \left. - 2\tau_{\lambda}\lambda_r\lambda_{rt} \right] - \left[\eta_t + (\eta_{\lambda} - \tau_t)\lambda_t - \xi_t\lambda_r \right. \\ & \left. - \tau_{\lambda}\lambda_t^2 - \xi_{\lambda}\lambda_r\lambda_t \right] = 0 \end{aligned} \quad (25)$$

The solution of eq. (25) gives the infinitesimal elements (ξ, τ, η) leaving invariant eq. (12). As a comparatively simple solution, the following relations were found:

$$\left. \begin{aligned} \xi &= \frac{1}{2}c_3 r + c_5 t + c_6, \\ \tau &= c_3 t + c_4, \text{ and} \\ \eta &= c_2 \lambda - \frac{c_5}{2D_*} r \lambda + c_1 \end{aligned} \right\} \quad (26)$$

where

$c_1, c_2, c_3, c_4, c_5,$ and $c_6 =$ arbitrary constants.

The similarity variables are obtained by solving the characteristics equation (Bluman and Cole, 1974):

$$\frac{dr}{\xi} = \frac{dt}{\tau} = \frac{d\lambda}{\eta} \quad (27)$$

The general solution of eq. (27) involves two constants, one of them becomes the similarity variable and the other plays the role of a new dependent variable. From the integrals of the two equations $dr/\xi = dt/\tau$ and $dt/\tau = d\lambda/\eta$, with $c_3 \neq 0$, the similarity variables are obtained:

$$\left. \begin{aligned} \rho_* &= \frac{1}{\sqrt{4D_*}} \rho_1 = \frac{1}{\sqrt{4D_*}} \frac{r}{\sqrt{t}} \\ &= \frac{r}{2\sqrt{D_*t}} \\ \lambda &= H(\rho_*) \end{aligned} \right\} \quad (28)$$

when substitute in eq. (28) into eq. (12), and rearranging, the result would be:

$$\frac{d^2H}{d\rho_*^2} + 2\rho_* \frac{dH}{d\rho_*} = 0 \quad (29)$$

subjected to:

$$\left. \begin{aligned} \rho_* &= \infty, \quad H(\infty) = 0, \text{ and} \\ \rho_* &= 0, \quad H(0) = r\mu_i \end{aligned} \right\} \quad (30)$$

because $\lambda = H(\rho_*)$ from eq. (28). After separating variables, integrating, and rearranging, eq. (19) is obtained.

RESULTS AND DISCUSSION

In order to utilize the developed exact solution of the soil-water flow equation to predict the radius of a hemispherical wetted soil volume, i.e., radius of wetting front, the solution needs to be verified by comparing the computed values of wetting front radii with available measured experimental values. The numerical solution has also been used for verification. One set of pertinent data has been found in the literature (data gathered by Clothier and Scotter (1982)) and used for verification. These data can be summarized as follows: initial soil water content, $\theta_i = 0.08$, saturated soil water content, $\theta_s = 0.36$, sorptivity, $S = 1.65 \text{ mm} / \text{s}^{1/2}$, the value of $\beta = 8$ which yields $\gamma = 1.44 * 10^{-3}$, and discharge of the emitter, $Q_e = 1.0 * 10^{-7} \text{ m}^3/\text{s}$. **Fig. 2** shows the



locations of the wetting front for a fine sandy loam soil (medium textured) predicted by the developed model and similar values measured experimentally by Clothier and Scotter (1982); values predicted by a numerical model, finite difference method (FDM), developed by Chung (1987); the hemispherical model developed by Ben-Asher, et al., (1986); and the analytical model developed by Clothier and Scotter (1982). The predicted wetting front patterns by the developed model were concentric hemispheric due to neglecting the gravity effect in the absorption solution. For the first 165 minutes, the predicted values of the wetting front patterns agree well with the experimental values measured by Clothier and Scotter (1982). The maximum relative error was (3.6 %). But, after 360 minutes the predicted wetting front patterns deviated from experimentally measured values, the relative error was about (7.9 %). This over prediction by the developed model is due to errors introduced in the solution when neglecting the gravity-force term in Richards' equation. On the other hand, the predicted wetting front patterns moved slightly slower than those predicted by the numerical finite difference model developed by Chung (1987). The maximum relative error between the two sets of values ranged from (0.44 %) at the first minute to (3.9 %) after 360 minutes. This is mainly due to the different basic assumptions adopted in the two models. In addition, the predicted wetting front patterns agrees with both values predicted by the hemispherical model developed by Ben-Asher, et al., (1986) and the analytical model developed by Clothier and Scotter (1982), respectively. Comparing the wetting front patterns predicted by the developed model with the results of both the hemispherical and analytical models gave an average relative error of (0.8 %) and (0.63 %), respectively, for the first 96 minutes. But after 6 hours, this relative error reached (4.5 %) for both models. Therefore, it can be concluded that the developed model generally provided an accurate-enough means to predict the locations of the wetted soil volume from a point source for medium and fine-textured soils. **Fig. 3** shows the effect of initial soil water content on the wetting front location by using the developed model. It is clear from the results shown in the figure that as initial soil water content increases the volume of wetted soil increases when the time is held constant. **Fig. 4** shows the effect of increasing the saturated soil water content on the movement of wetting front by using the developed model. It can be seen from

the results that as the saturated soil water content increases the rate of advance of the wetting front decreases.

CONCLUSIONS

The simulation of water in homogeneous, unsaturated soils is typically accomplished by solving the unsaturated flow equation. The governing unsaturated flow equation was derived by Richards in 1931. The governing unsaturated flow equation is a nonlinear partial differential equation and difficult to solve exactly in closed form. The aim of this research was to solve Richards' equation and analyze water flow from a point source through medium and fine-texture soils. A mathematical procedure has been developed to solve the unsaturated flow equation by applying Kirchhoff's transformation to linearize the equation. It is a transformation of the dependent variable and is a classical tool to solve nonlinear partial differential equations of water flow in unsaturated soil from a point source. The equation has been solved by two methods one solution utilized the similarity techniques and the other utilized Boltzmann's transformation. An exponential function of soil water diffusivity is selected to demonstrate the use of general similarity theory for describing infiltration of water in soil from a point source. The similarity solution of water infiltration for a functional form of soil water diffusivity compares well with the corresponding experimental data and numerical solutions. The results obtained from the analytical solution of Richards' equation were checked with data previously gathered which relate the distance from the point source to boundary of the saturated wetting front. A sensitivity analysis was also conducted to study the effects of major soil parameters on the movement of the saturated wetting front from a point source. The present analytical solution provides reasonable predictions for absorption problems and can be easily extended to general soil-water flow studies.

REFERENCES

- Abid, M.B., 2006, Analytical solution of unsaturated soil water flow from a point source, Ph D thesis, Department of Water resources Engineering, College of Engineering, Baghdad University, Iraq.

- Ames, W.F., 1967, Nonlinear partial differential equations, Academic Press, San Diego, Calif.
- Ben-Asher, J., Charach, C., Zemel, A., 1986, Infiltration and water extraction from trickle irrigation source: the effective hemisphere model, *Soil Sci. Soc. Am. J.* 50, 882-887.
- Battam, M.A., Sutton, B.G., Boughton, D.G., 2003, Soil pit as a simple design aid for subsurface drip irrigation systems, *Irrigation Science* 22, 135-141.
- Bluman, G.W., Cole, J.D., 1974, Similarity methods for differential equations, *Applied Mathematical Sciences* 13, Springer - Verlag, New York.
- Bluman, G.W., Kumei, S., 1989, Symmetries and differential equations, *Applied Mathematical Sciences* 81, Springer - Verlag, New York.
- Brandt, A., Bresler, E., Diner, N., Ben - Asher, I., Heller, J., Goldberg, D., 1971, Infiltration from a trickle source: I. mathematical models, *Soil Sci. Soc. Am. Proc.* 35, 675-682.
- Bresler, E., Heller, J., Diner, N., Ben - Asher, I., Brandt, A., Goldberg, D., 1971, Infiltration from a trickle source: II. experimental data and theoretical predictions, *Soil Sci. Soc. Am. Proc.* 35, 683-689.
- Chung, Sang-Ok, 1987, Simulation of three - dimensional infiltration from a point source, *Proceeding of the International Conference on Infiltration Development and Application*, 6-9 Jan, Jefferson Hall, The East - West Center, Honolulu, Hawaii, U. S. A. , 114-123.
- Clothier, B.E., Scotter, D.R., 1982, Constant - flux infiltration from a hemispherical cavity, *Soil Sci. Soc. Am. J.* 46, 696-700.
- Clothier, B.E., Scotter, D.R., Harper, E., 1985, Three - dimensional infiltration and trickle irrigation, *Trans. Am. Soc. Agr. Eng.*, ASAE, 28, 497-501.
- Cook, F. J., Thorburn, P.J., Bristow, K. L., Cote, C. M., 2003, infiltration from surface and buried point sources: The average wetting water content, *Water Resources Research*.
- Hachum, A.Y., Alfaro, J. F., Willardson, L.S., 1976, Water movement in soil from trickle source, *J. Irrig. and Drain. Eng. Div, ASCE*, 120, 179-192.
- Healy, R.W., Warrick, A.W., 1988, "A generalized solution to infiltration from a surface point source", *Soil Sci. Soc. Am. J.* 52, 1245-1251.
- Lafolie, F., Guennelon, R., Van Genuchten, M. Th., 1989, Analysis of water flow under trickle irrigation: I. theory and numerical solution, *Soil Sci. Soc. Am. J.* 53, 1310 - 1318.
- Lomen, D.O., Warrick, A.W., 1976, Time dependent linearized moisture flow solution for surface sources, *System Simulation in Water Resources*, G. C. Vansteenkiste, North Holland Publishing Co., Amsterdam, the Netherlands.
- Narda, N. K., Lubana, P. P. S., 2001, SW - soil and water: modeling soil water dynamics under trickle emitters - a review, *Journal of Agricultural Engineering Research* 78, 217-232.
- Olver, P.J., 1993, Applications of Lie groups to differential equations, *Graduate texts in Mathematics* 107, 2 nd edition, Springer - Verlag, New York.
- Ovsianikov, L.V., 1982, Group analysis of differential equations, Academic Press, New York.



Philip, J.R., 1969, Theory of infiltration, *Advan. Hydro-Sci.* 5, 215-296.

Philip, J.R., 1971, General theorem on steady infiltration from surface sources with application to point and line sources, *Soil Sci. Soc. Am. Proc.* 35, 867-871.

Philip, J.R., 1984, Travel times from buried and surface infiltration point sources, *Water Resources Research* 20, 990-994.

Raats, P.A., 1971, Steady infiltration from point sources, cavities and basins, *Soil Sci. Soc. Am. Proc.* 35, 689-694.

Remson, I., Hornberger, G.M., Molz, F. J., 1971, Numerical methods in subsurface hydrology, John Wiley and Sons, Inc., United States of America.

Revol, P., Clothier, B. E., Mailhol, J. C., Vachaud, G., Vauclin, M., 1997, Infiltration from a surface point source and drip irrigation: 2. An approximate time - dependent solution for wet - front position, *Water Resources Research* 33, 1869-1874.

Taghavi, S. A., Marino, M.A., Rolston, D.E., 1984, Infiltration from a trickle source, *J. Irr. Drain. Eng.*, ASCE, 110, 331-341.

Warrick, A.W., 1974, Time Dependent linearized infiltration: I. point sources, *Soil Sci. Soc. Am. Proc.* 38, 383-386.

$K(\theta)$: unsaturated soil hydraulic conductivity which is a function of volumetric soil water content, L/T.

r : radial distance from the source, L.

t : time, T,

z : gravitational potential head expressed as the depth below soil surface (positive downward), L.

ε : group parameter.

$O(\varepsilon^2)$: order of the parameter, ε .

θ_s : saturated soil water content, L^3/L^3 .

θ_i : initial soil water content, L^3/L^3 ,

∇ : the divergence operator.

$\psi(\theta)$: total water head which is a function of the volumetric soil water content, L.

ρ : the similarity variable.

θ : volumetric soil water content which is a function of location and time, L^3/L^3 .

∇ : the del operator (gradient operator).

ϕ : matric flux potential, L^2/T .

SYMBOLS AND ABBREVIATIONS

$D(\theta)$: unsaturated soil water diffusivity, L^2/T .

D^* : soil water diffusivity of linearized model, L^2/T .

h : matric potential head, L.

Table1: Analytical solution to water flow equation for some cases of soil water diffusivity.

Soil Water Diffusivity	Solution
$D(\theta) = \text{constant}$	$\frac{\theta - \theta_i}{\theta_s - \theta_i} = \text{erfc}(\rho)$
$D(\theta) = \text{variable}$	$\frac{\int_{\theta_i}^{\theta} D(\theta) d\theta}{\int_{\theta_i}^{\theta_s} D(\theta) d\theta} = \text{erfc}(\rho)$
$D(\theta) = D_0 (n+1) \theta^n$	$\frac{\theta^{n+1} - \theta_i^{n+1}}{\theta_s^{n+1} - \theta_i^{n+1}} = \text{erfc}(\rho)$
$D(\theta) = ae^{b\theta}$	$\frac{e^{b\theta} - e^{b\theta_i}}{e^{b\theta_s} - e^{b\theta_i}} = \text{erfc}(\rho)$

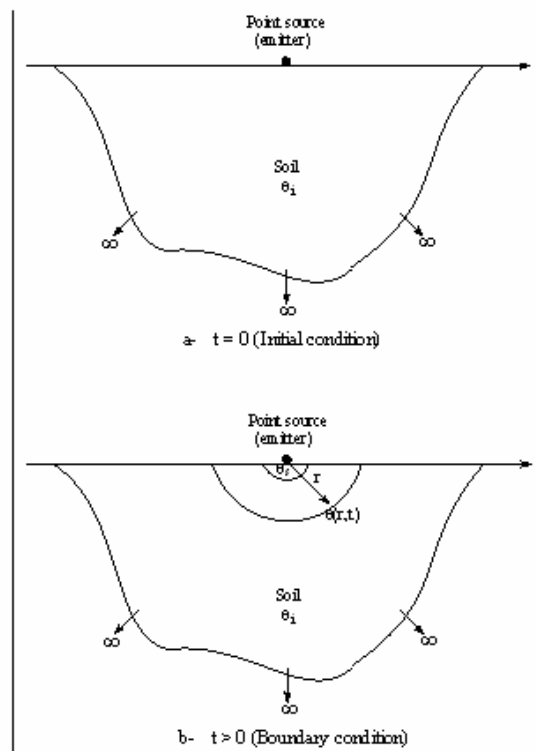


Fig. 1. Physical model of soil water flow.

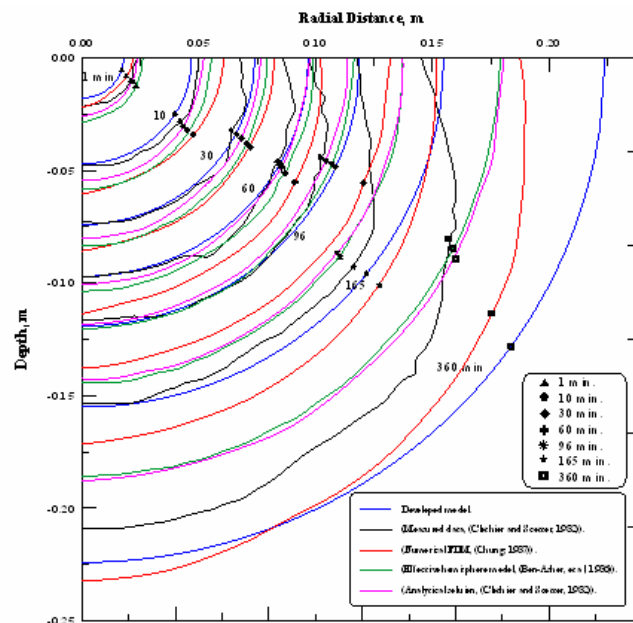


Fig. 2. Wetting front patterns.

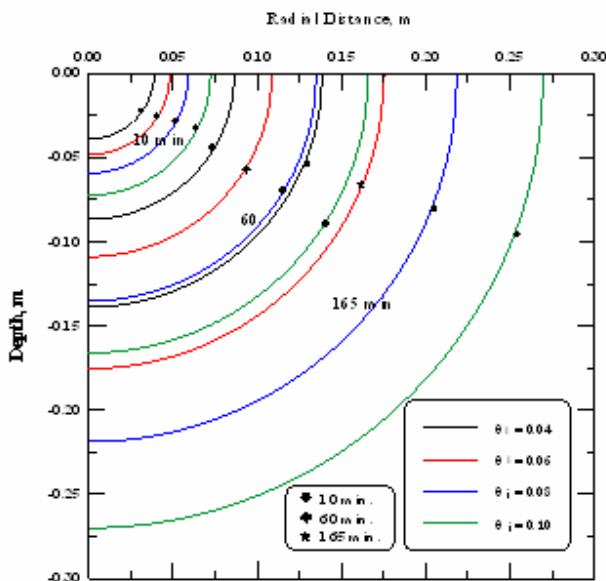


Fig.3. Effect of initial soil water content on the wetting front patterns.

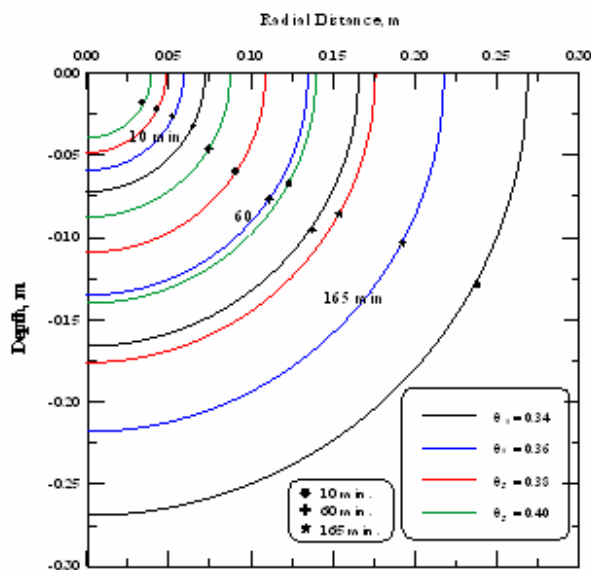


Fig.4. Effect of saturated soil water content on the wetting front patterns.



VARIATION OF SOME WATER QUALITY PARAMETERS OF HUWAIZA MARSH IN SOUTHERN IRAQ

Tariq J.Kadhem Al-Musawi

Department of Environmental Eng., College of Eng., Baghdad University

Abstract

Huwaiza marsh is considered the largest marsh in the southern part of Iraq. It is located between 31° and 31.75° latitude and extends over the Iraqi-Iranian border; but the largest part lies in Iraq. It is located to the east of Tigris River in Messan and Basra governorates.

In this research, the variation of some water quality parameters at different locations of Huwaiza marsh were studied to find out its efficacy in the treatment of the contamination coming from the wastewater outfall of Kahlaa brokendown sewage treatment plant which lies on the Kahlaa River. This rive is the main feeder of Huwaiza marsh. Ten water quality sampling locations were chosen in this marsh. The water samples were taken during 2009 for three months; January, April and August representing winter, spring and summer respectively. The results of water quality analyses showed that Kahlaa untreated sewage had a negative impact on the water quality of Huwazia marsh; especially in its upstream region. Analyses of water samples taken from the middle and downstream end of the marsh showed that the marsh water is safe for fishing and swimming in these regions.

الخلاصة

يعد هور الحويزة من اكبر الاهوار في جنوبي العراق. يقع الهور بين خطي طول 31° و 31,75° حيث يمتد عبر الحدود العراقية الايرانية ; ولكن يقع الجزء الاكبر منه في العراق شرق نهر دجلة في محافظتي ميسان و البصرة. في هذا البحث تم دراسة تغيرات بعض مؤشرات نوعية المياه في مواقع مختلفة من هور الحويزة لايجاد كفاءته في معالجة التلوث القادم اليه نتيجة طرح مياه الصرف الصحي غير المعالجة من محطة الكحلاء العاطلة والواقعة على نهر الكحلاء . يعد نهر الكحلاء من اهم الانهر المغذية للهوور. تم اختيار عشرة مواقع لاختبار عينات لتحديد نوعية المياه. أخذت العينات خلال سنة 2009 ولثلاثة اشهر ; كانون الثاني، نيسان و آب ممثلة للشتاء والربيع والصيف على التوالي. بينت نتائج التحليل ان مياه الصرف الصحي غير المعالجة لها تأثير سلبي على نوعية مياه هور الحويزة وخاصة في مناطق مصب نهر الكحلاء. كما بينت النتائج المأخوذة من وسط ونهاية الهور امكانية استخدامه لصيد الاسماك والسباحة في هذه المناطق.

Keywords: Wetlands, Huwaiza marsh, Water quality parameters, Organic pollution, Faecal Coliform.

Introduction

Wetlands, as defined by the Ramsar convention on wetlands, include a wide variety of habitats such as marshes, peat lands, floodplains, rivers and lakes, as well as coastal areas such as salt marshes, mangroves, and sea grass beds. It also includes coral reefs and other marine areas no deeper than six meters at low tide, in addition to human-made wetlands such as wastewater treatment ponds and reservoirs (**Ramsar Convention Secretariat, 2004**).

The amount of water in wetlands varies depending on the weather and the time of year. Plants, such as reeds, grow in wetlands area. Wetlands also provide a home for a host of different wildlife ranging from migratory and local birds to fish, reptiles, amphibians and insects (**Chouhan Paridhi, 2008**).

Many studies were conducted by Iraqi ministries, organizations, and associations as well as UNEP teams which were related to the restoration of water quality and ecology of marshes.

The demise of the marshes in Iraq began during the Iraq-Iran war. As a result many dykes, embankments, and drainage canals were constructed by the two countries as they struggled to gain military advantage using water as a military tool. After 1991 many diversion canals were constructed in the marshes to reclaim land for agricultural purposes. Additionally, Turkey and Iran have constructed dams on the headwaters of the Euphrates, Tigris and Karkha Rivers, resulting in the reduction of the amount and quality of the water reaching southern Iraq (**Alwash Azzam et al., 2007**).

The marshes of Iraq were once famous for their biodiversity and cultural richness. They were the permanent habitat for millions of birds and a migrating flyway between Siberia and Africa (**Maltby 1994, Evans 2002 qtd. by Richardson and Hussain, 2006**).

Partow (2001) studied the hydrology of the marshes of Iraq and mentioned that less than 10 % of their area remained as functioning marshland by the year 2000. The only remaining

VARIATION OF SOME WATER QUALITY PARAMETERS OF HUWAIZA MARSH IN SOUTHERN IRAQ

marsh was the northern portion of Huwaiza; the other two marshes, Hammar and Central were totally desiccated. This researcher also concluded that only 15 to 20 % of the dried marshes could be restored because of excessive salinity, environmental pollution, and lack of availability of fresh water. **Fig.1** shows the analysis of Landsat satellite imagery of marshlands area (**UNEP, 2001**).

After May 2003, water began to return to the marshlands. In 2004, up to 40% of the former marshlands were reflooded. Some of the reflooded areas experienced rapid regrowth of marshland vegetation, other areas are slowly recovering; while some reflooded areas remain barren. The marsh dwellers are also coming back, with as many as 42,000 people returning to their traditional life styles within the reflooded areas. **Fig. 2** shows the Iraqi marshland in 2007.

The background image in Fig.2 is Landsat satellite image of Huwaiza marsh with resolution 250 m and was taken in September 2007.

Al-Musawi (2009) studied the water quality of Al-Hammar marsh in the south of Iraq. He mentioned that due to unavailability of Iraqi environmental regulations regarding marsh water on the one hand and the lacking of any actual water quality parameter values of such waters prior to desiccation on the other hand, his only recourse was to compare the recently obtained parameter values with the various water use categories; notably, irrigation, drinking and fishing.

Sometimes marshes are used for wastewater treatment. This kind of use has increased dramatically in the last decade, particularly for small scale applications such as individual homes and small villages (**Wallace and Knight, 2006**). Marshes are useful for nutrient recovery and cycling, releasing excess nitrogen, inactivating phosphates, removing toxins, chemicals and heavy metals through absorption by plants. Removal of suspended solids from flowing water occurs through flow reduction. Additionally retention of water for a long time whereby biological, physical and chemical processes occur periodically is beneficial. Huwaiza marsh can be considered as a natural free water surface (FWS) marsh; a large area of water with a combination of floating vegetation. The major processes that occur within FWS marshes are summarized in **Fig.3**.



Huwaiza marsh is considered the largest marsh in the southern part of Iraq. It is located between 31° and 31.75° latitude and extends over the Iraqi-Iranian border; but the largest part lies in Iraq. It is located to the east of Tigris River in Messan and Basra governorates. There is no definite area for the marsh due to seasonal and annual changes resulting from variations in the water amount reaching the marsh. According to the satellite image shown in **Fig.2** and by using geographic information system programs like ArcView GIS version 9.3, the net surface area of the marsh is approximately 2400 km² on the date of this image.

Huwaiza marsh is fed directly by three sources: the western source is the Tigris River through the Kahlaa, Musharah and Majar branches; the eastern source is from Iran through Karkha River. The marsh water returns to the Tigris River by many outlets, the most important ones are Swaib and Kassara outlets. Huwaiza marsh has been included in the Ramsar Convention on Wetlands since 17 February 2009.

In this research, the variation of some water quality parameters of Huwaiza marsh was studied to find out its efficacy to treat the contamination coming from the wastewater outfall of Kahlaa brokendown sewage treatment plant. Kahlaa River is the main feeder of Huwaiza marsh.

Field Work and Experimental Data

Sampling is a vital part of studying the quality of water. A major source of error in the whole process of obtaining water quality information often occurs during sampling. Poor management decisions based upon incorrect data may result if sampling is performed in a careless and thoughtless manner. Obtaining good results will depend on a great extent upon the following factors:

1. Ensuring that the sample taken is truly representative of the water under consideration.
2. Using proper sampling technique (e.g use of sterilized bottles for microbiological testing).
3. Protecting and preserving the samples until they are analyzed in laboratories.

Samples were taken from locations that were considered representative of contamination sources or where contamination was suspected. Ten water quality sampling locations were chosen. All water samples were taken from 60 % of the water depth. The sample bottles were labeled with an identifying code (such as HZ 3, in which HZ refers to the Huwaiza marsh and 3 refers to sample location). The geographic coordinates of sample locations were fixed using GPS device (type: GARMIN,eTrex). The GPS measurements can be plotted on a map or used to return to the same site in the future. The following table shows the geographic coordinates of the ten water sample locations and their site description.

An important part of undertaking water quality studies is to know what parameters one should sample and analyze. There are a number of water quality parameters that could be measured and it is important to make a good judgment of what are likely to be the most important ones in a particular situation. Hence, an initial surveying was carried out to obtain information on any known activities that might affect water quality of Huwaiza marsh, e.g. sources of human and animal wastes, industrial activities and agricultural farms. Essential parameters to be measured would be those that indicate a risk to human health or the environment, those with potential to cause public complaints, and those which indicate a likelihood of causing operational problems in water treatment plants. Some chemical analyses are expensive and difficult to carry out, In addition it should be emphasized that laboratory facilities play an important role in the selection of water quality parameters that should be analyzed in an environmental assessment. **Mosley et al. (2004)** suggested the most important parameters to analyze in different water types. **Table 2** shows these parameters.

Initial surveying of Huwaiza marshland gave the following important information:

- Many organic waste sources are spreading near the feeder rivers of the marsh such as villages and small human settlements, so that biochemical oxygen demand (BOD) should be analyzed to find out the extent of organic pollution.

- Lack of industrial discharges containing metals so that there is no need to analyze metals.
- It is difficult and expensive to accurately analyze the following parameters: chemical oxygen demand (COD), ammonia, pesticides and radioactive constituents.
- Absence of oil fields/fuel spills in Huwaiza marsh area precludes oil and grease analyses.

Consequently, the following eleven surface water analyses became relevant: faecal coliform, turbidity, total dissolved solids (TDS), total suspended solids (TSS), nitrate (NO₃), phosphate (PO₄) and five-day biochemical oxygen demand (BOD₅), as well as direct measurements using portable devices for temperature, pH, dissolved oxygen (DO) and electrical conductivity (EC).

All the water samples were taken during 2009 for three months; January, April and August representing winter, spring and summer respectively. The water samples were submitted to analyses by "Standard Methods", (APHA, 1999). Fig.4 shows the locations of water samples taken from Huwazia marsh

Results and Discussion

The temperature of the natural water system depends mainly on the ambient temperature (temperature of the surrounding atmosphere). In general, as the temperature increases the saturation of dissolved oxygen in water decreases and vice versa. **Fig.5** shows the variation of water temperature in different location in Huwaiza marsh. It can be noticed that there is no or slightly change in water temperature along the marsh for three seasons, so that it can be conclude that the temperature of Huwaiza marsh depends on the ambient temperature to a great extend due to the large water surface area.

Many factors affect the concentrations of dissolved oxygen in a water body, among them organic pollution, temperature, light penetration, water movement, availability of plants and nutrients. **Fig.6** shows the results of dissolved oxygen concentrations of the ten samples. The lowest value of dissolved oxygen was obtained at location HZ 1, between 3 to 4 mg/l due to municipal wastewater pollution. At location HZ 2 it increases

VARIATION OF SOME WATER QUALITY PARAMETERS OF HUWAIZA MARSH IN SOUTHERN IRAQ

and reaches its maximum value at location HZ 7 (between 7 to 8.2 mg/l) in the middle of the marsh and then varies slightly at the end of the marsh. Therefore, the marsh improves the dissolved oxygen level due to the high rate of atmospheric aeration and photosynthetic process of aquatic plants abundant in the marsh.

pH is a measure of the hydrogen ion (H⁺) concentration in water, it is an important parameter for describing the state of chemical processes. Water with pH greater than 8.5 is called hardwater; hardwater does not pose a health risk, but can cause aesthetic problems (**Mosley et al. 2004**). In **Fig.7** the pH of all the water samples were around 8 except that at HZ 1 location which was greater than 8.5 due to the disposing of municipal wastewater from Kahlaa treatment plant.

Fig.8 shows the laboratory results of BOD₅ analyses and it can be noticed that there is a logical high concentration at HZ 1 location due to the high organic loading coming from Kahlaa plant. Nevertheless, a sharp decrease occurred after a few meters downstream of this location; reaching below 50 mg/l at the middle of the marsh. This can be attributed to two factors; first, there are no industrial activities that discharge pollutants directly into the marsh, and human pollution is low due to a limited number of small villages spreading inside Huwaiza marsh; second, the spreading of plants and the slow water velocity permit a long term of atmospheric aeration and photosynthetic activity which increase the efficiency of organic pollution digestion by bacteria.

Many inorganic ions such as sodium, chloride, magnesium, and calcium are present in surface water. EC or TDS is a measure of how much total salt (inorganic ions) is present in the water; the more ions the higher the conductivity. **Fig.'s 9 and 10** show the variation of EC and TDS concentrations respectively. It can be noticed that there is a fluctuating variation in the values of these parameters due to the following points:

- The first location reveals relatively high values of EC and TDS due to wastewater disposal from Kahlaa plant. These values decrease notably in samples taken from the middle of the marsh due to dilution from other feeders and the phytotechnology process that contributes to the decrease of TDS.



- EC and TDS values rise again especially at locations HZ 7 and HZ 8 because of the proximity of the Iranian dyke which sometimes leaked drainage water.

In **Fig.10** it can be seen that TDS concentrations were higher in summer compared with those in spring and winter. The high water losses in summer due to evapotranspiration process leads to higher TDS values in Huwaiza marsh. **Fig.11** shows the monthly evapotranspiration losses (**Iraqi Ministries of Water Resources, Municipalities and Public Works, and Environment, 2005**).

There are several different chemical compounds which are termed nutrients; most containing one of the elements nitrogen or phosphorous. In water, they provide nutrients for the primary producers such as algae, phytoplankton and seaweeds. If the nutrients reach high levels in water exposed to light, algal problems may arise. **Fig.'s 12 and 13** show the variation of NO_3 and PO_4 in Huwaiza marsh. There are high levels of NO_3 and PO_4 in the first half of the marsh because of the feeding of water containing high concentrations of NO_3 and PO_4 coming from the disposal of untreated municipal wastewater and a wide spread of agricultural farms that use fertilizers. These two ions gradually decrease subsequently due to the consumption by algae and phytoplankton whose spread at the water surface can be seen with the naked eye.

Fig.'s 14 and 15 show the variation of turbidity and TSS concentrations in the marsh. It is obvious that turbidity and TSS concentrations decrease as soon as the water flows through the marsh due to the low flow velocity (sometimes the water is virtually stagnant) and shallow water properties (**Al-Musawi, 2009**).

Disease causing microorganisms (pathogens) include salmonella, shigella, escherichia coli, cysts or entamoeba histolytica, parasite ova, viruses and infectious hepatitis. Usually the water is tested for faecal coliform to see the level of bacterial contamination (**Mosley et al., 2005**). Water used for primary contact activities (swimming, bathing) and for secondary contact activities (boating, fishing) should be safe from bacterial contamination. As pointed out previously, the water of the marshes may be used for these two kinds of contact activities. The Australian water quality guidelines for fresh and marine waters

recommend that for primary contact activities the water should not have more than 150 Faecal Coliform/100ml and for secondary contact activities the water should not have more than 1000 Faecal Coliform/100ml (**ANZECC 1992 qtd. by Mosley et al., 2005**).

Fig.16 shows that there is a high bacterial contamination in locations downstream of the outfall of Kahlaa sewage plant; i.e. at the upstream end of the marsh. However, the level of bacterial contamination farther inside the marsh was found to be low reaching below 100 Faecal Coliform/100ml especially at locations HZ 4 to HZ 10. It can be concluded that whenever the Kahlaa sewage treatment plant is properly put back to work, all the marsh water may be considered safe for both primary and secondary contact activities like fishing and swimming.

Conclusions

1. Due to Kahlaa sewage treatment plant being brokendown, the untreated sewage had a negative impact on the water quality of the upstream region of Huwazia marsh. However, the analyses of water samples taken from the middle and downstream end of the marsh showed that the marsh water is safe for fishing and swimming in these regions.
2. Because of the large surface area of Huwaiza marsh, the temperature of water varies slightly and depends largely on the ambient temperature.
3. The untreated wastewater from Kahlaa plant decreases the dissolved oxygen concentration below the allowable limit; but the marsh has the ability to improve the dissolved oxygen level back to its normal concentration.
4. All the water samples showed that the pH value was in the zone of low bacidity (7.5-8.5).
5. According to the laboratory results of BOD_5 , Huwaiza marsh was efficient in treating organic pollution, sometimes reaching above 80%.
6. In Huwaiza marsh, removal of suspended solids occurs at the first few meters when the water enters the marsh due to low flow or nearly stagnant conditions and shallow water.
7. Despite of the TDS concentration decrease due to dilution by fresh water, drainage water

Tariq J.Kadhem Al-Musawi

caused an increase in TDS concentration especially during the hot season.

8. The removal of nitrate and phosphate varied from 25 to 40% and depended on the agricultural season and the wastewater discharge.

Acknowledgment

I would like to express my sincere thanks and deep gratitude to the Ministry of Water Resources/ Center for the Restoration of Iraqi Marshlands (CRIM) and Dr.Abdul-Fattah Mohamed Ali for their support in this work.

References:

Al-Musawi Tariq J.Kadhem, (2009) "Water Quality of Al-Hammar Marsh South Iraq", Jou.of.Eng., Vol.15,No.3, Baghdad.

Alwash Azzam, Alwash Suzanne, and Cattarossi Andrea, (2007) "Iraq's marshlands-Demise and the Impending Rebirth of an Ecosystem", Technical Report. The Iraq Foundation, Baghdad, Iraq. 4 Feb. 2011. <<http://www.ag.unr.edu/swwf/readings/alwash.pdf>>.

APHA, American Public Health Association, (1999) "Standard Methods for the Examination of water and wastewater". 20th Edition. Washington, D.C.

Chouhan Paridhi, (2008) "Save Wetlands Save Water", the 12th World Lake Conference. 3 Feb.2011. <<http://www.wldb.ilec.or.jp/data/ilec/wlcl2/0-Socialculture Aspects Participation for Management /0-19.pdf>>.

Iraqi Ministries Of Water Resources, Municipalities and Public Works ,and Environment in cooperation with the Italian Ministry for The Environment and Free Iraq Foundation,(2005) " New Eden : Master Plan for Integrated Water Resources Management in the Marshlands Area", Interim Report, Italy-Iraq, 11 Feb. 2011. <<http://www.Iraqfoundation.org/edenagain/publications/pdfs/NewEden Master Plan-Interim Report 2005-REDUCED.pdf>>.

Mosley Luke, Singh Sarabjeet, and Aalbersberg Bill, (2005) "Water quality monitoring in pacific countries", SOPAC Technical Report 381,1st Revised Edition-Suva, SOPAC,14 Jan.2009.

VARIATION OF SOME WATER QUALITY PARAMETERS OF HUWAIZA MARSH IN SOUTHERN IRAQ

<<http://www.pacificwater.org/userfiles/file/TR0381.pdf>>.

Ramsar Convention Secretariat, (2004) " Ramsar Handbook for the Wise Use of Wetlands", 2nd Edition, Ramsar Convention Secretariat, Gland, Switzerland. 3 Feb. 2001. < http://www.ramsar.org/index_key_docs.htm#res>.

Richardson J.Curtis and Hussain A.Najah, (2006) "Restoration the Garden of Eden: An Ecological Assessment of the Marshes of Iraq", American Institute of Biological Sciences, Bioscience Journal, Vol. 56, No.6. 4 Feb.2011.<<http://www.bioone.org/doi/full/10.1641/00063568%282006%2956%5B477%3ARTGOEA%5D2.0.CO%3B2>>

Partow, H, (2001) "The Mesopotamian Marshlands: Demise of an Ecosystem", Early Warning and Assessment Technical Report, UNEP/DEWA/TR.01-3 Rev.1,Nairobi,Kenya.11 Feb. 2011. <<http://earthobservatory.nasa.gov/Newsroom/NewImages/Images/meso2.pdf>>.

UNEP, (2001) "UNEP Study Sounds Alarm About the Disappearance of the Mesopotamian", 11 Feb.2001. <http://www.grid.unep.ch/activities/sustainable/tigris/2001_may.php>.

Wallace, SD and Knight, RL, (2006) " Small-scale constructed wetland treatment system: feasibility, design criteria and O&M requirements", Final report, Project 01-CTS-5, Water Environment Research Foundation, Alexandria, Virginia. IWA Publishing. 27 Jan. 2011. < <http://www.iwapublishing.com/template.cfm?name=isbn1843397285>>.



Table 1: Code, geographic coordinate and site description of the ten water sample locations

Code of water sample	Location		Site description
	E	N	
HZ 1	717129	3505861	This point represents the mixing zone between fresh water and the sewage discharged from Kahlaa plant.
HZ 2	736687	3496408	Point at the mouth of Kahlaa River with the marsh.
HZ 3	746511	3493290	Point inside the marsh.
HZ 4	751514	3492804	Point inside the marsh.
HZ 5	750885	3486989	Point inside the marsh.
HZ 6	752790	3483178	Point inside the marsh and near Iranian dyke.
HZ 7	753343	3474203	Point inside the marsh and near Iranian dyke.
HZ 8	744430	3483793	Point inside the marsh
HZ 9	738098	3476047	Point at Kassara outlet to the Tigris River.
HZ 10	741356	3441007	Point at Al-Swaib outlet to the Tigris River.

Table 2: Typical water quality parameters to be measured in different water types (Mosley et al., 2004)

	Water Type		
	Drinking	Surface	Marine
Microbiology:			
Total Coliform	Yes	No	No
Faecal Coliform	Yes	Yes	Yes
Physical:			
pH	Yes	Yes	No
Temperature	Yes	Yes	Yes
Colour	Yes	No	No
Turbidity	Yes	Yes	Yes
Conductivity/Total Dissolved Solids	Yes	Yes	No
Salinity	No	No	Yes
Dissolved Oxygen	No	Yes	Yes
Total Suspended Solids	No	Yes	No
Chemical-Inorganic:			
Ammonia	No	Yes	Yes
Nitrate	Yes	Yes	Yes
Nitrite	No	Yes	Yes
Phosphata	No	Yes	Yes
Hydrogen Sulphide	Periodically	No	No
Sulphate	Periodically	No	No
Fluoride	Periodically	No	No
Chloride	Yes	No	No
Hardness	Periodically	Periodically	No
Metals:			
Aluminum	Periodically	Periodically	Possibly
Cadmium	Periodically	Periodically	Possibly
Copper	Periodically	Periodically	Possibly
Iron	Periodically	Periodically	Possibly
Manganese	Periodically	Periodically	Possibly
Lead	Periodically	Periodically	Possibly
Zinc	Periodically	Periodically	Possibly
Chemical-Organic:			
BOD	No	Yes	Yes
COD	No	Yes	No
Oil and Grease	No	Possibly	Possibly
Pesticides	Periodically	Possibly	Possibly
Radioactivity	Possibly	Possibly	Possibly

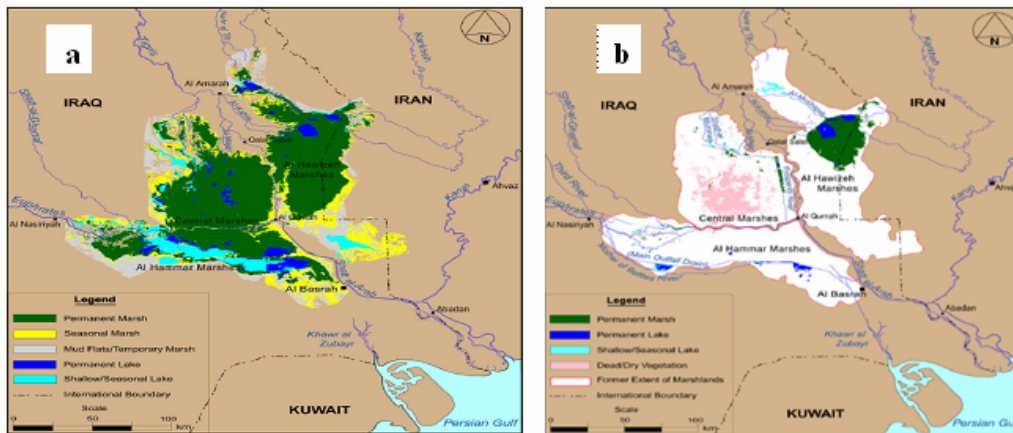


Fig.1 The Mesopotamian marshlands in Iraq, a: 1973-76, b: 2000 (After UNEP, 2001)

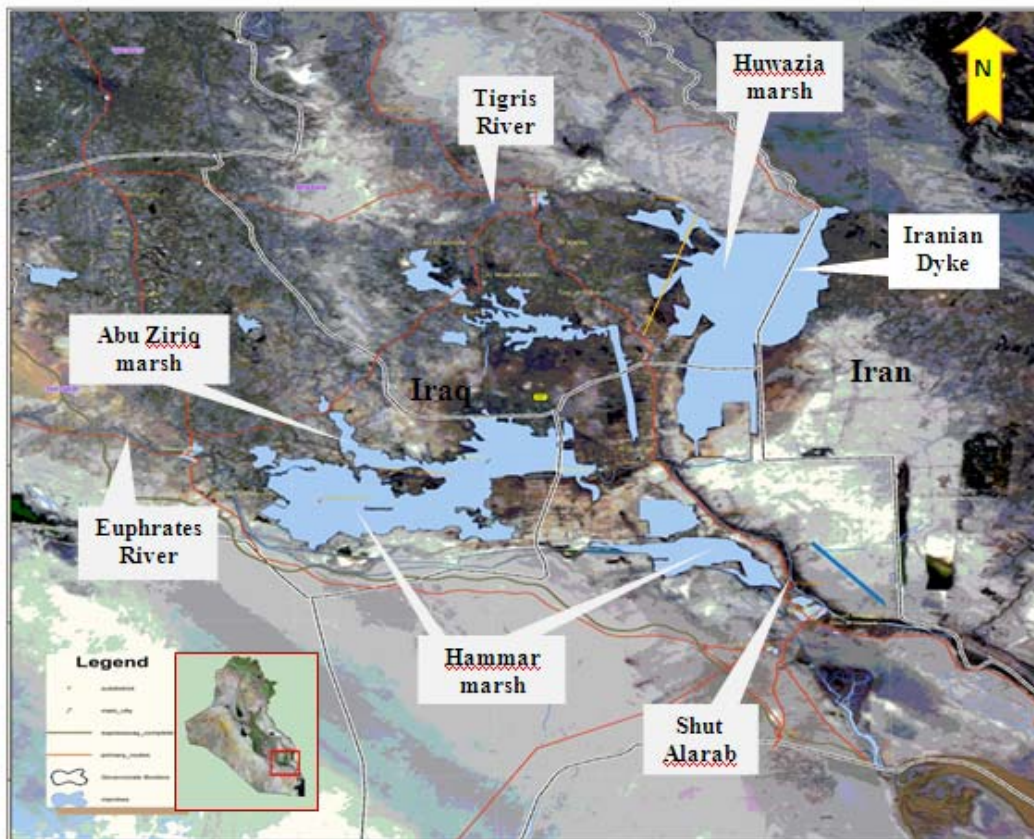


Fig.2 Iraqi marshland in 2007

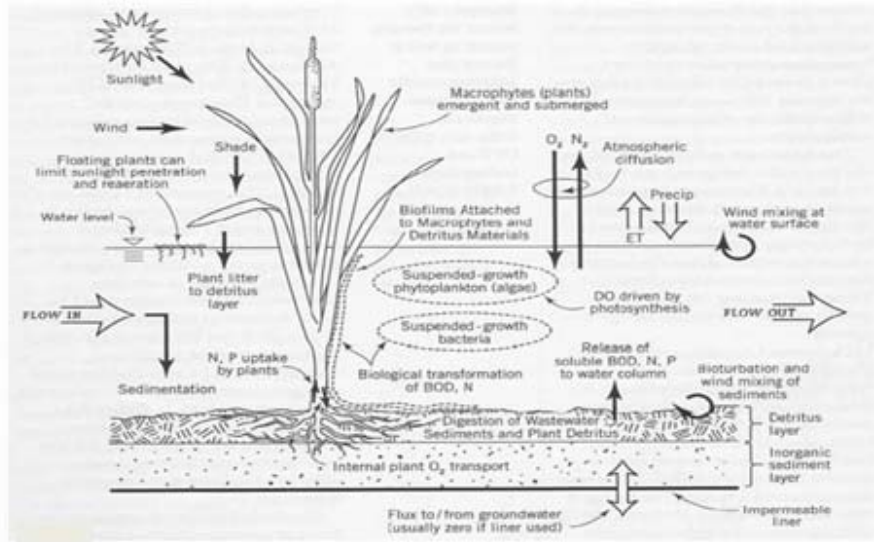


Fig.3 Major treatment processes in FWS marshes (After Wallace and Knight, 2006)

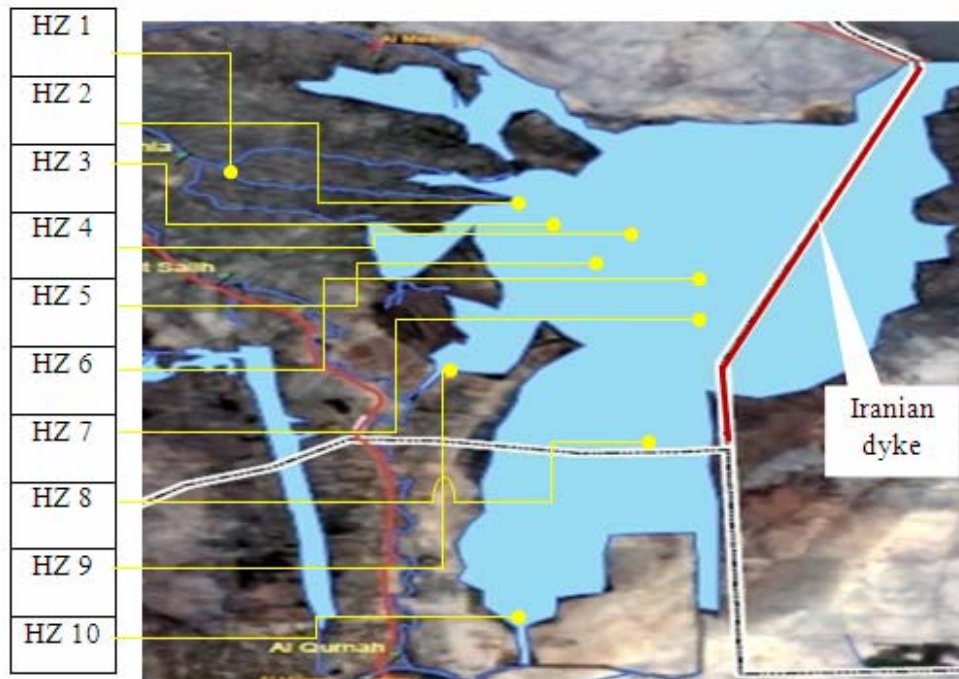


Fig.4 locations of water samples taken from Huwazia marsh

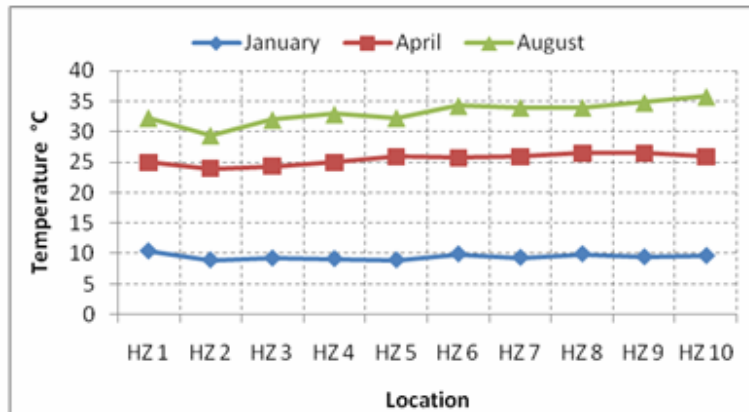


Fig.5 Variation of water temperature

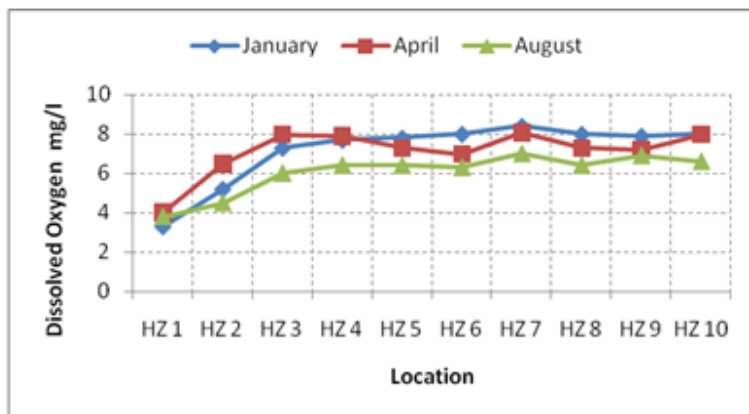


Fig.6 Variation of dissolved oxygen

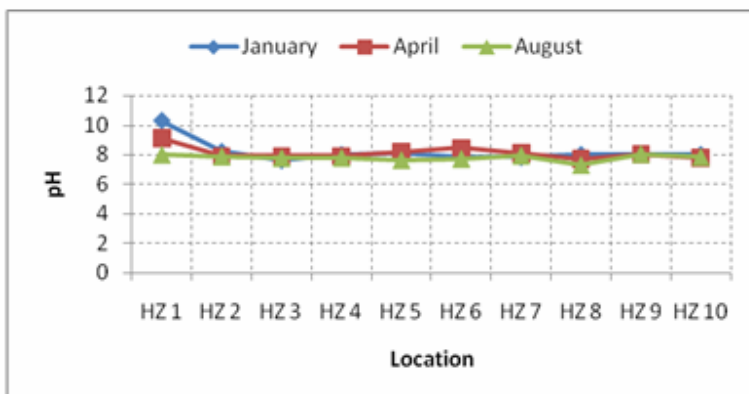


Fig.7 Variation of pH

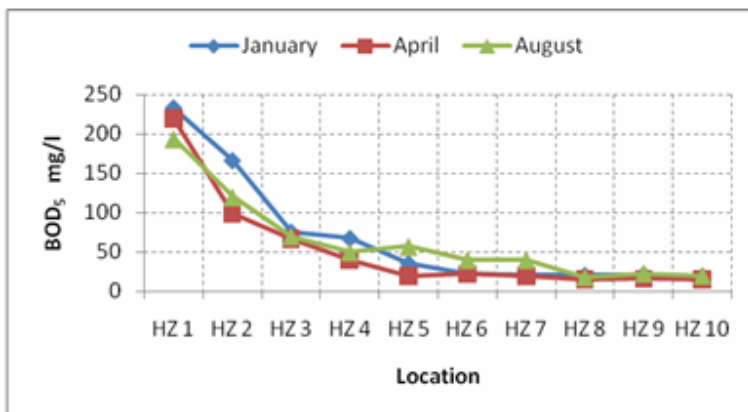


Fig.8 Variation of five-day biochemical oxygen demand

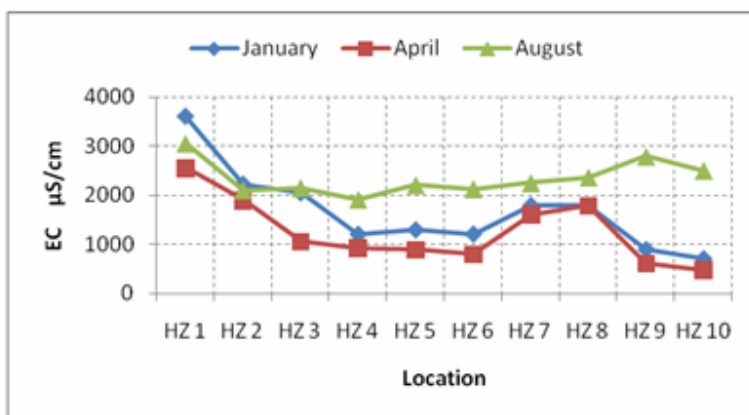


Fig.9 Variation of electrical conductivity

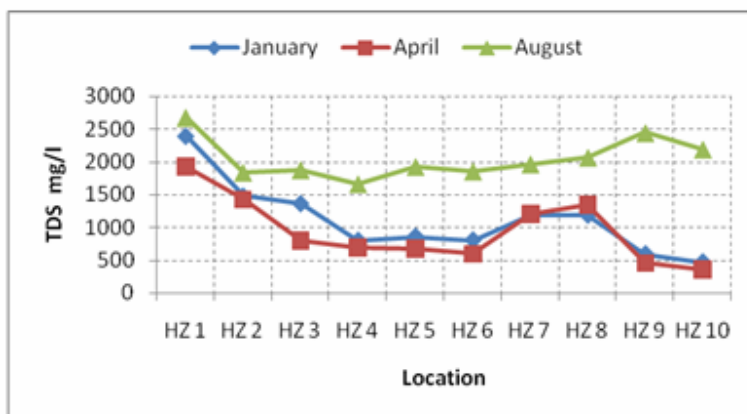


Fig.10 Variation of total dissolved solids

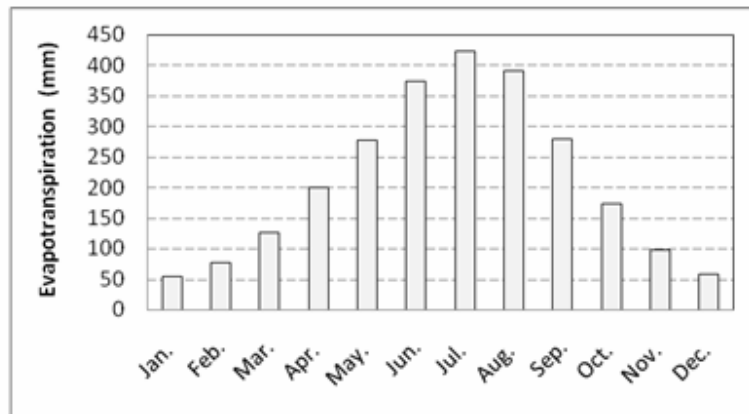


Fig.11 Monthly evapotranspiration losses in Huwaiza marsh

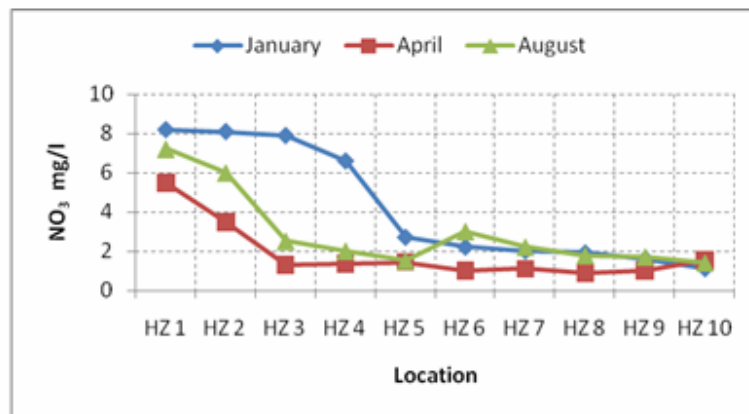


Fig.12 Variation of nitrate

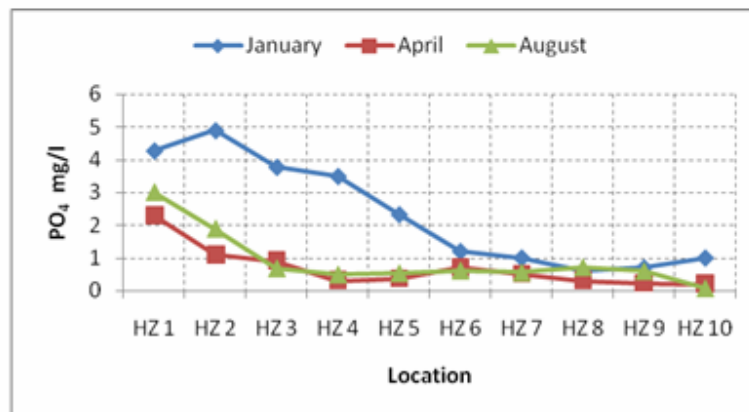


Fig.13 Variation of phosphate

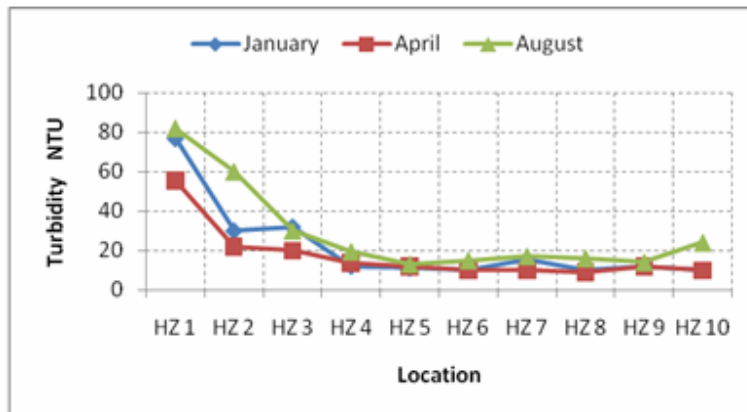


Fig.14 Variation of turbidity

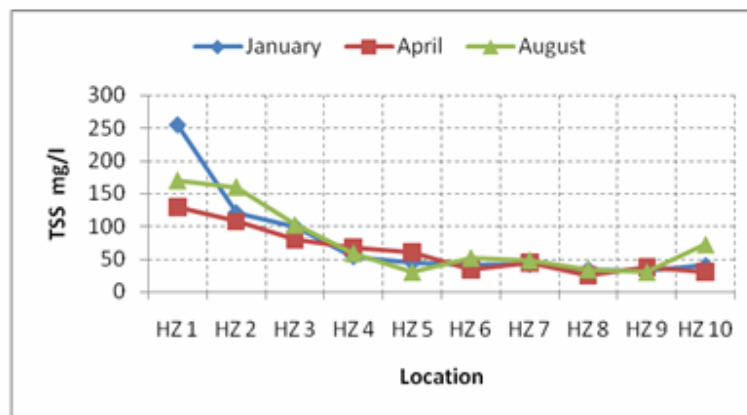


Fig.15 Variation of total suspended solids

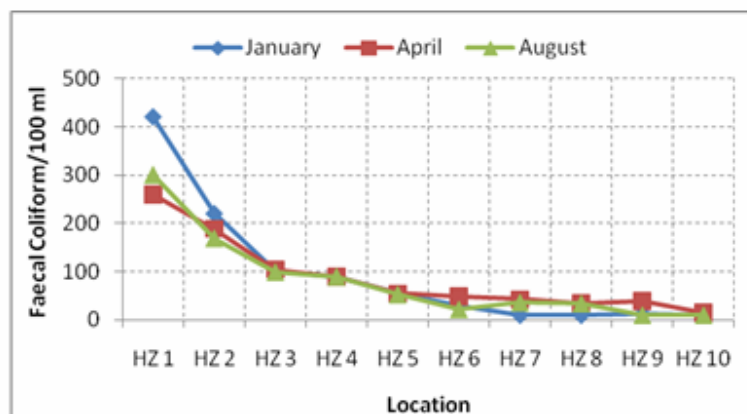


Fig.16 Variation of faecal coliform per 100ml water sample

DOUBLE DIFFUSIVE FREE CONVECTION IN A PACKED BED SQUARE ENCLOSURE BY USING LOCAL THERMAL NON-EQUILIBRIUM (LTNE) MODEL

Ahmed N. Mehdy
Assistant Lecturer
Department of Mechanical
Engineering
Engineering college

ABSTRACT

In the present study, free convection heat and mass transfer of fluid in a square packed bed enclosure is numerically investigated. For the considered geometrical shape, the left vertical wall of enclosure was assumed to be kept at high temperature and concentration while the opposite wall was kept at low temperature and concentration with insulating both the top and bottom walls of enclosure. The Brinkman–Forchheimer extended Darcy model was used to solve the momentum equations, while the energy equations for fluid and solid phases were solved by using the local thermal non-equilibrium (LTNE) model. Computations are performed for a range of the Darcy number from 10^{-5} to 10^{-1} , the porosity from 0.5 to 0.9 , and buoyancy ratio from -15 to 15 . The results showed that both the buoyancy ratio and the packed bed characteristics have significant effect on each one of the flow field, heat transfer and mass transfer.

الخلاصة

خلال الدراسة الحالية، انتقال الحرارة والكتلة بالحمل الحر خلال طبقات محشوة في تجويف مربع تم دراسته عددياً للنموذج الهندسي المقترض، تم اعتبار الجدار العمودي الأيسر للتجويف محفوظ عند درجة حرارة وتركيز مرتفعين بينما الجدار المقابل قد حُفظ عند درجة حرارة وتركيز واطنين مع عزل كل من الجدارين العلوي والسفلي. تم استخدام نموذج برنكمان-فورشمير المشتق من نموذج دارسي في حل معادلات الزخم، بينما تم حل معادلات الطاقة لكل من الطورين المائع والصلب باستخدام نموذج عدم الاتزان الحراري الموقعي (LTNE). لقد أنجزت الحسابات لمدى رقم دارسي من 10^{-5} إلى 10^{-1} ، المسامية من 0.5 إلى 0.9 ، ونسبة الطفو من -15 إلى 15 ، أظهرت النتائج بأن كلا من نسبة الطفو وخصائص الطبقات المحشوة تمتلكان تأثيراً مهماً على كل من حقل الجريان، انتقال الحرارة وانتقال الكتلة.

Keywords: Double Diffusive, Free Convection, Packed Bed, Local thermal non-equilibrium.

INTRODUCTION

Double-diffusive convection or thermosolutal convection is generally referred to a fluid flow generated by buoyancy effects due to both temperature and solutal concentration gradients. This type of flow is encountered in natural and technological applications. Such applications include the growth of crystals, solar energy systems, welding processes, thermal insulations.

The term double diffusive-convection is now widely accepted for all processes which involve simultaneous thermal and solutal concentration gradients and provides an explanation for a number of natural phenomena. Because of the coupling between the fluid velocity field and the diffusive (thermal and solutal concentration) fields, double-diffusive convection is more complex than the convection flow which is associated with a single diffusive scalar, and many different behaviours may be expected. Such double-diffusive processes occur in many fields, including chemical engineering (drying, cleaning operations, evaporations, condensation, sublimation, deposition of thin films, energy storage in solar ponds, roll-over in storage tanks containing liquefied natural gas, solution mining of salt caverns for crude oil storage, casting of metal alloys and photosynthesis), oceanography (melting and cooling near ice surfaces, sea water intrusion into freshwater lakes and the formation of layered or columnar structures during crystallisation of igneous intrusions in earth's crust), geophysics (dispersion of dissolvent materials or particulate matter in flows), etc. A clear understanding of the nature of the interaction between thermal and mass or solutal concentration

buoyancy forces is necessary in order to control these processes. **(Chaudhary and Jain, 2007)** studied the MHD flow past an infinite vertical oscillating plate through porous medium with the presence of free convection and mass transfer analytically by using Laplace-transform technique. **(Mohamed, 2009)** analyzed the double-diffusive convection-radiation interaction for the unsteady MHD flow over a semi-infinite vertical moving porous plate embedded in a porous medium in the presence of thermal & solutal diffusion and heat generation. A numerical study of the unsteady free convection and mass transfer flow of an electrically conducting fluid past an infinite vertical porous plate in the presence of a transverse magnetic field was presented by **(Shariful et. al. , 2005)**. **(Bukhari, 2003)** applied a linear stability analysis, using the spectral Chebyshev polynomial method, to obtain numerically the solution of a multi-layer system consisting of the finger convection onset in a fluid layer overlying a porous layer. **(Saha and Hossain, 2004)** studied numerically the laminar doubly diffusive free convection flows along an isothermal vertical finite plate immersed in a stable thermally stratified fluid by using an implicit finite difference method and local non-similarity method. **(Hajri et. al. , 2007)** presented a numerical simulation for the steady double-diffusive natural convection in a triangular cavity by using equal finite elements method. A numerical study was presented from **(Mamou et. al. , 2001)** for the unsteady double-diffusive convection in a two-dimensional horizontal confined enclosure by using the finite element technique. **(Masuda et. al. , 2002)** presented a numerical simulation by using finite differences

method for the unsteady two-dimensional double-diffusive convection in porous rectangular enclosure. After that, (Masuda et al., 2008) studied the peculiar oscillating convection which is observed when two-dimensional double-diffusive convection in porous medium is analyzed numerically. (Khanafer and Vafai, 2002) presented a numerical study of mixed-convection heat and mass transport in a lid-driven square enclosure filled with a non-Darcian fluid-saturated porous medium by using the finite volumes technique. (Rahli and Bouhadef, 2004) studied numerically the double-diffusive natural convection in a partially porous square enclosure with the presence of inclination effect by using the control volume method and the power law scheme. (Wang et al., 2007) presented a numerical investigation of natural convection of fluid (without mass transfer) in an inclined square enclosure filled with porous medium and submitted to a strong magnetic field by using (LTNE) model. However, the buoyancy force due to the double-diffusive effect has received more attention in the literature. But all the previous studies which deal with the double-diffusive convection in porous mediums assume that the porous medium in thermo dynamical equilibrium with the fluid which flow inside it, except (Wang et al., 2007) which studied the pure convection without mass transfer in the presence of heat transfer between the fluid and the porous media. The present study gives more attention to the interaction between the effect of the double-diffusive convection and the effect of heat transfer between the porous medium and the fluid which flows inside it.

MATHEMATICAL MODEL

Geometrical Shape of Studied Problem

The schematic view of the studied problem is shown in Fig.1. The square enclosure has a side length (a) and it is filled with a saturated packed bed. The left vertical wall of the square enclosure is kept at high temperature and concentration while the opposite wall is kept at low temperature and concentration, finally, the horizontal walls are insulated.

Governing Equations

In the model development, the following assumptions are adopted; the working fluid has a Prandtl number $Pr=0.71$ and assumed to be incompressible and Newtonian fluid, no phase change occurs and the process is in a steady state, the thermo physical properties of the fluid are assumed to be constant except the density variation in the buoyancy force, which is approximated according to the Boussinesq approximation. This variation, due to both temperature and solutal concentration gradients can be described as follow (Khanafer and Vafai, 2002);

$$\rho = \rho_0 [1 - \beta_T(T - T_L) - \beta_C(c - c_L)] \quad (1)$$

Where β_T and β_C are the coefficients of the thermal and solutal expansions, which are defined as follow (Khanafer and Vafai, 2002);

$$\beta_T = -\frac{1}{\rho_0} \left(\frac{\partial \rho}{\partial T} \right)_{p,c} \quad \& \quad (2)$$
$$\beta_C = -\frac{1}{\rho_0} \left(\frac{\partial \rho}{\partial c} \right)_{p,T}$$

The Brinkman–Forchheimer extended Darcy model is used to solve the momentum equations while the energy equations for fluid and solid phases are solved with the local thermal non-

equilibrium (LTNE) model. Thus, the governing equations for the present study will take the following forms as in (Amiri and Vafai, 1998) and (Khanafer and Vafai, 2002);

- Continuity equation

$$\frac{\partial u}{\partial x} + \frac{\partial v}{\partial y} = 0 \quad (3)$$

- Momentum equations

$$\frac{\rho_f}{\varepsilon^2} \left(u \frac{\partial u}{\partial x} + v \frac{\partial u}{\partial y} \right) =$$

$$\frac{\partial p}{\partial x} + \frac{\mu_f}{\varepsilon} \left(\frac{\partial^2 u}{\partial x^2} + \frac{\partial^2 u}{\partial y^2} \right) - \frac{\mu_f}{K} u + \frac{F \rho_f |\vec{u}| u}{\sqrt{K}}$$

$$\frac{\rho_f}{\varepsilon^2} \left(u \frac{\partial v}{\partial x} + v \frac{\partial v}{\partial y} \right) = - \frac{\partial p}{\partial y} + \frac{\mu_f}{\varepsilon} \left(\frac{\partial^2 v}{\partial x^2} + \frac{\partial^2 v}{\partial y^2} \right)$$

$$+ \rho_f g [\beta_T (T_f - T_L) + \beta_c (c - c_L)] - \frac{\mu_f}{K} v + \frac{F \rho_f |\vec{u}| v}{\sqrt{K}} \quad (4)$$

- Fluid phase energy equation

$$\rho_f c p_f \left(u \frac{\partial T_f}{\partial x} + v \frac{\partial T_f}{\partial y} \right) =$$

$$k_{eff} \left(\frac{\partial^2 T_f}{\partial x^2} + \frac{\partial^2 T_f}{\partial y^2} \right) + a_{sf} h_{sf} (T_s - T_f) \quad (5)$$

- Solid phase energy equation

$$k_{seff} \left(\frac{\partial^2 T_s}{\partial x^2} + \frac{\partial^2 T_s}{\partial y^2} \right) + a_{sf} h_{sf} (T_f - T_s) = 0 \quad (6)$$

- Solutal concentration equation

$$u \frac{\partial c}{\partial x} + v \frac{\partial c}{\partial y} = D \left(\frac{\partial^2 c}{\partial x^2} + \frac{\partial^2 c}{\partial y^2} \right) \quad (7)$$

The geometric function F , specific surface area of the packed bed a_{sf} and the fluid-to-solid heat transfer coefficient in a packed bed h_{sf} are determined as suggested by (Amiri and Vafai, 1998);

$$F = \frac{1.75}{\sqrt{150 \varepsilon^3}} \quad (9.a)$$

$$a_{sf} = \frac{6(1-\varepsilon)}{d_p} \quad (9.b)$$

$$h_{sf} = k_f \left[2 + 1.1 \text{Pr}^{1/3} \left(\frac{\rho_f |\vec{u}| d_p}{\mu_f} \right)^{0.6} \right] \quad (9.c)$$

where the sphere particle diameter d_p can be computed as follow (Amiri and Vafai, 1998);

$$d_p = (1 - \varepsilon) \sqrt{\frac{150 K}{\varepsilon^3}} \quad (9.d)$$

while the effective thermal conductivity k_{eff} and k_{seff} in fluid and solid phase energy equations and the mean thermal diffusivity α_m can be computed as follow (Wang et. al. , 2007);

$$k_{eff} = \varepsilon k_f \quad (10.a)$$

$$k_{seff} = (1 - \varepsilon) k_s \quad (10.b)$$

$$\alpha_m = \frac{k_{eff} + k_{seff}}{\rho_f c p_f} \quad (10.c)$$

Now we introduce the following non-dimensional quantities and parameters as in (Khanafer and Vafai, 2002) and (Wang et. al. , 2007);

$$\left. \begin{aligned} X &= \frac{x}{a}, & Y &= \frac{y}{a} \\ U &= \frac{au}{\alpha_m}, & V &= \frac{av}{\alpha_m}, \\ P &= \frac{pa^2}{\rho_f \alpha_m^2} \\ \theta_f &= \frac{(T_f - T_L)}{(T_H - T_L)}, \\ \theta_s &= \frac{(T_s - T_L)}{(T_H - T_L)}, \\ C &= \frac{(c - c_L)}{(c_H - c_L)} \end{aligned} \right\} \quad (11.a)$$

$$\left. \begin{aligned} \text{Pr} &= \frac{\mu_f c p_f}{k_{\text{feff}} + k_{\text{seff}}} = \frac{\nu_f}{\alpha_m} \\ \text{Gr}_T &= \frac{g a^3 \beta_T (T_H - T_L)}{\nu_f^2} \\ \text{Gr}_C &= \frac{g a^3 \beta_C (c_H - c_L)}{\nu_f^2} \\ Da &= \frac{K}{a^2}, & Sc &= \frac{\nu_f}{D} \\ N &= \frac{\beta_C (c_H - c_L)}{\beta_T (T_H - T_L)} = \frac{\text{Gr}_C}{\text{Gr}_T}, \\ \Lambda &= \frac{k_{\text{feff}}}{k_{\text{seff}}}, & \xi &= \frac{a_{sf} h_{sf} a^2}{k_{\text{feff}}} \end{aligned} \right\} \quad (11.b)$$

By substituting eqs.(11.a & 11.b) in eqs.(3, 4, 5, 6, 7 & 8), we get the dimensionless forms of governing equations as follow;

$$\frac{\partial U}{\partial X} + \frac{\partial V}{\partial Y} = 0 \quad (12)$$

$$\frac{1}{\varepsilon^2} \left(U \frac{\partial U}{\partial X} + V \frac{\partial U}{\partial Y} \right) - \frac{\partial P}{\partial X} + \frac{\text{Pr}}{\varepsilon} \left(\frac{\partial^2 U}{\partial X^2} + \frac{\partial^2 U}{\partial Y^2} \right) - \frac{\text{Pr}}{Da} U - \frac{F |\vec{U}| U}{\sqrt{Da}} \quad (13)$$

$$\frac{\text{Pr}}{Da} U - \frac{F |\vec{U}| U}{\sqrt{Da}}$$

$$\frac{1}{\varepsilon^2} \left(U \frac{\partial V}{\partial X} + V \frac{\partial V}{\partial Y} \right) = - \frac{\partial P}{\partial Y} + \frac{\text{Pr}}{\varepsilon} \left(\frac{\partial^2 V}{\partial X^2} + \frac{\partial^2 V}{\partial Y^2} \right) + \text{Pr}^2 \text{Gr}_T (\theta_f + N C) - \frac{\text{Pr}}{Da} V - \frac{F |\vec{U}| V}{\sqrt{Da}} \quad (14)$$

$$(1 + \Lambda^{-1}) \left(U \frac{\partial \theta_f}{\partial X} + V \frac{\partial \theta_f}{\partial Y} \right) = \left(\frac{\partial^2 \theta_f}{\partial X^2} + \frac{\partial^2 \theta_f}{\partial Y^2} \right) + \xi (\theta_s - \theta_f) \quad (15)$$

$$0 = \left(\frac{\partial^2 \theta_s}{\partial X^2} + \frac{\partial^2 \theta_s}{\partial Y^2} \right) + \Lambda \xi (\theta_f - \theta_s) \quad (16)$$

$$U \frac{\partial C}{\partial X} + V \frac{\partial C}{\partial Y} = \frac{\text{Pr}}{Sc} \left(\frac{\partial^2 C}{\partial X^2} + \frac{\partial^2 C}{\partial Y^2} \right) \quad (17)$$

By using the (stream function-vorticity) formulation we will reduce the dependent variables to only five variables by differentiating eq.(13) with respect to (Y) and differentiating eq.(14) with respect to (X), after that we subtract the first of the two resulted equations from the second to eliminate the pressure terms from the momentum equations, thus, eqs.(12, 13 & 14) will be transformed to the following equations;

$$\frac{\partial^2 \psi}{\partial X^2} + \frac{\partial^2 \psi}{\partial Y^2} = -\omega \quad (17)$$

$$U \frac{\partial \omega}{\partial X} + V \frac{\partial \omega}{\partial Y} = \varepsilon \text{Pr} \left(\frac{\partial^2 \omega}{\partial X^2} + \frac{\partial^2 \omega}{\partial Y^2} \right) \quad (18)$$

$$\left[\text{Pr}^2 \text{Gr}_T \left(\frac{\partial \theta_f}{\partial X} + N \frac{\partial C}{\partial X} \right) - \left(\frac{\text{Pr}}{Da} + \frac{F |\vec{U}|}{\sqrt{Da}} \right) \omega - \frac{F}{\sqrt{Da}} \left(V \frac{\partial \vec{U}}{\partial X} - U \frac{\partial \vec{U}}{\partial Y} \right) \right]$$

where ψ and ω are the (stream function & vorticity) respectively, and they are defined as follow;

$$U = \frac{\partial \psi}{\partial Y} \ \& \ V = - \frac{\partial \psi}{\partial X} \quad (19 .a)$$

$$\omega = \frac{\partial V}{\partial X} - \frac{\partial U}{\partial Y} \quad (19 .b)$$

After getting the final values of all dependent variables in the flow field, calculations will be made for local and mean Nusselt and Sherwood numbers, where the local Nusselt and Sherwood numbers at the hot wall can be found as in (Wang et. al. , 2007) and (Khanafer and Vafai, 2002);

$$Nu_l = \varepsilon \left(\frac{\partial \theta_f}{\partial X} \Big|_{x=0} + \Lambda^{-1} \frac{\partial \theta_s}{\partial X} \Big|_{x=0} \right) \quad (20.a)$$

$$Sh_l = \frac{\partial C}{\partial X} \Big|_{x=0} \quad (20 .b)$$

Boundary Conditions

The hydrodynamic boundary conditions for the present problem at all enclosure walls will obey to the non-slip condition, while the thermal and solutal boundary conditions are (the left side wall was kept at high temperature and solutal concentration, the right side wall was kept at low temperature and solutal concentration and finally each one of the top and bottom walls were kept insulated), thus the boundary conditions will be as follow;

$$\left. \begin{aligned} U = 0, V = 0, \theta_f = \theta_s = C = 1 \\ \text{at } X = 0; \\ U = 0, V = 0, \theta_f = \theta_s = C = 0 \\ \text{at } X = 1; \\ U = 0, V = 0, \frac{\partial \theta_f}{\partial Y} = \frac{\partial \theta_s}{\partial Y} = \frac{\partial C}{\partial Y} = 0 \\ \text{at } Y = 0 \& 1 \end{aligned} \right\} \quad (21)$$

NUMERICAL SOLUTION

The governing equations for ψ , ω , θ_f , θ_s & C can be written in a common form for the (convection-diffusion) problem as follow (Versteeg and Malalasekera, 1995);

$$\frac{\partial}{\partial X_i} (\rho u_i \Phi) = \frac{\partial}{\partial X_i} \left(\Gamma \frac{\partial \Phi}{\partial X_i} \right) + S \quad (22)$$

where the general scalar Φ stands for any one of the dependent variables under consideration, the diffusion coefficient Γ and the source term S in the cartesian form are listed below for each governing equation;

- Stream function equation

$$\Phi = \psi, \Gamma = 1, S = \omega \quad (23.a)$$

- Vorticity equation

$$\Phi = \omega, \Gamma = \varepsilon \text{Pr}, S = \left[\text{Pr}^2 Gr_T \left(\frac{\partial \theta_f}{\partial X} + N \frac{\partial C}{\partial X} \right) - \varepsilon^2 \left(\frac{\text{Pr}}{Da} + \frac{F|\vec{U}|}{\sqrt{Da}} \right) \omega - \frac{F}{\sqrt{Da}} \left(V \frac{\partial |\vec{U}|}{\partial X} - U \frac{\partial |\vec{U}|}{\partial Y} \right) \right] \quad (23.b)$$

- Fluid phase energy equation

$$\Phi = \theta_f, \Gamma = \frac{1}{1 + \Lambda^{-1}}, S = \frac{\xi(\theta_s - \theta_f)}{1 + \Lambda^{-1}} \quad (23.c)$$

- Solid phase energy equation

$$\Phi = \theta_s, \Gamma = 1, S = \Lambda \xi(\theta_f - \theta_s) \quad (23.d)$$

- Solutal concentration equation

$$\Phi = C, \Gamma = \frac{\text{Pr}}{Sc}, S = 0 \quad (23.e)$$

The numerical solution of the governing equations will be made according to the finite volume method to transform the governing equations from partial differential form to discrete algebraic form, this method is based on principle of dividing the flow field to a number of volume elements, each one of them is called (control volume), after that a discretization process (Versteeg and Malalasekera, 1995) was carried out by integrating eq.(22) (of the general conservation) over a control volume element, where this equation will be as follow;

$$a_p \Phi_p = a_E \Phi_E + a_W \Phi_W + a_N \Phi_N + a_S \Phi_S + S_u \quad (24)$$

where;

$$a_p = a_E + a_W + a_N + a_S - S_p \quad (25)$$

the source coefficients S_u and S_p represent the source terms of the discrete equation and their values for each governing equation are listed as follow;

- For the stream function equation

$$\left. \begin{aligned} S_u &= \omega \\ S_p &= 0 \end{aligned} \right\} \quad (26 . a)$$

- For the vorticity equation

$$\left. \begin{aligned} S_u &= \varepsilon^2 \left[\text{Pr}^2 Gr_T \left(\frac{\partial \theta_f}{\partial X} + N \frac{\partial C}{\partial X} \right) - \frac{F}{\sqrt{Da}} \left(V \frac{\partial |\vec{U}|}{\partial X} - U \frac{\partial |\vec{U}|}{\partial Y} \right) \right] \\ S_p &= -\varepsilon^2 \left(\frac{\text{Pr}}{Da} + \frac{F |\vec{U}|}{\sqrt{Da}} \right) \end{aligned} \right\} \quad (26.b)$$

- Fluid phase energy equation

$$\left. \begin{aligned} S_u &= \frac{\xi \theta_s}{1 + \Lambda^{-1}} \\ S_p &= - \frac{\xi}{1 + \Lambda^{-1}} \end{aligned} \right\} \quad (26 . c)$$

- Solid phase energy equation

$$\left. \begin{aligned} S_u &= \Lambda \xi \theta_f \\ S_p &= - \Lambda \xi \end{aligned} \right\} \quad (26 . d)$$

- Solutal concentration equation

$$\left. \begin{aligned} S_u &= 0 \\ S_p &= 0 \end{aligned} \right\} \quad (26 . e)$$

A computational program was written in Fortran-90 language to compute the values of the required variables, The discretized algebraic equations are solved by the tri-diagonal matrix algorithm (TDMA). The used mesh size is (60×60). Relaxation factors of about (0.7–0.9) are used for all dependent variables, Convergence was measured in terms of the maximum change in each variable during an iteration where the maximum change allowed for convergence check was 10^{-6} .

RESULTS AND DISCUSSION

All solution were carried out for solution of (Pr=0.71 & Sc=0.25) at $Gr_T = 10^5$, where the numerical code which is used in the present investigation has been carried out for number of simulations for a wide range of controlling parameters such as buoyancy ratio, Darcy number, and porosity of the packed bed. Figs.(2 - 9) show the effect of buoyancy ratio for different values of (-15≤N≤15) on the stream function, fluid phase temperature and solutal concentration contours respectively at $Da=10^{-1}$ and $\varepsilon=0.9$. Figs.[(2.a), (2.b) & (2.c)] represent these contours for the case of single diffusing effect at $N=0$, where there is only thermal diffusing without solutal diffusing. It is clear from the stream function contour at $N=0$ and as a result of the thermal buoyancy effect, the fluid at the left-hand side hot wall will be lighter than in other locations while the fluid at the right-hand side cold wall will be heavier than in other locations, so, the fluid particles move upward

along the hot wall while they move downward along the cold wall, and thus, the flow will take the direction of clockwise. The fluid phase temperature contour at $N=0$ indicates that the temperature levels will decrease gradually from the hot wall towards the cold wall, where the hot fluid rises up along the left-hand side hot wall and descends along the right-hand side cold wall because of the thermal buoyancy effect. Finally the solutal concentration contour at $N=0$ indicates that the solutal concentration will be maximum at the hot regions and decreases gradually with the decrease of the fluid phase temperature. After that, and with increasing the positive buoyancy ratio $N>0$ as shown in **Figs.(3, 4 & 5)** which represent the cases at $N=5, 10 & 15$, and as it is clear from these figures, the solutal buoyancy force which increases with the buoyancy ratio will cooperate with the thermal buoyancy and they'll drive the flow in the same direction to form a cooperated flow, where the stream function levels will increase with increasing in positive buoyancy ratio because of the increase of the total buoyancy force due to both the thermal and solutal diffusing, while as it is shown from the contours of fluid phase temperature, its distribution will keep on the same previous behavior, but the gradients will be stronger than them at $N=0$ and increase directly with increase of the buoyancy ratio, also a similar behavior to the fluid temperature distribution will appear in the contours of the solutal concentration, but their gradients will be relatively less than the gradients of the fluid phase contours because of the absence of internal transference sources as it is clear from **eq.(23.e)**. **Figs.(6, 7, 8, 9)** the cases of negative buoyancy ratio $N<0$, where the negative value of buoyancy ratio means that the value of solutal expansion coefficient β_C is negative too, and as it is clear from the density definition in **eq.(1)**, the

fluid density will increase with increase of the solutal concentration, and as a result, the flow begins to reverse its direction, So, the flow case at $N=-1$ as it is shown in **Figs.[(6.a), (6.b) & (6.c)]** represents a conversion point in the flow direction from clockwise to counterclockwise as it is shown from the stream function distribution at $N=-1$, where the clockwise main central vortex which formed at each of the previous cases of positive buoyancy ratio will divide into two main vortices in two opposite directions, also the distribution of both the fluid phase temperature and the solutal concentration at $N=-1$ will begin to change their directions and their gradient will be at the minimum levels at this case. With increasing the value of negative buoyancy ratio as it is shown in **Figs.[(7.a), (7.b) & (7.c)]** which represent the flow case at $N=-5$, the negative solutal buoyancy effect will be greater than the thermal buoyancy effect, and as a result of the total negative buoyancy effect, the fluid at the hot wall will be heavier than it in other locations while the fluid at the cold wall will be lighter than it in other locations, so, the fluid particles move downwards along the hot wall while they move upwards along the cold wall, and thus, the flow will take the direction of counterclockwise. The fluid phase temperature contour at $N=-5$ indicates that the temperature levels will decrease gradually from the hot wall towards the cold wall, where the hot fluid descends downwards along the hot wall and rises up along the cold wall because of the large negative effect of solutal buoyancy. Finally the solutal concentration contour at $N=-5$ indicates that the solutal concentration will be maximum at the hot regions and decreases gradually with the decrease of the fluid phase temperature. **Figs.(8 & 9)** represent the flow case at $N=-10 & -15$ respectively, and as it is clear that the levels of counterclockwise stream function will increase



with the increase of negative value of buoyancy ratio, while the fluid phase temperature and solutal concentration keep the same previous behaviours but their gradients increase with the increase of negative value of buoyancy ratio. **Figs.(10.a & 10.b)** indicate the variation of velocity components with buoyancy ratio at the intermediate vertical and horizontal locations respectively for $Da=10^{-1}$ and $\varepsilon=0.9$, where as it is shown in **Fig.(10.a)** the horizontal velocity component at the positive values of buoyancy ratio will direct to the right in top half of the enclosure while it will be in opposite direction in the bottom half of the enclosure because of the positive total buoyancy effect, while we'll note the conversion in flow direction nearly at $N=-1$ where the horizontal velocity begins to reverse its direction as it happens when the value of negative buoyancy ratio becomes $N<-1$, also as it is shown in **Fig.(10.b)**, the vertical velocity component at the positive values of buoyancy ratio will direct upwards in the left half of the enclosure while it will be in opposite direction in the right half of the enclosure because of the positive total buoyancy effect, where it begins to reverse its direction at the negative buoyancy ratios of $N<-1$. **Fig.(11)** represents the variation of local Nusselt number with buoyancy ratio at $Da=10^{-1}$ and $\varepsilon=0.9$, where it is clear that the value of local Nusselt number at $N\geq 0$ will be maximum at the bottom of the left-hand vertical wall and it descends gradually with rising to the wall top because the temperature gradient will be very strong at the bottom and it decreases gradually to the top, also it is clear the increasing in the local Nusselt number levels with the increase of positive buoyancy ratio, while the minimum levels of it will be at $N=-1$ because the temperature gradients were minimum at that buoyancy ratio value, also at $N<-1$ it is clear that

the value of local Nusselt number will be maximum at the top of the hot wall and it descends gradually with dropping down to the wall bottom because the temperature gradient will be very strong at the top and it decreases gradually to the bottom. **Fig.(12)** represents the variation of local Sherwood number with buoyancy ratio (which is analog to Nusselt number in heat transfer, where it gives an indication to the rate of mass transfer through the solution which happens by solutal concentration difference), where it is clear that the distribution of local Sherwood number will be similar to the distribution of local Nusselt number and for the same mentionable reasons previously. **Fig.(13)** explains the variation of the mean Nusselt number with buoyancy ratio for different values of Darcy number at $\varepsilon=0.9$, generally it is clear that the minimum rate of heat transfer is at $N=-1$ because of the minimum temperature gradients at that case, after that, heat transfer levels begin to increase with the increase of each one of positive or negative buoyancy ratios, also it is clear that the values of Nusselt number will be lower than them at the same values of positive buoyancy ratio because the thermal and solutal buoyancy effects at negative buoyancy ratios will be in opposite direction while they in same direction at positive buoyancy ratios to form (assisting flow), and finally it was noted that the mean Nusselt number generally increases with Darcy number increase because of the decreasing in overall bed resistance to the flow inside it as a result to the increasing in the volume of passable paths of fluid through the packed bed. **Fig.(14)** explains the variation of the mean Nusselt number with buoyancy ratio for different values of porosity at $Da=10^{-1}$, where it was noted that when porosity equals to a value in the range of ($\varepsilon=0.5\sim 0.8$), the values of mean

Nusselt number will increase gradually with the increase of porosity in that range, but when the porosity increases above that range, the values of mean Nusselt number will decrease, and for explaining this phenomenon clearly we must return to **Eq.(20.a)**, where it is noted that the whole value of local Nusselt number is multiplicand by the porosity while the second term in this equation (solid phase term) was multiplicand by the inverse of dimensionless thermal conductivity Λ^{-1} which decreases with the increase of porosity $[\Lambda^{-1} = (1 - \varepsilon) k_s / \varepsilon k_f]$, so, when the porosity values equal to or less than **(0.8)**, the value of Nusselt number will increase, while it decreases after that value of porosity because the value of dimensionless thermal conductivity will be very small and it causes decreasing in Nusselt number more than the increasing in it because of porosity. **Fig.(15)** shows the variation of the mean Sherwood number with buoyancy ratio for different values of Darcy number at $\varepsilon=0.9$, where Sherwood number will comport a similar behavior to Nusselt number variation with buoyancy ratio and Darcy number and for the same mentionable reason previously, while **Fig.(16)** explains the variation of the mean Sherwood number with buoyancy ratio for different values of porosity at $Da=10^{-1}$, where it is clear that the values of Sherwood number will increase with increase of packed bed porosity because the flow levels will increase as a result of decreasing in the occupied volume by the bed through enclosure, where the overall packed bed resistance to the flow will decrease. To exhibit the reliability of the presented results, the variation of mean Nusselt number with the buoyancy ratio at $Gr_T \approx 1.4 \times 10^5$ was compared with results of **(Rahli and Bouhadef, 2004)** as it is shown in **Fig.(17)**, where it is clear the

similarity in Nusselt number behavior with the mentionable study, but there is a small difference between these values because of the using of (LTNE) model in the present study which causes more heat transfer due to both the fluid and solid phases.

CONCLUSIONS

This paper has presented a numerical investigation of double-diffusive flow in a packed bed square enclosure by using local thermal non-equilibrium (LTNE) model, and from the obtained results, the following conclusions are drawn;

- 1- At the positive buoyancy ratios $N \geq 0$, the flow takes the clock wise direction, while at $N = -1$ the flow begins to reverse its direction as it happens at $N < -1$.
- 2- Generally, levels of flow, heat transfer and mass transfer increase with the increase of both the positive or negative buoyancy ratio as a result of increasing in the total buoyancy effects.
- 3- The values of Nusselt number increase with increase of Darcy Number.
- 4- The values of Nusselt number increase with increase of porosity until the porosity reaches a certain value of about ($\varepsilon \approx 0.8$) where the value of mean Nusselt number will decrease after that value of porosity.
- 5- The values of Sherwood number increase with increase of both Darcy Number and the porosity.

REFERENCES

- A. Amiri and K. Vafai, Transient analysis of incompressible flow through a packed bed, International Journal of Heat and Mass Transfer, 41, 4259-4279, 1998.



A. K. Bukhari, Double diffusive convection in a horizontal porous layer superposed by a fluid layer, Umm Al-Qura Univ. J. Sci. Med. Eng. Vol. 15, No. 2, pp. 95-113, 2003.

I. Hajri*, A. Omri and S. Ben Nasrallah, A numerical model for the simulation of double-diffusive natural convection in a triangular cavity using equal order and control volume based on the finite elements method, Desalination 206, 579-588, 2007.

K. Khanafer and K. Vafai, Double-diffusive mixed convection in a lid-driven enclosure filled with a fluid saturated porous medium, Numerical Heat Transfer, Part A, 42: 465-486, 2002.

M. Mamou, P. Vasseur and M. Hasnaoui, On numerical stability analysis of double-diffusive convection in confined enclosures, J. Fluid Mech., vol. 433, pp. 209-250, 2001.

Md. Shariful Alam, M. M. Rahman and Md. Abdul Maleque, Local similarity solutions for unsteady MHD free convection and mass transfer flow past an impulsively started vertical porous plate with Dufour and Soret effects, Thammasat Int. J. Sc. Tech., Vol. 10, No. 3, July-Sept., 2005.

O. Rahli and K. Bouhadeb *, Double-diffusive natural convection in a partially porous square enclosure; effect of the inclination, Laboratoire LTPMP, Faculté de Génie Mécanique et Génie des Procédés, USTHB, Alger – Algérie, 2004.

Q. W. Wang*, M. Zeng, Z. P. Huang, G. Wang, H. Ozoe, Numerical investigation of natural convection in an inclined enclosure filled with porous medium under magnetic field,

International Journal of Heat and Mass Transfer 50, 3684-3689, 2007.

R. A. Mohamed, Double-diffusive convection-radiation interaction on unsteady MHD flow over a vertical moving porous plate with heat generation and Soret effects, Applied Mathematical Sciences, Vol. 3, no. 13, 629 - 651, 2009.

R. C. Chaudhary and Arpita Jain, Combined heat and mass transfer effects on MHD free convection flow past an oscillating plate embedded in porous medium, Rom. Journ. Phys., Vol. 52, Nos. 5-7, P. 505-524, Bucharest, 2007.

S.C. Saha, M.A. Hossain, Natural convection flow with combined buoyancy effects due to thermal and mass diffusion in a thermally stratified media, Nonlinear Analysis: Modelling and Control, Vol. 9, No. 1, 89-102, 2004.

Versteeg H. K. and Malalasekera W., An introduction to computational fluid dynamics the finite volumes method, Longman Group Ltd, 1995.

Y. Masuda, M. Yonaya, T. Ikeshoji, S. Kimura, F. Alavyoon, T. Tsukada, M. Hozawa, Oscillatory double-diffusive convection in a porous enclosure due to opposing heat and mass fluxes on the vertical walls, International Journal of Heat and Mass Transfer 45, 1365-1369, 2002.

Yoshio Masuda, Michio Yoneya, Akira Suzuki, Shigeo Kimura and Farid Alavyoon, Numerical analysis of double-diffusive convection in a porous enclosure due to opposing heat and mass fluxes on the vertical walls -Why does peculiar oscillation occur?-, Research Center for Compact chemical Process, National Institute of Advanced Industrial Science and Technology, 4-

2-1 Nigatake, Miyagino-ku, Sendai 983-8551, Japan, 2008.

Nomenclature

- a side length of the enclosure (m)
- a_{sf} specific surface area of the packed bed (m^{-1})
- C dimensionless solutal concentration
- c solutal concentration ($kmol\ m^{-3}$)
- cp specific heat at constant pressure ($J\ kg^{-1}\ K^{-1}$)
- D concentration diffusion coefficient ($m^2\ s^{-1}$)
- Da Darcy number
- d_p sphere particle diameter (m)
- F geometric function
- Gr_C solutal Grashof number
- Gr_T Grashof number
- g gravitational acceleration ($m\ s^{-2}$)
- h_{sf} solid-fluid heat transfer coefficient ($Wm^{-2}K^{-1}$)
- k thermal conductivity ($W\ m^{-1}\ K^{-1}$)
- K permeability (m^2)
- N buoyancy ratio
- Nu Nusselt number
- p pressure (Pa)
- P dimensionless pressure
- Pr Prandtl number
- Sc Schmidt number
- Sh Sherwood number
- T temperature (K°)
- u, v velocity components ($m\ s^{-1}$)
- U, V dimensionless velocity components
- x, y x-, y-coordinates (m)
- X, Y dimensionless coordinates

Greek symbols

- α thermal diffusivity ($m^2\ s^{-1}$)
- μ dynamic viscosity ($kg\ m^{-1}\ s^{-1}$)
- ν kinematic viscosity ($m^2\ s^{-1}$)
- ρ density ($kg\ m^{-3}$)
- β_T thermal expansion coefficient (K^{-1})
- β_C solutal expansion coefficient ($kmol^{-1}\ m^3$)
- θ dimensionless temperature
- ψ dimensionless stream function
- ω dimensionless vorticity
- Φ general scalar dependent variable
- Γ diffusion coefficient
- ε porosity
- Λ dimensionless thermal conductivity
- ξ dimensionless solid-to-fluid heat transfer coefficient

Subscripts

- f fluid
- $feff$ effective properties for fluid
- H high
- i axis indication
- L low
- l local value
- m mean value
- s solid
- $seff$ effective properties for solid

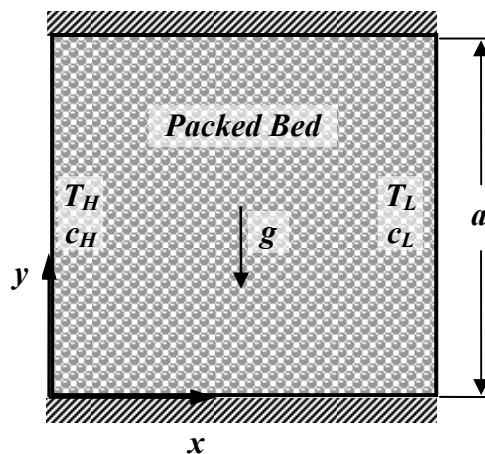


Fig.(1) schematic diagram of the physical system

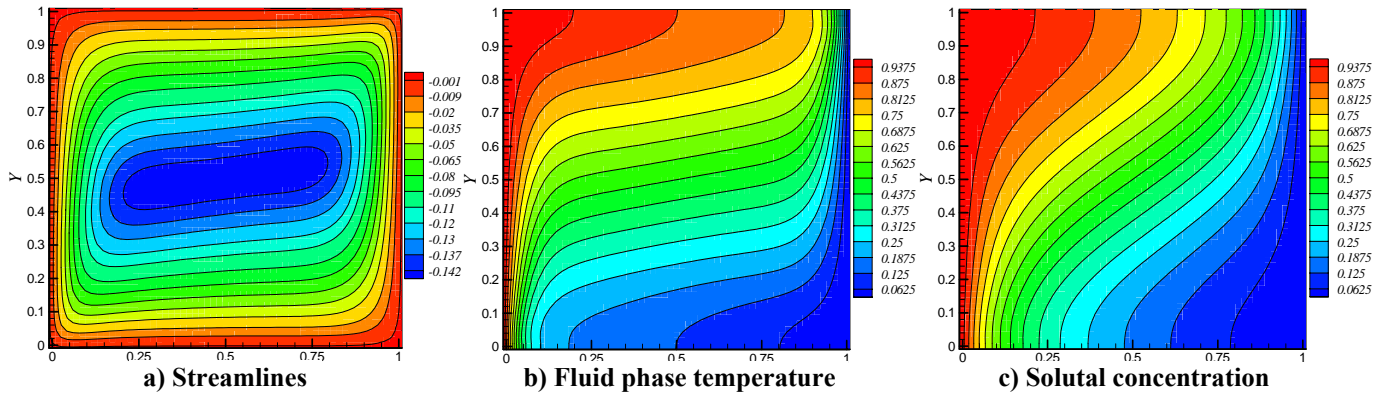


Fig. (2) Properties distribution at; $N=0, Da=1 \times 10^{-1}$ & $\epsilon=0.9$

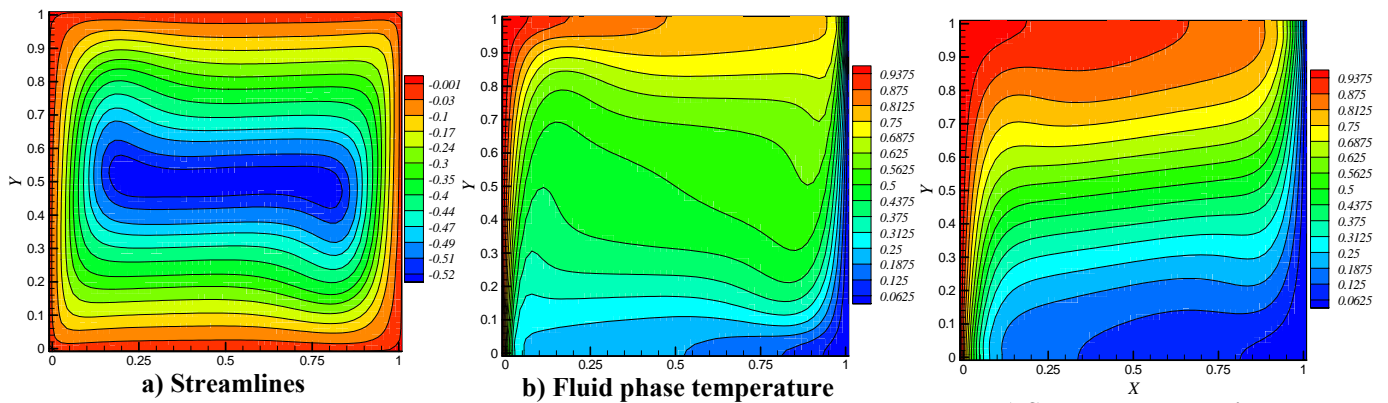


Fig. (3) Properties distribution at; $N=5, Da=1 \times 10^{-1}$ & $\epsilon=0.9$

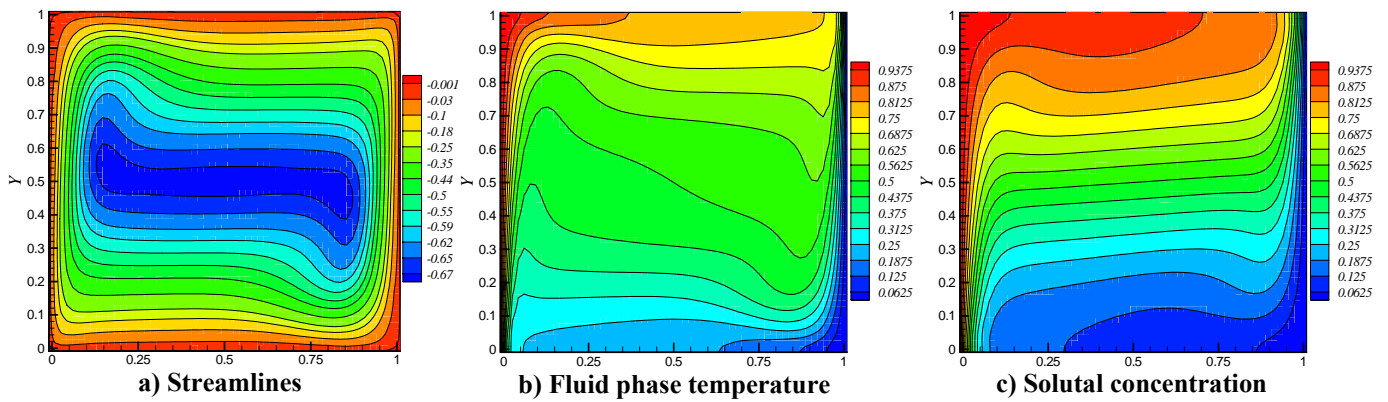


Fig. (4) Properties distribution at; $N=10, Da=1 \times 10^{-1}$ & $\epsilon=0.9$

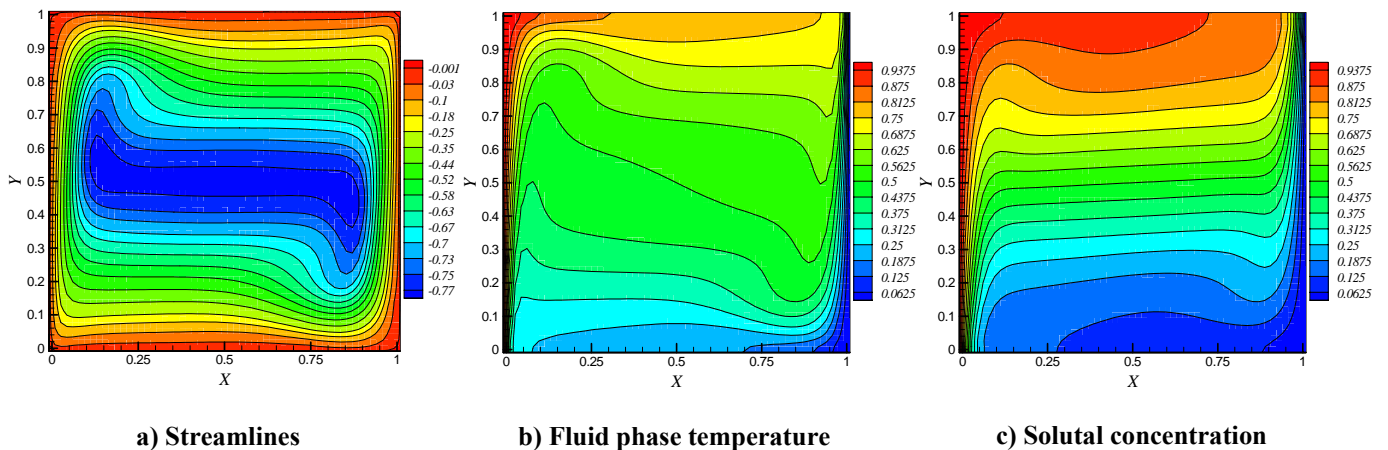


Fig. (5) Properties distribution at; $N=15, Da=1 \times 10^{-1}$ & $\epsilon=0.9$

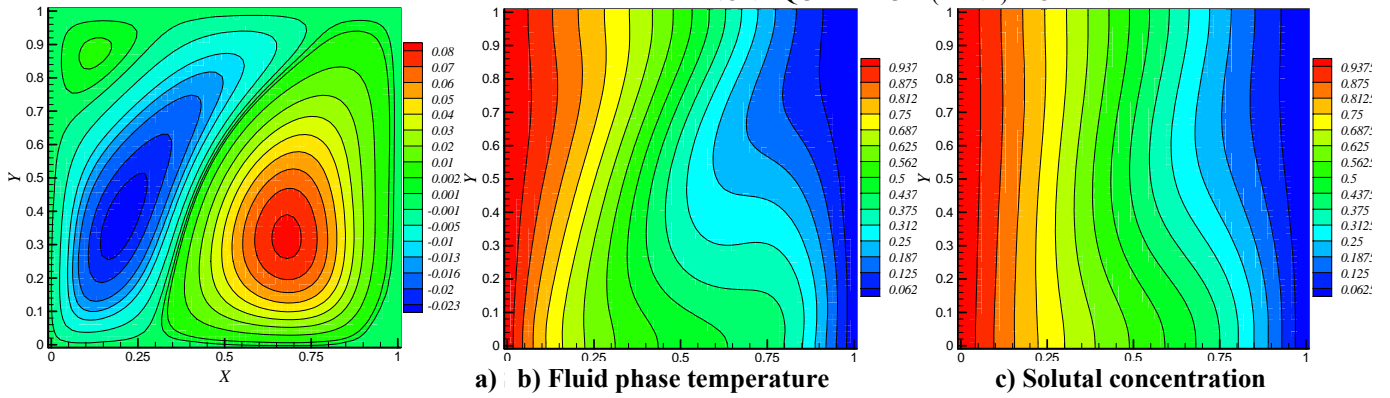


Fig. (6) Properties distribution at; $N=-1, Da=1 \times 10^{-1}$ & $\epsilon=0.9$

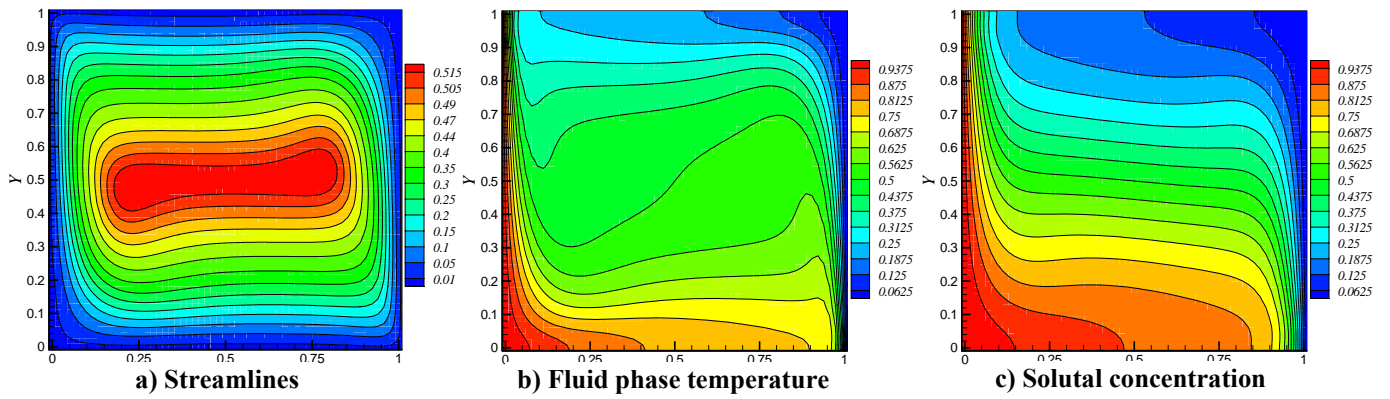


Fig. (7) Properties distribution at; $N=-5, Da=1 \times 10^{-1}$ & $\epsilon=0.9$

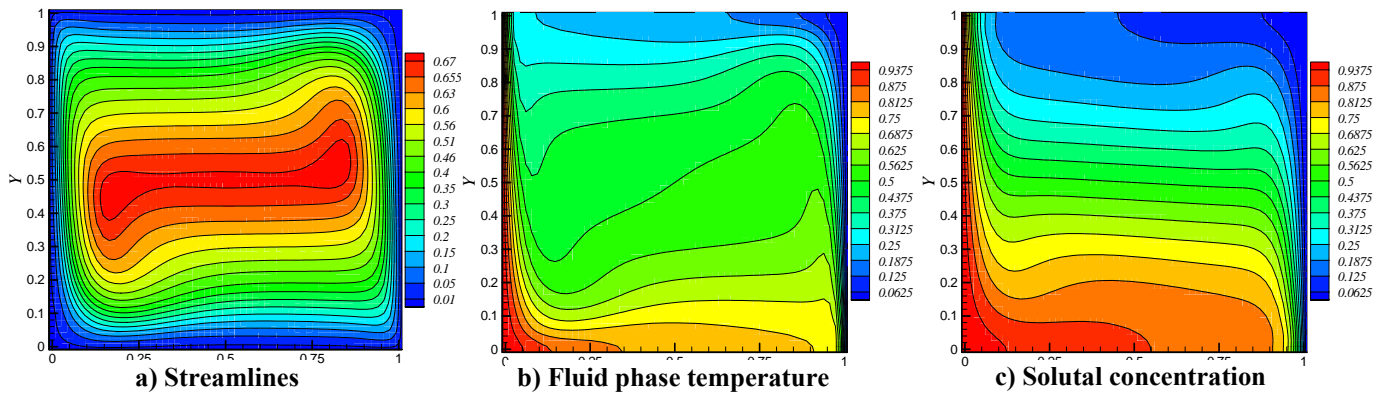


Fig. (8) Properties distribution at; $N=-10, Da=1 \times 10^{-1}$ & $\epsilon=0.9$

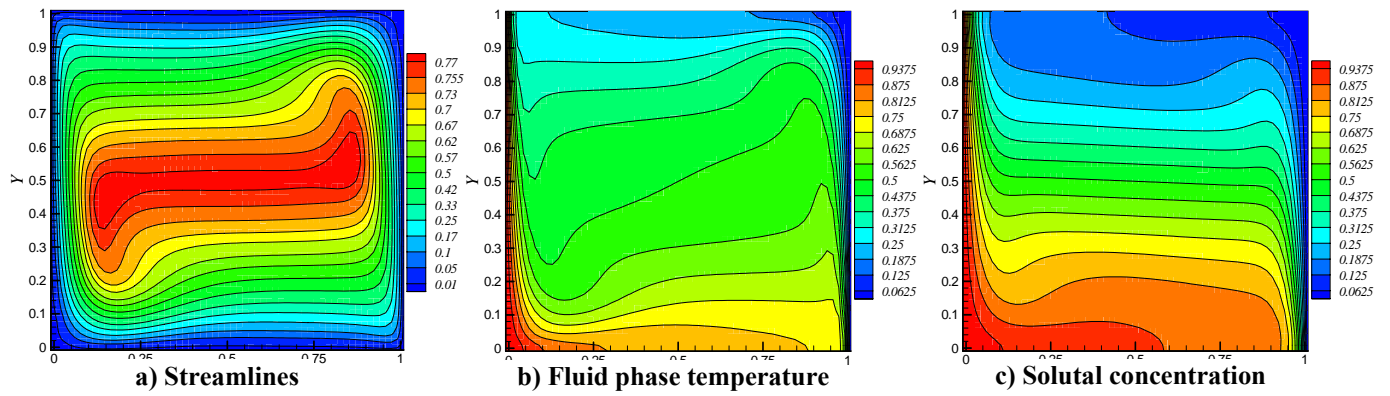


Fig. (9) Properties distribution at; $N=-15, Da=1 \times 10^{-1}$ & $\epsilon=0.9$

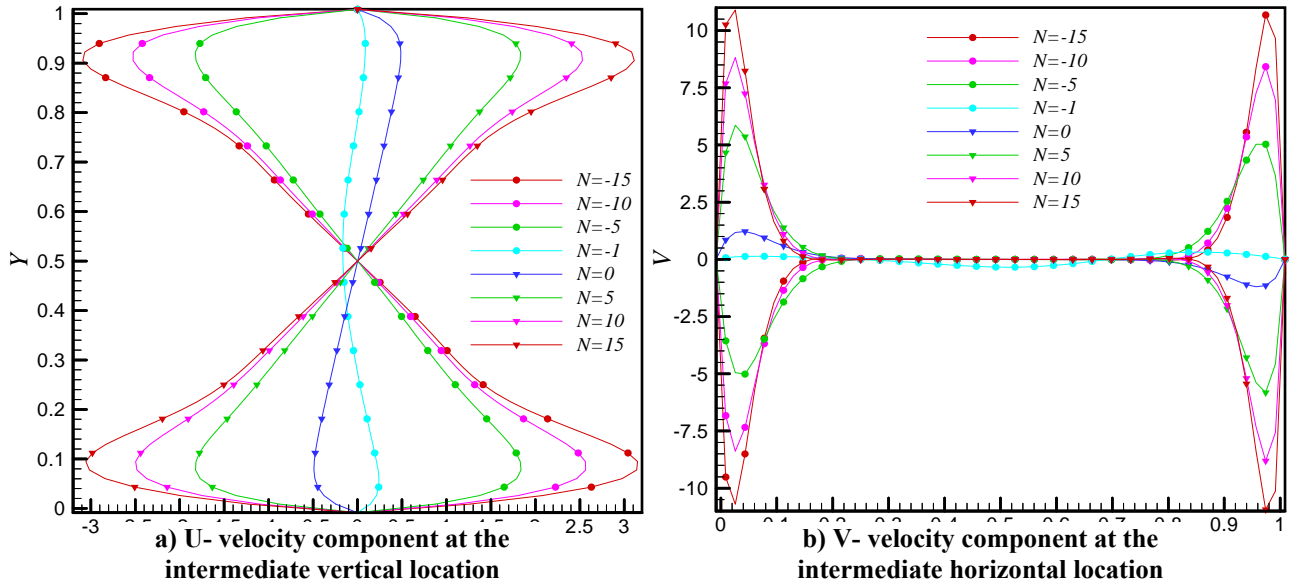


Fig. (10) Variation of velocity components with buoyancy ratio at the intermediate vertical and horizontal locations for $Da=1 \times 10^{-1}$ & $\epsilon=0.9$

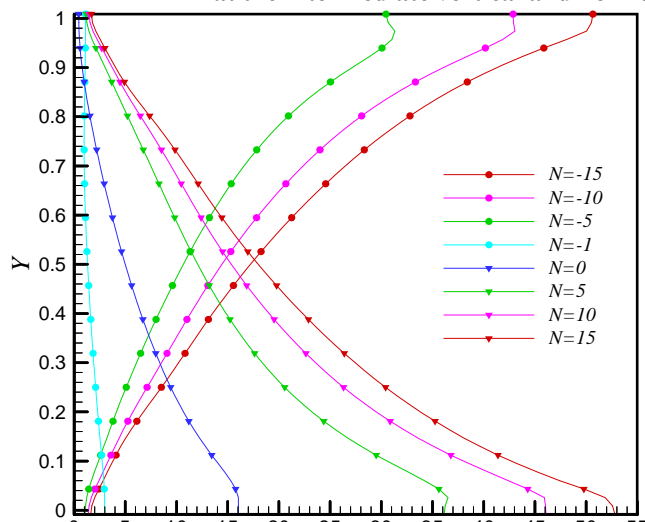


Fig. (11) Variation of local Nusselt number with buoyancy ratio at $\epsilon=0.9$ & $Da=1 \times 10^{-1}$

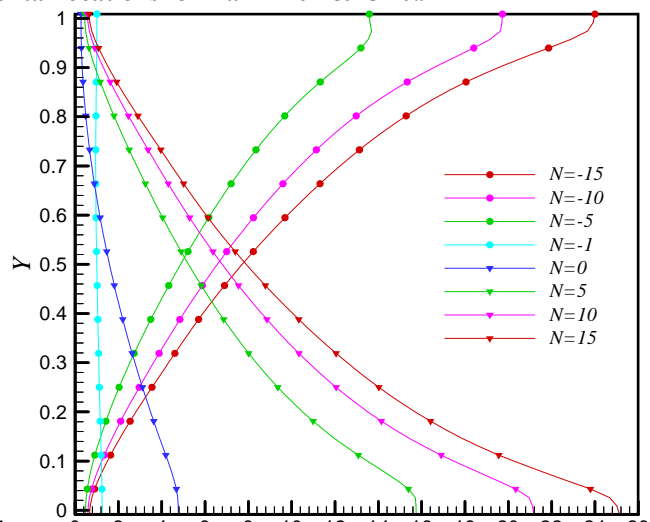


Fig. (12) Variation of local Sherwood number with buoyancy ratio at $\epsilon=0.9$ & $Da=1 \times 10^{-1}$

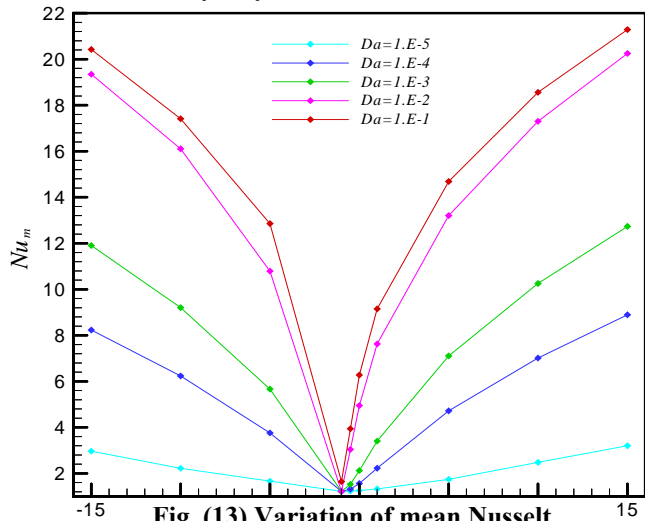


Fig. (13) Variation of mean Nusselt number with Darcy number at $\epsilon=0.9$

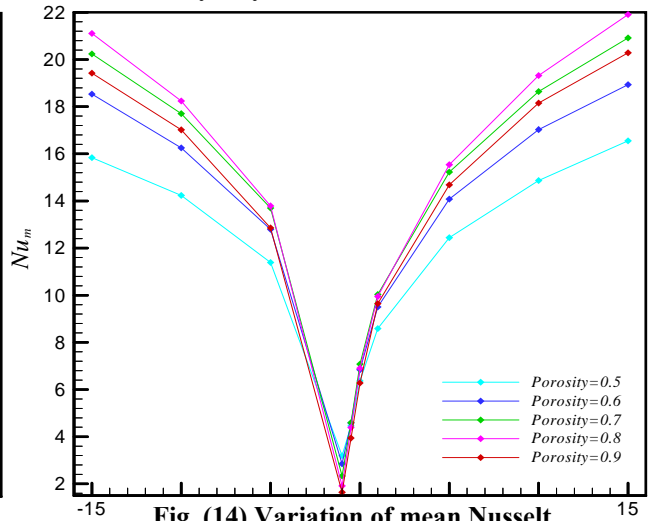


Fig. (14) Variation of mean Nusselt number with porosity at $Da=1.E-1$

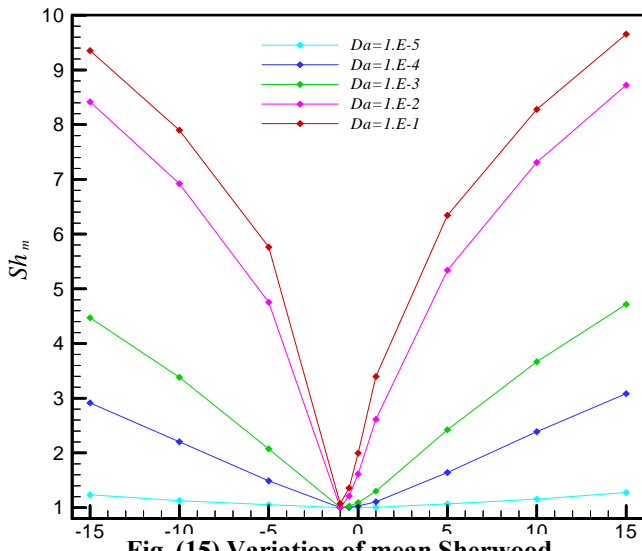


Fig. (15) Variation of mean Sherwood number with Darcy number at $\epsilon=0.9$

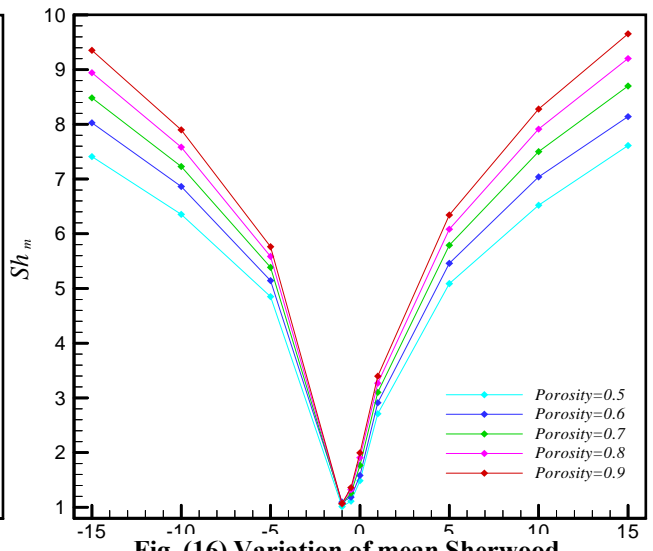


Fig. (16) Variation of mean Sherwood number with porosity at $Da=1.E-1$

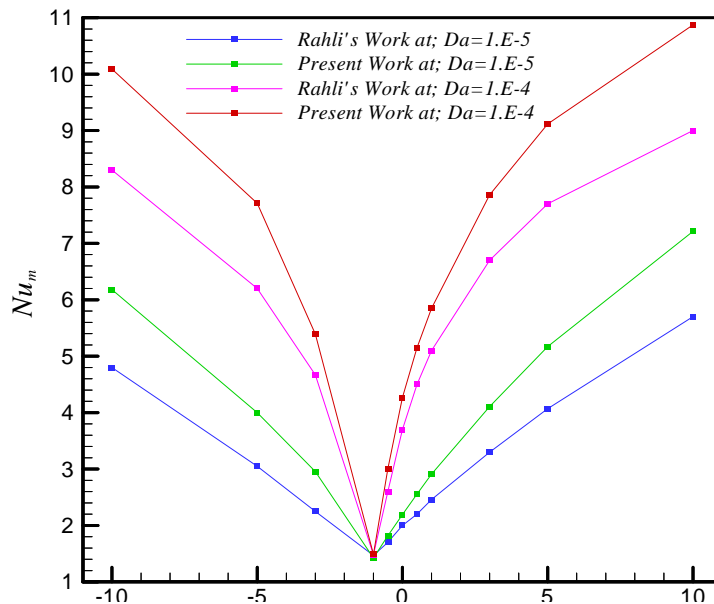


Fig. (17) Comparison the variation of mean Nusselt number with buoyancy ratio at $Gr_T \approx 1.4 \times 10^5$ with the work of (Rahli and Bouhadeb, (2004)

EXPERIMENTAL AND NUMERICAL STUDY OF FRICTION STIR SPOT WELDING FOR 2024 ALUMINUM PLATES

Asst. Lec. Ammar I. Saleh
Mechanical Engineering Department
Nahrain University
Baghdad-Iraq

ABSTRACT

Friction stir spot welding (FSSW) is a relatively new welding process that may have significant advantages compared to the fusion processes as follows joining of conventionally non-fusion weldable alloys, reduced distortion and improved mechanical properties of weldable alloys joints due to the pure solid-state joining of metals. In this paper, a three-dimensional model based on finite element analysis is used to study the thermal history in the spot-welding of aluminum alloy 2024. The model take place the thermomechanical property on the process of the welded metals.

The thermal history and the evolution results with numerical model at the measured point in the friction stirred spot weld have a good matching, then the prediction of the temperature history from the numerical model in the welded plates is acceptable.

The experimental results of measuring the shear force of the welded plates show that there is a good agreement with the increase of the rotational speed of the tool with shear force.

الخلاصة

اللحام النقطي بالخالط و الاحتكاك من طرق اللحام الحديثة نسبيا والتي تمتاز عن غيرها من طرق اللحام الانصهاري بالاتي: إمكانية لحام السبائك الغير قابلة للحام الانصهاري، تقليل التشوه وتغير المواصفات الميكانيكية للسبائك الملحومة لأنها تعتبر من طرق الربط بالحالة الصلبة للمعادن. في هذا البحث تم إنشاء نموذج ثلاثي الأبعاد بطريقة العناصر المحددة لغرض دراسة السلوك في تغيير درجة الحرارة في القطعة الملحومة باللحام النقطي لسبيكة الألمنيوم 2024. النموذج اخذ بنظر الاعتبار تأثير الخواص الميكانيكية الحرارية في عملية اللحام على المعادن الملحومة.

تم الحصول على نتائج متقاربة بين القياس العملي لدرجة الحرارة في نقطة مع النتائج المستحصلة من النموذج الحسابي، لذا يمكن القبول بنتائج سلوك تغيير درجة الحرارة المتوقعة من قبل النموذج الحسابي. النتائج العملية لقياس قوة القص للحام أظهرت أن هناك توافق جيد مع زيادة السرعة الدورانية لعدة اللحام مع قوة القص.

KEYWORDS: Friction stir spot welding, Numerical simulation, ANSYS program, Aluminum 2024.

INTRODUCTION

Friction stir welding (FSW) is a solid-state welding process invented out at TWI (Cambridge, United Kingdom) in 1991 [Ayad M. Takahakh 2010]. Friction stir welding (FSW) is a solid state joining process, which is particularly adapted for difficult to weld high strength aluminum alloys (e.g. the 2XXX and 7XXX series). [Thomas W.M., et al. 1991] from The Welding Institute, TWI, patented the FSW process. A hard cylindrical tool with a

threaded pin and a shoulder rotates and slowly plunges into the joint line between two workpieces butted together. Friction and stirring generate heat dissipation so that the metal pieces do not reach their melting point. The material is plastically deformed and transferred from the leading edge to the trailing edge of the tool, leaving a solid phase bond between the two pieces when the tool is moved along the joint line [D. Jacquina, et al. 2011]. Friction Stir Spot Welding (FSSW) is a process developed recently and has been studied for applications in automotive, aeronautic and

other industries. This welding technology is quite similar to Friction Stir Welding process (FSW), and the main difference is the type of joint. In FSSW, the plates form a lap-joint and the tool penetrates the plates only in a point. In the FSW process the plates are positioned in a butt-joint configuration and the tool moves towards the joint direction [Malafaia, A. M. S., et al., 2010].

EXPERIMENTAL WORK

Lap shear specimens clamped with fixture as shown in fig.1, and friction stir spot welding were prepared using 2024 alloy, 100x25x3.8 mm plates and 30x25 mm overlap. The welding process was performed in a CNC milling machine fig.1 with difference rotation speed 700 and 900 rpm at constant preheating time, plunging time, stirring time and depth as shown in table 1. To carry out the FSSW process two aluminum plates were placed overlap on flat steel plate. These two plates were then clamped with special clamps so they would not separate during welding process, a thermocouple was fixed by hand during the welding process to measure the temperature in the point at the end of the lap plates shown in fig.1.

A 25 mm in diameter flat tool with a pin of 7 mm length and 5 mm in diameter were employed. The material used was special tool steel X38 Cr MoV 51 (DIN 1.2343).

The ANSYS is a package program that uses finite element method to calculate the numerical solution of complex problems whose analytical solution is tedious or not easy to achieve. The FSSW model depend on the assumptions that used to get the required results, the assumptions are

1- The element that is used in the analysis is three dimensional, 8 nodes, has a temperature as a degree of freedom and accepts the convection, conduction as a load in each face and heat generation on the volume of the element.

2- The plate metal has the following material properties (thermal conductivity, specific heat and density) which have different values with temperature as shown in table 2 [Kenneth C Mills 2002].

3- The heat generation in the model has a constant value in each four steps (preheating,

plunging, stirring, drawing out and cooling) depends on calculations that based on the areas of contact, friction coefficient, rotation speed and the normal force which have approximate value (because the difficult of measuring) [Fuluthelo Masithulela 2009].

4- The heat convection coefficients (H) values are (100 W/m² C) for the bottom side of the plate and (10 W/m² C) for the top side of plate [Manthan Malde 2007].

5- The time period of each step is equal to the experiment case study.

The heat transfer conditions at specific areas and volume in the body are important to solve the problem. Heat transfer by convection takes place from top and bottom of the plate. Heat generation was taken place in the volume under the shoulder area as shown in fig.2.

RESULTS AND DISCUSSION

The FSSW process, similar to plunge phase of linear friction stir welding, provides frictional heating between the interface of the tool pin and the top sheet that effectively increase that hot workability of the specimens. With sufficient reduction in flow stress at temperature a combination of forging and stirring joints the two sheets without melting the base materials. Heat generation during the plunge phase softens materials that are mixed both axially about the tool and vertically through the thickness of the sheet interface [Y. Hovanski, et al., 2007].

The experimental results in sample 1 (700rpm) and numerical results are shown in fig.3 which represents the value of temperature have a small difference at the end of the stirring stage because the metal became very soft at high temperature then the heat generation will decrease whereas the numerical solution assumed constant heat generation at each stage.

As tool rotation speed increase from 700 rpm to 900 rpm for a given preheating time, plunging time and depth, It will cause an increase in shear force (weld force) as shown in fig.4, Maximum lap shear weld failure force of 9500 N was obtained at tool rotation speed 900 rpm, because the increase in rotational speed to certain value leads to increase in temperature and material flow around the tool, as represented in the numerical model in fig.5 and

6 which show that the temperature distribution at 210 sec (maximum temp) for sample 1 (700 rpm) and sample 2 (900 rpm).

CONCLUSIONS

A three-dimensional thermal model including the thermomechanical effect of the weld material is developed for the FSSW of Al-alloy, in order to build qualitative framework to understand the thermomechanical process in FSSW. Modeling and measurement of the temperature evolution in the FSSW of 2024-T6 Al alloy is conducted, and the experimental values validate the efficiency of the proposed model. The good agreement between the prediction and measurement temperature at the point of the end of lap show that the temperature distribution at the prediction model is acceptable. The increase of the rotational speed from 700 rpm to 900 rpm for a fixed other parameters caused an increase mechanical properties of the weld joint.

REFERENCES

- Ayad M. Takahakh "Effect of Tool Rotational Speed on Properties of 1060 Aluminum Friction Spot Stir welding" F.I.T. Scientific International Conference 2010.
- D. Jacquina B. de Meesterb, A. Simarb, D. Deloisonc, F. Montheilleta, C. Desrayauda "A simple Eulerian thermomechanical modeling of friction stir welding" *Journal of Materials Processing Technology* 211 (2011) 57–65.
- Fulufthelo Masithulela "Conceptual Design of a FSSW Machine for Joining Rails" M.Sc. research at University of the Witwatersrand, Johannesburg, 2009.
- Kenneth C Mills "Recommended values of thermophysical properties for selected commercial alloys" Woodhead Publishing Limited 2002.
- Malafaia, A. M. S, Milan, M.T., Oliveira, M. F., Spinelli, D. "Fatigue behavior of friction stir spot welding and riveted joints in an Al alloy" *ScienceDirect Procedia Engineering* 2 (2010) 1815–1821.
- Manthan Malde " thermomechanical modeling and optimization of FSW" *COMSEL News a technical computing magazine*, www.comsel.com, 2007.
- Thomas, W.M., E.D. Nicholas, J.C. Needham,. Friction-stir butt welding. GB Patent No. 9125978.8, International patent application No. PCT/GB92/02203(1991).
- Y. Hovanski, M .L. Santellab, G. J. Grant, "Friction stir spot welding of hot stamped boron steel", *Scripta materialia* 57 (2007)873-876.



Fig.1 FSSW process using CNC machine in the workshop at Nahraien University represents the welded plates, clamping, tool, and thermocouple device.

Table 1 Friction spot stir welding parameters.

Sample	Rotation speed (rpm)	Preheating time (sec)	Plunging time (sec)	Stirring time (sec)	Depth of pin plunging (mm)
1	700	30	120	60	7
2	900	30	120	60	7

NUMERICAL MODEL

Table 2 Thermal properties of Al 2024 [Kenneth C Mills 2002].

Temperature C	Density kg/m ³	Heat Capacity kJ/kg	Thermal Conductivity W/(m ² .C)
25	2785	850	175
200	2750	950	193
400	2707	1000	190
538	2674	1100	188
632	2500	1140	85

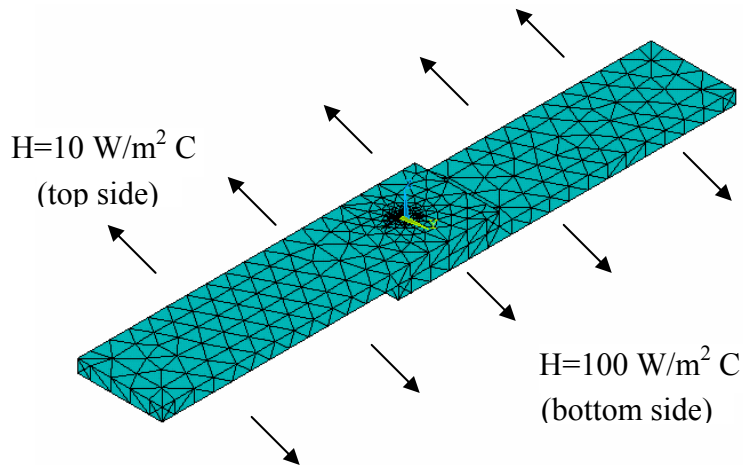


Fig.2 The mesh geometry with conditions of welding process.

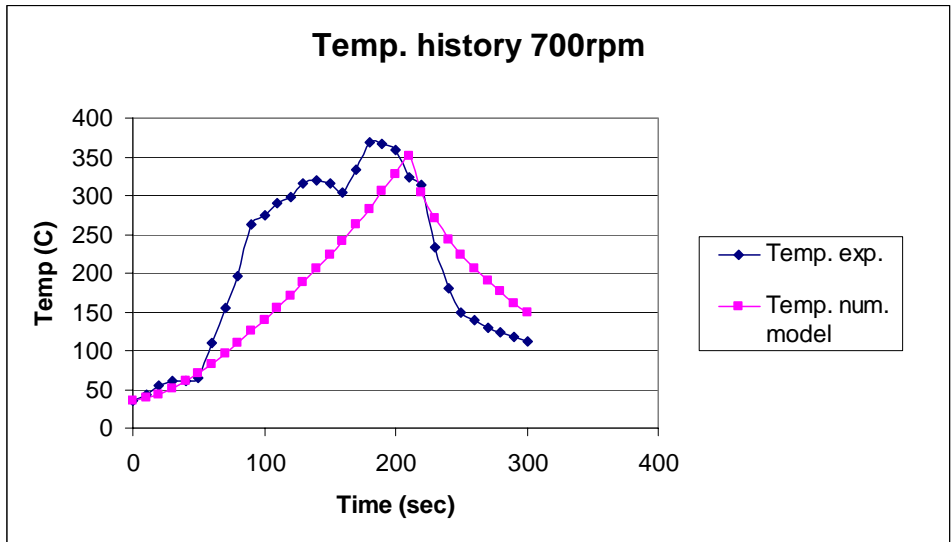


Fig.3 Temperature history comparison of exp. and num. models, sample 1 (700rpm).

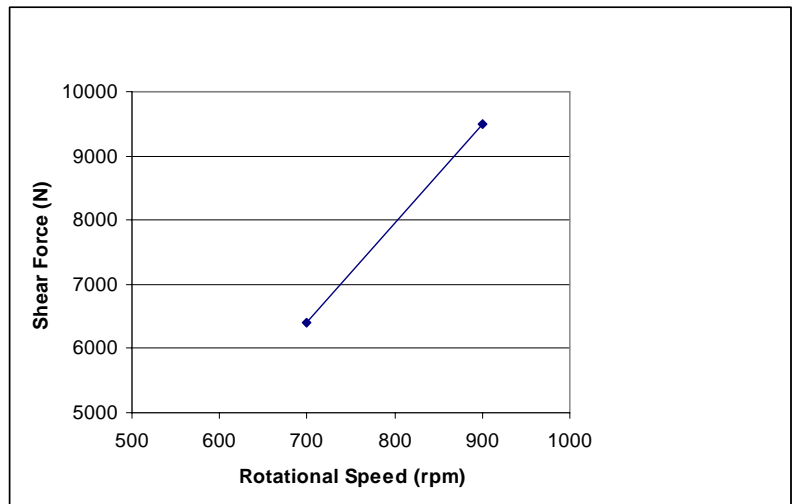


Fig. 4 Effect of rotational speed on the weld force that measured in the laboratory of Mech. Eng. Dep. at Nahrai University .

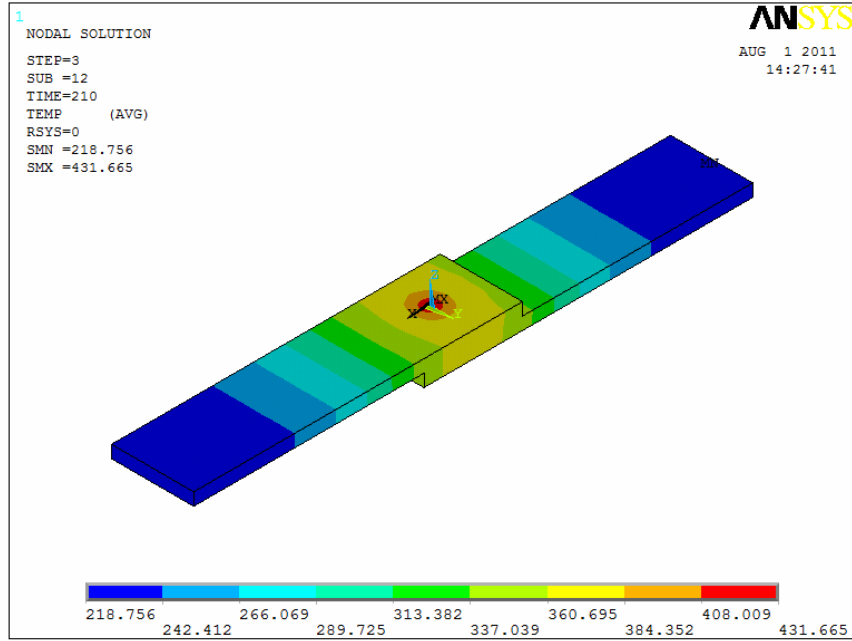


Fig. 5 The temperature distribution at 210 sec for 700 rpm.

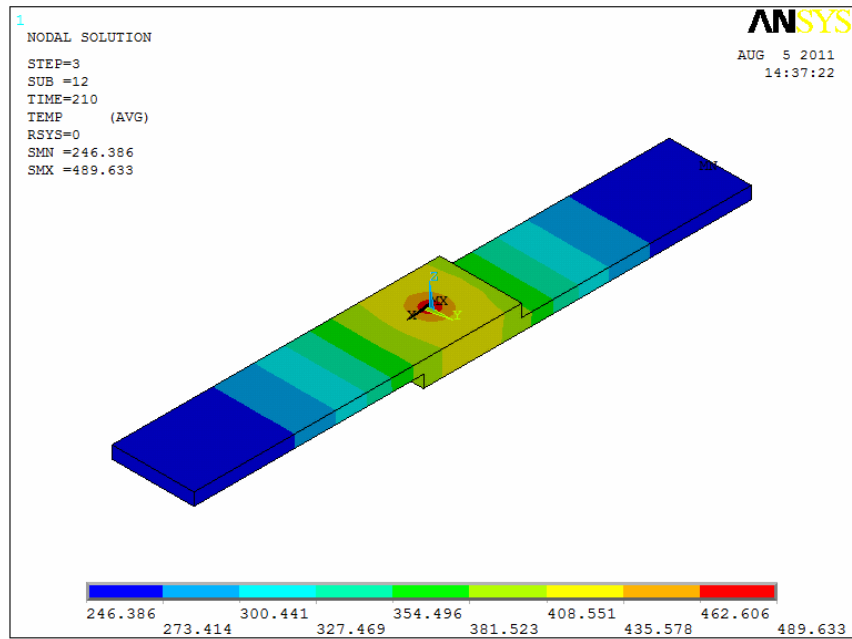


Fig. 6 The temperature distribution at 210 sec for 900 rpm.